ornl

ORNL-6924

OAK RIDGE
NATIONAL
LABORATORY

LOCKHEED MARTIN

Fossil Energy Program Annual Progress Report for April 1996 Through March 1997

R. R. Judkins
Program Manager

Fossil
Energy
Program

MANAGED AND OPERATED BY
LOCKHEED MARTIN ENERGY RESEARCH CORPORATION
FOR THE UNITED STATES
DEPARTMENT OF ENERGY

ORNL-27 (3-96)

ORNL-6924

FOSSIL ENERGY PROGRAM

FOSSIL ENERGY PROGRAM ANNUAL PROGRESS REPORT FOR APRIL 1996 THROUGH MARCH 1997

R. R. Judkins
Program Manager

July 1997

Prepared for the
DOE Office of Fossil Energy
(AA, AB, AC, AW, AZ, SA)

Prepared by the
OAK RIDGE NATIONAL LABORATORY
Oak Ridge, Tennessee 37831-6285
Managed by
LOCKHEED MARTIN ENERGY RESEARCH CORP.
for the
U.S. DEPARTMENT OF ENERGY
under Contract DE-AC05-96OR22464

CONTENTS

FOSSIL ENERGY PROGRAM ANNUAL PROGRESS REPORT FOR APRIL 1996 THROUGH MARCH 1997[1]

R. R. Judkins, Program Manager

ABSTRACT

This report covers progress made during the period April 1, 1996, through March 31, 1997, for research and development projects that contribute to the advancement of various fossil energy technologies. Projects on the Fossil Energy Program are supported by the DOE Office of Fossil Energy, the DOE Federal Energy Technology Center, the DOE Fossil Energy Clean Coal Technology Program, the DOE National Petroleum Technology Office, and the DOE Fossil Energy Office of Strategic Petroleum Reserve.

INTRODUCTION

The Oak Ridge National Laboratory (ORNL) Fossil Energy Program research and development activities, performed for the Department of Energy (DOE) Assistant Secretary for Fossil Energy, cover the areas of coal, clean coal technology, gas, petroleum, and support to the Strategic Petroleum Reserve. The coal activities include materials research and development; environmental analysis support; bioprocessing of coal to produce liquid or gaseous fuels; and coal combustion research. The work in support of gas technologies includes activities on the Advanced Turbine Systems Program, primarily in the materials and manufacturing aspects. Several activities are contributing to petroleum technologies in the areas of computational tools for seismic analysis and the use of bioconversion for the removal of impurities from heavy oils.

The Fossil Energy Program has projects in several ORNL divisions. Included as part of the Fossil Energy Program is the technical management of all activities on the DOE Fossil Energy Advanced Research and Technology Development (AR&TD) Materials Program. The AR&TD Materials Program includes research at other DOE and government laboratories, at universities, and at industrial organizations.

[1]Research sponsored by the U.S. Department of Energy, Office of Fossil Energy, under contract DE-AC05-96OR22464 with Lockheed Martin Energy Research Corp.

MATERIALS RESEARCH AND DEVELOPMENT

Materials research and development activities at Oak Ridge National Laboratory include development of ceramic composites for high temperature applications; new alloys with unique mechanical properties for advanced fossil energy systems; development of functional materials, such as ceramic filters, ceramic membranes, and carbon materials; and corrosion research to understand the behavior of materials in coal processing environments. The transfer of technology developed on this program is enhanced through interactions with industry and joint research programs with those interested in using the technology. Transfer to industry of the technology developed on the program is reflected in an active CRADA involvement.

ENVIRONMENTAL ANALYSIS SUPPORT

Activities in environmental analysis support included assistance to the Federal Energy Technology Center (FETC) at Morgantown and Pittsburgh in reviewing and preparing documents required by the National Environmental Policy Act (NEPA) for projects selected for the Clean Coal Technology (CCT) Program and the Combustion 2000 Program. An important activity was the preparation for Morgantown of an Environmental Assessment (EA) for the proposed atmospheric circulating fluidized bed (CFB) technology to be demonstrated in Seward, Pennsylvania. Another important activity was the initiation for Pittsburgh of an Environmental Impact Statement (EIS) for a new coal- fired Low Emission Boiler System (LEBS) for electric power generation at the proof-of-concept scale.

BIOPROCESSING RESEARCH

Work on the Fossil Energy Bioprocessing Research Program includes fundamental research for coal applications that investigates advanced reactor design for conversion of coal and coal liquids, the use of enzymes in pure organic media, and development of biological processes for the conversion of coal residuum. In addition, the program includes studies on advanced bioreactor systems for the treatment of flue gases and the conversion of synthesis gas to liquid fuels, removal of heteroatoms from heavy oils, renewable hydrogen production, and remediation

of oil containing soils. The program also includes natural gas and oil technology partnership support and studies on crude oil composition and oil recovery.

COAL COMBUSTION RESEARCH

It is known that fossil energy combustion devices, such as fluidized beds and pulsed combustors, can exhibit characteristic features of deterministic chaos. The ability to measure and describe chaotic components will contribute to greatly improved methods for characterizing, modeling, designing, and controlling commercial fossil energy processes such as combustion, coal gasification, hot-gas cleanup, and oil retorting. The Fossil Energy Program is involved in the evaluation of chaotic components in data from fluidized beds and other coal combustion processes.

FOSSIL FUEL SUPPLIES MODELING AND RESEARCH

The Strategic Petroleum Reserve (SPR) is a government-owned stockpile of crude oil intended to serve as a buffer against possible oil market disruptions. The overall purpose of this project is to develop and apply improved models and tools for SPR management. Current project efforts emphasize developing new modeling tools to explicitly and flexibly portray oil market uncertainty and SPR planning risk. Another task in this program area is the development of advanced computational tools for three-dimensional seismic analysis.

ADVANCED TURBINE SYSTEMS

The objective of the Advanced Turbine Systems Program, sponsored by the DOE Offices of Fossil Energy and Energy Efficiency and Renewable Energy, is to develop ultra-high efficiency, environmentally superior, and cost competitive gas turbine systems for utility and industrial applications. One of the supporting elements of the ATS Program is the Materials/Manufacturing Technologies Task. The objective of this element is to address the critical materials and manufacturing issues for both industrial and utility gas turbines.

MATERIALS RESEARCH AND DEVELOPMENT

R. R. Judkins

Materials research and development activities at Oak Ridge National Laboratory include development of ceramic composites for high temperature applications; new alloys with unique mechanical properties for advanced fossil energy systems; development of functional materials, such as ceramic filters, ceramic membranes, and carbon materials; and corrosion research to understand the behavior of materials in coal processing environments. The transfer of technology developed on this program is enhanced through interactions with industry and joint research programs with those interested in using the technology, as well as an active CRADA involvement.

FABRICATION OF FIBER-REINFORCED COMPOSITES BY CHEMICAL VAPOR INFILTRATION

T. M. Besmann, K. J. Probst, and D. P. Stinton

ABSTRACT

Silicon carbide-based heat exchanger tubes are of interest to energy production and conversion systems due to their excellent high temperature properties. Fiber-reinforced SiC is of particular importance for these applications since it is substantially tougher than monolithic SiC, and therefore more damage and thermal shock tolerant. This paper reviews a program to develop a scaled-up system for the chemical vapor infiltration of tubular shapes of fiber-reinforced SiC. The efforts include producing a unique furnace design, extensive process and system modeling, and experimental efforts to demonstrate tube fabrication.

INTRODUCTION

Fiber-reinforced SiC-matrix composites are candidates for a number of high temperature applications due to their high-temperature strength, high thermal conductivity, light weight, thermal shock resistance, creep resistance, and damage tolerance. However, in the current commercial isothermal, isobaric chemical vapor infiltration process, thick-walled parts are difficult to densify. A leading alternative process is forced chemical vapor infiltration (FCVI) (1, 2). In FCVI, a preform is placed in a reactor where one side is heated and the other side is cooled, resulting in a thermal gradient across the preform. The reactant gases are constrained to flow from the cooled to the heated side, undergoing a surface, chemical vapor deposition reaction forming the ceramic matrix and an effluent gas. In the case of SiC deposited from chlorosilanes, the effluent HC1 gas, has a poisoning effect on the reaction rate. This poisoning, combined with the depletion of the reactant, tends to retard the deposition rate. However, since the gases are traveling toward the hot side of the preform their temperature increases, resulting

in faster deposition rates due to the Arrhenius behavior of the deposition reaction. Control over deposition is thus maintained by using the increase in temperature to offset reactant depletion and effluent gas buildup and poisoning effect.

In the current work, emphasis is on the development of composites with tubular geometries. In order to demonstrate the fabrication of a prototypical tube, the efforts have centered on component diameters approaching 100 mm with a 6.4 mm wall thickness. As a result, a unique furnace system was designed and constructed that facilitates the FCVI of such tubes with lengths of 300 mm. Supporting the developmental effort has been extensive process modeling which has successfully described and aided in the optimization of the FCVI of composite plates (3,4).

CVI MODEL

The modeling of CVI involves the mathematical description of transport and reaction phenomena within a simulation domain. The simulation domain for the tube FCVI system includes the fibrous preform, fixturing, and open gas space. The open spaces include the gas injection system and the area between the preform and the heating element. Fundamental processes to be modeled include heat transfer by conduction, convection, and radiation, transport and reaction of gaseous reactant species, and pressure-driven flow of the gas. Differential equations representing these phenomena can be written in the following steady-state form:

$$\nabla(\rho u \phi) = \nabla \cdot (\Gamma \nabla \phi) + S \qquad [1]$$

where ϕ is temperature, pressure, or concentration, u is the gas velocity, ρ and Γ are constants, and S is a source term. Using the finite volume method of Patankar (5), the discretized version of this equation is solved over the simulation domain which is divided into control volumes.

Heat Transfer

The heat transfer equation contains both diffusion and convection components, and a source term:

$$\nabla\left(C_p\, u\, T\right) = \nabla\cdot(\mathrm{K}\nabla T) + S \qquad [2]$$

where C_p is the heat capacity of the flowing gas and K is the thermal conductivity of the material. The source term S contains any heat generated or absorbed by the volume element, such as heat from chemical reactions or from absorption of microwave energy. This source term also will be used to account for the thermal radiation.

Calculation of the diffusive and convective contributions to the heat balance for each volume element is straightforward given the flow rate and heat capacity of the gas, the thermal conductivities of the materials, and the thermal boundary conditions. The heat flux terms for each volume element depend only on these quantities and on the temperatures of the adjoining volume elements. Since the radiation contribution may depend on the temperatures of more distant volume elements, these cannot be included as flux terms in the same manner. Instead, these are calculated and included as a source term. To do this a ray tracing program is coupled to the main finite-volume program as a pre-processing step. Based on the discretization of the simulation domain the ray tracing program calculates the view factors of the control volume surfaces. The view factors are then stored for later use. During the solution of the heat transfer equation the view factors are used to calculate the energy exchange between the radiating surfaces by standard formulas based on the nodal temperatures. The radiant energy is then added as a source term to the heat flow equation. To obtain a self-consistent solution several iterations of the heat flow equation are required to incorporate the non-linear behavior of the radiant energy exchange.

Mass Transport and Reaction

The flow of the carrier gas and the concentrations of reacting species are determined by differential equations in the form of equation [1]. For pressure-driven gas flow,

$$\nabla \cdot \left(\frac{k}{\mu V} \nabla P \right) = 0 \qquad [3]$$

where k is the Darcy permeability for the material of each volume element, V is the gas molar volume, and μ is the gas viscosity. This formulation of gas transport does not include source or convective (inertial) terms. It will not be accurate for high velocity gas flow in open reactors but is suitable for the pressure-driven gas flow through semi-permeable materials as is the case for FCVI.

The transport equation for the reacting species includes convection, diffusion, and source terms,

$$\nabla (u\ C_i) = \nabla \cdot \left(D_i^{eff} \nabla C_i \right) + S \qquad [4]$$

where C_i is the species concentration and D_i^{eff} is the effective diffusion coefficient for species i.

Two species are included in the relationship for SiC deposition, methyltrichlorosilane (MTS) and HCl. The MTS is the input species which decomposes into solid SiC which deposits on the preform fibers and gaseous HCl, which is a by-product. The matrix deposition rate depends on the concentrations of both species. The carrier hydrogen, while playing a catalytic role, is not considered.

The coupled systems of differential equations for temperature, pressure, and chemical species concentration are solved in the steady-state. For a selected time increment the local reaction rate is used to calculate a new density for each preform volume element. A new steady-state solution is then calculated and the density incremented again, producing a series of "snap shots" of the densification process.

MODELING TUBULAR GEOMETRY

In a preliminary effort, the CVI model has been applied to a system for preparation of tubular composites by FCVI. The preform is made up of seven layers of Nextel 312™ (alumino-borosilicate fiber, 3M Company, Minneapolis, MN) cloth. The calculations are performed in cylindrical geometry due to its ease of use and symmetry. The preform, fixturing, and open gas space are discretized into a grid of radial and axial volume elements. No discretization in the θ-direction is considered. The grid size chosen for the modeling domain is 31 radial volume elements by 49 axial volume elements. The preform itself is discretized into six radial volume elements and 29 axial volume elements. The preform is 37 cm in length and 6.4 mm in thickness with an inside diameter of 4.8 cm, and has a 40% fiber volume.

The transport properties for all materials in the modeling domain are defined in separate material files. The thermal conductivities for the graphite, stainless steel, preform, and ceramic fiberboard which make up the structure of the system are functions of temperature. The hydrogen heat capacity, viscosity, and binary diffusivities of MTS and HCl in hydrogen are also functions of temperature. The, thermal conductivity, permeability, and surface area of the preform are functions of fractional density.

Several key boundary conditions are applied to the model. The preform is heated by a cylindrical furnace which surrounds it and is lined with a graphite coating chamber. The thermal gradient is imposed by a stainless steel cooling line that is positioned along the centerline of the system. The temperatures of the graphite coating chamber and stainless steel cooling line are fixed. The total molar flux and mole fraction of MTS are specified at the gas inlet, which is at the centerline on the left side of the preform. Atmospheric pressure is fixed at the gas exhaust and the ends of the domain are specified as adiabatic.

The modeling considered in this paper investigates three key parameters that affect the CVI process: The temperature of the graphite coating chamber, the ratio of hydrogen to MTS

(alpha), and the hydrogen flow rate. The temperature range is 1100°C to 1200°C, the alpha range is 5 to 10, and the hydrogen flow rate range is 2.5 to 7.5 l/min.

Figure 1 shows the preform density profile after 24 hours of infiltration at the baseline modeling parameter values of 1200°C, an alpha of 5, and a hydrogen flow rate of 5 l/min. The profile represents a longitudinal section of the tube with the hot side at the top and the cooled side at the bottom. τ is the dimensionless thickness and η is the dimensionless length. Figure 2 illustrates an increase in alpha to 10 and Fig. 3 uses a hydrogen flow rate of 7.5 l/min. Figures 4 and 5 show preform temperature profiles at the baseline conditions at the start of infiltration and after 12 hours, respectively.

The density profiles in Figs. 1-3 show approximately the same radial and axial gradients. The densities are highest at τ=1 and η=0 and 1. The fractional density is higher in these areas because of the higher temperature. The higher temperature at the ends is due to the graphite felt insulation placed just outside the preform. In Fig. 2, the absolute density values are somewhat lower across the preform. The higher alpha used in Fig. 2 lowers the MTS concentration in the gas phase and thus lowers the SiC deposition rate. Due to the greater reactant flux, the absolute densities in Fig. 3 are slightly higher than those of Fig. 1.

In Fig. 4, the temperature gradient across the preform thickness at η=0.5 is about 80°C. At lower η, near the gas inlet, the gradient is greater due to the radial convective gas cooling. Figure 5 shows the temperature profile after 12 hours of infiltration. The radial temperature gradient is reduced to 50°C due to enhanced radial heat conduction by the SiC matrix in the gas inlet region.

EXPERIMENT

An initial infiltration experiment has been attempted utilizing a tubular preform of the same material and dimensions as that described in the modeling efforts. The Nextel™ preform was rigidized by impregnation with a resin to prevent it from sagging in the horizontal furnace.

The infiltration conditions utilized were a hydrogen flow of 5 l/min, an alpha of 4.5, a coating chamber temperature of 1200°C, and a centerline coolant temperature of 50°C. The infiltration time was 24 hours.

Figure 6 is a photograph of the tube showing that, at least superficially, it is well-infiltrated. The average fractional density based on weight is approximately 80%. However, adjustments for the somewhat heavy overcoating of the inner surface of the tube may cause some uncertainty. The model estimated an average preform fractional density of 76% after 24 hours of infiltration.

CONCLUSIONS

The efforts to model the FCVI of tubular geometries has indicated generally successful conditions for infiltration. Decreasing the coating chamber temperature increases the densification time. This reduces the temperature across the preform, causing slower deposition rates. Increasing alpha also increases the densification time. At higher hydrogen flow rates, the densification time decreases. However, a higher gas flow imposes a higher temperature gradient near the gas inlet.

Application of the modeling conditions to experiment gave initial indications that high quality composite tubes can be fabricated, which is also indicated by the experimental results.

Future efforts will be focused on better validating the model through comparison with experiment, optimizing processing time and composite density, and increasing the preform outer diameter to 10 cm.

ACKNOWLEDGEMENTS

The comments and suggestions of T. N. Tiegs and L. L. Snead are gratefully acknowledged.

REFERENCES

1. W. J. Lackey and A. J. Caputo, *U. S. Patent No. 4,580,524* (April 8, 1986).

2. T.M. Besmann, B.W. Sheldon, R.A. Lowden, and D.P. Stinton, *Science* **253**, 1104 (1991).

3. T.M. Besmann, in *Proc. High Temperature Matrix Composites II, Ceramic Transactions,* A. G. Evans and R. Naslain, Editors, **58**, p. 1, American Ceramic Society, Westerville, OH (1995).

4. W.M. Matlin, D.P. Stinton, T.M. Besmann, and P.K. Liaw, in Ceramic Matrix *Composites - Advanced High-Temperature Structural Materials*, R.A. Lowden, M.K. Ferber, J.R. Hellman, K.K. Chawla, and S.G. DiPietro, Editors, **365,** p. 309, Materials Research Society, Pittsburgh, PA (1995).

5. S. V. Patankar, *Numerical Heat Transfer and Fluid Flow*, Hemisphere Publishing Corp., New York (1980).

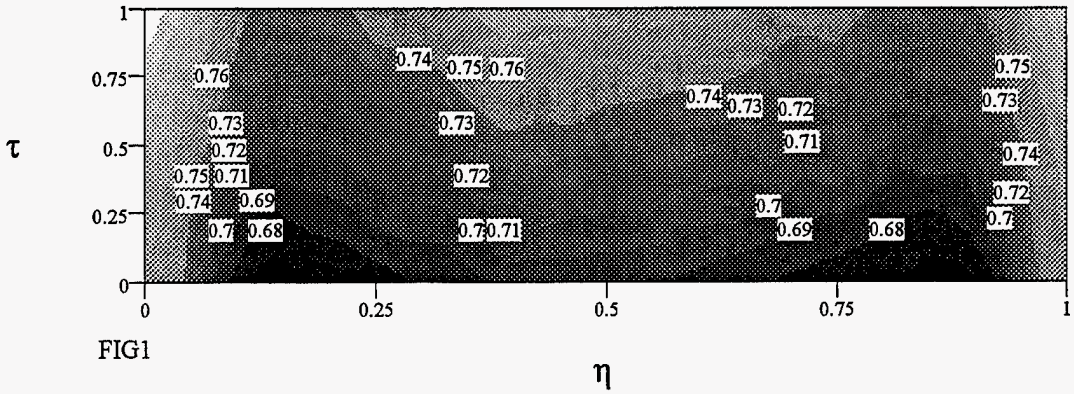

Figure 1: Density profile at baseline conditions.

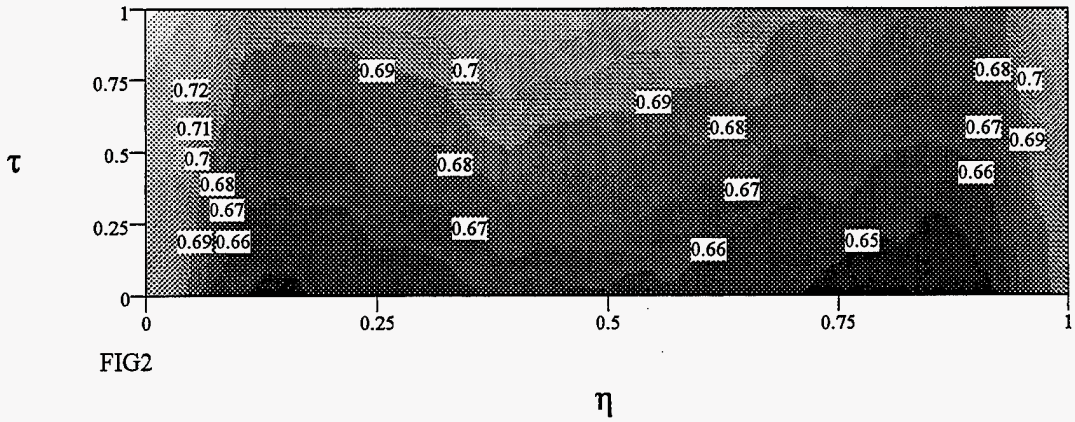

Figure 2: Density profile when alpha = 10.

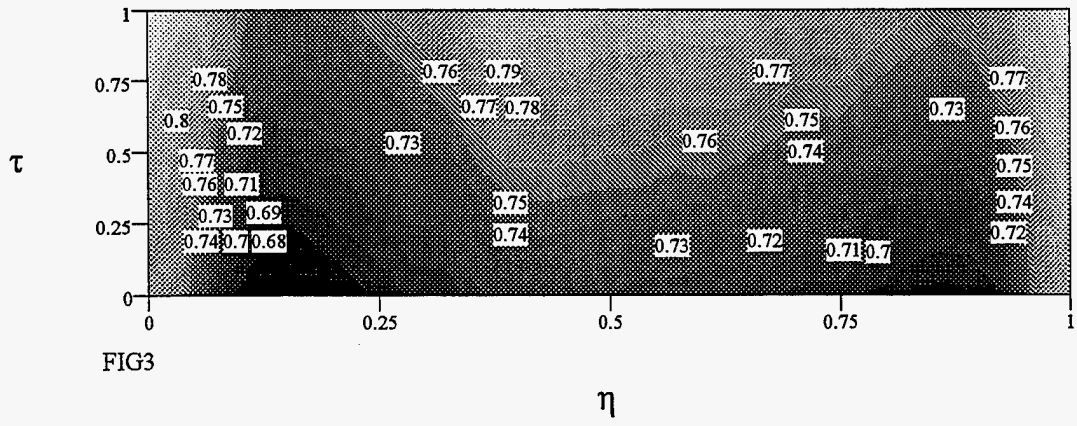

Figure 3: Density profile when hydrogen flow rate = 7.5 l/min.

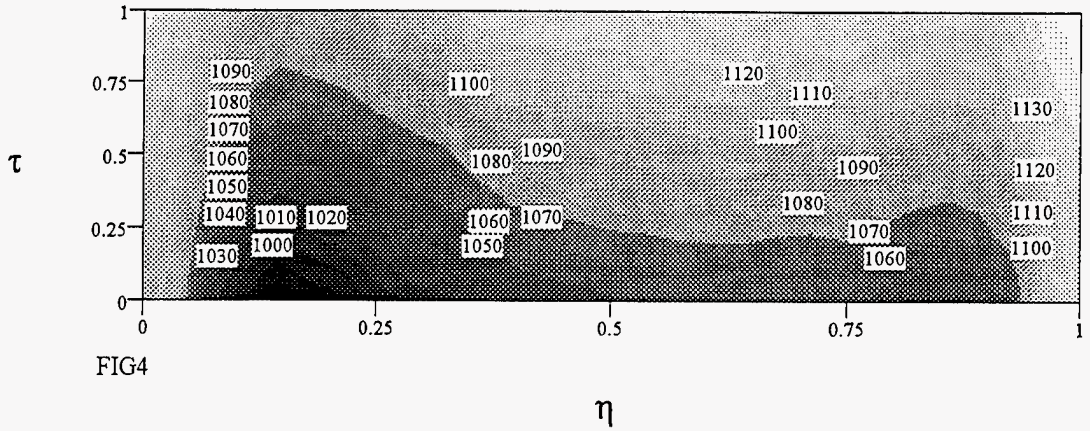

FIG4

Figure 4: Baseline temperature profile at the start of infiltration.

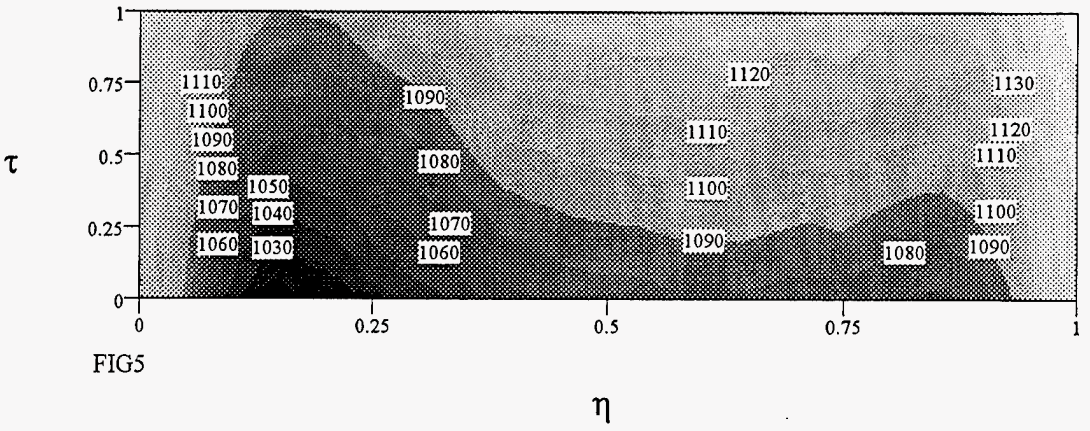

FIG5

Figure 5: Baseline temperature profile after 12 hours of infiltration.

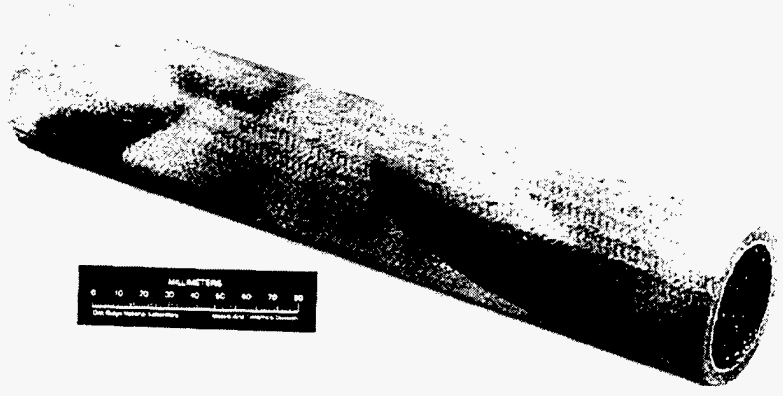

Figure 6: Photograph of Nextel 312^{TM}, SiC matrix composite tube fabricated by FCVI.

OXIDE COATING DEVELOPMENT

D. P. Stinton, D. M. Kupp, and R. L. Martin

ABSTRACT

SiC-based heat exchangers have been identified as the prime candidate material for use as heat exchangers in advanced combined cycle power plants. Unfortunately, hot corrosion of the SiC-based materials created by alkali metal salts present in the combustion gases dictates the need for corrosion-resistant coatings. The well-documented corrosion resistance of CS-50 combined with its low (and tailorable) coefficient of thermal expansion and low modulus makes CS-50 an ideal candidate for this application. Coatings produced by gelcasting and traditional particulate processing have been evaluated.

INTRODUCTION

Gelcasting of sodium-zirconium-phosphate (NZP) based materials[1-3] has been identified as a candidate process for applying high temperature, corrosion resistant coatings on to ceramic substrates. The gelcasting process, normally most useful in producing relatively large or complex ceramic or metallic monoliths, is being considered as a technique for applying conformal coatings to SiC composite heat exchanger tubes. The corrosion resistance of the $Ca_{0.5}Sr_{0.5}Zr_4P_6O_{24}$ (CS-50) material for the prescribed application has been well documented[4,5]. This characteristic, combined with its low (and tailorable) coefficient of thermal expansion (CTE) makes CS-50 an ideal candidate for evaluation in this application. The major hurdle has been in identifying an application technique which is both technically and economically feasible. While various chemical vapor deposition (CVD) and physical vapor deposition (PVD) techniques can be used to apply desirable coatings to idealized substrates, the complex composition of the coatings and the large size of the heat exchanger tubes (up to 15 feet long) makes the use of these techniques difficult and costly. Application techniques such as plasma spraying have also been tried with varying degrees of success.

By combining the attributes of polymer chemistry with those of traditional particulate processing, gelcasting has proven itself to be a viable contender in this area. However, while gelcasting of CS-50 based monoliths has proven to be relatively straightforward, the mechanical interaction of a gelcast body with a rigid substrate throughout the various processing steps addresses some of the most fundamental (and persistent) problems in traditional particulate processing (e.g. drying/sintering shrinkage and thermal expansion).

The development of an NZP-based coating was undertaken from a product development (rather than a scientific interest) point of view in an effort to maximize the amount of applicable progress made. Experiments were conducted using multivariate, small sample sizes. Since both the gelcasting process and the NZP type materials are well understood, it made sense to directly focus upon the new application, i.e. the gelcasting of NZP materials as a coating on a SiC/SiC composite substrate.

Since the gelcasting of CS-50 was previously proven to be feasible in standard gelcasting applications (i.e. monolithic geometries), an effort to improve the basic process was undertaken. The major problems envisioned in the process (and initially addressed) included:

1. Shrinkage of the CS-50 coating during processing leading to catastrophic failure of the coating.
2. Matching of the CTE of the coating to that of the substrate without detrimentally affecting other downstream processes.
3. Selection of a stable material systems which is non-reactive with the substrate and offers maximum corrosion protection.

From a fundamental standpoint, tailoring of the CTE of the coating to match that of the substrate is straightforward. By combining the CS-50 with a material having a CTE greater than that of the substrate in the proper ratios, a material system having the appropriate CTE could be customized. By approximating the CTE of the SiC ceramic matrix composite, the CTE of CS-50 can be increased to that of the SiC substrate by the correct addition of alumina for example. Trials evaluating various coating to substrate CTE ratios must be carried out to determine the optimal coating CTE.

One of the major obstacles in the application of a particulate coating on to a substrate is the accommodation of the shrinkage of the applied coating due to such things as polymer cross linking, drying, binder removal, etc. The most direct way of reducing such shrinkage is through the optimization of the particle packing or solids loading of the powder system (i.e. slurry) being used. While many complex models exist for predicting and interpreting particle packing behavior, it is sufficient for current purposes to simply maximize the amount of solid material per quantity of slurry liquid (water and/or liquid chemicals) while still maintaining a usable slurry rheology. By maximizing the solids loading level, more particle to particle contacts are generated, reducing shrinkage through particle rearrangement and increasing green strength.

Assuming a roughly equiaxed particle morphology where random particle orientation produces a more or less homogeneous, isotropic particle array, a solids loading level can generally be maximized by using a powder with a very narrow (i.e. monosized) or very broad particle size distribution. This distribution width, S_w, can be calculated from the following:

$$S_w = \frac{2.56}{\log\left[\frac{d_{90}}{d_{10}}\right]} \qquad \text{where}$$

d_{90} = particle diameter equivalent to 90% of the cumulative distribution

d_{10} = particle diameter equivalent to 10% of the cumulative distribution

Ideally, the distribution width should be very wide ($S_w \leq 2$) or very narrow ($S_w \geq 7$) to achieve maximum particle packing density (i.e. solids loading) in a slurry or green/fired component. Since it can be difficult and expensive to produce a monosized powder in reasonable quantities, a powder with a wide particle size distribution is generally more desirable. Since the base low expansion powder will likely be amended with a relatively high CTE material to develop a suitable coating CTE, intelligent selection of the "modifier" in terms of thermomechanical properties and particle size characteristics will also enhance the particle packing and rheological behavior of the powder system.

DISCUSSION OF CURRENT ACTIVITIES

The processability and composition of the components of the corrosion resistant coating were the two basic concerns initially addressed. Sodium-zirconium-phosphate (NZP) material ($Ca_{0.5}Sr_{0.5}Zr_4P_6O_{24}$) was selected as the primary component based on its low CTE and excellent corrosion resistance[4,5]. As previously discussed, the CTE of the NZP material (grade CS-50 from LoTEC, Inc.) was selected as the base material to be amended by another corrosion resistant material in order to tailor the coating CTE. Alumina (grade RCHP/no MgO from Reynolds) was selected as the modifying material based on previous gelcasting performance and its generally excellent corrosion resistance. This specific grade of material has a fine median particle size (<1 μm) which would enhance the packing and rheological behavior of a CS-50/alumina mixture. Initially, gelcasting of pure CS-50 was carried out to establish a baseline procedure for the NZP family of base materials. Prior art in the gelcasting of these materials established basic formulations and procedures. The standard monomer solution (which is crosslinked in a downstream process) was a 15 wt. % aqueous solution of a 6:1 ratio of MAM (methacrylamide) to MBAM (methylene bisacrylamide). This solution served not only as the polymeric precursor but also as the fluid in which the particulate materials were ball milled and mixed. Since it was critical to maximize the solids loading of the slurry (i.e. volume % ratio of solids to liquids), solids loading levels of the slurries began at ~ 50 vol.% and were gradually increased until the desired viscosity had been reached. Eventual solids loading levels of ~60 vol. % were reached for the pure CS-50 gelcastable slurry.

Milling was carried out in HDPE jars (~750 ml.) with 6 mm. diameter zirconia media. Darvan 821A was added to the precursor solution as a dispersant. Generally, gentle milling was carried out only to disperse, homogenize and wet the powder, not necessarily to modify the particle shapes or size distributions.

Once it was determined that an optimized solids loading level had been reached, the slurry was strained through a -325 mesh screen to remove media and dried mill residue. The slurry was then de-aired using a vacuum dessicator until a bubble-free slurry resulted. At this point the slurry is suitable to begin the casting procedure. A combination of crosslinking catalysts and accelerants [TEMED(tetramethylethyl diamine) and 10% aqueous solution of APS (ammonium

persulfate)] is added to convert the monomer precursor solution to a polymeric binder. Since the kinetics of crosslinking is relatively slow (and controllable), time is available to pour the slurry into a mold before complete gelation of the binder/powder system occurs.

Since the gelcasting trials of the pure CS-50 composition were successful, preliminary efforts incorporating the CTE modifier, alumina, were started. By approximating the CTE of the SiC ceramic matrix composite to be ~ 4.5 x 10^{-6}/°C, the CTE of CS-50 (3.0 x 10^{-6}/°C) can be increased to that of the SiC substrate by the correct addition of alumina for example (CTE ~ 8.0 x 10^{-6}/°C). Using the rule of mixtures as a basis for formulation, a body comprised of 70 vol. % CS-50 / 30 vol. % Al_2O_3 (66 wt. % CS-50/34 wt. % Al_2O_3) was formulated, approximating the CTE of the SiC/SiC substrate.

A particle size analysis was completed on the CS-50 powder using a Horiba LA-700 particle size analyzer. The particle size distribution for the powder was bimodal (0.3 μm and 20 μm), with a mean particle size of ~ 13.4 μm. The distribution width, S_w, is calculated to be ~1.4 (very wide). However, visually and to the touch, the powder seemed to contain a fraction of grit (i.e. large, hard agglomerates) which can be broken with moderate pressure. These agglomerates can also be disintegrated somewhat with intensive ultrasonic agitation. The mean particle size for a sample which received intensive agitation with an outboard ultrasonic horn was reduced by 17% from 13.4 μm to 11.1 μm with additional agitation (beyond that provided in the Horiba chamber prior to analysis). Furthermore, the percentage of particles greater than ~30 μm decreased from 8.5 to 4.5%, likely due to the breaking up of the hard agglomerates.

After sustained, but gentle milling, the solids loading level and related rheological behavior of the CS-50 and alumina powder mix appears to be outstanding at 70 vol. % CS-50 / 30 vol. % alumina at 66 vol. % solids loading. Approximately 0.7 wt. % Darvan 821A (based on total solids) was added as a dispersant to the 70/30 slurry in the aqueous MAM/MBAM solution. Most notable from the particle size distribution is the lack of particles greater than 20 μm in comparison to the standard and ultrasonically agitated slurries which show particle sizes for the as-received and sonicated CS-50 powder to be 60-75 μm. It appears that the low intensity ball milling done to homogenize the powder/monomer slurry, is sufficient to break up the light aggregate suspected of existing in the as-received CS-50. Once the CS-50 powder is dispersed,

along with the addition of 30 vol. % alumina, a very wide distribution width, Sw, of 1.51 is achieved. This wide distribution combined with the deagglomerated slurry components provides the basis for a high solids loading level (>66 vol. % solids). While the particle size distribution of the as-received CS-50 powder is also very wide (Sw = 1.46), the distribution appears to be an artifact of particle agglomeration and fines, not the true, primary particle size distribution measured after mechanical deagglomeration.

Two component slurries at 60/40, 70/30, 80/20 and 90/10 vol.% CS-50/alumina were prepared and evaluated for rheological behavior and powder co-processing behavior related to slurry additives (e.g. dispersants and anti-foaming agents) and critical solids loading levels. Samples 25 mm. x 25 mm. were gelcast and dried without apparent problems. Samples were processed through thermal binder removal (1°C/min. to 600°C, hold for 1 hour) and sintered in air at 1325°C for 4 hours without physical damage. Compositional analysis was not completed on any samples.

Since the processing of a gelcast CS-50/alumina monolith was successful for each composition, the application of a similar slurry to a SiC composite substrate was tried. SiC/SiC tube sections (25 mm. diameter x 20 mm. long) were dipped into each of the CS-50/alumina slurries which had been catalyzed but had not crosslinked. Multiple dips on different samples provided a variety of coating thicknesses for analysis of adhesion and cracking behavior through drying and firing steps. Freshly dipped samples were suspended in a relatively airtight container (since contact with air inhibits gelation) until gelation had completed and residual moisture had dried. After a standard binder burnout cycle was completed, the coated samples were heat treated at 1200°C (in air) for 5 days. While the sintering temperature for CS-50 based materials (especially when "alloyed" with alumina) is >1300°C, a maximum temperature of 1200°C was used to avoid degradation of the SiC composite. Relatively long sintering times were used to promote densification of the coating at the lower firing temperature and also to evaluate the thermomechanical performance of the coating.

Two distinct phenomena were investigated; coating thickness and composition. After long term firing, samples with coating thicknesses greater than about 2 mm. exhibited severe cracking throughout the surface of the coating in the form of continuous crazing, as well as deeper fissures

appearing radially on the ends of the tube section. Other substantial cracking occurred on the circumference of the tube section, apparently as a result of the shrinkage of the particulate coating during drying and sintering. Thinner coatings (<1 mm.) did not exhibit the same cracking pattern as the thicker coatings, with only a thin crack occurring at the edge of the tube section (juncture between the tube end and outside diameter). Samples of the composition 90 vol.% CS-50 /10 vol.% alumina also showed reduced overall cracking due to proper tailoring of the CTE. In these cases, a continuous, adherent and somewhat densified coating was developed.

As a result of the improved adhesion and resistance to cracking associated with the reduced coating thickness, the gelcasting technique used to produce these coatings (and in general, much larger monolithic structures) was abandoned in favor of a much more straight forward "non-monomer" slurry approach. By utilizing a traditional aqueous slurry, the need for expensive and toxic monomer precursor materials was eliminated. Furthermore, the problem of gelation being inhibited by exposure to air is no longer an issue since the monomer crosslinking phase is no longer a requirement of the process. The air exposure limitation of gelcasting may have led to some costly and complicated engineering problems if larger tubes were ever to be coated.

As an initial characterization of the fired composite/coating sample, XRD was performed to determine the extent (if any) of the CS-50 degradation related to substrate exposure, prolonged high temperature use and/or the alloying with another material (i.e. alumina). Samples of 70 vol.% CS-50/30 vol.% alumina were prepared using a non-gelcasting slurry to dip coat SiC/SiC tube sections. Samples were dipped and dried followed by a binder burnout at 600°C./1hr. The coated tube sections were sintered at 900, 1000, 1100 and 1200°C for 48 hrs. A standard coating of pure CS-50 was also prepared identically and sintered at 1200°C for 48 hrs. XRD results (Figure 1) show the generation of an unidentified phase in the 70/30 sample at 1200°C. The intensity of this phase decreases with sintering temperature and does not exist in the pure CS-50 coating at 1200°C exposure. Furthermore, three low angle peaks (11-14° 2θ) which exist in the XRD trace for pure CS-50 at 1200°C decrease in intensity with increasing process temperature. While the XRD data is open to interpretation and is not fully completed, it does indicate that the addition of the alumina to the pure CS-50 as a CTE modifier reacts to form what may be an undesirable phase.

Without further analysis or actual corrosion testing to evaluate the performance of the unidentifiable phase(s), it was decided to consider modification of the CS-50 CTE with other materials such as:

1. 4% Y_2O_3 stabilized ZrO_2
2. 12% CeO stabilized ZrO_2
3. Cr_2O_3

Using established procedures and general compositions, the above materials were used to make three new slurries as follows: 90 vol.% CS-50/10 vol%. modifier at 65 vol.% solids loading. SiC composite tube sections were dip coated with each slurry and dried. Following binder burnout, the samples were heat treated at 1200°C for 4 days.

SUMMARY

Initial trials using alumina modified CS-50 indicated that a relatively thin coating of a 90 vol.% CS-50/10 vol. % alumina provided the best adhesion to the SiC tube section in addition to providing a relatively crack free, continuous coating. Corrosion tests were not performed on these samples, but x-ray diffraction indicated a possible degradation of the CS-50 or generation of a phase non-existent in the as-received raw materials. A new selection of CTE modifiers based on individual corrosion resistance replaced the alumina. Stabilized ZrO_2 and Cr_2O_3 were added to the CS-50 in the same relative volume fraction. It became apparent that it was not the matching of the coating and substrate CTEs, but the relative CTEs which were important. Therefore, as a convenient and comparable starting point, the 90/10 ratio of CS-50/CTE modifier was maintained. The ZrO_2 and Cr_2O_3 modified coatings processed well and remained intact through a 1200°C/5 day soak.

In general, the theory involving maximizing the solids loading of the slurry proved to be useful. Powder particle sizes can be modified "ad nauseum" if necessary to obtain a highly loaded slurry with desirable rheological characteristics. The viscosity of a given slurry is only important as it relates to the coating technique used to apply the slurry to the substrate. If the slurry is fluid enough to mix and/or mill and can be applied by the method of choice (e.g. dipping, painting, spraying etc.) with minimal dripping or deformation, then that is the most appropriate slurry rheology.

The deviation from gelcasting technology to more traditional particulate processing also simplifies the process tremendously. Not only are the expensive and somewhat toxic chemicals avoided, but such things as working time (until gelation) and processing techniques are streamlined as well. Preliminary XRD analysis of the CS-50 plus ZrO_2 and Cr_2O_3 coatings indicated much less degradation of CS-50 than for CS-50 plus Al_2O_3. Samples of each of the new compositions have been fabricated and are awaiting CTE determination and high temperature, flowing gas corrosion tests.

REFERENCES

(1) C.-Y. Huang, D. K. Agrawal, H. A. McKinstry, and S. Y. Limaye, "Synthesis and Thermal Expansion Behavior of $Ba_{1+x}Zr_4P_{6-2x}Si_{2x}O_{24}$ and $Sr_{1+x}Zr_4P_{6-2x}Si_{2-x}O_{24}$ Systems," *J. Mater. Res.*, **9**, 2005(1994).

(2) S. Y. Limaye and R. Nageswaran, "Development of NZP Ceramic-Based "Cast-in-Place" Diesel Engine Port Liners," Final Report, LoTEC, Inc., West Valley City, UT, November 1994.

(3) T. B. Jackson, S. Y. Limaye, and W. D. Porter, "The Effects of Thermal Cycling onthe Physical and Mechanical Properties of [NZP] Ceramics"; pp. 63-80 in Ceramics Transactions, Vol. 52, *Low-Expansion Materials*. Edited by D. P. Stinton and S. Y. Limaye, American Ceramic Society, Westerville, OH, 1995.

(4) W. Y. Lee, D. P. Stinton, and D. L. Joslin, "Interaction of Low-Expansion NZP Ceramics with Na_2SO_4 at 1000°C," *J. Am. Ceram. Soc.*, **79**, 484(1996).

(5) W. Y. Lee, K. M. Cooley, C. C. Berndt, D. L. Joslin, and D. P. Stinton, "High-Temperature Chemical Stability of Plasma-Sprayed $Ca_{0.5}Sr_{0.5}Zr_4P_6O_{24}$ Coatings on Nicalon/SiC Ceramic Matrix Composite and Ni-Based Superalloy Substrates," *J. Am. Ceram. Soc.*, **79**, 2759(1996).

OXIDATION-RESISTANT INTERFACE COATINGS FOR NICALON/SiC COMPOSITES

D. P. Stinton, T. M. Besmann, and R. A. Lowden

Oak Ridge National Laboratory
Oak Ridge, Tennessee

P. K. Liaw and S. Shanmugham

University of Tennessee
Knoxville, Tennessee

ABSTRACT

Nicalon/SiC composites with thin C and C/oxide/C interfaces were fabricated. The oxide layers, mullite and Al_2O_3-TiO_2, were deposited by a sol-gel process, while the C layer was deposited by a chemical vapor infiltration method. The fabricated composites were flexure tested in both as-processed and oxidized conditions. Composites with C and C/oxide/C interfaces retained graceful failure even after 500 h oxidation at 1000°C, but with reduced flexural strengths.

INTRODUCTION

It is well established that the fiber-matrix interface plays a key role in determining the mechanical properties of ceramic matrix composites [1-3]. Currently, Nicalon-fiber/SiC-matrix composites owe their good mechanical properties at room temperature to either carbon © or boron nitride (BN) interfaces, which provide a weak interfacial bond. However, C and BN oxidize at elevated temperatures resulting in degradation of mechanical properties of these composites in oxidizing environments [3]. Hence, alternative oxidation-resistant interface materials need to be identified and developed.

Recent analytical and finite element modeling studies have indicated that low modulus interfacial coatings may be desirable to reduce residual radial compressive stresses at fiber-matrix interfaces which develop upon cooling from processing to room temperature [4, 5]. Two oxides, mullite and aluminum titanate, were chosen as interface materials for Nicalon/SiC and Nextel/SiC composites based on their relatively low modulus and their good oxidation resistance at elevated temperatures.

Mullite and aluminum titanate precursor sols were developed for coating applications [6, 7]. High temperature X-ray diffraction studies in air identified that mullite crystallizes at or above

950°C, while aluminum titanate forms at or above 1300°C. Nicalon tows were embrittled during the formation of mullite at 1000°C, and hence, there is a need to protect the fibers by an inert material during the sol-gel oxide processing. The aluminum titanate formation temperature is high and would damage the Nicalon fibers. However, Nicalon fibers dip-coated in an aluminum titanate sol and heat treated at 1000°C for 10 h in air, forming an Al_2O_3-TiO_2 mixture, were not embrittled. Based on the non-embrittlement of the fibers, the Al_2O_3-TiO_2 mixture was chosen as an alternative to aluminum titanate for an interface material. Thermochemical analysis also identified the need to protect the oxide coatings from the HCl attack, a by-product of the SiC matrix deposition reaction. In order to protect the fibers and oxides during processing, a C coating was selected because of its inertness and ease of processing.

To study the effect of protecting the fibers by an inert material during sol-gel oxide coating, oxide/C, and C/oxide/C interfaces were used with Nicalon/SiC composites, and the results were reported earlier [8]. Since composites with C/oxide/C interfaces exhibited higher flexural strengths than composites with oxide/C interfaces in the as-processed condition, C/oxide/C interfaces were given further consideration. On this basis, Nicalon/SiC composites with C/oxide/C interfaces were chosen for further investigation and a control sample, Nicalon/SiC composite with a thin C (40 nm) interface, was also fabricated.

EXPERIMENTAL PROCEDURE

Table 1 summarizes the fabricated Nicalon/SiC composites along with their interfaces, sols used for the deposition of oxides, and the C deposition time. The mullite coating was deposited using either an ethanol or 2-methoxy ethanol based mullite precursor sol, while the Al_2O_3-TiO_2 coating was deposited from an aluminum titanate precursor sol. The C layer was deposited using argon and propylene as reactants for either 15 or 30 min.

Processing of Nicalon/SiC composites involve three steps: preparation of the Nicalon preform, deposition of the interface coatings, and the infiltration of the SiC matrix. The procedure used for fabricating Nicalon/SiC composites is described in detail elsewhere [6, 8], however, a brief description is given below. Fibrous preforms were prepared by stacking 50 layers of Nicalon cloth (45 mm in dia) in a 0°/30°/60° sequence in graphite holders to a thickness of 12.5 mm thick. The C coating was deposited under isothermal and reduced pressure conditions using argon and propylene on the virgin as well as oxide-coated Nicalon preforms. The oxide precursor coatings were

produced on C-coated Nicalon preforms by vacuum infiltration of the oxide sol followed by drying at 110°C in air. This process was repeated 3-4 times till a desired coating thickness of 150-300 nm was obtained (determined by weight gain). Then, the oxide precursor coatings obtained on the preforms were heat treated in argon at 1050°C for 1 h to produce the oxide coatings. This was followed by the deposition of the outer C layer. Finally, the SiC matrix was deposited using a forced-flow thermal gradient chemical vapor infiltration process, with methyltrichlorosilane and hydrogen as reactants.

Table 1: Nicalon/SiC composites samples

CVI#	Interface	Sol used for oxide deposition	C deposition time	Oxidation time (h) at 1000°C in air
1077	C	-	30 min	24, 200, and 500
986	C/mullite/C	Ethanol based mullite precursor sol	Inner C: 15 min Outer C: 15 min	24, 200, and 500
1080	C/mullite/C	2-methoxy ethanol based mullite precursor sol	Inner C: 15 min Outer C: 15 min	24, 200, and 500
1002	C/Al_2O_3-TiO_2/C	Aluminum titanate precursor sol	Inner C: 15 min Outer C: 15 min	24, 200, and 500
1066	C/Al_2O_3-TiO_2/C	Aluminum titanate precursor sol	Inner C: 15 min Outer C: 15 min	24, 200, and 500

24 flexure bars of dimensions ~ 2.5 x 3.0 x > 33 mm were obtained from each of the fabricated composites using a standard grinding and cutting procedure. The geometrical density was determined from the weight and dimension measurements of each bar. Four to six specimens were flexure tested at room temperature in the as-processed condition and again after oxidation at 1000°C for 24 h, 200 h, and 500 h. Flexural strengths of composite bars were determined using a four-point bend test fixture (with 20 or 30 mm outer span and 10 mm inner span) on an Applied Testing System machine equipped with a 4375 N load cell. The specimen was placed in the fixture and loaded during the downward motion of the crosshead. The crosshead speed utilized was 2.54 mm/min.

After flexure testing, samples which did not completely fracture were broken by hand for fracture surface examination. The fracture surfaces were examined using a Hitachi S-800 SEM equipped with an energy dispersive X-ray system. The fiber-matrix interfaces of selected samples were examined by transmission electron microscopy using a Hitachi HF-2000 cold field emission gun microscope at 200 kV, which is equipped with a Noran/4 II EDX system. EDS patterns were obtained on fiber-matrix interfaces and were used to identify the coatings.

RESULTS AND DISCUSSION

Table 2 summarizes the geometrical density of fabricated composites along with the inner and outer C layer coating thickness, based on weight gain. The C in the control sample, composite with a C interface, was 43 nm thick. In other composites, the inner C and outer C coatings were each < 30 nm thick. The oxide coating thickness values are not indicated in Table 2 since some of the oxide coatings adhere to the graphite holder, and hence, a good estimate of their thickness cannot be obtained from the weight gain measurements.

Table 2. Density of the fabricated composites along with the C coating thickness (based on weight gain)

CVI #	Density (g/cm^3)	Inner C layer thickness (nm)	Outer C layer thickness (nm)
1077	2.36±0.14	43**	-
986	2.47±0.06	22	21
1080	2.40±0.11	22	21
1002	2.46±0.06	28	27
1066	2.45±0.07	16	16

** control sample where the total C thickness was 43 nm

Table 3 summarizes the flexural strength results of fabricated composites. It should be noted that all the fabricated composites exhibited graceful failure (composite behavior) in both as-processed and oxidized conditions. In the as-processed condition, flexural strengths of composites

were between 255 to 311 MPa, and the CVI 1080 composite (C/mullite/C interface) had the highest flexural strength. The control sample, composite with a C interface, had a flexural strength of 311±74 MPa, and is comparable to the value obtained by Walukas [9] for a composite with a 40 nm thick C interface (325±8 MPa). Flexural strengths of the composites decreased with increasing exposure time at 1000°C in air. The CVI 1066 composite (C/Al_2O_3-TiO_2/C interface) and the CVI 1080 composite (C/mullite/C interface) underwent the minimum (21%) and maximum percentage reduction (40%) in flexural strength, respectively, after 500 h oxidation at 1000°C. The composite with a C interface had a 32% strength reduction after 500 h oxidation at 1000°C.

Table 3. Flexural strengths of fabricated composites in the as-processed as well as oxidized conditions

CVI #	Interface	Flexural Strength (MPa) Oxidation at 1000°C in air			
		As-processed	24 h	200 h	500 h
1077	C	311±74	238±43	224±62	214±68
986	C/mullite/C	268±52	260±61	200±47	184±28
1080	C/mullite/C	320±24	238±54	239±39	193±27
1002	C/Al_2O_3-TiO_2/C	255±35	189±45	217±35	159±20
1066	C/Al_2O_3-TiO_2/C	298±23	314±29	257±64	234±52

In the as-processed condition, the fracture surfaces of composites with C, C/mullite/C, and C/Al_2O_3-TiO_2/C interfaces displayed considerable amount of fiber pullout. However, with increased exposure time at 1000°C, the fracture surfaces revealed reduced fiber pullout, and the fiber pullout was confined to the interior. The samples displayed only brittle fracture along the periphery. An illustration of this effect is shown in Fig. 1.

The persistence of graceful failure in a composite with a C interface even after 500 h oxidation at 1000°C in air, is similar to that reported by Walukas [9]. Walukas [9] observed substantial amount of fiber pullout in the interior in a composite with a thin C interface (40 nm)

even after 1000 h oxidation at 1000°C yet with 42% strength reduction, while the regions near the edges were embrittled. His TEM study identified that C was retained in the interior, and hence, the graceful behavior might have been due to the remaining presence of a C interface in the composite.

The TEM study of a CVI 986 composite (C/mullite/C interface) sample in the as-processed condition indicated that the mullite coatings were non-uniform i.e., the mullite layer was absent in many fiber-matrix interfaces. In fiber-matrix interfaces where the C/mullite/C interface was observed, the inner and outer C coatings were each 20 nm thick, while the mullite was ~70 nm thick.

In the CVI 1002 composite, the TEM study identified that the C/Al_2O_3-TiO_2/C interface was present and appeared uniform. The inner and outer C layers were each 30 nm thick, while the Al_2O_3-TiO_2 interface was 30-50 nm thick. Both Al O and TiO were crystalline. After oxidation at 1000°C for 500 h in air, the TEM images indicated that the C layers were replaced by SiO_2, but the Al_2O_3-TiO_2 layer was intact. Hence, in the oxidized condition, only a SiO /Al O -TiO_2/SiO interface was observed. Further, the Nicalon fiber surface was oxidized such that 30-50 nm of SiO_2 was observed on the fiber. Thus, the decrease in strength of composite with a C/Al_2O_3-TiO_2/C interface may also be attributed to fiber degradation. Interface C layers may have been retained in the interior of the C/Al_2O_3-TiO_2/C sample after oxidation since it was not clear where the TEM images were obtained. Hence, there is uncertainty involved in the extent to which C is replace by SiO_2.

Nicalon/SiC composites with C, C/mullite/C, and C/Al_2O_3-TiO_2/C interfaces retained damage-tolerant behavior even after 500 h oxidation at 1000°C in air. As examples, Figs. 2 and 3 show the load vs. displacement curves of a CVI 1077 composite (C interface), and a CVI 1066 (C/Al_2O_3-TiO_2/C interface) composite as-processed and after oxidation at 1000°C for up to 500 h in air.

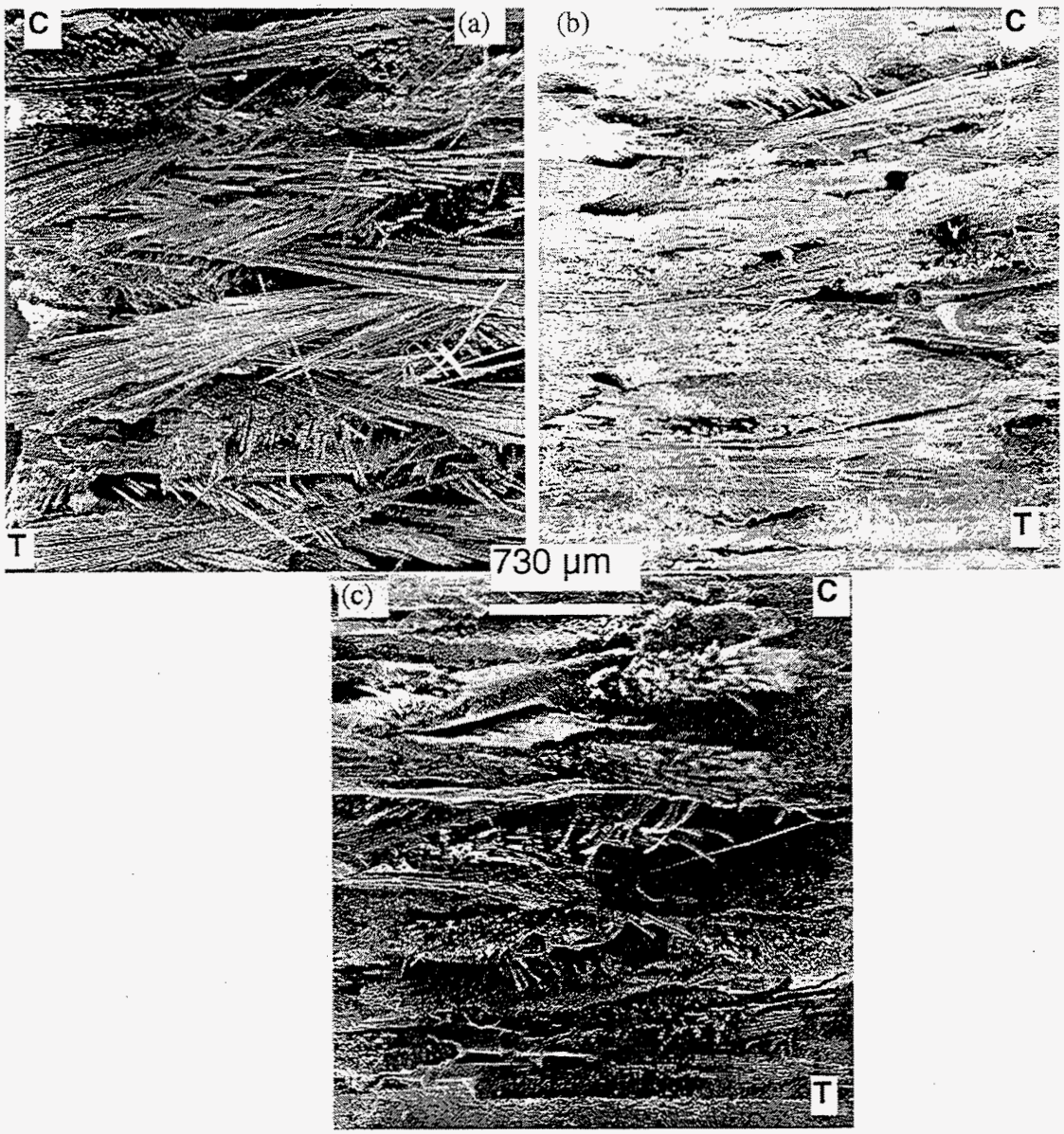

Fig. 1. Fracture surface of a CVI 986 composite sample (a) as-processed condition, (b) after 24 h oxidation at 1000°C, and (c) after 500 h oxidation at 1000°C

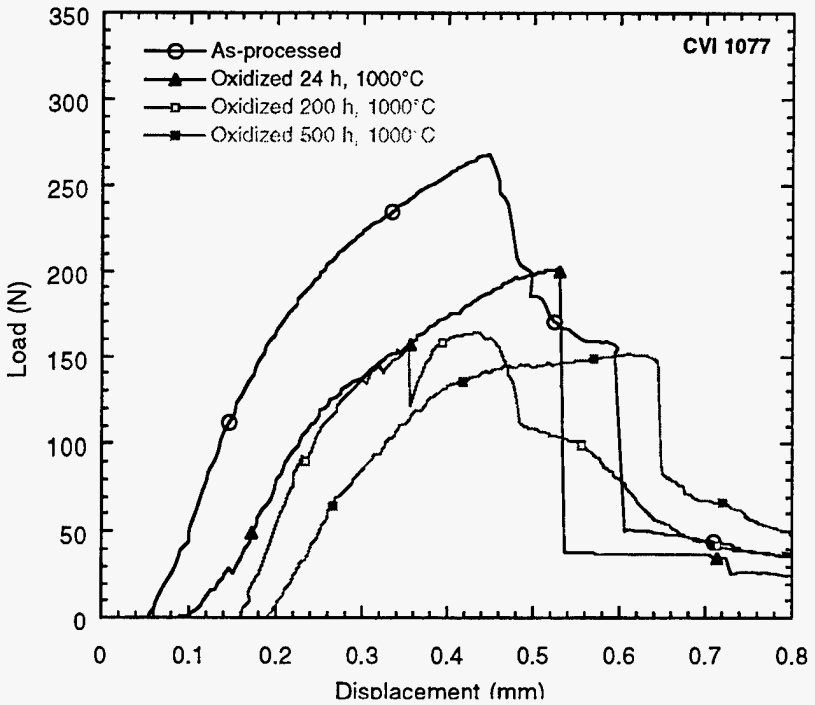

Fig. 2. Representative load vs displacement curves for a CVI 1077 (C interface) composite in the as-processed and oxidized conditions

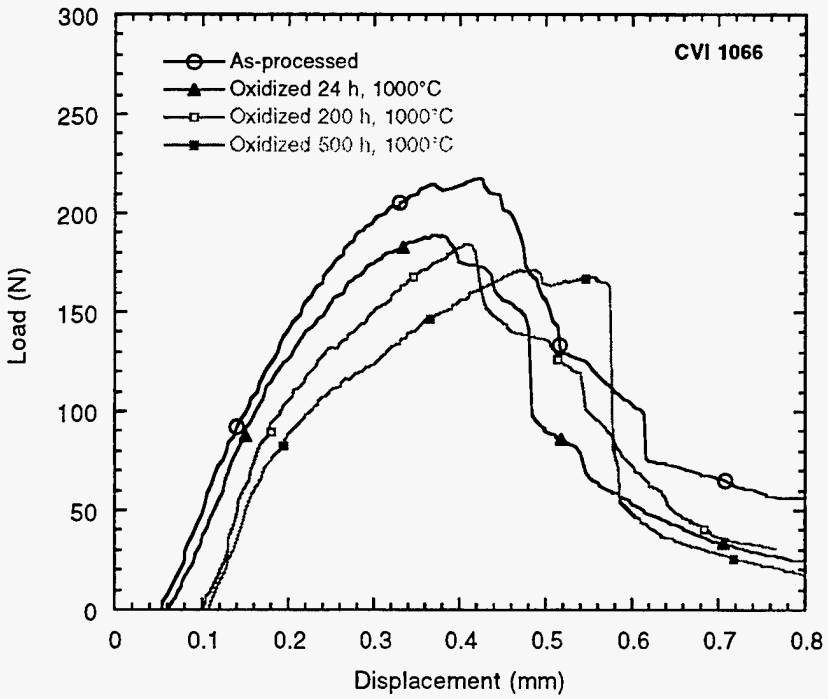

Fig. 3. Load vs displacement curves for a CVI 1066 (C/Al_2O_3-TiO_2-C interface) composite as-processed and after oxidation at 1000°C for up to 500 h in air

CONCLUSIONS

Nicalon/SiC composites with thin C and C/oxide/C interfaces retained damage-tolerant behavior even after 500 h oxidation at 1000°C, but with reduced flexural strengths (21-40%). With increased exposure time at 1000°C, flexural strengths as well as fiber pullout amounts were reduced, and the fiber pullout was confined to the sample interior. TEM analysis indicated that the C layers were replaced by SiO_2, however, there is uncertainty involved in the extent of SiO_2 replacement.

REFERENCES

1. R. J. Kerans, "Issues in the Control of Fiber-Matrix Interface Properties in Ceramic Composites," Scripta Metall. et Mater., 31 [8], 1079-84 (1994).

2. J. J. Brennan, "Interfacial Characteristics of Glass-Ceramic Matrix/SiC Fiber Composites," J. de Physique, Colloque C5 Suppl., 10 [49], 791-809 (1988).

3. R. Naslain, "The Concept of Layered Interphases in SiC/SiC Composites," pp. 23-40 in High Temperature Ceramic Matrix Composites II: Manufacturing and Materials Development in Ceramic Transactions, Vol. 58, Edited by A. G. Evans and R. Naslain, The American Ceramic Society, Ohio, 1995.

4. C. H. Hsueh, P. F. Becher, and P. Angeline, "Effects of Interfacial Films on Thermal Stresses in Whisker-Reinforced Ceramics," J. Am. Ceram. Soc., 71 [11], 929-33 (1988).

5. S. Shanmugham, D. P. Stinton, F. Rebillat, A. Bleier, T. M. Besmann, E. Lara-Curzio, and P. K. Liaw, "Oxidation-Resistant Interfacial Coatings for Continuous Fiber Ceramic Composites," Ceram. Eng. Sci. Proc., 16 [4], 389-99 (1995).

6. S. Shanmugham, P. K. Liaw, D. P. Stinton, T. M. Besmann, K. L. More, W. D. Porter, A. Bleier, and S. T. Misture, "Development of Sol-Gel Derived Coatings for Nicalon/SiC Composites," pp. 71-78 in Advanced Synthesis and Processing of Composites and Advanced Ceramics II, Ceramic Transactions, Vol. 79, The American Ceramic Society, 1996.

7. S. Shanmugham, "Processing and Mechanical Behavior of Nicalon/SiC and Nextel/SiC Composites with Sol-Gel Derived Oxide Interfacial Coatings," Doctoral Dissertation, The University of Tennessee, Knoxville, Tennessee, May 1997.

8. D. P. Stinton, E. R. Kupp, J. W. Hurley, R. A. Lowden, S. Shanmugham, and P. K. Liaw, "Oxidation-Resistant Interface Coatings for SiC/SiC Composites," Fossil Energy Program Annual Progress Report for April 1995 Through March 1996, ORNL-6902, pp. 21-29, June 1996.

9. D. Walukas, "A Study of the Mechanical Properties and Oxidation Resistance of Nicalon/SiC Composites with Sol-Gel Derived Oxide Interfacial Coatings," Masters Thesis, The University of Tennessee, Knoxville, Tennessee, May 1993.

CARBON FIBER COMPOSITE MOLECULAR SIEVES

T. D. Burchell and M. R. Rogers

INTRODUCTION

Monolithic adsorbents based on isotropic pitch fibers have been developed jointly by ORNL and the University of Kentucky, Center for Applied Energy Research. Our monoliths are attractive for gas separation and storage applications because of their unique combination of physical properties and microporous structure. At ORNL we currently produce the monoliths in billets that are 10 cm in diameter and 25 cm in length. The monolithic adsorbent material is being considered for guard bed applications on a natural gas (NG) powered device. In order for the material to be successful in this application, we must attain a uniform activation to modest micropore volumes throughout the large monoliths currently being produced. Here we report the results of a study directed toward attaining uniform activation in these billets.

EXPERIMENTAL

The manufacturing process for our carbon fiber composite molecular sieve (CFCMS) materials has been reported elsewhere [1,2]. Activation was performed in a three-zone Lindburgh furnace fitted with an 20-cm diameter Inconel retort. The CFCMS samples were dried in vacuum at 300°C, heated to 850°C under He for one hour, cooled to 200°C for a chemisorption treatment in flowing O_2, and then heated again to 850°C in He. The chemisorption and activation steps were repeated until the desired total burn-off (weight loss) was attained. Micropore structure characterization was performed using a Quantichrome Autosorb-1 apparatus.

RESULTS AND DISCUSSION

A total of five billets were subjected to two cycles each of O_2 chemisorption/activation. The burn-off attained ranged from 8.5 to 13.4%, with an average burn-off of 10.4%. A typical (Type I) N_2 isotherm (77K) for sample SMW-8A is shown in Fig. 1. The Dubinin-Redushkevich (DR) micropore volume; Brunauer, Emmett, and Teller (BET) surface area; and Dubinin-Astakhov

(DA) micropore width for four SMW billets are reported in Table 1. The designations A and B indicate samples taken from opposite ends of the 25-cm long billets.

Table 1. Micropore volume, micropore size, and surface area data for CFCMS billets

Billet Number	BET Surface Area (m^2/g)	DR Micropore Volume (cm^3/g)	DA Micropore Diameter [mode] (nm)
SMW1-A	567	0.27	1.54
SMW1-B	425	0.16	1.64
SMW3-A	607	0.23	1.44
SMW3-B	448	0.17	1.48
SMW4-A	940	0.34	1.56
SMW4-B	488	0.19	1.54
SMW8-A	707	0.27	1.48
SMW8-B	441	0.16	1.54

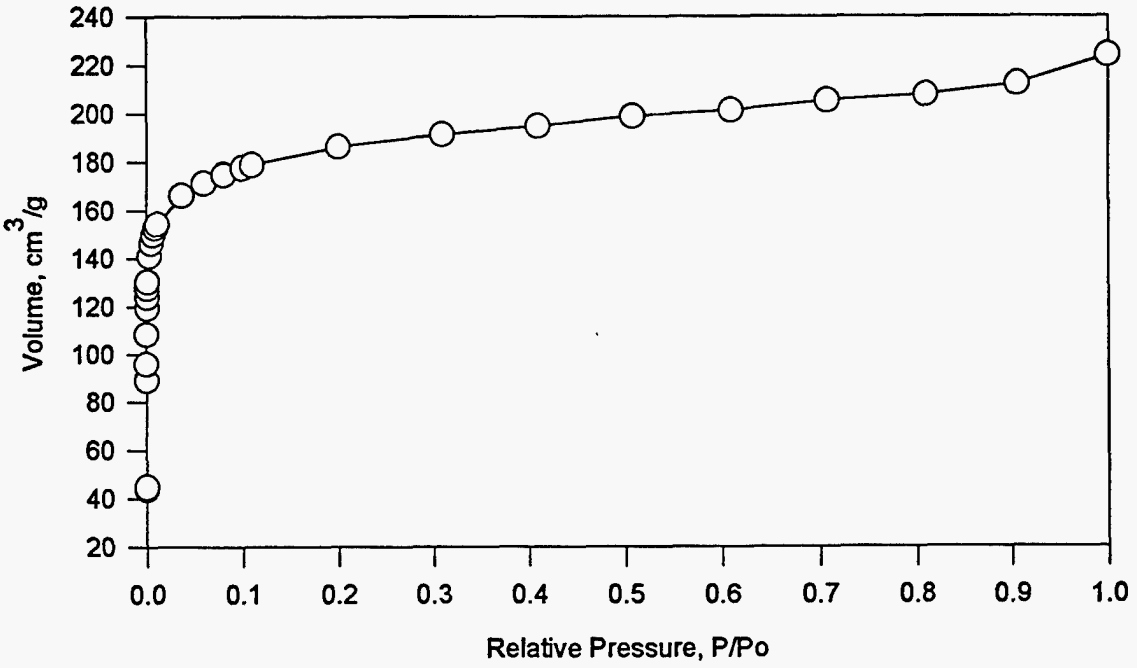

Figure 1. Typical 77K N_2 isotherm for sample SMW8A

The micropore volumes varied from 0.16 to 0.34 cm^3/g and the BET surface areas range from 425 to 940 m^2/g. Billet SM-15 was subjected to a more detailed examination to determine the uniformity of activation throughout the billet. Samples were taken at several radial locations across slices cut periodically along the billet length (Fig. 2). The BET surface area, DR micropore volume, and DA micropore size distribution were determined from the N_2 adsorption isotherm measured for each sample, and are shown in the 3D plots in Figs. 3-5. The BET surface area varied from 944 to 312 m^2/g and the DA pore diameter varied from 14 to 19.2 nm. Figure 6 shows the variation of DR micropore volume throughout billet SM-15, plotted as a function of diametral position for the five axial sampling positions. The DR volume varied from 0.12 to 0.35 cm^3/g, but there was no systematic radial or axial variation.

Figure 7 shows a breakthrough plot for an $Ar/H_2S/H_2$ mixture flowing through a sample of our CFCMS material. The H_2S was adsorbed, and breakthrough occurs some 18 minutes into the experiment. The H_2 and Ar were not adsorbed. Upon total breakthrough, the feed gas mixture flow was terminated and the desorption of the adsorbed H_2S was achieved by applying an electric current (4.5A @ 1V). Desorption occurred rapidly, as indicated by the increased concentration of H_2S in the exhaust gas stream. Regeneration of the CFCMS was thus achieved by direct electrical heating of the CFCMS. The ability of the material to readily adsorb H_2S suggests the removal of natural gas (NG) odorant additives might be achieved with a guard bed containing a billet of activated CFCMS. Consequently, a three-bed guard system was constructed and is depicted schematically in Fig. 8. The device contains three monolithic adsorbent pieces with approximate dimensions of 4.25-inches (10.8-cm) diameter and 10.0-inches (254-cm) length. Pressure drop data for He flow through an activated billet are shown in Fig.9. The measured pressure drop is slightly greater than for a packed bed of granular carbon. CFCMS is currently being evaluated as a guard-bed material for a NG fueled device.

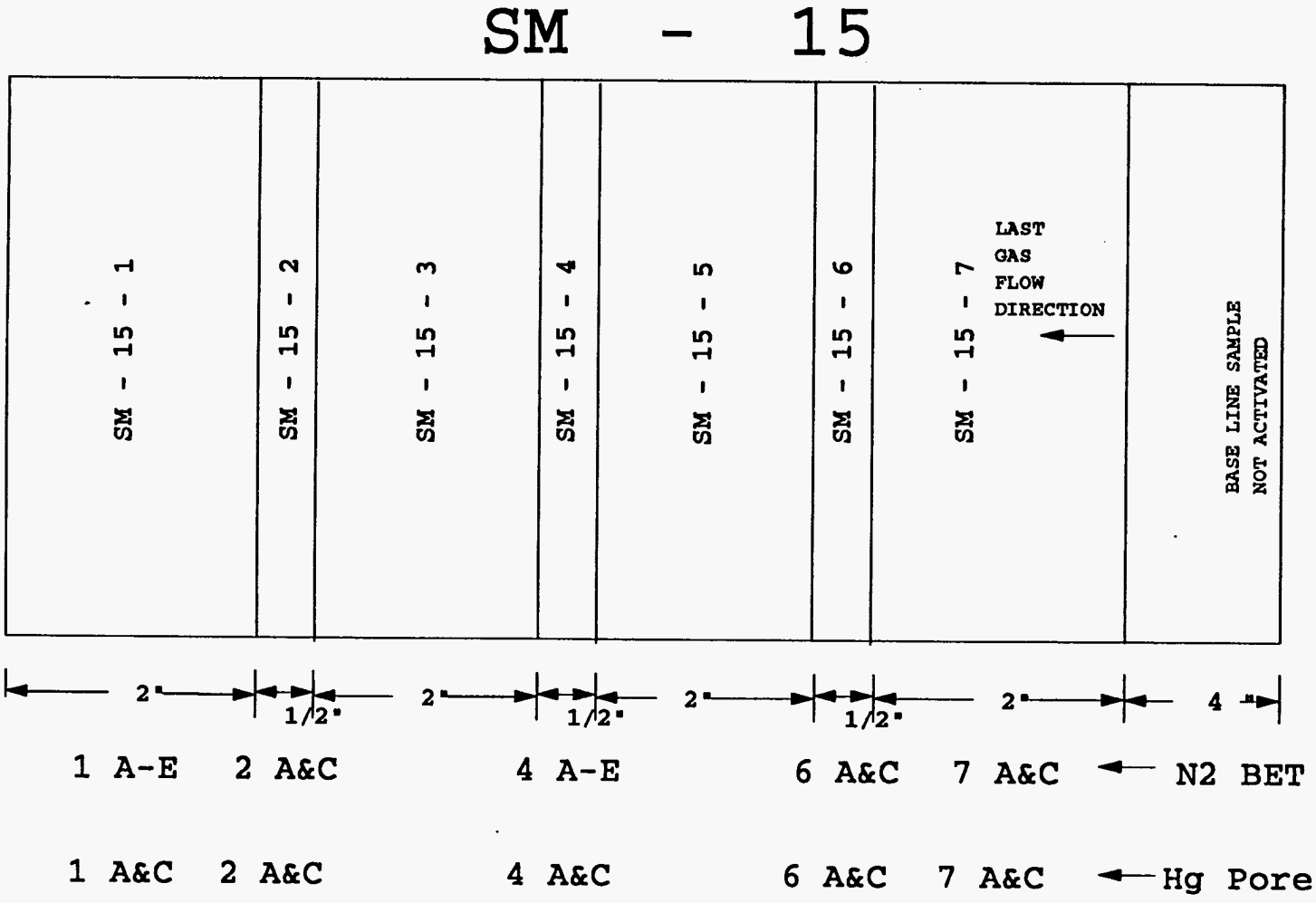

Figure 2. Sample locations in CFCMS billet SM-15

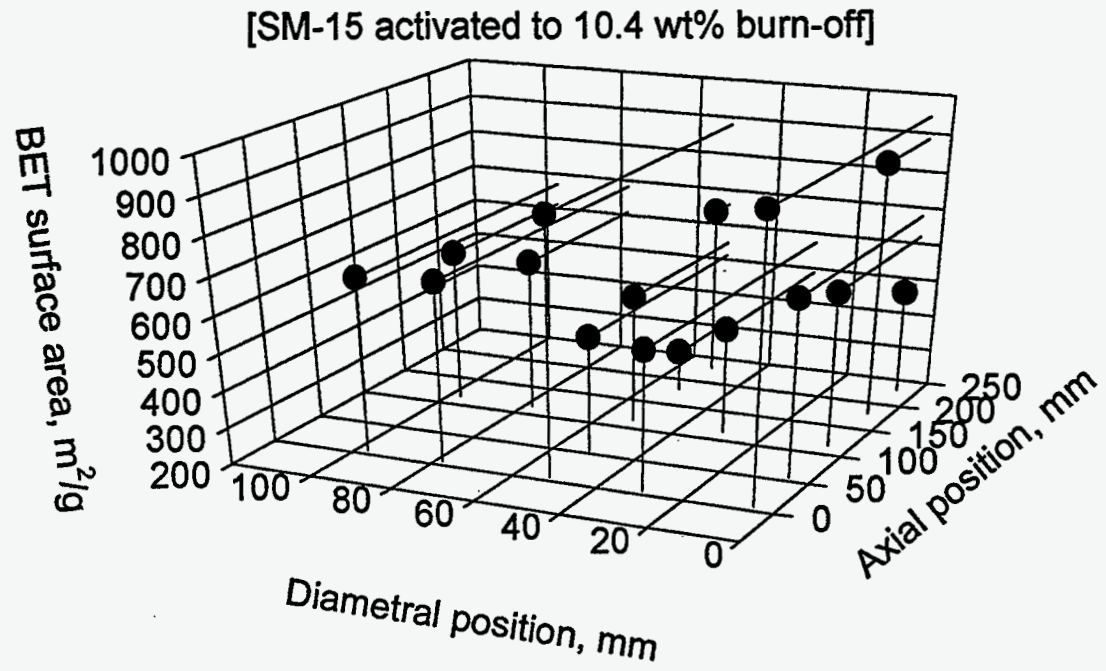

Figure 3. BET surface area as a function of position in billet SM-15

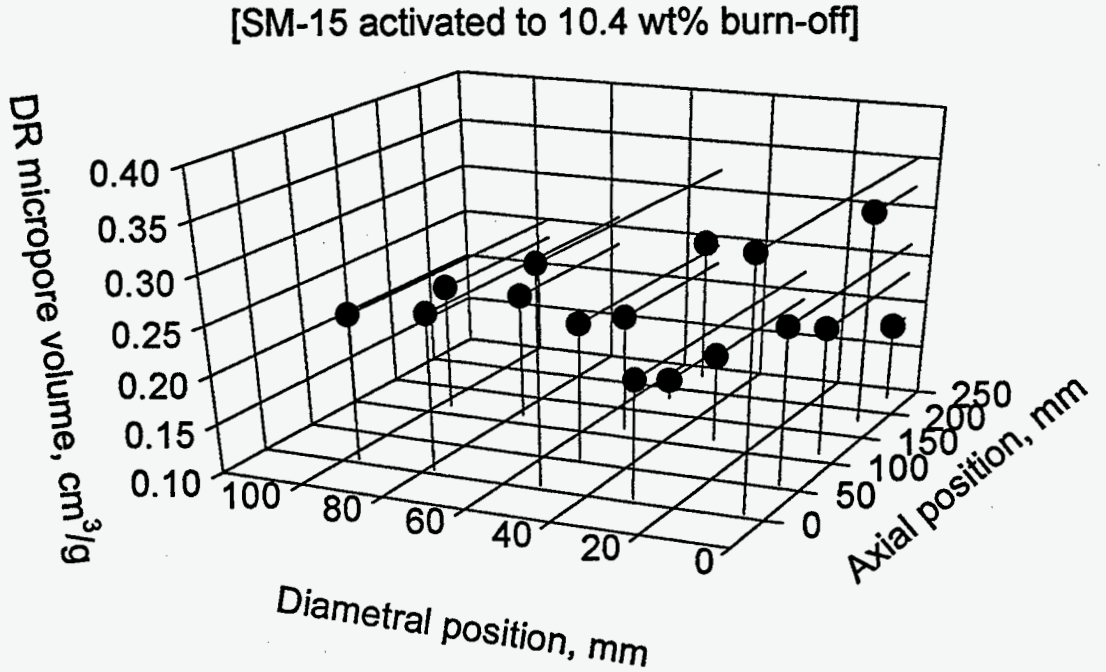

Figure 4. DR micropore volume as a function of position in billet SM-15

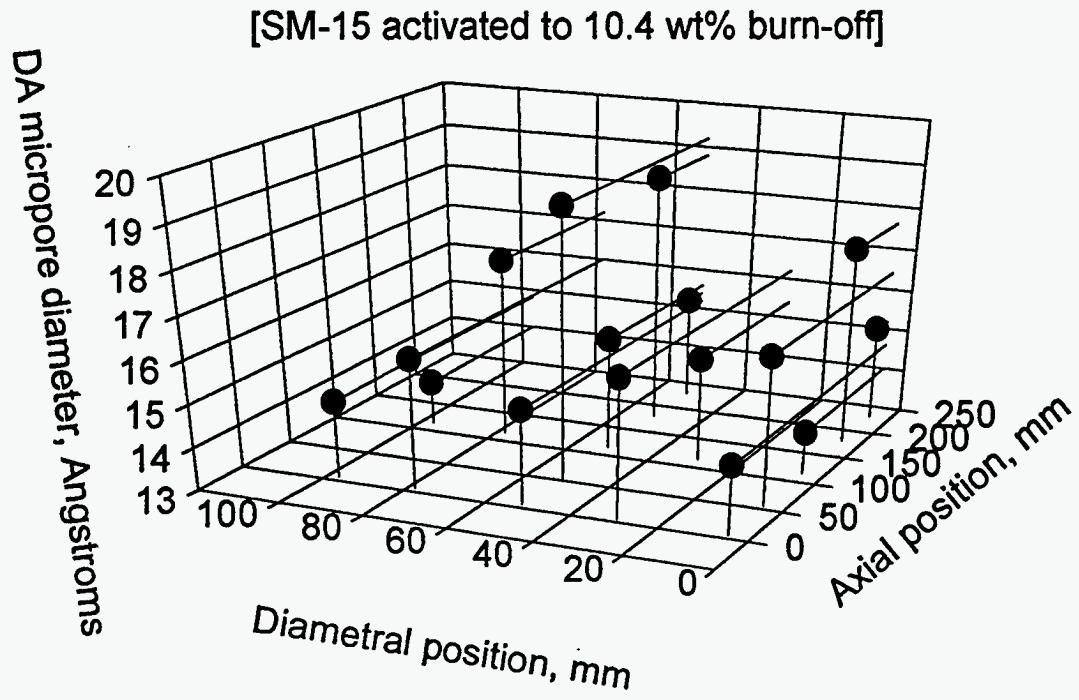

Figure 5. DA micropore diameter as a function of position in billet SM-15

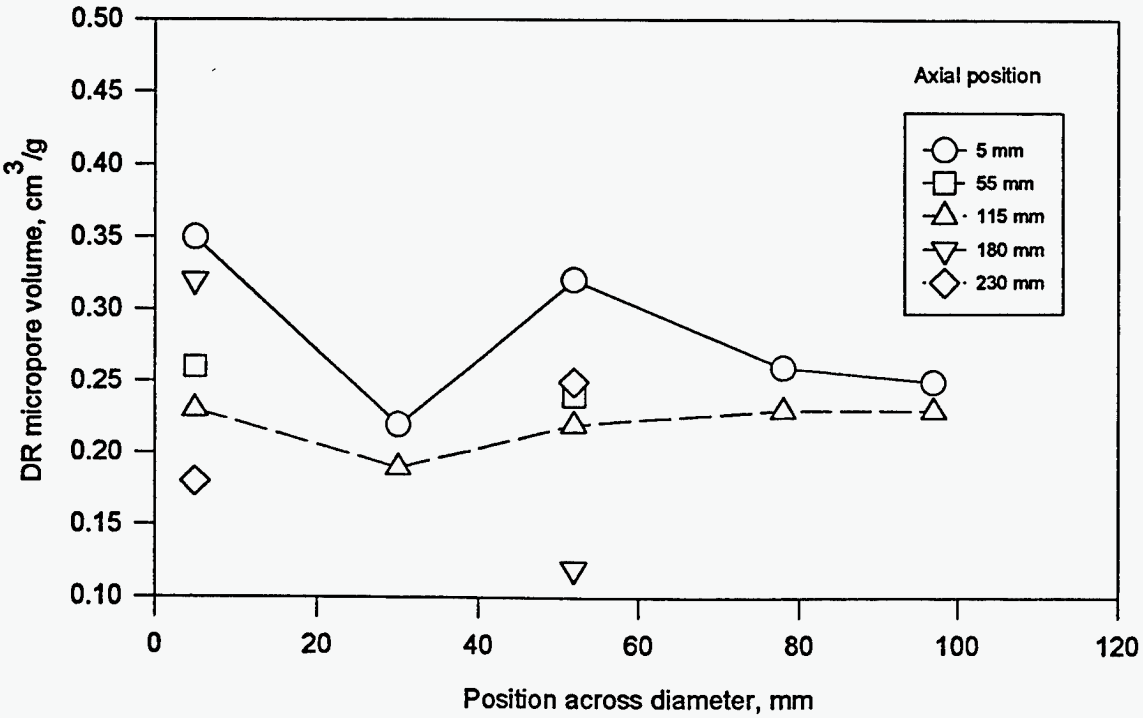

Figure 6. Variation of DR micropore volume in a CFCMS billet SM-15

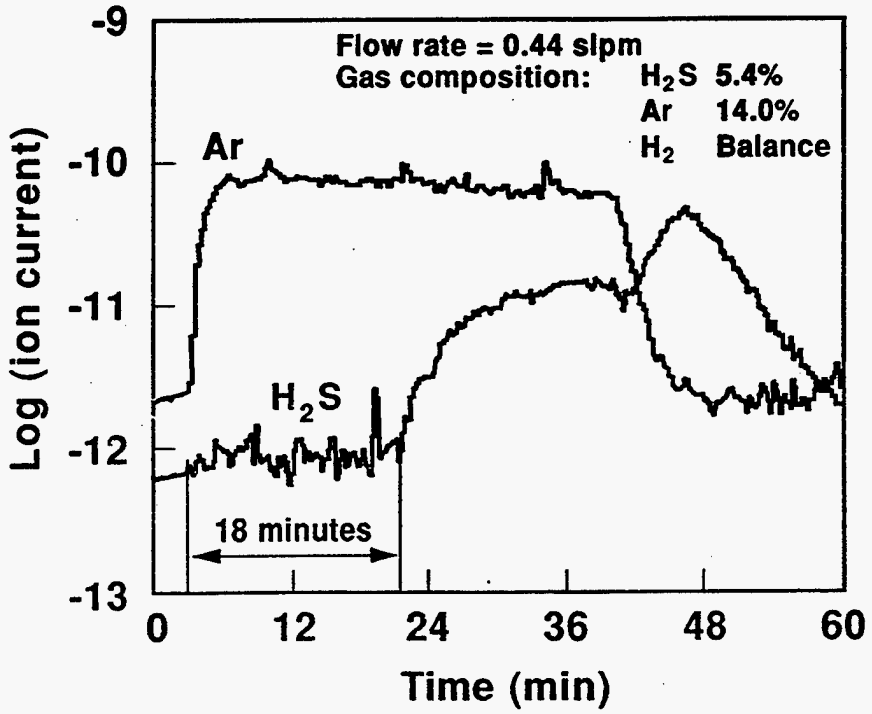

Figure 7. H_2S breakthrough plot for activated CFCMS showing the electrical desorption of the H_2S

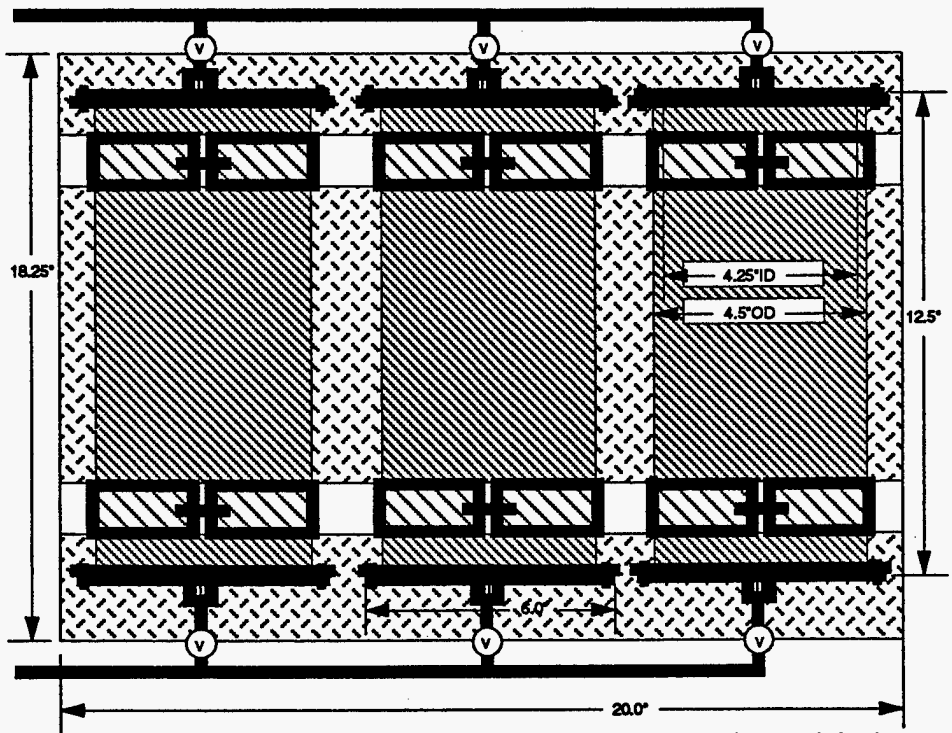

Figure 8. Schematic representation of our three-bed NG guard device containing CFCMS monoliths

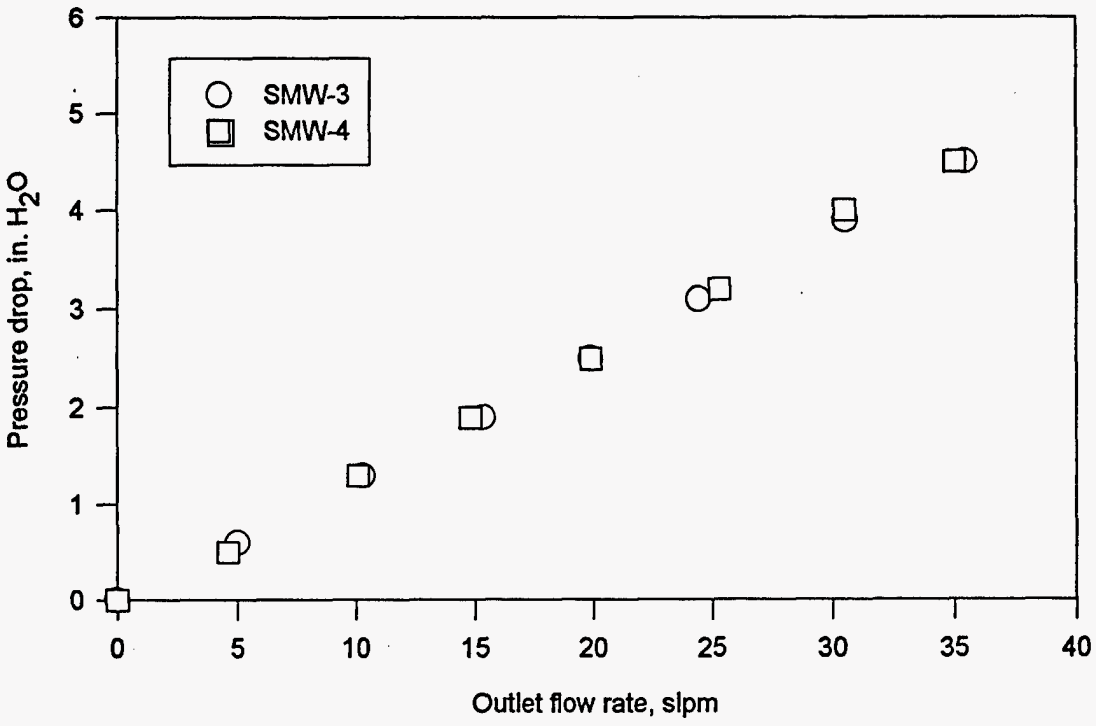

Figure 9. Pressure drop through a large monolith as a function of the He flow rate

CONCLUSIONS

Reasonably uniform activation was achieved in our CFCMS materials. Micropore volumes of 0.12 to 0.35 cm^3/g were attained. The ability of the materials to adsorb H_2S, the acceptable pressure drop, and its electrical heating capability suggests that CFCMS will make an ideal guard-bed material. Our three bed NG guard device is currently undergoing field trials.

REFERENCES

1. Burchell, T. D., Judkins, R. R., Rogers, M. R. and Williams A. M., *Carbon* **35** (1997) in press.
2. Burchell, T. D. in. *Proc. 8th Ann. Conf. on Fossil Energy Materials, CONF-9405143, ORNL/FMP-94/1*, pub. Oak Ridge National Laboratory, Aug. 1994, pp. 63-70.

DEVELOPMENT OF A MODIFIED 310 STAINLESS STEEL

R. W. Swindeman

INTRODUCTION

Because of their relatively low cost, good strength, fabricability, and corrosion resistance, austenitic stainless steels are widely used for high-temperature structural applications. Many 300 series stainless steels are Code-approved for pressure containment to 815°C and several specialty steels have been developed for construction of components operating above 815°C. Generally, steels containing at least 20% chromium are needed for adequate corrosion resistance above 650°C. The addition of strong carbide formers has significantly improved the load bearing capacity of the 20 to 25%Cr-bearing stainless steels, and the temperature range of their potential usage extends from 650 to 925°C. The purpose of the research on modified 310 and 20Cr-25NiNb stainless steels is to examine their behavior over a broad range of applications and to compare the performance of these stainless steels to higher alloys.

The potential usage of the stainless steels for fossil energy application were identified earlier and included superheater tubing in advanced steam cycle boilers, structural components for fluidized bed combustors, structural components for hot gas cleanup system components, and anchors for refractory liners (1). Criteria for design with these materials for service above 815°C were also reviewed (2, 3).

DISCUSSION OF CURRENT ACTIVITIES

During the past year, activities included the procurement and characterization testing of tubing of modified 310 and 20Cr25NiNb stainless steels, the continuation of long-time creep testing of base metals and autogenous weldments, and the continuation of fatigue and crack growth testing of the stainless steels and HR 120.

Two small heats of 310TaN stainless steel were argon-induction melted by Allegheny-Ludlum and extruded to tubing at ORNL. Coupons were machined from one of the heats for tensile and creep testing. Initial data trends indicated that the newer heats did not attain the strength and ductility levels of the VAR-ESR heat produced earlier, but further optimization of the fabrication schedule is planned. The long-time testing of 310TaN stainless steel has reached 40,000 h at 871°C (1600°F), and plots of log stress versus log

rupture life for various temperatures are shown in Fig. 1. Over the temperature range of testing 600 to 1038°C, the steel exhibited a fairly uniform behavioral pattern with no indication of structural instability. The long-time strength of the 310TaN stainless steel was estimated to be a least twice the strength of 310S stainless steel. The 310TaN stainless steel was found be be stronger than most other stainless steels used above 815°C, including 310HCbN, 253MA, RA85H, and the 20Cr-32Ni-Ti-Al alloy 811.

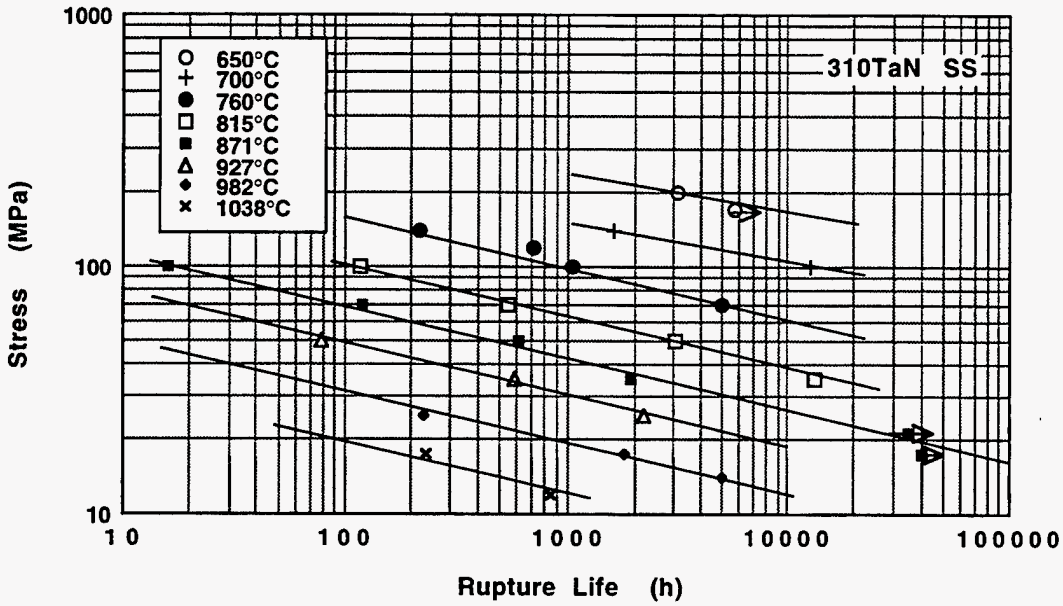

Fig. 1. Log stress versus log rupture life for a VAR/ESR heat of 310TaN stainless steel.

The modified 25Cr20NiNb stainless steel was found to have excellent strength and ductility. Slightly stronger than the 310TaN stainless steel, the 25Cr20NiNb steel was observed to have excellent weldability and good resistance to embrittlement. This stainless steel was judged to be a good alternative to the 310TaN stainless steel for service at 815°C and above.

The high Cr-Ni alloy HR120 was selected for the tubesheet in the Westinghouse hot gas cleanup vessel at Wilsonville, and its usage in such an application requires good low cycle fatigue and crack growth resistance. Material from the Wilsonville tubesheet was supplied to ORNL for evaluation. Low cycle fatigue testing of HR 120 at 871°C has shown that the alloy is comparable to 310TaN stainless steel, RA333, and HR160. The creep crack growth testing has been completed but results await final analysis.

SUMMARY

Studies of the 310TaN and 20Cr-25NiNb stainless steels show that these steels offer good strength and long-time stability properties and could replace standard 300 series stainless steels and some specialty stainless steels for non-pressure-bearing service at 815°C and above.

REFERENCES

1 R. W. Swindeman, *The Potential of Modified 310 Stainless Steel for Advanced Fossil Energy Application*, ORNL/TM-12057, March 1992.

2 R. W. Swindeman and D. L. Marriott, "Criteria for Design with Structural Materials in Combined-Cycle Application above 815°C, " *J. Engineering for Gas Turbines and Power*, 116, 352-59 (April, 1994).

3 G. Bruck, "Alloy Selection for Hot Gas Cleaning Systems," Paper No. 137, NACE CORROSION '97 Conference, New Orleans, Louisiana, March 10-14, 1997.

CERAMIC TUBESHEET DESIGN ANALYSIS

R. W. Swindeman, R. H. Mallett*, J. L. Bitner*, and P. M. Eggerstadt**

INTRODUCTION

An all-ceramic tubesheet was designed and constructed for evaluation at the DOE transport combustor demonstration plant in Wilsonville, Alabama. Because of the uniqueness of the concept, a thermal/mechanical analysis of the tubesheet was undertaken that provided some guidance in the minimization of stresses and optimization of design (1). The analysis required materials data, including thermal, physical, and mechanical properties, and the purpose of this activity was to provide data within the funding and material availability constraints.

DISCUSSION OF CURRENT ACTIVITIES

The collection of data for the thermal/mechanical analysis was completed in FY 1996. It was recommended that more materials characterization be undertaken and that testing of structure-like geometry (beams for example) be undertaken for a better definition of design and failure criteria in the design of ceramic components.

SUMMARY

The final report covering the design analysis was prepared and distributed (2) . Within the restraints and scope of the analysis, the results indicated that the thermal and mechanical stresses developed in the tubesheet were within the performance capabilites of the structural material. The report contained recommendations for confirmatory analyses and data collection.

REFERENCES

1. J. L. Bitner, R. H. Mallett, P. M. Eggerstedt, and R. W. Swindeman, "Evaluation of an All-Ceramic Tubesheet Assembly for a Hot-Gas Filter," paper submitted for the Conference on Fossil Energy Materials, Knoxville, Tennessee, May 20-22, 1997.

2. R. H. Mallett and J. L. Bitner, *Thermal and Structural Design Analysis of a Ceramic Tubesheet*, ORNL/Sub/94-SR776V/01, November 22, 1996.

---

* Mallett Technology, Research Triangle Park, NC
** Industrial Filter & Pump Mfg. Co., Cicero, IL

APPLICATION OF ADVANCED AUSTENITIC ALLOYS TO FOSSIL POWER SYSTEM COMPONENTS

R. W. Swindeman and D. A. Canonico*

INTRODUCTION

The low emission boiler (LEB) project supported by the Department of Energy is considered to be an advanced steam cycle unit in the sense that steam temperatures and pressures will be higher than those normally used in U.S. boilers. To address issues related to the selection of materials in the boiler, an activity was begun, partly funded through a CRADA with ABB-Combustion Engineering, to evaluate candidate tubing and piping materials. Issues include the relative merits of an all-ferritic steel system, the performance of dissimilar metal welds, the effect of cold work on the performance of stabilized and nonstabilized stainless steels, the relative performance advanced austenitic stainless steel tubing, and techniques of assessing damage due to excursions of temperature or pressure.

DISCUSSION OF CURRENT ACTIVITIES

During this period, T91 tubing was removed from the superheater of the Unit 5 boiler at the TVA power station at Kingston, Tennessee. The T91 tubing was replaced by 321 stainless steel fabricated by ABB Combustion Engineering. Inspection of the T91 tubing, exposed for more than 16 years at temperatures as high as 580°C, revealed slight oxide wedging at dissimilar metal welds between T91 and the austenitic filler metal joining to 321 stainless steel, minor type IV cracking under a stainless steel lug welded to a straight section of T91, coarsening of the metallurgical structure in T91, and slight cracking in the 321 stainless steel at the crown of the dissimilar metal weld. The room-temperature tensile strength and ductility of the T91 exceeded the requirements for the materials specification ASME SA-213). A loss in the short-time creep strength was observed that was similar to losses found after thermal aging for similar times (140,000 h), and these short-time data are compared to the database for T91 in Fig. 1.

---

* ABB-Combustion Engineering, Chattanooga, TN

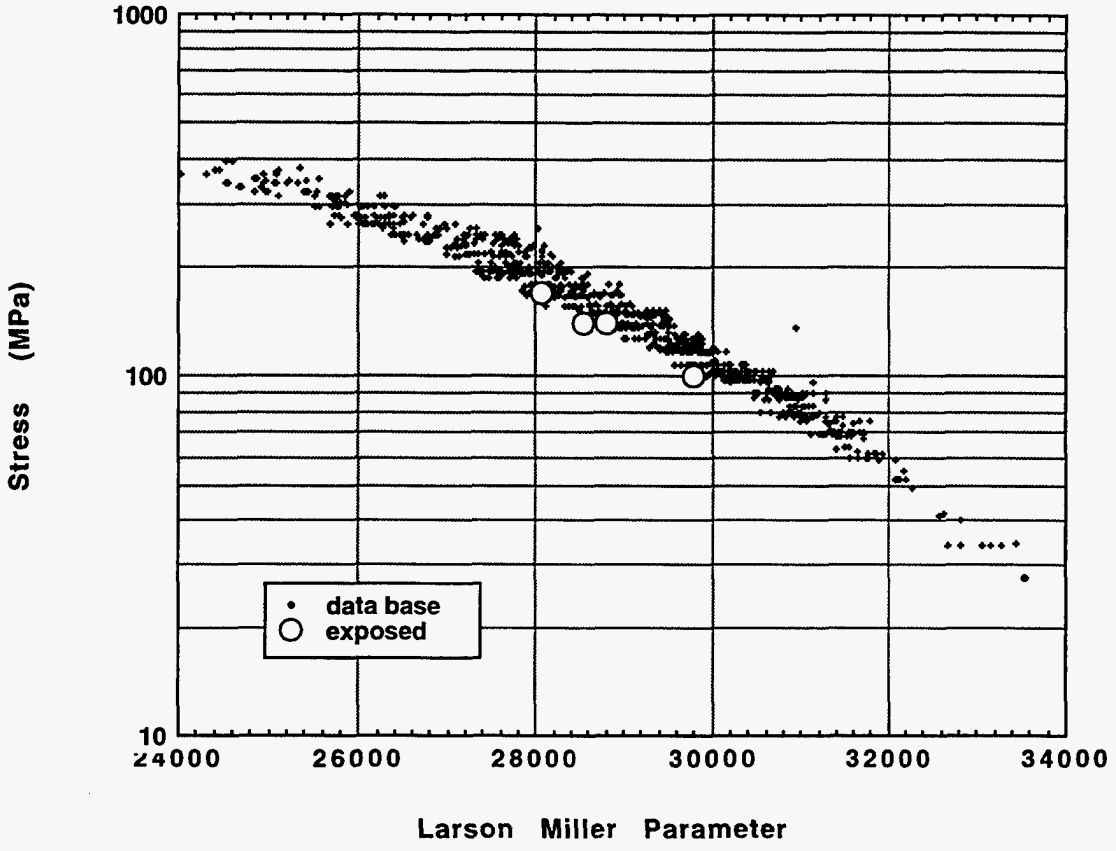

Fig. 1. Comparison of short-time stress-rupture data for T91 superheater tubing exposed 140,000 h in a power boiler to the stress rupture database for uniaxial test coupons.

Austenitic stainless steel (type 304H) tubing containing two degrees of cold bending was supplied by ABB-Combustion for creep testing and comparison to advanced austenitic stainless steels (1). The steel was found to posses average strength, relative to the ASME data base. Butt welds were made in the tubing to permit a further assessment of the weldment stress reduction factors contained in ASME Sect. III, subsection NH, since these factors are being considered for use in ASME piping code B31.1. The 308CRE filler metal was found to be stronger than weld of 308 stainless steel and all weldment specimens failed in the base metal. Creep-rupture of the advanced austenitic stainless steels at comparable temperatures was continued. Testing times for annealed tubing exceeded 50,000 h were at 650 °C.

Testing of 310TaN, 310HCbN, and 20Cr25NiNb stainless steels continued for long times. All steels exhibit excellent strengths at temperatures of interest to the LEB. Of the three steels, only 20Cr25NiNb stainless steel was found to approach the strength level of the HT-UPS steels developed for the advanced steam cycle applications (2).

SUMMARY

Evaluation of service exposed T91 was undertaken and it was observed that some degradation was experienced as a result of long-time boiler exposure at temperatures to 580°C. The extent of degradation was similar to test coupons that were exposed to similar times and temperatures.

Testing of the advanced austenitic stainless steels has shown the modified 20Cr25NiNb steel has the best overall performance in terms of strength.

REFERENCES

1. D. A. Canonico and R. W. Swindeman, papers presented to the American Boiler Manufacturers Association annual meeting, Jupiter Beach Florida, April 18, 1997.

2. P. J. Maziasz, Developing an Austenitic Stainless Steel for Improved Performance in Fossil Power Facilities," *J. Met.* **41**, 14-20.

ADVANCED STAINLESS STEELS FOR RECUPERATOR APPLICATIONS

R. W. Swindeman, P. J. Maziasz, B. A. Pint
M. Fitzpatrick*, J. P. Montague*, and A. Metcalfe*

INTRODUCTION

Work on advanced austenitic stainless steels for superheaters has shown that the application basic concepts of alloy design and fabrication technology can be effectively used to improve the performance of stainless steels, provided that the target properties are well-defined (1). These principals are being brought to bear on the objective of improving the performance of recuperators for simple cycle advanced turbine systems. A CRADA with the Solar Turbines, Inc. for this purpose has two goals. The first goal is to enhance the strength of 347 stainless steel foil to permit extension the operating life for existing recuperator designs. The second goal is to develop a stainless steel with improved strength and oxidation resistance that will permit an increase in the operating temperature of recuperator materials to near 700°C.

DISCUSSION OF CURRENT ACTIVITIES

The initial research efforts were focused on techniques to produce fine-grained 347 stainless steel foil with good oxidation resistance and mechanical strength. Foils from commercial and experimental heats of 347 stainless steel with non-optimized microstructures were exposed to oxidation for times to 1000 h at 700 and 800°C. Results from the testing were used in conjunction with models (2) to estimate lifetimes based on oxidation limits, and the results were encouraging with respect to meeting goal 1. Experimental heats of 347 stainless steel were obtained from an industrial supplier of stainless steel foil. These heats were used to examined the effectiveness of alternative fabrication and heat treating schedules in optimizing grain size and metallurgical stability. While optimization of fabrication schedules was being pursued for 347 stainless steel, exploratory oxidation and creep testing of alternate materials was begun. Steels included

* Solar Turbines, Inc., San Diego, CA

in the exploratory studies were 253MA, 310HCbN, 310TaN, and modified 20Cr25NiNb stainless steels. Of these, the 20Cr25NiNb steel exhibited exceptional oxidation resistance. Creep testing of alternate foil materials was begun at 704°C and 75.8 MPa. The 310TaN and modified 20Cr25NiNb steels were found to have the best creep strength, relative to standard 347 stainless steel foil. Comparison of creep curves are shown in Fig. 1. Here it may be seen that 253MA stainless steel had similar creep strength to commercial 347 stainless steel foil, while the non-optimized m347 foil was quite weak and the two advanced stainless steels (310TaN and m20Cr25NiNb steels) were relatively strong.

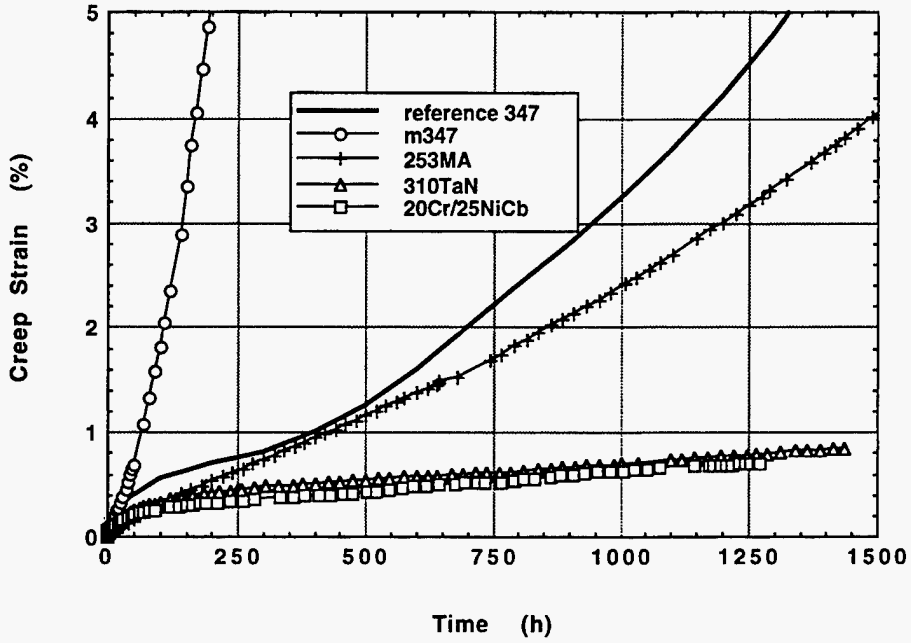

Fig. 1. Comparison of creep curves for stainless steel foils at 704°C and 75.8 MPa.

SUMMARY

Experimental work is underway to develop improved materials for construction of advanced recuperators for simple cycle gas turbines. Initial results are encouraging.

REFERENCES

1. P. J. Maziasz, Developing an Austenitic Stainless Steel for Improved Performance in Fossil Power Facilities," *J. Met.* **41**, 14-20.

2. W. J. Quadakkers, et al., *Materials for Advanced Power Engineering 1994*, D. Coutsouradis, et al. Eds, Kluwer Academic Publishers, 1994, pp. 1533-42.

ULTRAHIGH TEMPERATURE INTERMETALLIC ALLOYS

**M. P. Brady, J.H. Zhu, C. T. Liu, P. F. Tortorelli,
J.L. Wright, C.A. Carmichael, and L.R. Walker**

INTRODUCTION

The objective of this work is to develop a new generation of structural materials based on intermetallic alloys for use at high-temperatures in advanced fossil energy conversion systems. Target applications of such ultrahigh strength alloys include hot components (for example, air heat exchangers) in advanced energy conversion systems and heat engines. However, these materials may also find use as wear-resistant parts in coal handling systems (for example, nozzles), drill bits for oil/gas wells, and valve guides in diesel engines.

The developmental effort to date has focused on the Cr_2Nb and Cr_2Zr Laves phases[1-6]. Such Laves phases possess high melting points[7-9] and offer the potential for exceptional high-temperature strength[1-5]. However, they are extremely brittle at ambient temperatures[1-5,8]. In order to improve ambient temperature mechanical properties, two-phase "CN" alloys based on a soft Cr-rich solid solution phase reinforced with the hard Cr_2Nb or Cr_2Zr Laves phases have been developed[1-5].

For some Cr-Cr_2Nb based alloys, very high strengths at temperatures of 1200°C have been obtained[1,2]. However, improvements in ambient-temperature toughness and ductility have been modest[1,2]. This is thought to be due in part to thermal expansion mismatch between the Cr solid solution phase and the Cr_2Nb Laves phase, which leads to defects during fabrication, and extensive precipitation of the Cr_2Nb phase in the Cr solid solution phase[1].

The Cr-Cr_2Zr system shows better fabricability and crack resistance than the Cr-Cr_2Nb system, possibly due to a smaller mismatch of the coefficients of thermal expansion of the Cr solid solution and Laves phases[1]. The solubility of Zr in Cr is also much lower than that of niobium[9], which prevents extensive Cr_2Zr Laves phase preciptation in the Cr solid solution phase. However, the Cr-Cr_2Zr based alloys have poor oxidation resistance, and generally tend to be weaker at high-temperatures than the Cr-Cr_2Nb based alloys[1]. Significant property improvements in the Cr-Cr_2Zr based alloys beyond those already achieved appear unlikely.

The metallurgical insights gained from the study of the Cr-Cr_2Nb and Cr-Cr_2Zr systems have provided the basis for the selection of a promising new Cr-Cr_2X system with superior properties. Current efforts are focused on compositional optimization of alloys based on this new system. This report presents an overview of microstructural characterization, mechanical properties, and oxidation behavior for a near-optimized Cr-Cr_2Zr based alloy and several promising new Cr-Cr_2X based alloys.

ALLOY PREPARATION AND PROCESSING

CN alloys based on the Cr-Cr_2Zr and Cr-Cr_2X systems weighing 400-500 g were prepared by arc melting and drop casting in a copper mold (2.5 cm diam x 7.6 cm long) preheated to 200°C. Small 40 g castings of Cr-Cr_2X based alloys were also prepared by arc melting and drop casting in a chilled copper mold. High-purity chromium and other metal chips were used as charge materials. In particular, the Cr-Cr_2X based alloys were easily cast and showed no evidence of cracking. After heat treatment, the large 400-500 g alloy ingots were clad inside Mo billets and hot extruded at 1480°C and an extrusion ratio of 4:1. The hot-extruded material was then heat treated and used for tensile specimens. The small 40 g castings were used as-cast to provide specimens for oxidation exposures.

MICROSTRUCTURAL ANALYSIS

Figure 1 shows optical and scanning electron micrographs of hot-extruded CN129, which is a near-optimized Cr-Cr_2Zr based alloy containing four alloying additions (see Table 1). The microstructure consists of patches of the Cr solid solution phase surrounded by interconnected Cr_2Zr Laves phase. It is important to note that, unlike the Cr-Cr_2Nb system[1], no precipitation of Cr_2Zr particles was found in the primary Cr-rich patches (by scanning electron microscopy). Wavelength dispersive electron probe microanalysis (pure element standards) of the Cr solid solution and Laves phases in CN129 are shown in Table 1.

Figure 2 shows optical and scanning electron micrographs of hot-extruded CN130, which was one of the first Cr-Cr_2X based alloys to be studied. The microstructure consists of a fine dispersion of spherodized Cr_2X Laves phase particles dispersed in a Cr solid solution matrix. Such a microstructure is expected to be nearly ideal for achieving optimum mechanical properties. Electron microprobe analysis of CN130 is shown in Table 2.

TENSILE PROPERTIES

Button-type tensile specimens with gage dimensions 0.31 cm diam x 0.95 cm long were machined by electro-discharge machining from hot-extruded material, followed by grinding and polishing with "0" Emery paper. The tensile specimens were tested in an Instron Testing Machine at room temperature, 800°C, and 1000°C in air, and at 1200°C in vacuum (crosshead speed of approximately 0.25 cm/minute).

a)

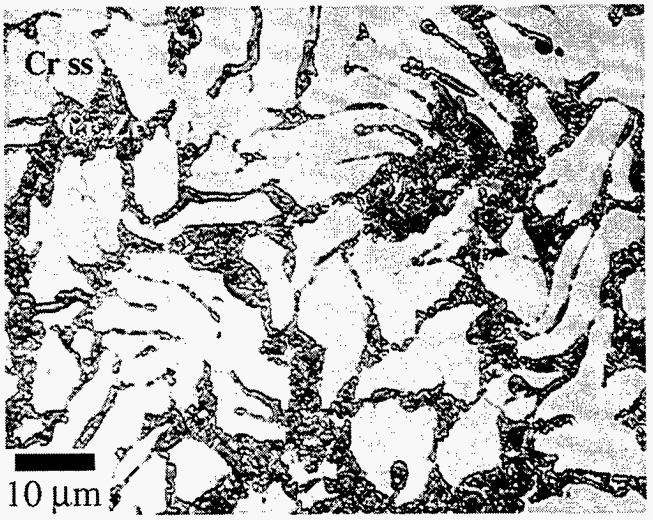

b)

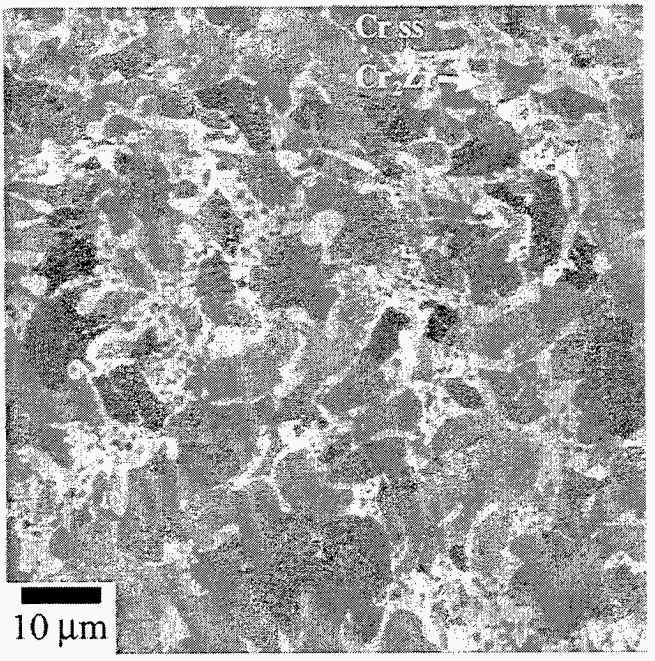

Fig. 1- Microstructure of hot-extruded CN129. a) Optical (light microscopy): Cr solid solution (Cr ss) light, Cr_2Zr Laves dark b) Scanning Electron (secondary): Cr ss dark, Cr_2Zr Laves light.

Table 1- Electron probe microanalysis of hot-extruded CN129 (at.%). An average of 3-6 measurements for each phase is reported. The data is estimated to be accurate within ± 1-2 at.%.

CN129	Cr	Zr	X1	X2	X3	X5
Cr solid solution	93.04	0.02	4.99	0.53	1.27	0.16
Laves	49.12	26.08	6.37	11.19	3.30	3.94
Nominal	84	5	5	3	2	1

a)

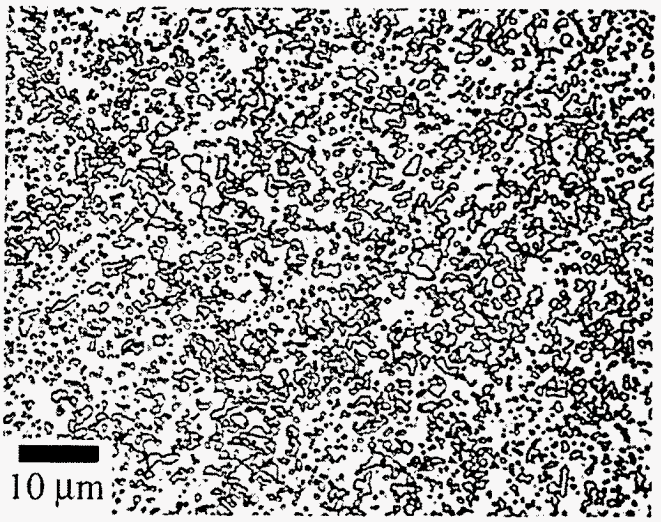

b)

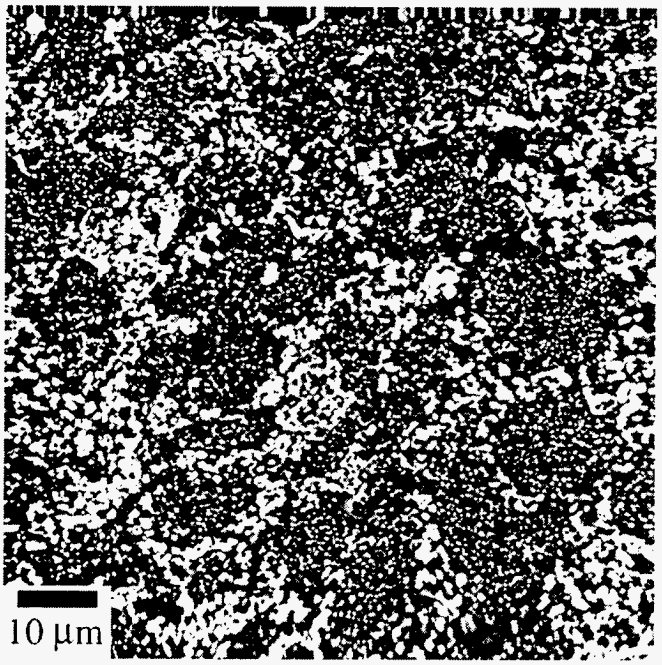

Fig. 2- Microstructure of hot-extruded CN130. a) Optical (light microscopy): Cr ss matrix, Cr_2X Laves second phase b) Scanning Electron (secondary): Cr ss dark, Cr_2X Laves light, Oxide inclusion black.

Table 2- Electron probe microanalysis of hot-extruded CN130 (at.%). An average of 3-6 measurements for each phase is reported. The data is estimated to be accurate within ± 1-2 at.%.

*CN130	Cr	X	X1	X3
Cr solid solution	93.69	0.95	5.33	0.03
Laves	68.01	27.16	4.824	0.003
Nominal	86.5	8	5	0.5

*X3-rich oxide particles and a very minor volume fraction phase of Cr-33X-8.5X1 were also observed.

Table 3 summarizes the tensile properties of two near-optimized Cr-Cr_2Zr based alloys, CN128 and CN129. No macroscopic yielding prior to fracture was observed. However, room-temperature fracture strengths of greater than 80 ksi (550 MPa) were obtained. These fracture strengths are slightly higher than that of the best Cr-Cr_2Nb based alloys[1,2].

Table 3- Tensile properties of hot-extruded Cr-Zr base alloys.

Alloy No.	Alloy Composition (at. %)	Yield Strength (ksi)	Fracture Strength (ksi)	Elongation (%)
	Room Temperature			
CN128	Cr-6Zr-5X1-3X2-1X3-1X5	>83.6	83.6	*
CN129	Cr-5Zr-5X1-3X2-2X3-1X5	>81.5	81.5	*
	1000°C			
CN129		>81.3	81.3	*
	1200°C			
CN129		45.1	58.6	>63+

* Fracture prior to macroscopic yielding

+ The test was stopped after straining to 63%

The alloy CN129 also showed no macroscopic tensile ductility at 1000°C, but was extremely ductile at 1200°C. This suggests that the ductile to brittle transition temperature (DBTT) of Cr-Cr_2Zr based alloys is around 1100°C. At 1200°C, the alloy is very strong, with an ultimate tensile strength of greater than 58 ksi (400 MPa).

The tensile properties of the first generation of Cr-Cr_2X based alloys are summarized in Table 4. Strengths of over 100 ksi (689 MPa) were obtained at room temperature (no macroscopic yielding prior to fracture was observed). At 800°C, elongation on the order of 1% and fracture strengths in excess of 130 ksi (896 MPa) were obtained. Although not yet optimized, this first generation of Cr-Cr_2X based alloys already exhibits much better lower-temperature tensile behavior than the best Cr-Cr_2Nb and Cr-Cr_2Zr based alloys[1]. The tensile elongation increases with temperature, and reaches around 20% at 1200°C. At 1200°C, one Cr-Cr_2X based alloy exhibited an ultimate tensile strength of greater than 50 ksi (345 MPa), which is in the range of the tensile properties obtained for the Cr-Cr_2Nb and Cr-Cr_2Zr based alloys at 1200°C[1].

Table 4- Tensile properties of hot-extruded Cr-8X based alloys.

Alloy No.	Alloy Composition (at. %)	Yield Strength (ksi)	Fracture Strength (ksi)	Elongation (%)
	Room Temperature			
CN130	Cr-8X-5.0X1-0.5X3	>104	104	*
CN132	Cr-8X-5.0X1-3.0X2-0.5X3-0.05X6	>71	71	*
CN133	Cr-8X-2.5X1-3.0X2-0.5X3	>101	101	*
	800°C			
CN130		120	120	0.8
CN132		134	137	1.2
CN133		>69	69	*
	1000°C			
CN130		86	97	7.6
CN132		97	104	3.0
CN133		81	89	8.6
	1200°C			
CN130		37	45	16.6
CN132		42	51	18.5
CN133		30	36	22.0

*Fracture prior to macroscopic yielding.

While it is unlikely that CN alloys will ever be able to exhibit appreciable room-temperature tensile ductility, significant room-temperature fracture toughness may be possible because of the two-phase microstructure. Quantitative measurements of room temperature fracture toughness of the Cr-Cr_2X based alloys have not yet been made. However, qualitative assessment of room-temperature toughness by simple "drop" and "hammer-impact" tests suggest that the Cr-Cr_2X based alloys possess superior toughness to the Cr-Cr_2Nb and Cr-Cr_2Zr based alloys. The best Cr-Cr_2Nb and Cr-Cr_2Zr based alloys to date exhibit room-temperature fracture toughness on the order of 7-8 MPa$\sqrt{m}$. The Cr-Cr_2X based alloys are therefore expected to have fracture toughness greater than this range.

OXIDATION BEHAVIOR

All CN alloys will require an oxidation-resistant coating at temperatures above approximately 1000°C because of chromia (Cr_2O_3) scale volatility[10]. Previous and ongoing work at The Ohio State

University has demonstrated that silicide coatings applied by a pack cementation process can substantially improve the isothermal and cyclic oxidation resistance of CN alloys at temperatures above 1000°C in air[11-13]. However, in application, the CN alloys must demonstrate a degree of oxidation resistance at these high temperatures to provide for survivability in the event of coating failure. Therefore, a screening test that consisted of 1100°C exposures in room air was adopted to evaluate the high-temperature oxidation resistance of the newly developed CN alloys.

Disk shaped oxidation specimens of 8-13 mm in diameter and 1 mm thickness were sectioned from as-cast or hot-extruded material and polished to a 600 grit finish using SiC paper. The oxidation specimens were placed in an alumina crucible and covered with an alumina lid. At intervals of 1, 4, 10, 30, 48, and 120 hours, the samples were removed from the furnace at temperature, air-cooled, weighed, and returned to the furnace at temperature. Using this interrupted weight change procedure, both isothermal and cyclic oxidation resistance may be surveyed. Volatilization of chromia occurred during the test, as evidenced by a green stain on the inside surfaces of the alumina crucible and lid.

The interrupted weight change oxidation data for Cr-10X, Cr-10Nb, and pure Cr are shown in Figure 3. Comparison data for the Cr-Cr_2Zr based alloy CN129 are also provided. Cr-10X exhibited excellent oxidation resistance for a chromia-former at this high-temperature and was the only one to survive the interrupted weight change screening intact. After 6 cycles and 120 h of exposure at 1100°C, a uniform scale with only very slight evidence of spallation at the sample edges was observed. In contrast, Cr-10Nb and pure Cr suffered from extensive scale spallation. CN129 catastrophically failed between the 10 and 30h cyclic intervals. Preliminary cross-section analysis of isothermally oxidized CN129 indicates that Zr in the Cr_2Zr Laves phase is extensively internally oxidized. This may have led to catastrophic failure during the interrupted weight change exposure as a result of coefficient of thermal expansion mismatch between the internal zirconium oxide and the surrounding metal.

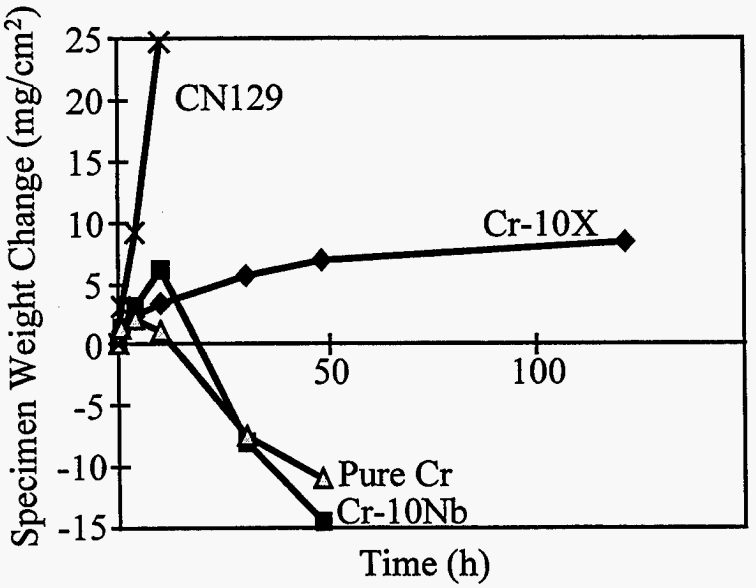

Fig. 3- Interrupted weight change data for as-cast Cr-10X, Cr-10Nb, and pure Cr at 1100°C in room air (at.%). Data for hot-extruded CN129 (Cr-5Zr-5X1-3X2-2X3-1X5 at.%) are also shown.

Cross-section scanning electron micrographs of Cr-10X, Cr-10Nb, and pure Cr after 6 cycles and 120 hours of exposure at 1100°C are shown in Figure 4. A continuous chromia scale formed on Cr-10X. Microhardness measurements in the metal beneath the metal/scale interface showed no evidence of interstitial O or N penetration (note that this technique is only sensitive to within about 5-10 microns of the metal/scale interface). The scale that formed on Cr-10Nb consisted primarily of a complex mixture of chromium and/or chromium plus niobium oxides. X-ray diffraction data from 1200°C exposed Cr-10Nb suggests the presence of Cr_2O_3 and $CrNbO_4$, in agreement with prior observation on Cr-Cr_2Nb alloys oxidized at 950°C[14]. No scale remained on pure Cr. Microhardness measurements in both Cr-10Nb and pure Cr indicate significant hardening and embrittlement in the metal beneath the metal/scale interface.

Figures 5 and 6 show 1100°C interrupted weight change data for alloying additions of X1 or X2 to a Cr-8X based alloy. Cr-8X was less oxidation resistant than Cr-10X due to a tendency to spall, but was preferred from a mechanical property standpoint. Additions of X1 to Cr-8X resulted in comparable oxidation resistance to Cr-10X (Figure 5). However, additions of X2 were deleterious to the oxidation resistance of Cr-8X (Figure 6). These results are surprising because the reverse effect had been observed for additions of X1 and X2 to Cr-Cr_2Nb based alloys[15], although that data was obtained isothermally at lower temperatures. The reasons for these differences are under investigation

SUMMARY AND FUTURE WORK

A new family of Cr-Cr_2X based alloys has been identified, whose fabricability, mechanical properties, and oxidation resistance are dramatically better than that of previously developed Cr-Cr_2Nb and Cr-Cr_2Zr based alloys. Future work will concentrate on a more complete evaluation of mechanical properties, including room temperature fracture toughness, and compositional modification for optimum mechanical properties and oxidation resistance.

ACKNOWLEDGMENTS

The authors thank Dewey Easton for the hot extrusions, and Bruce Pint, Joachim Schneibel, and Jim Distefano for their reviews of the manuscript. This research was sponsored by the Fossil Energy Advanced Research and Technology Development (AR&TD) Materials Program, U S. Department of Energy, under contract DE-AC05-96OR22464 with Lockheed Martin Energy Research Corporation.

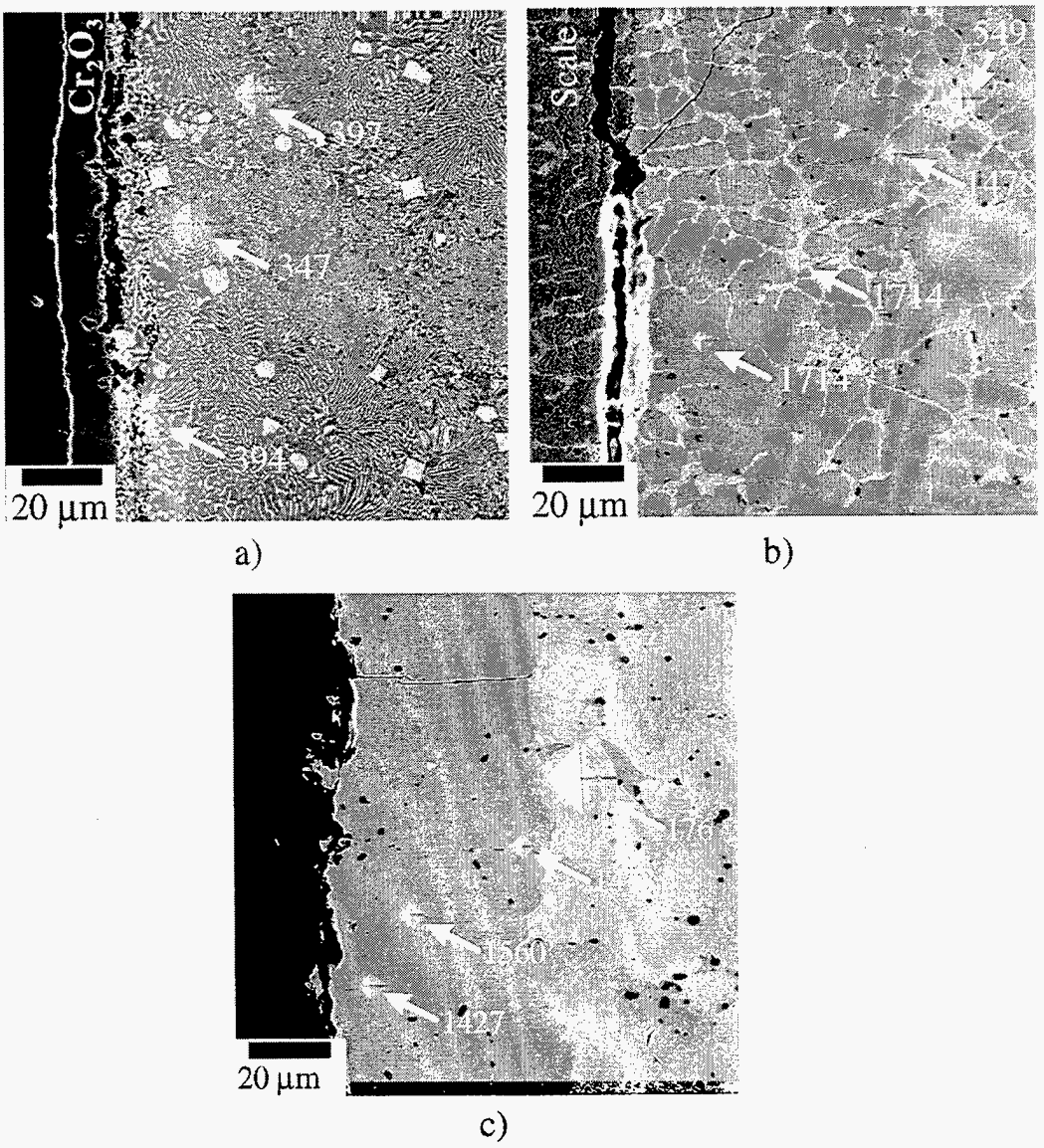

Fig. 4- Cross-section scanning electron (secondary) micrographs of as-cast (a) Cr-10X (≅ 15µm thick scale), (b) Cr-10Nb (≅ 550 µm thick scale), and (c) pure Cr (complete scale spallation) after 6 cycles and 120 h at 1100°C in room air. The Vicker's hardness indentation was performed at a load of 100 g for 15 seconds.

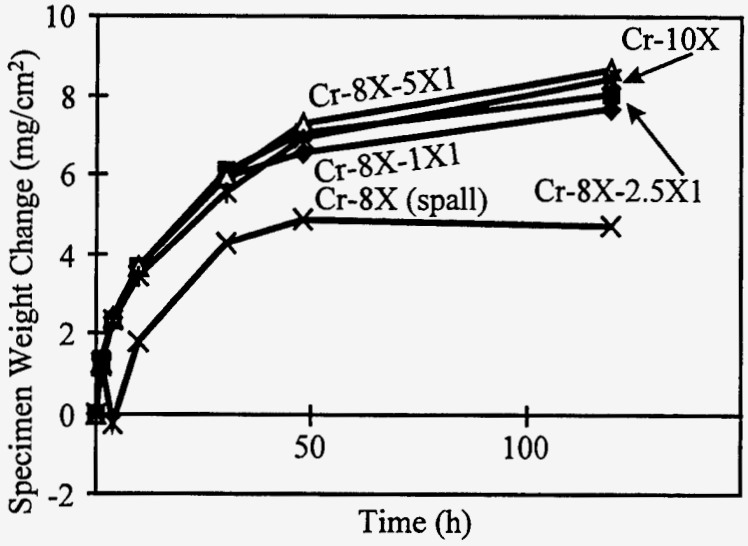

Fig. 5- Interrupted weight change data for as-cast Cr-8X-1X1, Cr-8X-2.5X1, Cr-8X-5X1, Cr-8X, and Cr-10X at 1100°C in room air (at.%).

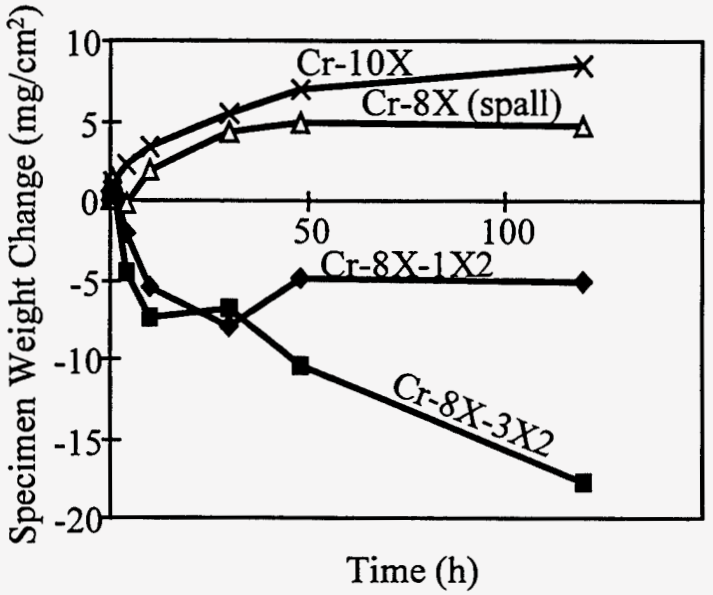

Fig. 6- Interrupted weight change data for as-cast Cr-8X-1X2, Cr-8X-3X2, Cr-8X, and Cr-10X at 1100°C in room air (at.%).

REFERENCES

1. C. T. Liu, P. F. Tortorelli, J. A. Horton, D. S. Easton, and L. Heatherly, pp. 477-89 in *Proc. Tenth Annual Conf. Fossil Energy Materials*, N. C. Cole and R. R. Judkins (comp.), U. S. Department of Energy, August 1996.
2. C. T. Liu, P. F. Tortorelli, J. A. Horton, D. S. Easton, J. H. Schneibel, L. Heatherly, C. A Carmichael, M. Howell, and J. L. Wright, pp. 415 - 26 in *Proc. Ninth Annual Conf. Fossil Energy Materials*, N. C. Cole and R. R. Judkins (comp.), U. S. Department of Energy, August 1995.
3. C. T. Liu, J. A. Horton, and C. A. Carmichael, pp. 377-390 in *Proc. 8th Annual Conf. on Fossil Energy Materials*, N. C. Cole and R. R. Judkins (comp.), U. S. Department of Energy, August 1994.
4. C. T. Liu, J. A. Horton, and C. A. Carmichael, pp. 297-307, in *Proc. 7th Annual Conf. on Fossil Energy Materials*, N. C. Cole and R. R. Judkins (comp.), U. S. Department of Energy, July 1993.
5. C. T. Liu, pp. 375-383 in *Proc. 6th Annual Conf. Fossil Energy Materials*, N. C. Cole and R. R. Judkins (comp.), U. S. Department of Energy, July 1992.
6. F. Laves, p. 124 in Theory of Alloy Phases, American Society for Metals, Metals Park, OH, 1956.
7. D. J. Thoma and J. H. Perepezko, Mat. Sci. and Eng. A156 (1992) 97.
8. H. J. Goldschmidt and J. A. Brand, J. Less-Common Met. 3 (1961) 44.
9. T. B. Massalski, J. L. Murray, L. H. Bennett, and H. Baker (eds.), Binary Alloy Phase Diagram, American Society for Metals, Metals Park, OH, 1986.
10. P. Kofstad, High-temperature Corrosion, Elsevier, London, 1988.
11. Y-R. He, M. Zheng, and R.A. Rapp, 465-476, in *Proc. Tenth Annual Conf. Fossil Energy Materials*, N. C. Cole and R. R. Judkins (comp.), U. S. Department of Energy, August 1996.
12. Y-R. He, R. A. Rapp, and P. F. Tortorelli, "Oxidation-Resistant Ge-Doped Silicide Coating on Cr-Cr_2Nb Alloys by Pack Cementation," pp. 109-117, *Mater. Sci. and Eng. A*, A222, 1997.
13. Y-R. He and R. A. Rapp, these proceedings.
14. P.F. Tortorelli and B.A.. Pint, pp.174-185 in Fundamental Aspects of High-Temperature Corrosion, D.A.. Shores, R.A.. Rapp, and P.Y. Hou (eds.), Proceedings Volume 96-26, The Electrochemical Society, Pennington, New Jersey, 1997.
15. P.F. Tortorelli and J.H. DeVan, pp.391 - 400 in *Proc. Eighth Annual Conf. Fossil Energy Materials*, N.C. Cole and R.R. Judkins (comp.), CONF-9405143, U. S. Department of Energy, August 1994.

WELD OVERLAY CLADDING WITH IRON ALUMINIDES

G. M. Goodwin

ABSTRACT

We have established a range of compositions for these alloys within which hot cracking resistance is very good, and within which cold cracking can be avoided in many instances by careful control of welding conditions, particularly preheat and postweld heat treatment. For example, crack-free butt welds have been produced for the first time in 12-mm thick wrought Fe3Al plate. Cold cracking, however, still remains an issue in many cases.

We have developed a commercial source for composite weld filler metals spanning a wide range of achievable aluminum levels, and are pursuing the application of these filler metals in a variety of industrial environments. Welding techniques have been developed for both the gas tungsten arc and gas metal arc processes, and preliminary work has been done to utilize the wire arc process for coating of boiler tubes.

Clad specimens have been prepared for environmental testing in-house, and a number of components have been modified and placed in service in operating kraft recovery boilers.

In collaboration with a commercial producer of spiral weld overlay tubing, we are attempting to utilize the new filler metals for this novel application.

INTRODUCTION

To utilize the excellent properties of alloys based on the Fe3Al nominal composition, particularly resistance to high temperature oxidation and corrosion, we are continuing to develop welding filler metals, procedures, and parameters aimed at introducing these

new alloys into commercial service. Although emphasis is still placed on conventional weld overlay techniques, considerable progress has been made recently toward joining thick section monolithic materials, and applying alternative cladding techniques, including spiral weld cladding and wire arc thermal spraying.

Prior efforts (1-6) have identified the causes of hot cracking in these alloys, and, by compositional modification, essentially eliminated it. Cold cracking, however, remains an issue, although recent efforts have made progress toward minimizing it, primarily by control of composition and welding parameters, especially preheat and postweld heat treatment.

Development of filler metals, processes, and procedures is ongoing concurrent with introduction of the materials into service in a variety of industrial applications.

Filler Metal Development

Using the approach described earlier (6), we have developed and now have available a family of filler metal compositions spanning a range of aluminum content from less than 8 to greater than 26 weight percent (Table I). These composite wires are 0.0625-in (1.6mm) diameter, in spooled form, and can thus be used with automatic wire feeders in a number of welding and cladding processes. The actual deposit composition can be modified as desired by control of dilution, deposition rate, and other welding parameters.

Heat Treatment Effects

It was established earlier (4,5) that weld preheat and postweld heat treatment could be effective at avoiding cold cracking of the weld deposits. Based on extensive testing over the range of filler metal compositions, efforts to reduce preheat below 350°C, or postweld heat treatment below 750°C have consistently been unsuccessful at preventing cracking. We conclude, therefore, that these conditions are required, as a minimum, to reliably avoid cold cracking. Using these parameters, however, we have been able to use

TABLE I. COMPOSITION OF IRON ALUMINIDE ALLOY FILLER METALS

	WEIGHT %	Al	Cr	C	Zr	Mo
Stoody I	Aim, all weld metal	20.0	7.0	0.10	0.25	0.25
	Actual, all weld metal	21.8	7.3	0.06	0.40	NA[c]
	Actual, clad deposit [a]	12.6	6.0	0.08	0.20	0.44
	Actual, clad deposit [b]	15.3	12.7	0.05	0.22	0.40
Stoody II	Aim, all weld metal	20.0	--	0.10	0.25	0.25
	Actual, all weld metal	21.5	--	0.08	0.25	NA
	Actual, clad deposit [a]	12.6	--	0.10	0.12	0.40
Stoody III	Aim, all weld metal	12.0	--	0.10	0.25	0.25
	Actual, all weld metal	12.5	--	0.06	0.40	NA
	Actual, clad deposit [a]	7.6	--	0.07	0.32	0.40
Stoody IV	Aim, All weld metal	26.0	--	0.10	0.25	0.25
	Actual, all weld metal	26.5	--	0.08	0.60	NA
	Actual, clad deposit [a]	14.1	--	0.09	0.32	0.40

[a] Single layer automatic gas metal arc on 1-in. thick type 2 1/4 Cr-1Mo steel
[b] Single layer manual gas tungsten arc on 1/2-in. thick type 310 stainless steel
[c] NA - Not Analyzed

the new filler metals to join monolithic sections of plate material which had previously been considered unweldable. Figure 1 shows a metallographic cross-section of a multipass gas tungsten arc weld in 1/2-in (12.7mm) thick alloy FA-129 plate. To match the aluminum level of the base plate (16 weight %), we chose the 20 weight % weld wire (Stoody II), thus allowing for arc losses and dilution by the base plate. As is seen in figure 1.b, the weld microstructure is free of cracks and porosity, and has a narrow heat affected zone and relatively fine-grained fusion zone.

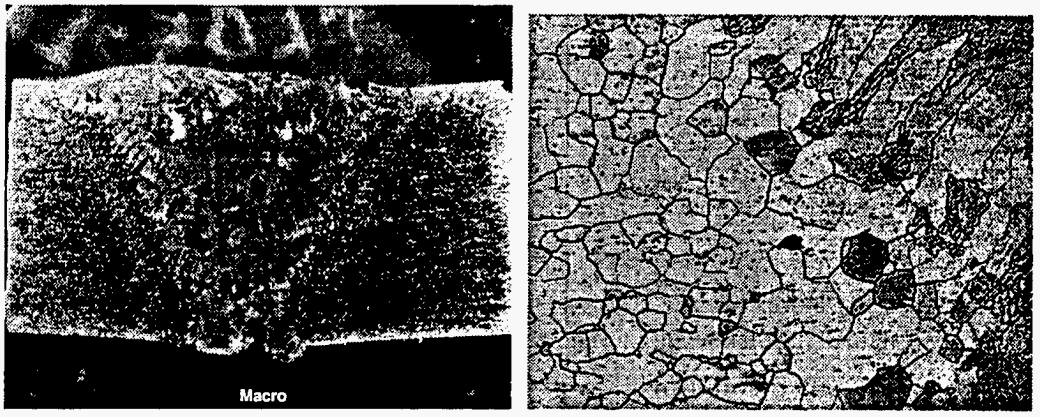

Fig. 1. Multipass Gas Tungsten Arc Weld in 12.7-mm Thick Alloy FA-129 Plate a) Macrosection, and b) Microstructure; note narrow heat affected zone, fine grained fusion zone, and absence of cracks and porosity.

Industrial Service Testing

Pursuing the tasks started earlier (6), we have prepared several additional components for in-service testing in commercial paper mill recovery boilers, and continue to monitor the condition of parts previously modified by weld overlay. As a basis for comparison, we have also prepared components using high-chromium commercial filler wires, E-Brite 26-1 and Inconel 617 with 26% and 23% chromium, respectively. These alloys would be considered the primary competition for the iron aluminides in high temperature oxidizing/sulfadizing environments.

Wire Arc Cladding*

Wire arc cladding, also known as arc spraying, is being investigated as an alternative to conventional gas tungsten arc or gas metal arc weld cladding. The process is shown schematically in figure 2, from (7). Basically, an arc is struck between two independently fed wires, and compressed gas is used to detach molten droplets from the arc zone and propel them to the substrate. It is a high velocity, high deposition rate process, with droplet temperatures high enough to assure good bond strength. Figure 3.a is an overall view and figure 3.b shows a cross-section of 3-in (76mm) OD carbon

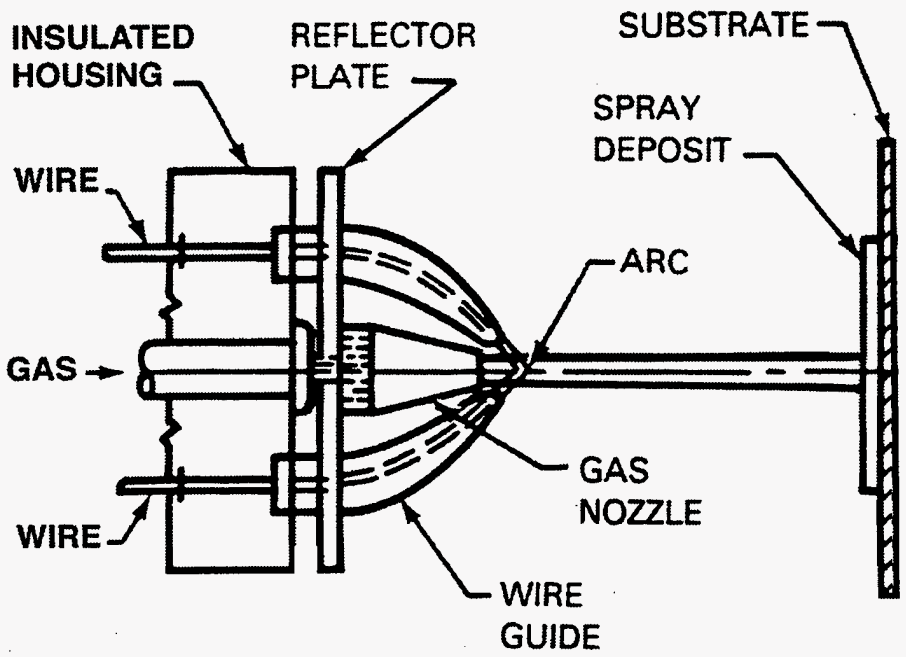

Fig. 2. Wire Arc Spray Process

steel boiler tube clad with composite filler wire. Spray parameters were 100 amperes DC, 30 volts, and 90 psi air pressure. As seen in figure 3, the coating is heterogeneous,

*This task is being performed in collaboration with E. A. Franco-Ferreira of the Engineering Technology Division.

but sound. Thermal cycling of clad specimens to 427°C in air has shown no evidence of spalling after 25 cycles. In order to control the degree of oxidation of the coating, additional specimens are being prepared using nitrogen and argon as carrier gases.

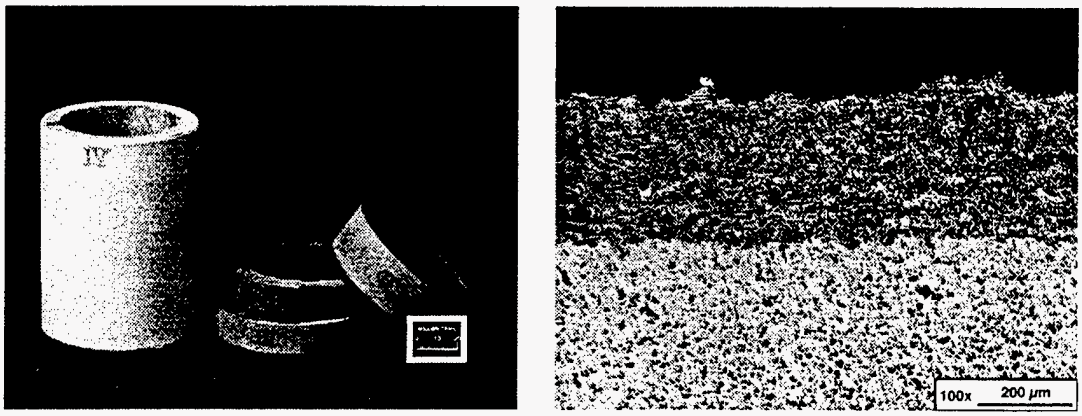

Fig. 3. Boiler Tube Coated by Wire Arc Cladding: a) Overall and b) Microstructure

Spiral Weld Cladding

The spiral weld cladding technique (figure 4 shows an example) uses a combination of gas metal arc and gas tungsten arc welding to overlay boiler tubing prior to fabrication of tube panels. In collaboration with a commercial supplier of spiral welded product, we are using the process to clad carbon steel with the Stoody I composite filler wire composition. If this approach is successful, it will provide a viable alternative to coextruded bimetallic tubing.

CONCLUSIONS

- Hot cracking has essentially been eliminated, but cold cracking still remains an issue in many cases; preheat (350°C minimum) and postweld heat treatment (750°C minimum) are required to reliably avoid it.
- We have developed and have available a family of filler metal compositions from less than 8 to greater than 26 weight % aluminum.

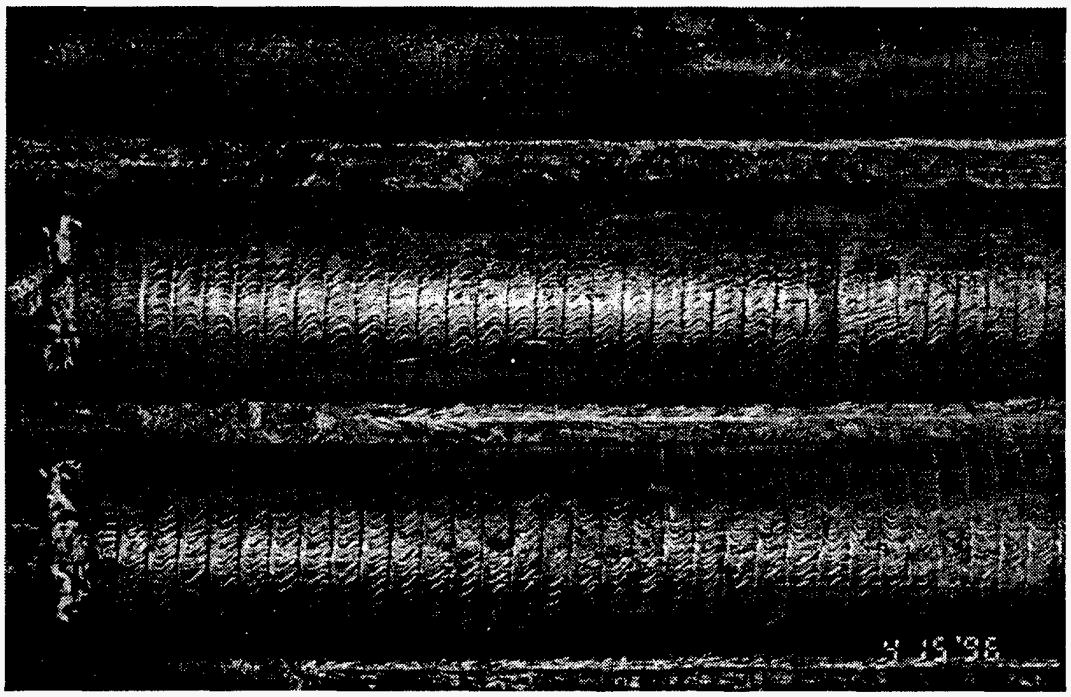

Fig. 4. Spiral Weld Clad Tubing

- Plate thicknesses can be successfully welded under proper conditions.
- Industrial service testing in recovery boilers is continuing.
- Wire arc cladding is being developed as an alternative to conventional weld overlay cladding.
- Spiral weld cladding is being investigated as a replacement for coextruded bimetallic tubing.

REFERENCES

1. T. Zacharia and S.A. David, *"Weldability of Iron Aluminides,"* proceedings of the Fifth Annual Conference on Fossil Energy Materials, ORNL/FMP-91/1, Oak Ridge National Laboratory, September 1991.

2. T. Zacharia, P.J. Maziasz, S.A. David, and C.G. McKamey, *"Weldability of Fe_3Al Based Iron Aluminide Alloys,"* proceedings of the Sixth Annual

Conference on Fossil Energy Materials, ORNL/FMP-92/1, Oak Ridge National Laboratory, July 1992.

3. G.M. Goodwin, C.G. McKamey, P.J. Maziasz, and V.K. Sikka, *"Weldability of Iron Aluminides,"* proceedings of the Seventh Annual Conference on Fossil Energy Materials, ORNL/FMP-93/1, Oak Ridge National Laboratory, July 1993.

4. G.M. Goodwin, P.J. Maziasz, C.G. McKamey, J.H. Devan, and V.K. Sikka, *Weldability of Iron Aluminides,"* proceedings of the Eighth Annual Conference on Fossil Energy Materials, ORNL/FMP-94/1, Oak Ridge National Laboratory, August 1994.

5. G.M. Goodwin, *"Weld Overlay Cladding With Iron Aluminides,"* proceedings of the Ninth Annual Conference on Fossil Energy Materials, ORNL/FMP-95/1, Oak Ridge National Laboratory, August 1995.

6. G.M. Goodwin, *"Weld Overlay Cladding with Iron Aluminides,"* proceedings of the Tenth Annual Conference on Fossil Energy Materials, ORNL/FMP-96/1, Oak Ridge National Laboratory, August 1996.

7. Welding Handbook, **2**, Eighth Ed., pp. 872-74, American Welding Society, Miami, Fla., 1991.

HIGH-STRENGTH IRON ALUMINIDE ALLOYS

C. G. McKamey and P. J. Maziasz

INTRODUCTION

Past studies have shown that binary Fe_3Al possesses low creep-rupture strength compared to many other alloys, with creep-rupture lives of less than 5 h being reported for tests conducted at 593°C and 207 MPa.[1,2] The combination of poor creep resistance and low room-temperature tensile ductility due to a susceptibility to environmentally-induced dynamic hydrogen embrittlement[3-5] have limited use of these alloys for structural applications despite their generally excellent corrosion behavior.[6] With regard to the ductility problem, alloy development efforts have produced significant improvements, with ductilities of 10-20% and tensile yield strengths as high as 500 MPa being reported.[7,8] Initial improvements in creep resistance have been realized through small additions of B, C, Mo, Nb, and Zr.[1,9-13] Control of the amounts of these additions was also found to be important for producing improved weldability in these alloys.[12]

In recent years, further creep strengthening has been produced by using heat treatments to control the microstructure.[14,15] This paper summarizes work performed during the last three years to determine the effect of annealing temperature and the post-anneal cooling rate on creep-rupture properties and microstructural behavior.

DISCUSSION OF CURRENT ACTIVITIES

The alloy composition used in this study was Fe-28Al-5Cr (at.%) with 0.5% Nb, 0.8% Mo, 0.025% Zr, 0.05% C, and 0.005% B (Oak Ridge National Laboratory designation FA-180). A 7-kg ingot was prepared by arc-melting and drop-casting into a chilled copper mold. Fabrication to an 0.8-mm-thick sheet was accomplished by hot-rolling, beginning at 1000°C and finishing at 600-650°C. After a stress relief heat treatment of 1 h at 700°C, flat tensile specimens (0.8 x 3.18 x 12.7 mm) were mechanically punched from the rolled sheet. Before creep-rupture testing, specimens were annealed in air for 1 h at 1150°C and then were either air cooled to room temperature (slower cooling rate) or were quenched in oil or water (faster cooling rate).

Creep-rupture tests were performed in air at temperatures between 593 and 750°C under stresses of 138 to 310 MPa (20-45 ksi). In order to obtain creep exponents and activation energies, minimum creep rates (MCR) were measured as the slope of the linear portion of the test curve and the data were plotted to a power-law equation. Tensile tests were also conducted at room temperature in air at a strain rate of 3.3×10^{-3}/s.

As shown in Fig. 1, a 1-h heat treatment at 1150°C followed by air cooling to room temperature produced creep lives of over 2000 h for tests conducted at 593°C and 207 MPa. This is a significant improvement over the 100-h life observed for specimens of FA-180 heat treated at 750°C (signified by the horizontal line in Fig. 1). Especially interesting in Fig. 1 is the sharp dependence of creep strength on heat treating temperature. Transmission electron microscropy (TEM) of as-heat-treated specimens revealed the presence of a very fine DO_3 ordered structure within coarser B2 ordered domains (see Fig. 2). Also present in the matrix of specimens annealed at 1150°C was a fine dispersion of Zr-based precipitates (Fig. 2). These precipitates appeared to pin dislocations during creep, as shown in Fig. 3 for a specimen creep tested at 593°C.[14] This, together with an activation energy for creep of approximately 150 kcal/mole (a value which is about twice that obtained earlier[1] for the binary alloy heat treated at 750°C) and high creep exponents of 7-12 (ref. 15), indicated that the observed strengthen-

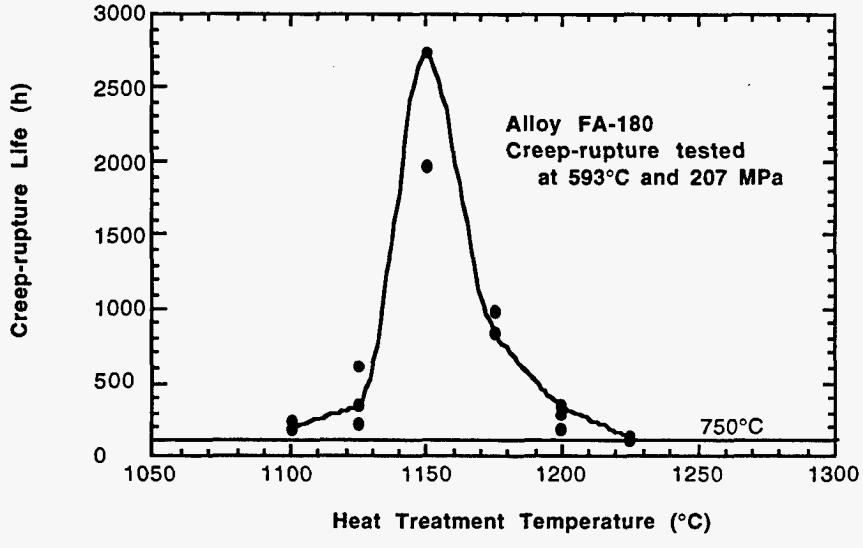

Fig. 1. Creep-rupture life as a function of heat treatment temperature for tests conducted on alloy FA-180 at 593°C and a stress of 207 MPa. The horizontal line at a life of 100 h represents the test of a FA-180 specimen heat treated for 1 h at 750°C.

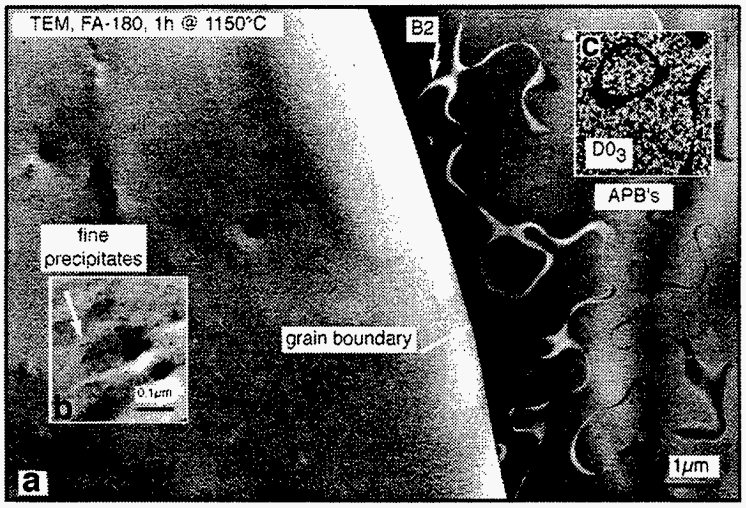

Fig. 2. Electron micrographs showing microstructural features of FA-180 as-heat-treated at 1150°C: (a) clean grain boundaries and low density of matrix dislocations, (b) fine matrix precipitates, and (c) the ordered structures produced by air cooling from 1150°C; fine $D0_3$ structure within coarse B2 structure.

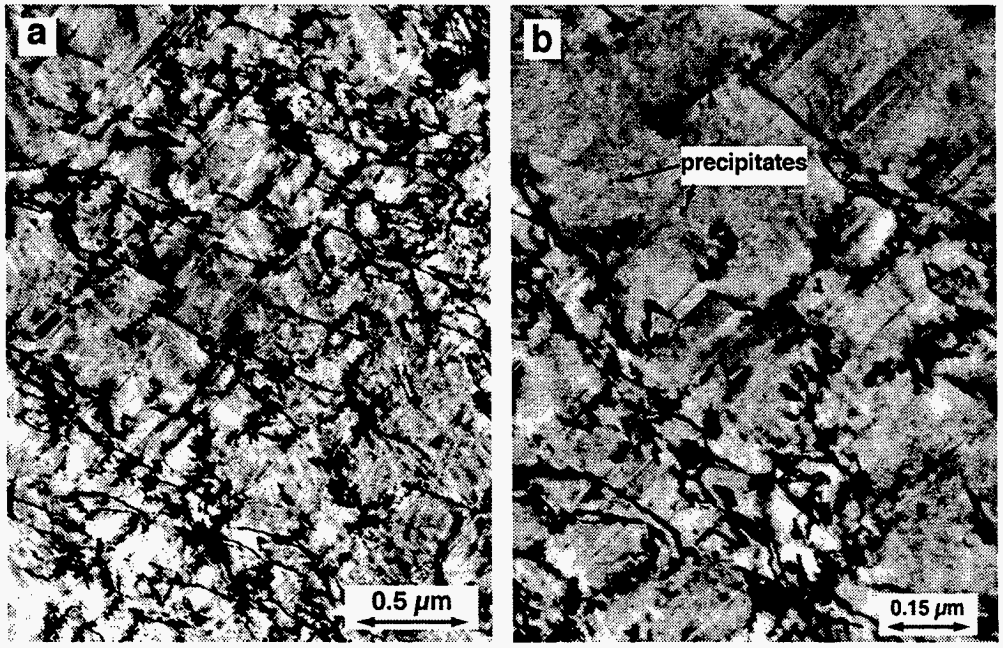

Fig. 3. Transmission electron micrographs showing (a) dislocation tangles and (b) fine matrix precipitates in alloy FA-180 air cooled from a heat treatment at 1150°C and creep tested at 593°C.

ing was being produced by a precipitation mechanism. The general conclusion was that the 1150°C heat treatment resulted in the dissolution of some of the coarse particles remaining from the melting and casting process. The finer Zr-based precipitates then formed during cooling or during the early stages of creep.

Creep-rupture tests were conducted on specimens cooled by different methods from the 1150°C heat treatment temperature and the data are presented in Table I. The more rapidly cooled specimens (oil or water quenched) exhibited the best resistance to creep. Even though the air-cooled specimen exhibited a very good rupture life of approximately 1959 h when tested at 593°C and 207 MPa, a specimen that had been quenched in oil showed no signs of rupturing (no increase in the very low, steady-state creep rate) after 6480 h, at which time the test was stopped. At more severe test conditions (650°C and 241 MPa), the ability of air-cooled specimens to resist creep was lost and failure occurred after an average of only 3 h, while an oil quenched specimen retained its resistance to rupture for over 240 h. Additionally, a water quenched specimen lasted 1637 h at 650°C and 241 MPa before rupture. In each case the fracture mode was observed to be ductile-dimpled rupture. This data suggest that there are fundamental differences in the strengthening mechanism for the quenched versus air cooled specimens.

The strengthening effect produced by quenching from 1150°C was also evident in room temperature tensile data, shown in Table II. The data in this table shows that quenching in oil resulted in hardening with an increase in yield strength from 255 to 481 MPa, even though the grain size was approximately 150 μm for both conditions. The hardening was also evident in the elongation to fracture. For all annealing conditions listed in Table II, the fracture mode was predominantly transgranular cleavage. These results are consistent with strengthening produced by quenched in defects, as has already been well established.[16-18] The reduced creep-

Table I. Creep-Rupture Data for Alloy FA-180 as a Function of the Method Used for Cooling from the 1150°C Heat Treatment

Test Temp. (°C) Stress (MPa)	Air Cooled			Oil Quenched		
	Life (h)	Elong. (%)	MCR (/s)	Life (h)	Elong. (%)	MCR (/s)
593, 207	1959	10	8.3×10^{-7}	>6480[a]	>5	2.7×10^{-8}
650, 207	1059	11	5.5×10^{-7}			2.8×10^{-7}
675, 207	2	32	1.8×10^{-3}	467	12	6.9×10^{-7}
700, 207	1	29	3.9×10^{-3}	104	11	5.5×10^{-6}
650, 241	3	42	2.2×10^{-3}	242	15	1.9×10^{-6}
650, 241				1637[b]	9[b]	2.2×10^{-7}
650, 241				86[c]	13[c]	2.6×10^{-6}

[a]Test stopped before rupture.
[b]Water-quenched from 1150°C.
[c]Oil quenched from 1150°C, then reannealed for 1 h at 750°C and air-cooled before creep testing.

Table II. Effect of Heat Treatment on Room Temperature Tensile Properties of Alloy FA-180

Heat Treatment	Cooling Medium	Yield Strength (MPa)	Ultimate Tensile Strength (MPa)	Elongation (%)
1h/1150°C	air	255	347	2.7
1h/1150°C	oil	481	538	1.0
1h/1150°C+ 1h/750°C	oil/air	293	384	2.4

rupture resistance and tensile yield strength of specimens which were oil quenched from 1150°C and then reannealed at 750°C and air cooled (see data in Tables I and II) support this assumption.

Creep tests were conducted as a function of temperature and stress, and the data were fitted to a power-law creep equation of the form $\dot{\varepsilon} = A\sigma^n(e^{-Q/RT})$ (ref. 19) in order to determine if the appparent activation energies for creep (Q) and the creep exponents (n) were the same in both the air-cooled and oil-quenched conditions. The results are shown in Figs. 4 and 5, respectively. At a stress of 207 MPa (30 ksi), the apparent Q for creep in the oil-quenched specimens was determined to be 84 kcal/mol, compared to a Q of 141 kcal/mol for air-cooled specimens. (The values of Q reported here are slightly different from those reported earlier[15,20] because more recent data have been included.) The large creep exponents shown in Fig. 5 for both the air-cooled and oil-quenched specimens are indicative of alloys which have

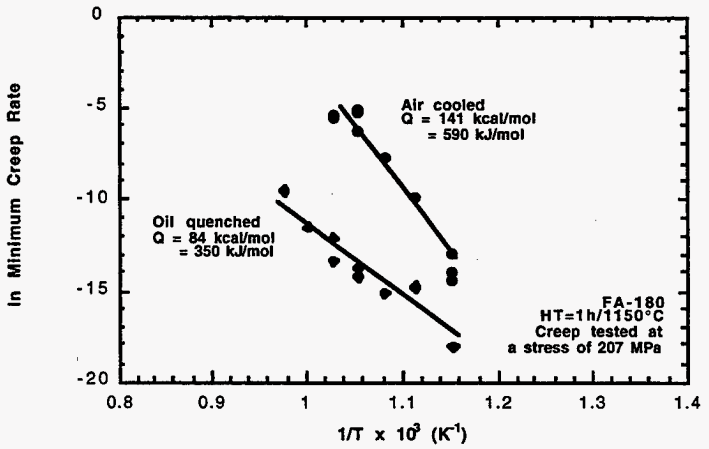

Fig. 4. Determination of creep activation energies for air cooled or oil quenched FA-180 heat treated at 1150°C.

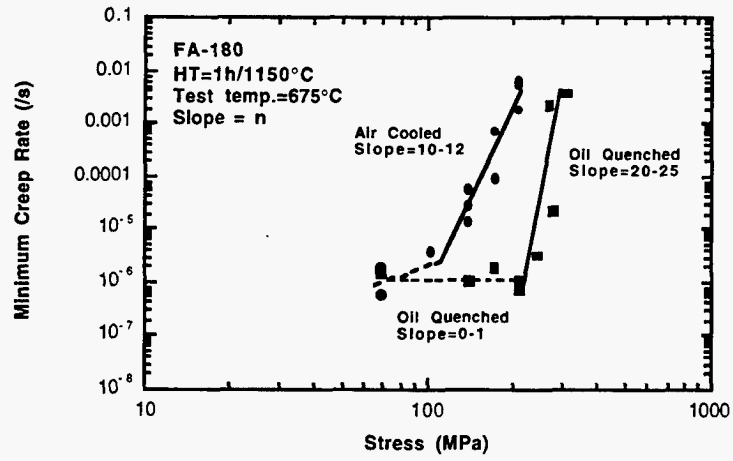

Fig. 5. Determination of creep exponents at a test temperature of 675°C for air cooled or oil quenched FA-180 heat treated at 1150°C.

been strengthened through some kind of dislocation-pinning mechanism,[21-24] although the much larger slope for the oil-quenched specimens indicate a significant difference compared to the air-cooled specimens. For the oil-quenched specimens, a distinct change was observed in the slope of the minimum creep rate versus stress curve in Fig. 5. The break occurred at approximately 200-250 MPa, with the creep exponent decreasing from nearly 20 at the higher stresses to less than 1 at the lower stresses. Data for the air-cooled specimens also suggest the possibility of a change in slope at stresses below 100 MPa. At this point in the research, the reason for this change in slope is unknown, but it could relate to a change in the creep mechanism with stress level.

In order to better determine the stability of the microstructures produced by quenching from 1150°C, creep tests of oil-quenched specimens were conducted as a function of temperature at a constant stress of 207 MPa (30 ksi) and the data are included in Table I. The data indicate that a more efficient and stable strengthening mechanism is operative in the oil-quenched specimens. The air-cooled specimens showed good creep strengths at temperatures as high as 650°C. Above this temperature, however, the specimens quickly became severely weakened, resulting in dramatically reduced creep lives and large elongations to failure at 675°C and above. The oil-quenched specimens, on the other hand, exhibited excellent creep strength at temperatures up to and including 650°C and a creep life of over 100 h at 700°C. This data supports the idea that the dislocation pinning mechanism operating in the oil-quenched specimens is more stable than that in the air-cooled specimens, in that it provides strengthening to higher temperatures and loses its effectiveness more gradually as the

temperature is increased. This could mean that either more and/or finer precipitates (identified previously as the strengthening mechanism in the air-cooled specimens[14]) are present in the oil-quenched specimens, or a more stable kind of pinning mechanism is active.

TEM examination of a control specimen oil quenched from 1150°C showed the presence of coarse B2 domains (Fig. 6) enclosing much smaller $D0_3$ domains, similar to the structure for the air cooled specimen shown in Fig. 2. In this as-heat-treated condition, the specimen also contained only a sparse distribution of dislocations. However, instead of a dispersion of precipitates, the oil-quenched specimen contained ultrafine (<10 nm) defects that were visible as black-white lobed images using **g**=011[B2] (see Fig. 6). These tiny defects exhibited a sharp line separating the black and white lobes that did not rotate with changes in **g**, consistent with the established contrast behavior of small edge loops.[25] Similar image analysis performed on the air-cooled specimen showed that those black-white strain contrast images did rotate with changes in **g**, consistent with their defect nature as 3-dimensional precipitates instead of 2-dimensional edge loops. Although loop nature (vacancy/interstitial) remains to be determined, many investigators observe higher vacancy concentrations in quenched FeAl type alloys,[16,17] and the likelihood of self-interstitial defects without irradiation is remote; therefore, it is reasonable to assume these are vacancy-type loops.

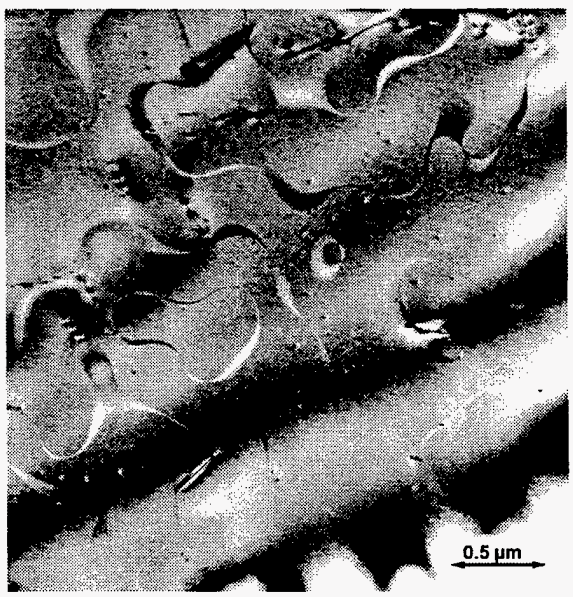

Fig. 6. TEM micrograph of alloy FA-180 showing B2 domains and fine dislocation loops (black dots) produced by oil-quenching from 1150°C (**g**=011 [B2], s=0).

A TEM micrograph of the creep-induced microstructure in the gage of an oil-quenched specimen creep-tested at 593°C and 207 MPa for 6480 h without rupture is shown in Fig. 7. This microstructure clearly shows many large (>0.2 µm) loops uniformly dispersed throughout the matrix, accompanied by long pairs of 2-fold superdislocations. The growth of loops during creep from the "black dots" observed in the oil-quenched control specimen in Fig. 6 to the large loops observed in the creep-tested specimen is consistent with a vacancy nature. The loops observed in Fig. 7 have a basic square or rectangular shape,

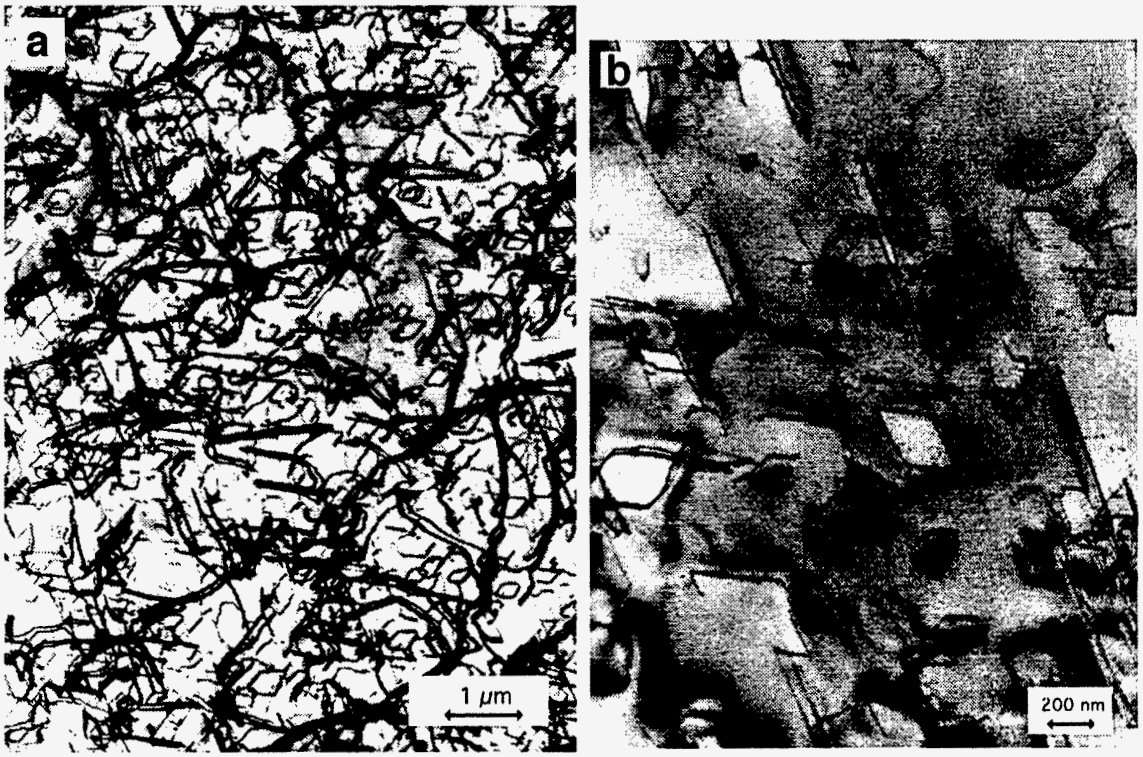

Fig. 7. TEM microstructure of FA-180 (1150°C/oil quenched) specimen creep tested at 593°C/207 MPa for 6480 h without rupture (gage section), showing (a) creep-induced dislocation network structure together with a dense dispersion of dislocation loops, and (b) higher magnification showing several individual loops containing kinks and jogs, present on orthogonal habit planes (**g**=011[B2]).

but with many kinks and jogs that would indicate intersections with network dislocations during creep. They appear to be distributed on orthogonal habit planes [either (110) or (100) types], and their contrast behavior (completely visible or invisible with **g**=011) is consistent with the behavior of edge loops.

The conclusion from TEM and the Q and n analyses shown in Figs. 4 and 5, respectively, is that vacancy loops, rather than fine precipitates, are the obstacles to dislocation motion in the oil-quenched material. The very low creep-rates and extended secondary creep regimes at 593°C and 650°C relative to the air-cooled material indicate that the vacancy loops are more effective barriers to dislocation climb despite their coarseness relative to the ultrafine precipitates observed in the air-cooled material. Their growth by vacancy absorption from the matrix and their direct interaction with intersecting network dislocations are likely factors making dislocation climb and glide through this loop structure more difficult than the ultrafine precipitate structure, consistent with the data in Table I. Although the general description of a mechanism which could produce creep-rupture

strengthening through the pinning of dislocations on point defects would be similar for both precipitates and vacancies, fundamental differences (such as size of the defect, interfacial strength, coherency, stability as a function of temperature, etc.) could be responsible for the differences in Q and n shown in Figs. 4 and 5. The analysis of this data using a model for dispersion-strengthened materials[26] would probably be helpful in understanding the differences in the strengthening mechanisms involved.

CONCLUSIONS

The improved creep-rupture strength of an Fe_3Al-based alloy, FA-180 (Fe-28Al-5Cr-0.5Nb-0.8Mo-0.025Zr-0.05C-0.005B, at.%), was shown to be dependent on processing-induced microstructure. The creep-rupture resistance of this alloy was significantly improved by a solution-annealing heat treatment of 1 h at 1150°C. In specimens air-cooled from 1150°C, microstructural analysis revealed that strengthening was due to a fine dispersion of ZrC precipitates in the matrix and along grain boundaries. These precipitates were not observed in specimens heat treatmented at higher or lower temperatures. Their presence was attributed to the dissolution of coarser ZrC particles (formed during casting) during solution annealing, followed by reprecipitation during cooling or creep testing. Specimens solution-annealed at 1150°C and quenched to suppress the ZrC precipitation were found to be hardened by a dispersion of small quenched-in loops. These loops grew and evolved during creep testing at temperatures of 593-750°C and significantly delayed the onset of tertiary creep. Microstructural and creep activation/exponent analyses suggested that these were vacancy loops that acted as barriers to dislocation climb, resulting in the observed improvement in creep strength and rupture resistance.

ACKNOWLEDGEMENTS

This research was sponsored by the U.S. Department of Energy, Office of Fossil Energy, Advanced Research and Technology Development Materials Program, and by the Assistant Secretary for Energy Efficiency and Renewable Energy, Office for Industrial Technologies, Advanced Industrial Materials Program, under contract DE-AC05-96OR22464 with Lockheed Martin Energy Research Corp.

REFERENCES

1. C. G. McKamey, P. J. Maziasz, and J. W. Jones, *J. Mater. Res.*, **7(8)** (1992), 2089-2106.
2. C. G. McKamey, J. H. DeVan, P. F. Tortorelli, and V. K. Sikka, *J. Mater. Res.*, **6(8)** (1991), pp. 1779-1805.
3. C. T. Liu, C. G. McKamey, and E. H. Lee, *Scripta Metall. Mater.*, **24(2)** (1990), 385-90.
4. C. T. Liu and C. G. McKamey, in *High Temperature Aluminides and Intermetallics*, eds. S. H. Whang, C. T. Liu, D. P. Pope, and J. 0. Stiegler, (TMS, Warrendale, PA, 1990), pp. 133-151.
5. C. G. McKamey and C. T. Liu, in *Proceedings of ADVMAT/91, First International Symposium on Environmental Effects on Advanced Materials*, eds. R. D. Kane, (Houston, TX: NACE, 1992), paper no. 17-1.
6. P. F. Tortorelli and J. H. DeVan, in *Processing, Properties, and Applications of Iron Aluminides*, eds. J. H. Schneibel and M. A. Crimp (TMS, Warrendale, PA, 1994), pp. 257-70.
7. V. K. Sikka, *SAMPE Quart.*, **22(4)** (1991), 2-10.
8. V. K. Sikka, S. Viswanathan, and C. G. McKamey, *Structural Intermetallics*, eds. R. Darolia, J. J. Lewandowski, C. T. Liu, P. L. Martin, D. B. Miracle, and M. V. Nathal, (Warrendale, PA: The Metallurgical Society, 1993), 483-91.
9. P. J. Maziasz and C. G. McKamey, *Mater. Sci. & Eng.*, **A152** (1992), 322-34.
10. D. M. Dimiduk, M. G. Mendiratta, D. Banerjee, and H. A. Lipsitt, *Acta Metall.*, **36** (1988), 2947-58.
11. P. J. Maziasz, C. G. McKamey, and C. R. Hubbard, in *Alloy Phase Stability and Design*, eds. G. M. Stocks, D. P. Pope, and A. F. Giamei (MRS, Pittsburgh, PA, 1990), pp. 349-55.
12. C. G. McKamey, P. J. Maziasz, G. M. Goodwin, and T. Zacharia, *Mat. Sci. & Eng.*, **A174** (1994), 59-70.
13. D. G. Morris, M. Nazmy, and C. Noseda, *Scripta Metall. Mater.* **31**, 173 (1994).
14. C. G. McKamey and P. J. Maziasz, in *Processing, Properties, and Applications of Iron Aluminides*, eds. J. H. Schneibel and M. A. Crimp (TMS, Warrendale, PA, 1994), pp. 147-58.
15. C. G. McKamey, Y. Marrero-Santos, and P. J. Maziasz, in *High Temperature Ordered Intermetallic Alloys VI*, eds. J. A. Horton, I. Baker, S. Hanada, R. D. Noebe, and D. S. Schwartz (MRS, Pittsburgh, 1995), pp. 249-254.
16. P. Nagpal and I. Baker, *Metall. Trans.* **21A**, 2281 (1990).
17. A. Ball and R. E. Smallman, *Acta Metall.* **16**, 233 (1968).
18. D. J. Gaydosh and M. V. Nathal, *Scripta Metall. Mater.* 24, 1281 (1990).
19. O. D. Sherby and P. M. Burke, *Prog. Mat. Sci.* 13, 325 (1968).
20. C. G. McKamey and P. J. Maziasz, in *Proceedings of the Tenth Annual Conference on Fossil Energy Materials*, compiled by N. C. Cole and R. R. Judkins, ORNL/FMP-96/1, Aug. 1996, pp. 215-23.
21. O. D. Sherby and P. M. Burke, *Prog. Mater. Sci.* **13**, 325 (1968).
22. R. Lagneborg and B. Bergman, *Met. Sci. J.* **10**, 20 (1976).
23. K. Sadananda, H. Jones, C. R. Feng, and A. K. Vasudevan, in *High Temperature Ordered Intermetallic Alloys IV*, eds. L. A. Johnson, D. P. Pope, and J. O. Stiegler (MRS, Pittsburgh, 1991), pp. 1019-25.
24. I. Jung, M. Rudy, and G. Sauthoff, in *High Temperature Ordered Intermetallic Alloys II*, eds. N. S. Stoloff, C. C. Koch, C. T. Liu, and O. Izumi (MRS, Pittsburgh, 1987), pp. 263-74.
25. J.W. Edington, *Interpretation of Transmission Electron Micrographs*, Monograph 3 in Practical Electron Microscopy in Materials Science, N.V. Philips, Eindhoven, Netherlands, 1975.
26. J. Rösler and E. Arzt, *Acta Metal. Mater.* 38(4), 671 (1990).

INGOT METALLURGY OXIDE DISPERSION STRENGTHENED (ODS) IRON ALUMINIDE

V. K. Sikka and C. R. Howell

and

F. Hall* and J. Valykeo*

INTRODUCTION

The Fe_3Al-based intermetallic alloys have been under development ([1-5]) at the Oak Ridge National Laboratory (ORNL) for a number of years. These alloys are attractive for coal gasification systems because of their excellent resistance ([6]) to high-temperature oxidation and sulfidation. To date, significant progress has been made in the development of alloy compositions with improved room-temperature ductility and high-temperature strength. However, the high-temperature strength at temperatures above 650°C continues to be a limiting factor in their applications to take full advantage of their excellent oxidation and sulfidation resistances. The oxide dispersion strengthening (ODS) is one possible method of improving the high-temperature strength of the iron aluminides. One method of producing the ODS materials is the attritor milling of alloy powder with Y_2O_3 powder, followed by consolidation, and grain-growth heat treatment. This method is the same as that used by Inco Alloys International, Inc. (Inco) [Huntington, West Virginia] to produce the commercial alloy MA-956. However, the cost of conventional processing of ODS materials is the limiting factor in their wide spread use. The purpose of this study was to ODS produce the Fe_3Al-based alloy by using an alternate low-cost method developed by Hoskins Manufacturing Company (Hoskins) [Hamburg, Michigan]. The low-cost method is designated as ingot metallurgy ODS iron aluminide. This paper will present the details of processing, microstructure, and properties of a heat of Fe_3Al-based alloy FAS that was ODS produced by Hoskins' method.

Processing

The Fe_3Al-based alloy FAS was chosen for this study. The FAS alloy consists of Fe-15.9 Al-2.2 Cr-0.01 B (weight percent) and has the best sulfidation resistance among the Fe_3Al-based alloys. A 500-kg heat of this alloy was prepared by air-induction melting at Hoskins. Table 1 is the chemical analysis of the heat which shows that it met the target

*Hoskins Manufacturing Company, 10776 Hall Road, Hamburg, Michigan.

Table 1. Comparison of target and check analyses of FAS alloy[a]

Element	Weight percent	
	Target	Powder
Al	15.9	16.0
Cr	2.2	2.17
B	0.01	0.010
C	--	0.014[b]
S	--	0.001[c]
Mo	--	0.01
Cb	--	<0.01
Zr	--	<0.01
N_2	--	0.005
O_2	--	0.030

[a]FAS alloy prepared by air-induction melting and used for oxide dispersion strengthening.

[b]Carbon was specified as 0.01 max.

[c]Sulfur was specified as 0.0020 max.

composition extremely well. The alloy ingots were subsequently machined to remove any surface oxide and inert gas atomized to powder. The powder was blended with 0.5 wt % Y_2O_3 and processed by Hoskins' proprietary steps to billets that were subsequently processed to plate and bar. The plate was 15.875 mm thick, and the bar was 60.3 by 60.3 mm square with rounded corners. Figure 1 shows the plate and bar product received from Hoskins. The FAS + 0.5 wt % Y_2O_3 material is designated as 920 alloy, and its heat number is 21870.

A small section of the 15.875-mm plate was processed into 0.762-mm-thick sheet at ORNL. The processing steps consisted of hot rolling at 1100°C from 17.0 to 8.64 mm thickness, hot rolling at 800°C from 8.64 to 4.32 mm thickness, and warm rolling at 650°C from 4.32 to 0.762 mm thickness.

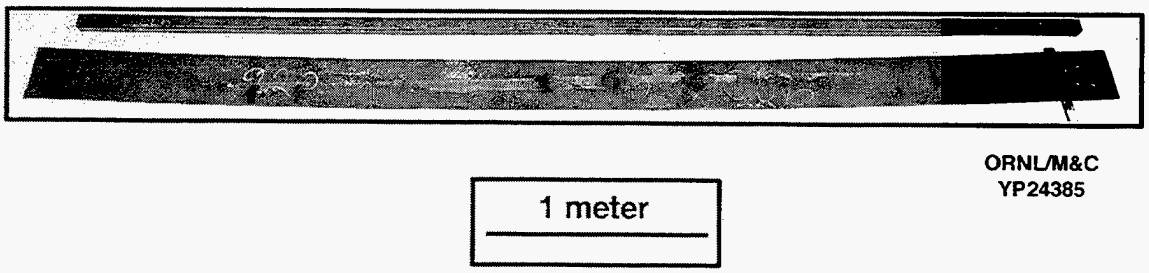

Figure 1. Hot-rolled plate and bar of 920 alloy. The plate is 15.875 mm thick by 210 mm wide, and the bar is 60.3 by 60.3 mm square with rounded corners.

DISCUSSION OF CURRENT ACTIVITIES

The effort during this fiscal year continued to procure a large ingot metallurgy ODS iron-aluminide heat and characterize it for its mechanical and microstructural properties. The following activities were carried out and are briefly described below.

Testing Details

The 0.762-mm-thick sheet was die punched into 1-in. gage length tensile specimens. The specimens were tested after two heat treatments: 1 h at 700°C followed by oil quenching and 1 h at 1250°C in vacuum. Both sets of specimens were tensile tested from room temperature to 1000°C. Tensile specimens of 6.35 mm diam in the gage section were machined from the plate and bar product. These were tensile tested in the as-hot rolled condition in the temperature range from room temperature to 1000°C. A limited number of creep tests were also conducted on the sheet, plate, and bar specimens. Optical and scanning electron microscopy were used to characterize the material.

Results

Tensile data on the sheet, plate, and bar are summarized in Table 2 and plotted in Figures 2 through 4. Data for the base FAS alloy is also included for comparison. These plots show the following:

1. The grain coursening treatment of 1250°C has a strong effect in reducing the room-temperature yield and ultimate tensile strengths. It also reduces the ductility by nearly 50%.
2. The large differences in yield strength between the grain coarsened sheet and the round specimens of plate and bar are associated with the specimen size.

Table 2. Tensile property data for 920 alloy (heat 21870) of FAS + 0.5 wt % Y_2O_3

Specimen no.	Test temperature (°C)	Heat treatment	Yield strength (Mpa)	Tensile strength (Mpa)	Total elongation (%)	Reduction of area (%)
2L[a]	23	Sheet Annealed 700°C/1 h OQ[b]	414.46	979.23	16.45	14.16
8L[a]	23	Sheet Annealed 1250°C/1 h Vacuum	370.13	775.07	7.37	8.84
14L[c]	23	Plate As rolled	515.40	578.49	2.18	2.23
22L[c]	23	Bar As rolled	491.20	571.60	1.91	3.34
4L[a]	600	Sheet Annealed 700°C/1 h Oq[b]	365.16	381.64	43.95	55.14
10L[a]	600	Sheet Annealed 1250°C/1 h Vacuum	356.20	401.63	42.00	62.80
15L[c]	600	Plate As rolled	393.77	398.74	46.53	70.04
23L[c]	600	Bar As rolled	385.64	393.43	59.84	77.76

Table 2. (Continued)

Specimen no.	Test temperature (°C)	Heat treatment	Yield strength (Mpa)	Tensile strength (Mpa)	Total elongation (%)	Reduction of area (%)
5L[a]	800	Sheet Annealed 700°C/1 h Vacuum	94.67	97.15	53.75	69.95
9L[a]	800	Sheet Annealed 1250°C/1 h	89.01	91.98	42.95	73.75
16L[c]	800	Plate As rolled	85.50	95.15	62.86	86.36
24L[c]	800	Bar As rolled	107.70	108.94	63.64	93.80
6L[a]	1000	Sheet Annealed 700°C/1 h OQ	17.44	19.93	79.30	81.99
11L[a]	1000	Sheet Annealed 1250°C/1 h Vacuum	17.58	18.48	102.10	71.80
17L[c]	1000	Plate As rolled	16.13	18.41	111.08	89.75
25L[c]	1000	Bar As rolled	16.55	18.00	111.20	--

[a]Strain rate: $3.33 \times 10^{-3} s^{-1}$.

[b]OQ = oil quenched.

[c]Strain rate: $2.67 \times 10^{-3} s^{-1}$.

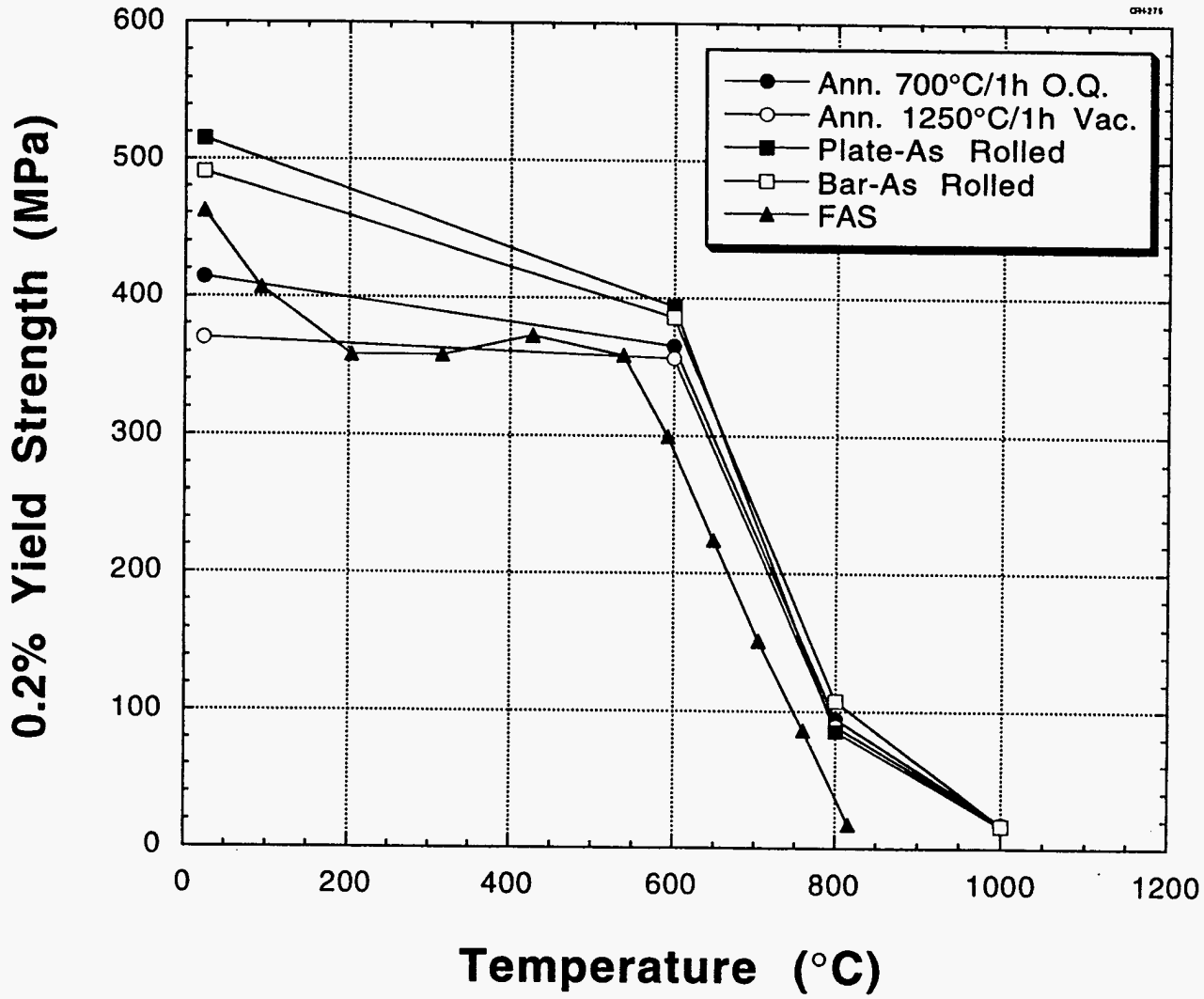

Figure 2. Yield strength (0.2% offset) as a function of test temperature for sheet, plate, and bar of 920 alloy.

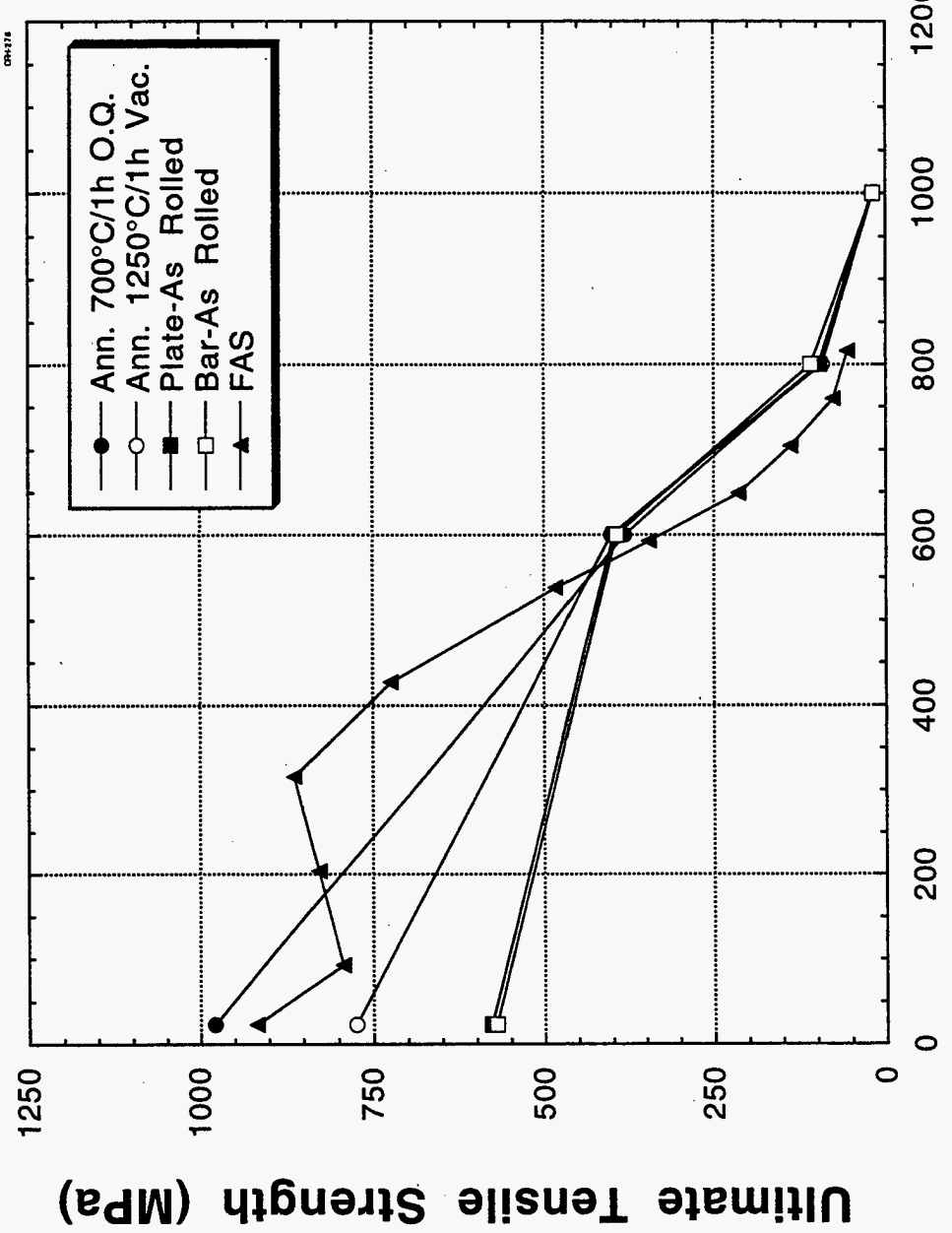

Figure 3. Ultimate tensile strength as a function of test temperature for sheet, plate, and bar of 920 alloy.

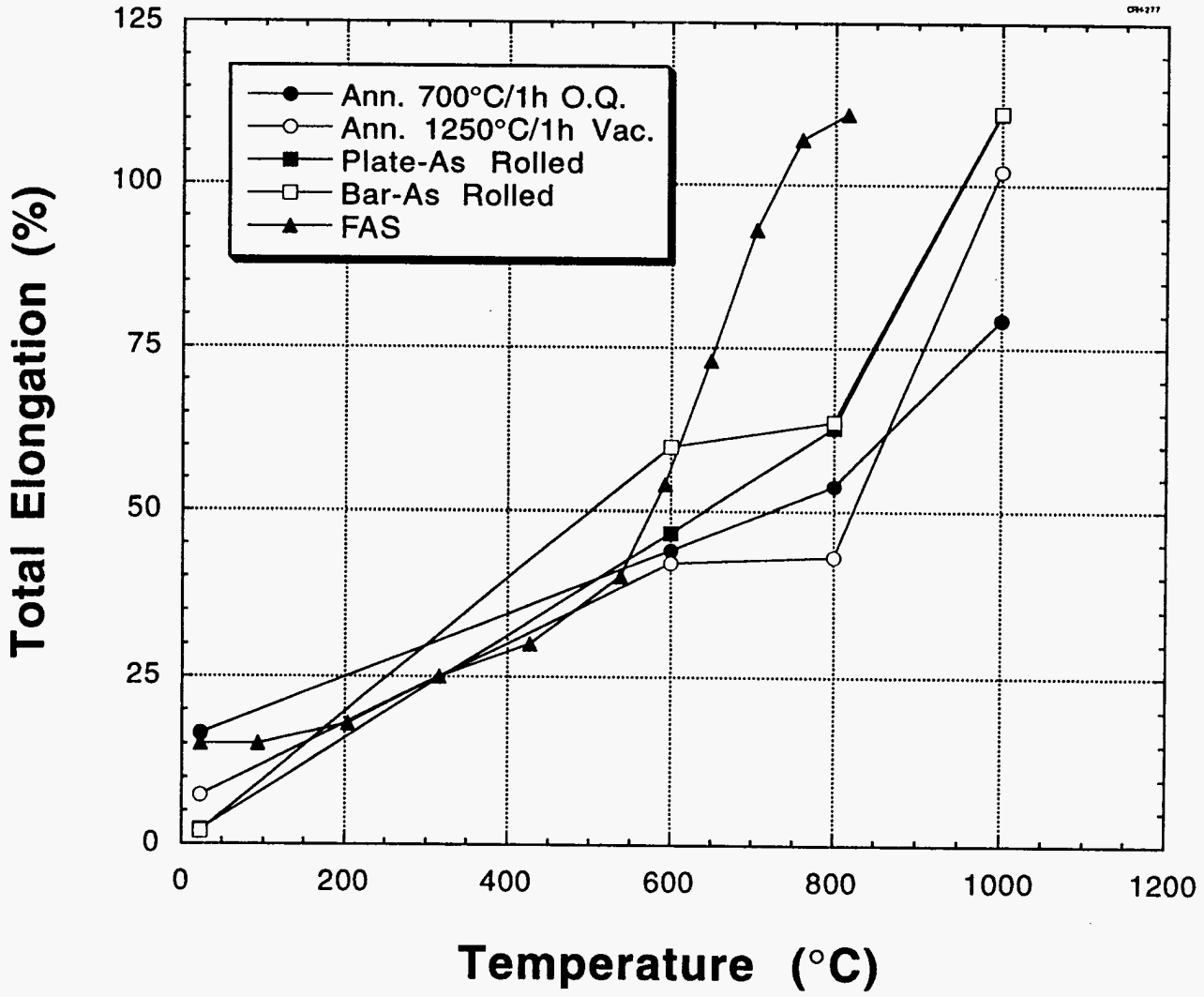

Figure 4. Total elongation as a function of test temperature for sheet, plate, and bar of 920 alloy.

3. The ultimate tensile strength, which is insensitive to the testing procedure, is more indicative of the true behavior. Data in Figure 3 shows that sheet has the highest strength in the fine-grained condition, which is reduced by the grain coarsening treatment of 1250°C for 1 h. The plate and bar of coarse-grained structure show even lower values at room temperature.
4. The yield and ultimate tensile strength properties are relatively unaffected by test temperatures of 600, 800, and 1000°C.
5. The room-temperature elongation is most affected by either grain coarsening treatment of the sheet or testing of coarse-grained hot-rolled plate and bar. It is interesting to note that the coarse-grained plate and bar have the highest ductility, and the fine-grained sheet has the lowest ductility at room temperature. The elongation trends at intermediate temperatures of 600 and 800°C are not quite straightforward. In any event, the ductility at test temperatures of 600, 800, and 1000°C is sufficiently high to be of no concern.
6. At test temperatures of ≥ 600°C, the ODS produced material is consistently higher in strength than the base material. At 800°C, the yield and ultimate tensile strengths are higher by a factor of nearly two.

The creep rupture data for the sheet, plate, and bar are plotted as Larson Miller parameter in Figure 5 and shown in Table 3. Also included in this plot are the data for the base Fe_3Al alloys (FAS, FAL, and FA-129), a commercially produced mechanically alloyed MA-956 produced by Inco, and an ingot metallurgy Fe-Cr-Al-based ODS material (877) produced at Hoskins. This figure shows that while the Hoskins process significantly enhanced the creep properties of their Fe-Cr-Al alloy, it produced only a small effect for the FAS alloy. Note however that even though small, it is still a factor of nearly two improvement in creep rupture strength of the base FAS alloy.

The optical microstructures of the sheet in the fine- and coarse-grained heat-treated conditions are shown in Figure 6. The microstructures of the plate and bar are shown in Figures 7 and 8. The sheet and plate show elongated grains in the rolling direction, and the microstructure is uniform across the thickness. The bar showed a inhomogeneous microstructure that consisted of large grains and large grains with colonies of fine grains, which may have resulted from the dynamic recrystallization process.

The backscattered electron micrographs of transverse sections of the plate and bar are shown in Figure 9. The low magnification micrographs show a fairly uniform distribution of Y_2O_3 particles. The higher magnification micrographs show the Y_2O_3 particles to be clusters. The porosity observed in the high magnification micrographs is a result of Y_2O_3 particle drop-out during metallographic specimen preparation.

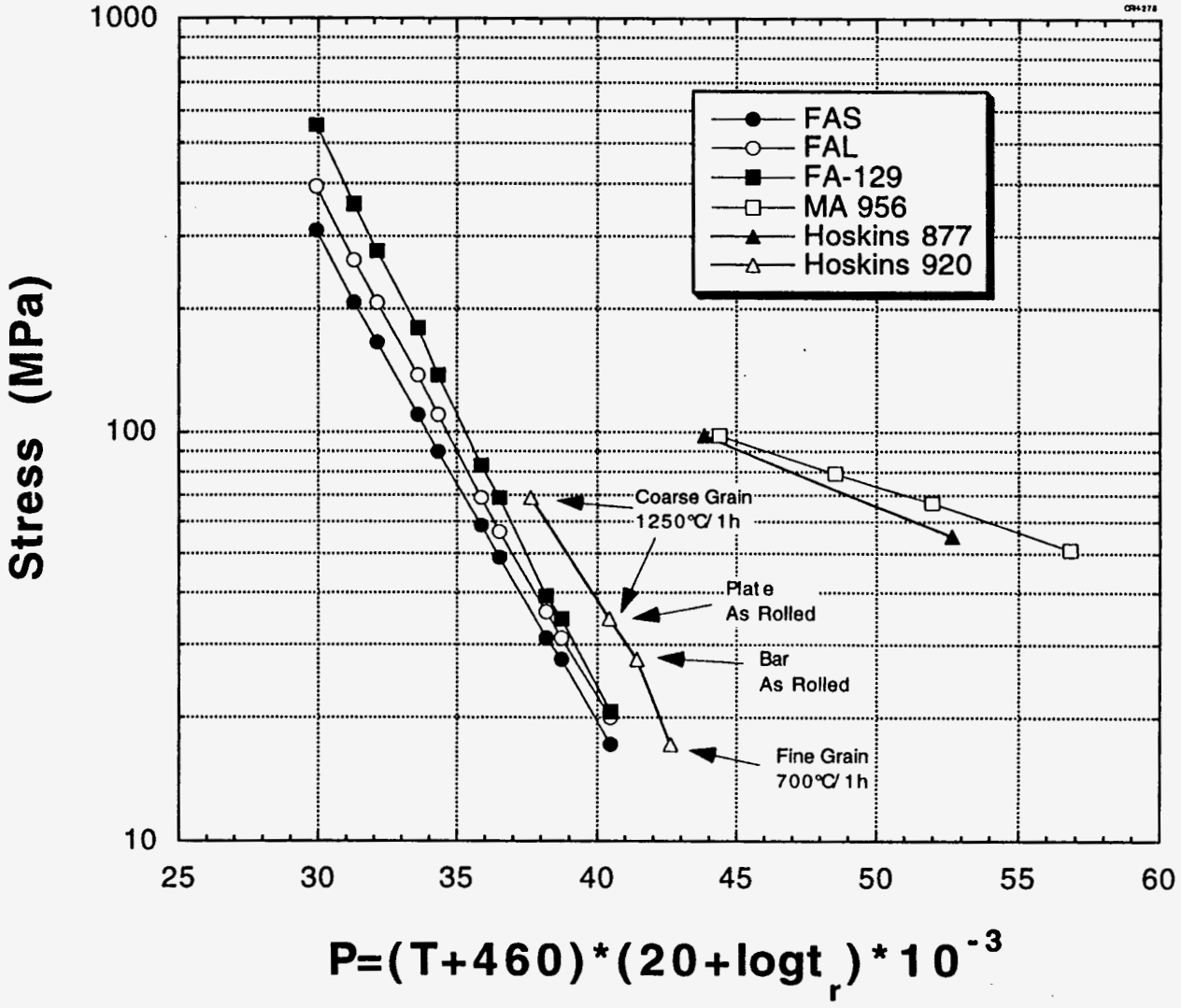

Figure 5. Larson Miller plot of creep rupture data for sheet, plate, and bar of 920 alloy.

Table 3. Creep property data for 920 alloy (heat 21870) of FAS + 0.5 wt % Y_2O_3

Specimen no.	Heat treatment	Test temperature (°C)	Stress (Mpa)	Status[a]	Time (h)	Total elongation (%)	Reduction of area (%)
1L	Sheet Annealed 700°C/1 h OQ[b]	980	68.9	R	0.0	3.72	83.30
3L	Sheet Annealed 700°C/1 h OQ[b]	800	17.2	R	113.8	3.53	29.20
7L	Sheet Annealed 1250°C/1 h Vacuum	800	34.5	R	11.7	62.50	61.50
12L	Sheet Annealed 1250°C/1 h Vacuum	700	68.9	R	29.9	71.40	63.97
13L	Plate As rolled	800	34.5	R	6.0	126.37	85.33
21L	Bar As rolled	800	27.6	R	27.5	99.76	86.88

[a]R = ruptured.

[b]OQ = oil quenched.

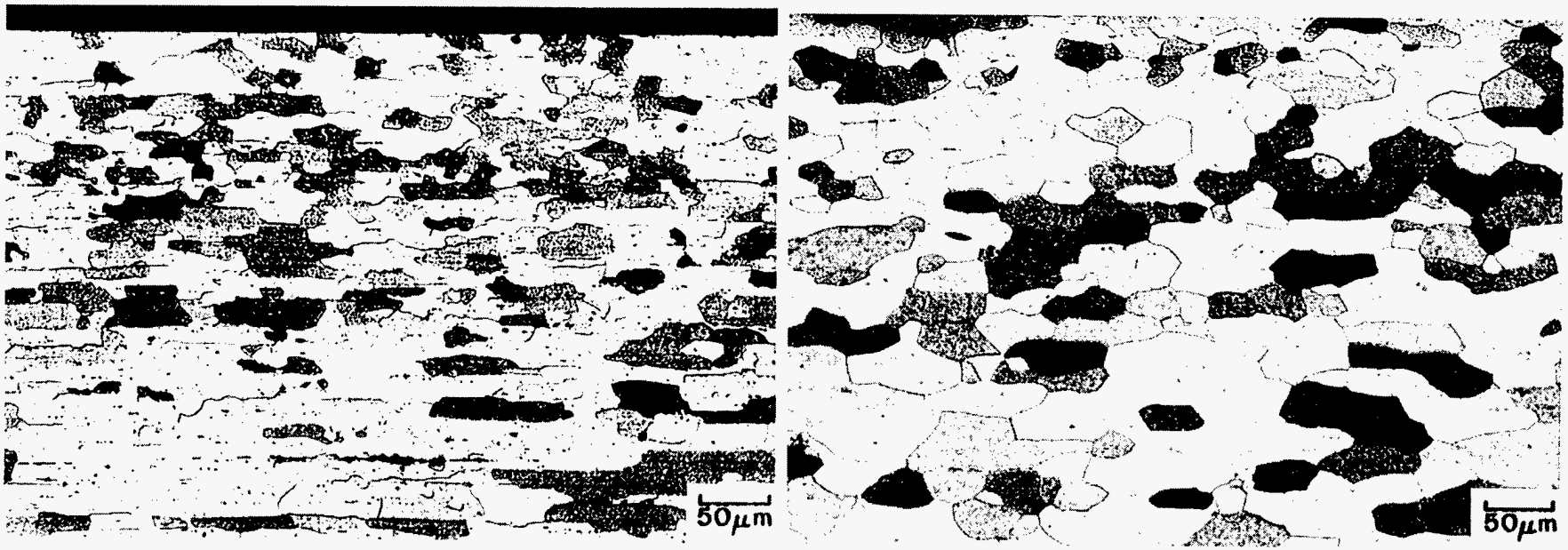

(*a*) 97-0524-10 (*b*) 97-0700-2

Figure 6. Optical microstructure of the longitudinal section of a 0.762-mm-thick sheet of ingot metallurgy oxide dispersion strengthened FAS alloy: (*a*) air annealed for 1 h at 700°C followed by oil quenching, and (*b*) vacuum annealed for 1 h at 1250°C. The magnification for both (*a*) and (*b*) is 200×.

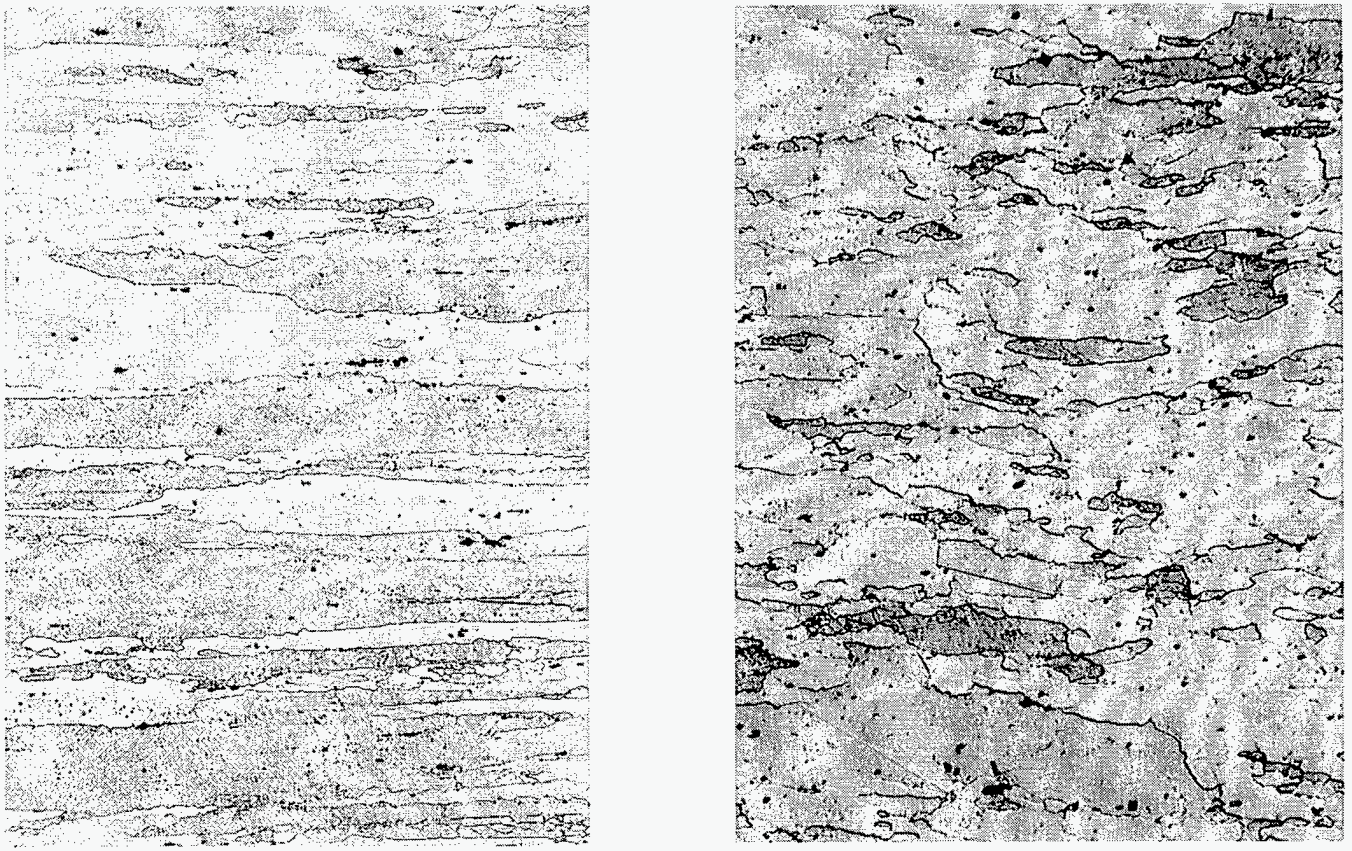

Figure 7. Optical micrographs of etched 15.875-mm-thick plate of ingot metallurgy oxide dispersion strengthened FAS alloy: (*a*) longitudinal and (*b*) transverse. The magnification for both (*a*) and (*b*) is 200×.

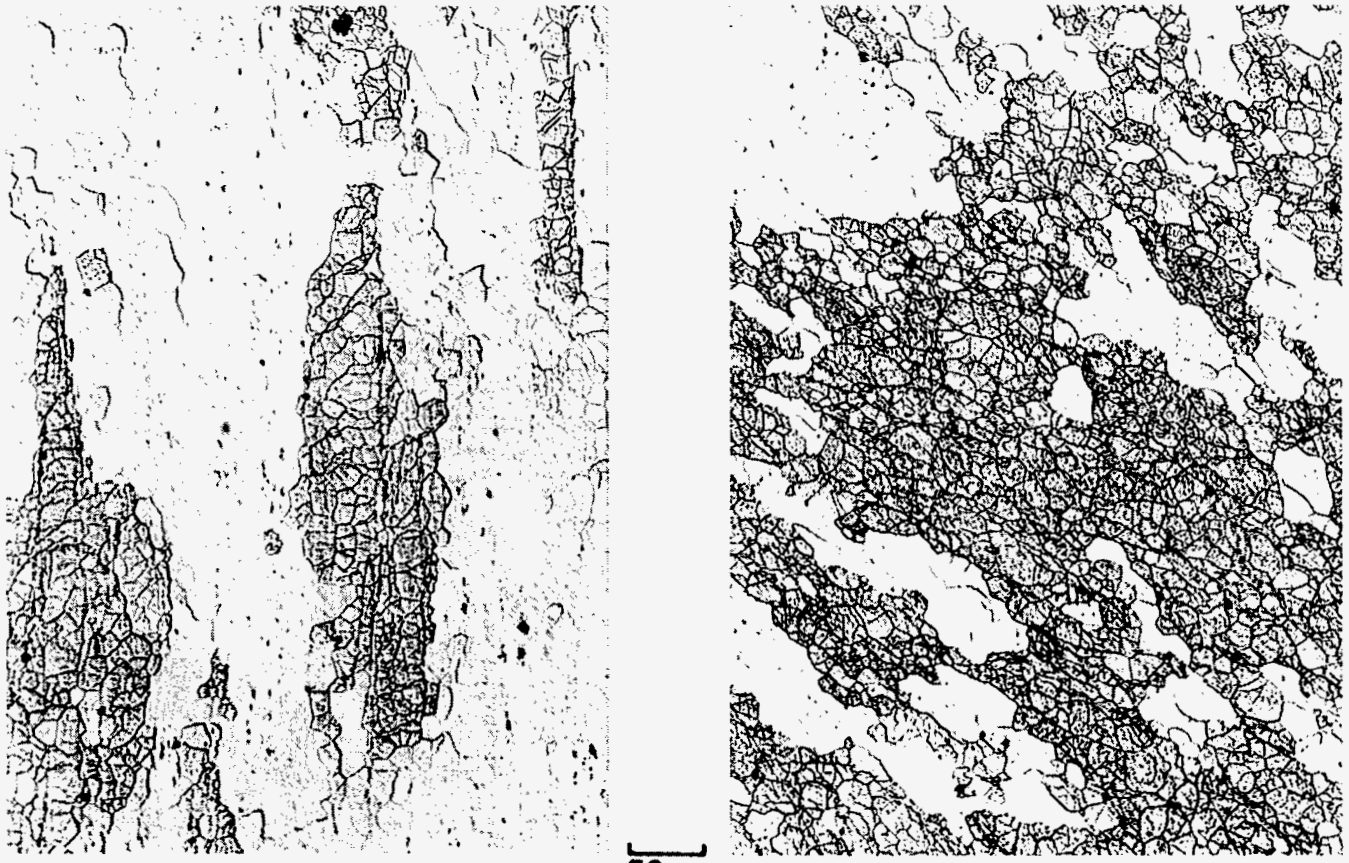

(*a*) 97-0469-003

(*b*) 97-0470-003

Figure 8. Optical micrographs of etched 60.3 mm rounded corner bar of ingot metallurgy oxide dispersion strengthened FAS alloy: (*a*) longitudinal and (*b*) transverse. The magnification for both (*a*) and (*b*) is 200×.

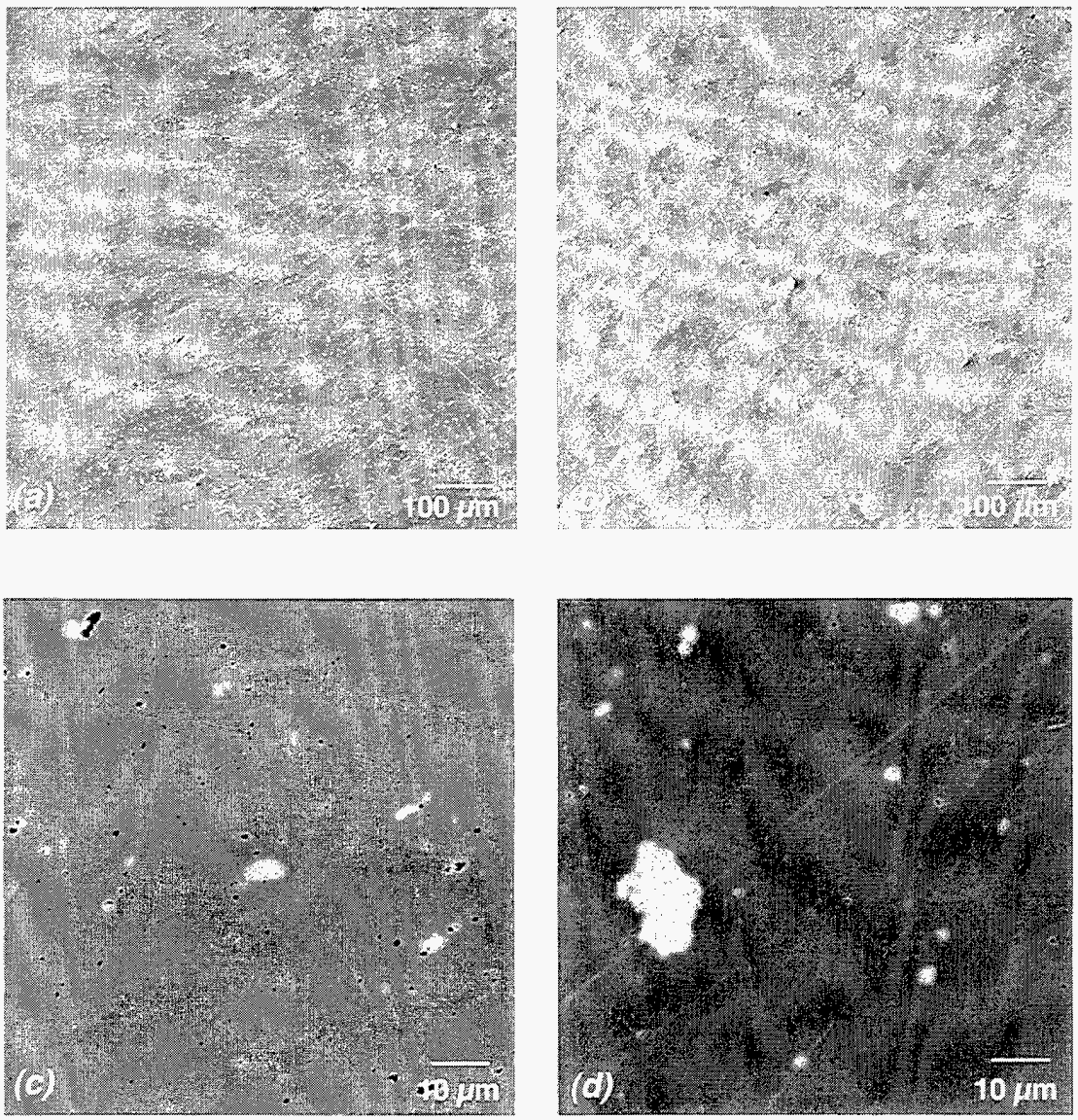

Figure 9. Scanning electron micrographs of transverse sections of plate and bar products of ingot metallurgy oxide dispersion strengthened FAS alloy: (*a*) plate and (*b*) bar are low magnification, and (*c*) plate and (*d*) bar are high magnification.

Elemental mapping was carried out on one of the large particle areas to determine their composition (Figure 10). It is clear from these maps that the large particles consist of yttrium and oxygen and have no iron or aluminum associated with them.

DISCUSSION

The ingot metallurgy method for ODS, developed by Hoskins, has worked effectively for creep strengthening of their Fe-Cr-Al alloy. However, the same method when applied to the ORNL-developed Fe_3Al-based alloy FAS showed less benefit in improvement of creep strength. Detailed metallography has revealed that the primary cause for less improvement in the FAS material is the presence of Y_2O_3 agglomerates rather than the finer distribution that is required for strengthening. Even though the full property enhancement was not observed, the Y_2O_3-treated FAS alloy still showed nearly two times higher creep rupture strength values than the untreated material. The Y_2O_3-treated alloy also showed nearly a factor of two higher yield and ultimate tensile strengths at temperatures $\geq 600°C$. A second heat of the alloy is planned to check if Y_2O_3 distribution can be refined to produce a finer uniform distribution.

The sheet produced by rolling the plate was used to determine if grain growth treatment resulted in further improvement of creep strength. Metallography of the sheet specimens with 700 and 1250°C treatments showed that the later treatment did not produce a significant increase in grain size. Work is currently under way to look at heat-treatment temperatures of 1350 and 1400°C for 1 h. The specimens heated for grain growth will be subjected to creep testing to determine the resulting strength improvement.

SUMMARY AND CONCLUSIONS

A lower cost method developed by Hoskins was used to produce an ODS heat of Fe_3Al-based alloy FAS. The alloy contained 0.5% Y_2O_3 and was processed into plate, bar, and sheet. Tensile, creep, and metallography were carried out on all three products. To date, data have shown only moderate improvement in creep properties as opposed to Y_2O_3-free material. It is also shown that the Hoskins process works for a Fe-Cr-Al alloy (877). It is believed that Y_2O_3 particle clusters are the cause for limited improvement observed in creep properties. A second heat of FAS is being planned by Hoskins' method.

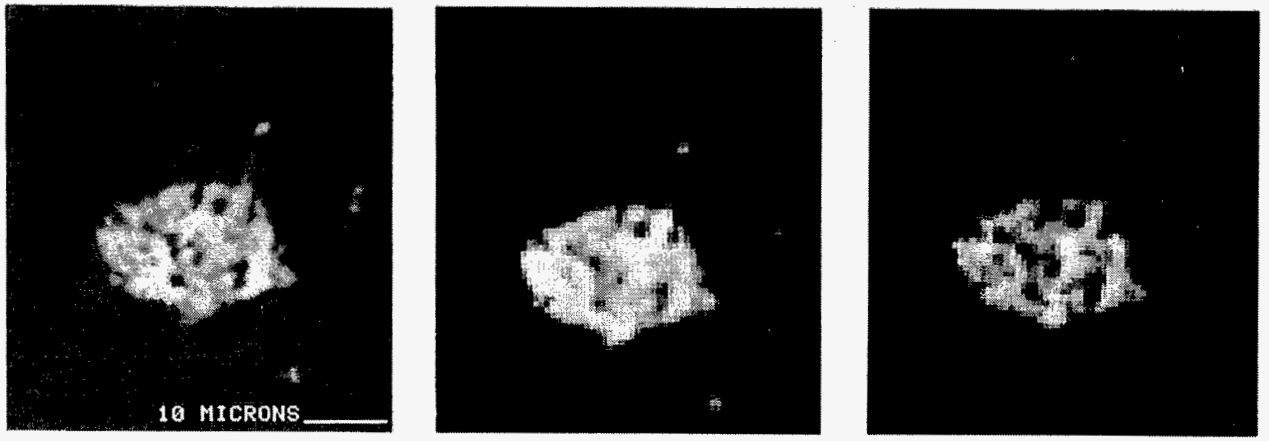

(*a*) Backscattered electron image (*b*) Yttrium (*c*) Oxygen

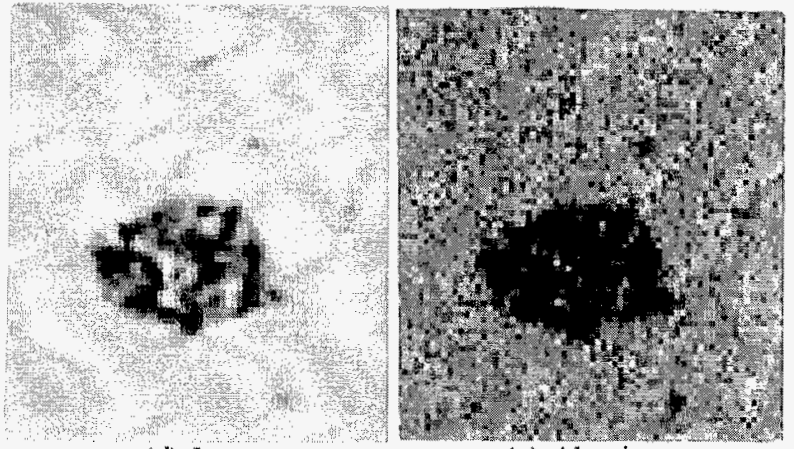

(*d*) Iron (*e*) Aluminum

Figure 10. Scanning electron micrographs showing: (*a*) backscattered electron image of the particles in ingot metallurgy oxide dispersion strengthened FAS. Elemental maps of yttrium, oxygen, iron and aluminum are shown in (*b*), (*c*), (*d*), and (*e*), respectively.

REFERENCES

1. C. G. McKamey, J. H. DeVan, P. F. Tortorelli, and V. K. Sikka, *J. Mater. Res.*, **6**, 1779-805 (1991).
2. V. K. Sikka, S. Viswanathan, and S. Vyas, *High Temperature Ordered Intermetallic Alloys V*, Vol. 288, p. 971, Materials Research Society, Pittsburgh, Pennsylvania, 1993.
3. V. K. Sikka, S. Viswanathan, and C. G. McKamey, *Structural Intermetallics*, p. 483, The Minerals, Metals and Materials Society, Warrendale, Pennsylvania, 1993.
4. C. G. McKamey and D. H. Pierce, *Scr. Metall. Mater.*, **28**, 1173-6 (1993).
5. P. G. Sanders, V. K. Sikka, C. R. Howell, and R. H. Baldwin, *Scr. Metall. Mater.*, **25**, 2365-9 (1991).
6. K. Natesan and P. F. Tortorelli, *International Symposium on Nickel and Iron Aluminides: Processing, Properties, and Applications*, p. 265, ASM International, Materials Park, Ohio, 1997.

SCALE-UP OF LOW-ALUMINUM ALLOY FAPY

V. K. Sikka and C. R. Howell

and

F. Hall* and J. Valykeo*

INTRODUCTION

The Fe-Al alloy containing 8.5 wt % Al developed at the Oak Ridge National Laboratory (ORNL). The detailed composition of the FAPY alloy is given in Table 1. The FAPY is a Fe-Al solid solution alloy with room-temperature ductility of approximately 25% in the wrought condition. Good oxidation resistance and excellent performance under simulated heating element test conditions make the alloy attractive as heating element material. The ORNL and Hoskins Manufacturing Company (Hoskins) (Hamburg, Michigan) have worked together during this year to scale up the FAPY alloy and develop steps for commercial processing of large ingots into heating element wire. Significant progress made during this year is described below.

Results and Discussion

Two 500-kg heats of FAPY alloy were air-induction melted and cast into square, cross-sectional tapered ingots. Chemical analysis of the two heats is compared with the target composition in Table 1. The ingots were hot-processed through blooming and bar mill into 9.5-mm-diam rod stock. The rod was subsequently preheated to approximately 200°C and drawn in three steps to 40-mil-diam wire. An 800°C intermediate anneal was used between major reduction steps of approximately 60%. The wire was subjected to optical metallography in both transverse and longitudinal directions.

The transverse and longitudinal cross sections of the wire in the unetched condition are shown in Figure 1. The microstructure in this figure shows the presence of small inclusions. The etched microstructures of transverse and longitudinal directions are shown in Figure 2. These micrographs show extremely fine and highly worked microstructure.

---

*Hoskins Manufacturing Company, 10776 Hall Road, Hamburg, Michigan.

Table 1. Comparison of chemical analysis[a] of two FAPY alloy heats made at Hoskins Manufacturing Company with the target composition

		Heat	
Element	Target	899-21689	899-21690
Al	8.46	8.69	8.45
Cr	5.50	5.46	5.49
Zr	0.20	0.20	0.21
C	0.03	0.054	0.21
Mo	2.00	2.06	2.10
Y	0.10	0.13[b]	0.16[b]
Mn	--	0.34	0.34
S	--	0.006	0.007
Nb	--	0.012	0.01
B	--	<0.001	<0.001
N2	--	0.003	0.002
O2	--	0.003	0.003
Fe	*c*	*c*	*c*

[a]Weight percent.
[b]Estimated
[c]Balance.

The most significant aspect of this project is the demonstration by Hoskins that they can follow the ORNL-developed procedures to fabricate FAPY wire using the commercially available process. This paves the way for marketing FAPY wire for heating element applications.

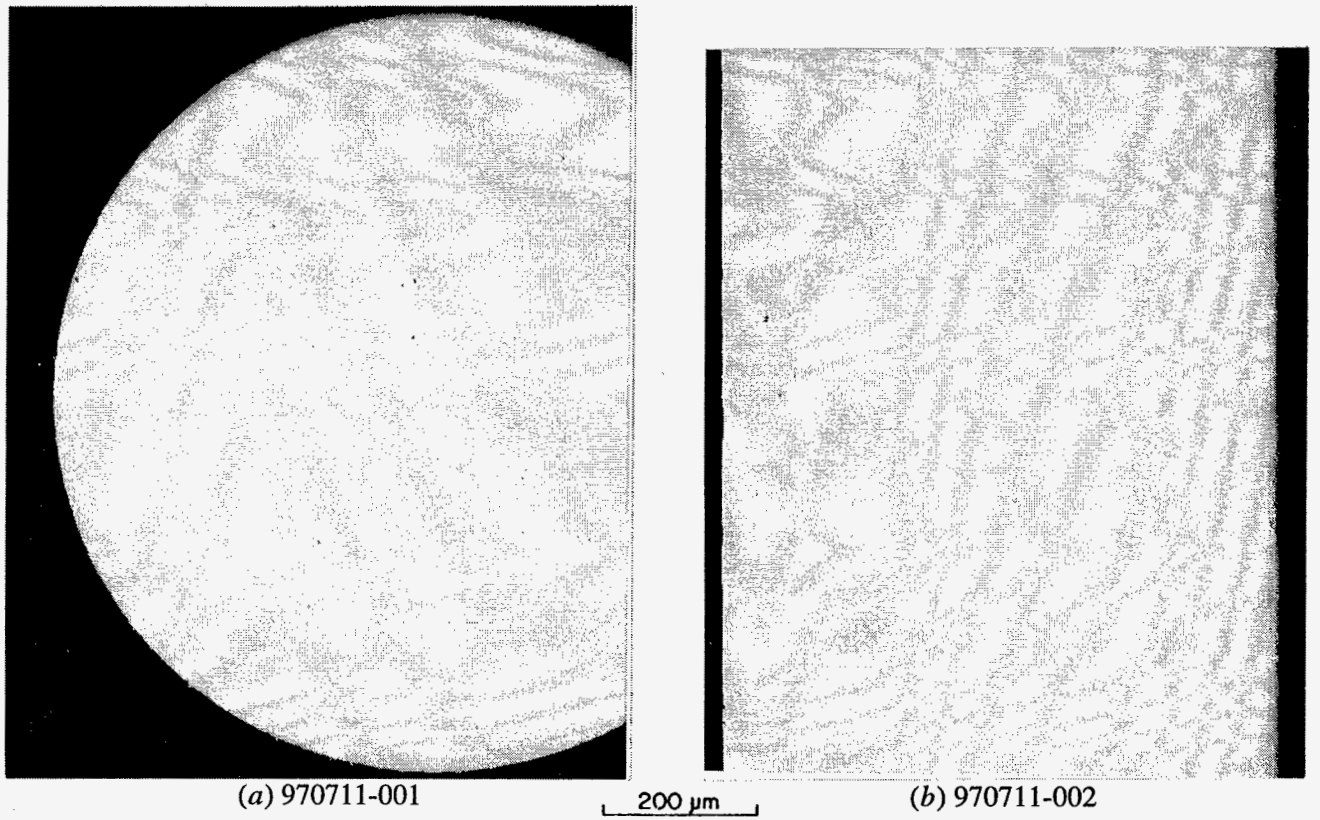

Figure 1. Optical micrographs in unetched condition of: (*a*) transverse and (*b*) longitudinal cross sections of 40-mil-diam wire of FAPY alloy fabricated at Hoskins Manufacturing Company (Hamburg, Michigan).

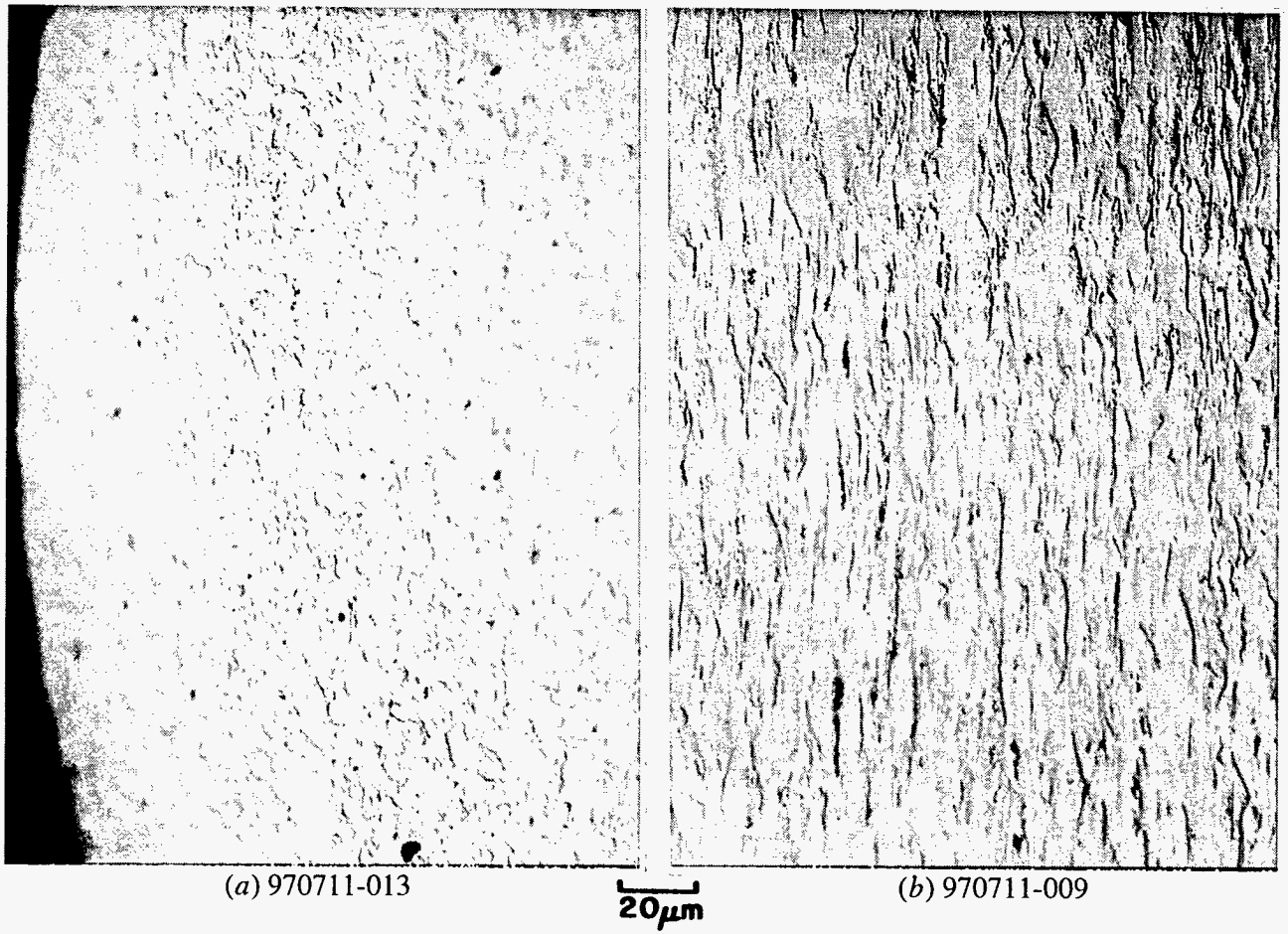

Figure 2. Optical micrographs in etched condition of: (*a*) transverse and (*b*) longitudinal cross sections of 40-mil-diam wire of FAPY alloy fabricated at Hoskins Manufacturing Company (Hamburg, Michigan).

IRON-ALUMINIDE CLADDING OF BOILER TUBES

V. K. Sikka and M. L. Santella

INTRODUCTION

This task is a Cooperative Research and Development Agreement between the Oak Ridge National Laboratory and ABB Combustion Engineering (ABB CE) [Chattanooga, Tennessee]. The purpose of this task is to identify the compositions of iron-aluminide alloys as corrosion protection coatings on boiler tubes. A further objective of this task is to develop a cost effective method of applying the coatings on a commercial basis. Significant progress was made towards accomplishing this task during this fiscal year.

Results and Discussion

The Fe-Al composition containing an aluminum content of ≥ 8 wt % were considered acceptable for most corrosion conditions expected under boiler operating conditions. A very simple and highly economical method for weld overlaying the Fe-Al compositions was identified. The details of the process have been filed in a patent disclosure. The boiler tubes of T22, 2-1/4 Cr-Mo, and Grade T91 were weld-overlaid using the newly developed process. The weld-overlaid coatings were of excellent quality and showed no weld defects. Samples from the weld-overlaid tubes have been supplied to ABB CE for testing and evaluation.

Nondisclosure agreements are being signed with commercial vendors in an effort to license the newly developed weld-overlay technology for Fe-Al alloy coatings.

HIGH-TEMPERATURE CORROSION BEHAVIOR OF IRON-ALUMINIDE ALLOYS AND COATINGS

P. F. Tortorelli, B. A. Pint, and I. G. Wright

INTRODUCTION

Iron aluminides containing greater than about 20-25 at.% Al have oxidation/sulfidation resistance at temperatures well above those at which these alloys have adequate mechanical strength.[1,2] In addition to alloying and processing modifications for improved creep resistance of wrought material, this strength limitation is being addressed by development of oxide-dispersion-strengthened (ODS) iron aluminides[3,4] and by evaluation of Fe_3Al alloy compositions as coatings or claddings on higher-strength, less corrosion-resistant materials.[5-9] As part of these efforts, the high-temperature oxidation and oxidation-sulfidation behaviors of iron-aluminide weld overlays and ODS alloys are being characterized and compared to results for ingot-processed material. Other recent oxidation results for ODS Fe_3Al, as related to lifetime prediction, can be found elsewhere.[4]

OXIDATION OF Fe_3Al ALLOYS

The long-term oxidation performance of ingot- (I/M) and powder-processed (P/M) Fe-28% Al-(2-5)% Cr alloys was characterized for exposures in air at 1000-1300°C. (All compositions are in at.%.) The P/M alloys were prepared by mechanically blending powders of gas-atomized Fe-28% Al-2% Cr (FAS) and submicron oxides in a flowing Ar atmosphere using a high-speed attritor and stainless steel balls.[3,10] The blended powder was canned, degassed, and extruded at 1100°C. For comparison, ingot-processed Fe-28% Al-2 or 5% Cr alloys and a commercial ZrO_2-dispersed (0.06% Zr) Fe-20% Cr-10% Al composition (Kanthal alloy APM) were also tested. The APM alloy is used as the benchmark for oxidation resistance as it typically displays low scale-growth and spallation rates at high temperatures under both isothermal and thermally cycled conditions.[11] Cyclic oxidation experiments were conducted at 1200°C in air.

As illustrated in Figs. 1-4, the I/M Fe-28% Al-2% Cr (denoted FASN in this paper) consistently showed rapid weight gain kinetics under cyclic oxidation conditions at 1000-1300°C. At 1000°C (Fig. 1) and 1100°C (Fig. 2), Fe-28% Al-5% Cr-0.1% Zr (FAL) and P/M FAS-Y_2O_3 displayed similar oxidation resistance. However, while not apparent from the gravimetric data in Fig. 2, the alumina scales that developed at 1100°C showed different

characteristics: after about 500 h, the product on FAL was thicker and more convoluted and cracked on cooling, while the oxide on FAS-Y_2O_3 showed a greater spallation tendency. Nevertheless, comparison of the data for these alloys to those for FASN clearly indicates that additions of Zr or yttria substantially improved the adhesion of alumina scales grown on iron aluminides. These results are not unexpected;[2,9,12] the present observations simply reinforce the importance of small amounts of oxygen-active elements, and oxides based on the same, in improving oxidation resistance.[13] The two iron aluminides with such dopants had oxidation rates comparable to that of ZrO_2-dispersed FeCrAl (APM) at 1000°C (Fig. 1). At 1100°C (Fig. 2), APM showed superior oxidation resistance.

While the oxidation resistance of FAL was about the same as that of the FAS-Y_2O_3 at 1000 and 1100°C, significant differences between these two alloys were noted from experiments at 1200 and 1300°C (see Figs. 3 and 4). At these temperatures, the aluminum consumption rate, as measured by the total weight gain (that of the specimen as well as any oxide that has spalled) was higher for the FAL alloy. (With respect to the data shown in Fig. 4, the FAS-Y_2O_3 specimen went into breakaway oxidation[14] before the FAL simply because it was about half the thickness of the latter and thus had a substantially smaller aluminum reservoir to continually form protective Al_2O_3.[15-17]) This difference in oxidation behavior between the FAL and FAS-Y_2O_3 alloys may be at least partially explained by some localized inward growth of alumina observed for the former specimens (see Fig. 5). These areas of accelerated reaction could possibly be related to sites of casting/forming defects.

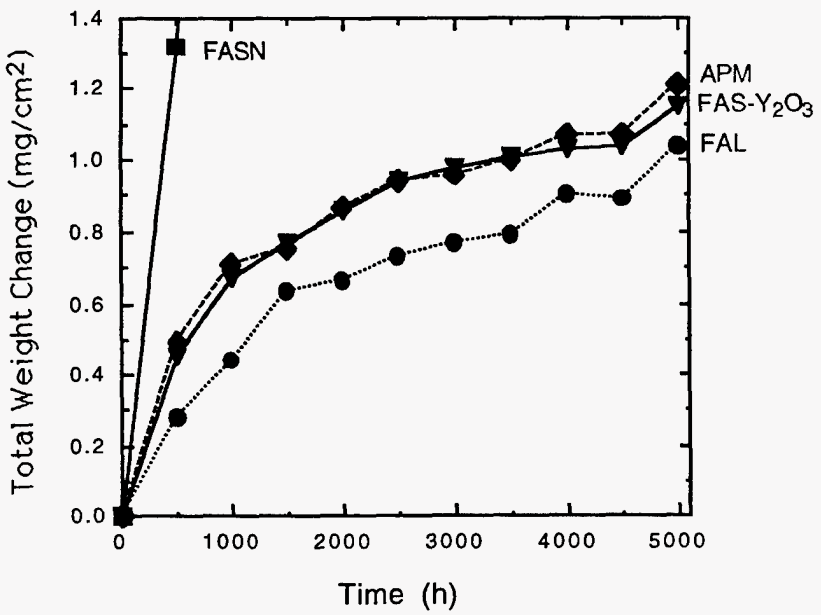

Fig 1. Total weight gain (specimen + spall) for 500-h cycles at 1000°C in laboratory air.

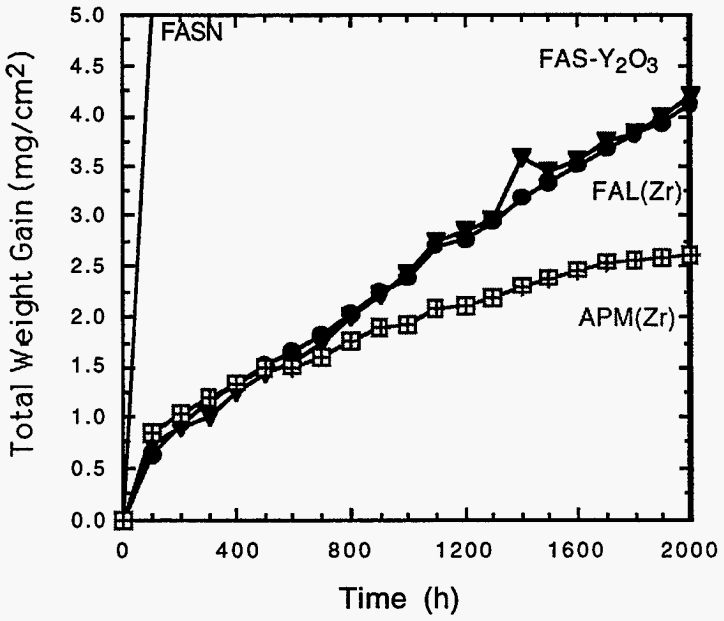

Fig. 2. Total weight gain (specimen + spall) for 100-h cycles at 1100°C in laboratory air.

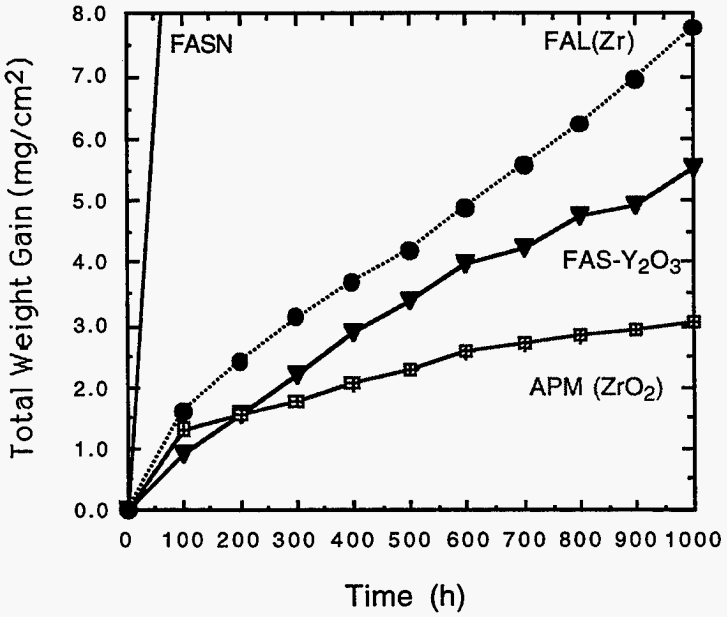

Fig. 3. Total weight gain (specimen + spall) for 100-h cycles at 1200°C in laboratory air.

A second contributing factor for the higher oxidation rate of FAL very well may be the respective substrate strengths. While the creep strengths of these alloys have not been determined, it appeared from evaluation of the as-oxidized specimens that the I/M FAL was weaker than the P/M Y_2O_3-containing FAS in that it was more easily deformed during high-temperature oxidation. Evidence for such has been shown previously for 1300°C oxidation[15,18] and from the present experiments at this temperature. For example, Fig. 5 shows

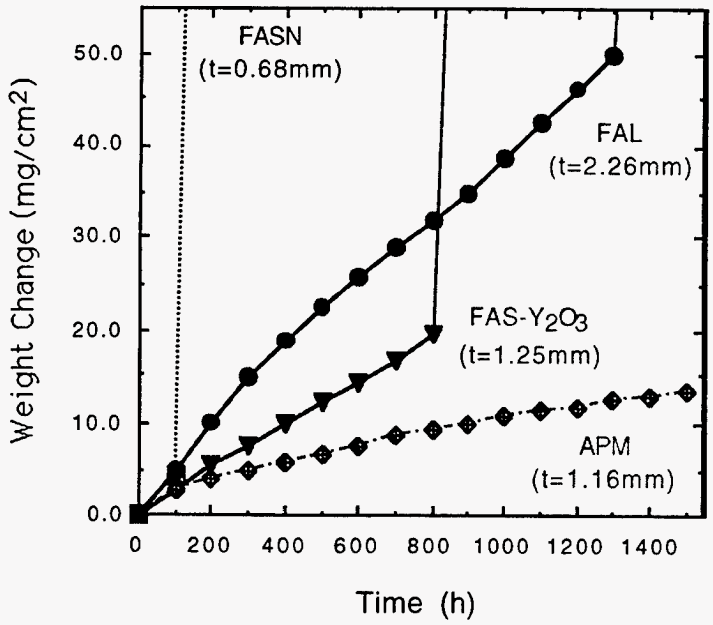

Fig. 4. Total weight gain (specimen + spall) for 100-h cycles at 1300°C in laboratory air. Starting specimen thicknesses (t) are noted.

that the growth of alumina on FAL apparently significantly deformed the substrate. This ultimately results in a highly cracked and convoluted alumina scale. This deformation compromises the ability of the alumina scale formed on FAL to fully protect the substrate from reaction with the oxidizing species. Observations of an FAL specimen oxidized at 1200°C using 1-h cycles revealed similar scale cracking and convolutions. In contrast, the ODS iron aluminides exposed under the same conditions tended to show scale spallation due to interfacial void formation.

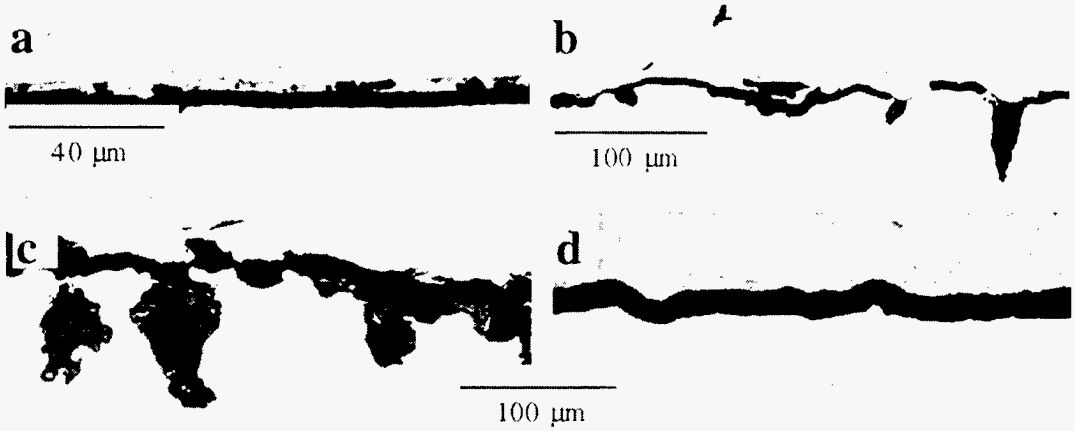

Fig. 5. Optical micrographs of cross sections of alumina-forming alloys exposed isothermally for 100 h in laboratory air (a) - (c) FAL, 1300°C; (d) APM, 1200°C. Specimens were coated with copper (upper light area) before sectioning. Comparison of (b) and (d) shows the scale grown on FAL is convoluted while the oxide on APM is relatively flat. Intermittent inward growth of alumina can be seen in (b) and (c).

Although Y_2O_3 in FAS and Zr in FAL have beneficial effects on oxidation resistance, previous and present results indicate that these dopants are not as effective in iron aluminides as when they are added to FeCrAl and β-NiAl.[18] As shown in Figs. 1-5, neither of these additions resulted in oxidation behavior as good as that of APM at 1100°C and above. The APM alloy remained relatively flat and the substrate-oxide interface was void-free (Fig. 5d). The reasons for the variations in oxidation performance between these different alumina-forming alloy systems are not known, but substrate strength, and associated effects on scale buckling and void formation,[18] are probably contributing factors.

As the high-temperature corrosion resistance of iron aluminides critically depends on the ability to grow and maintain a protective alumina layer, the minimum aluminum concentration necessary for formation of a continuous Al_2O_3 scale in air (c_{Al}) has been determined to be approximately 19% for I/M Fe-Al(-Cr) alloys.[19] As shown by the solid circles in Fig. 6, aluminum concentrations lower than this value lead to substantially greater weight gains for similar oxidation conditions. For 100-h exposures at 900°C, weight gains in excess of about 1 mg/cm^2 indicate that the oxidation product contains significant amounts of iron oxide and thus is not protective. Using such as an indicator of alumina formation, recent measurements have shown that c_{Al} for some ODS (P/M) Fe_3Al alloys was lower than the value determined for I/M Fe-Al(-Cr) alloys . This shift in c_{Al} is illustrated in Fig. 6, which shows that the critical aluminum concentration for the P/M alloys was ~13%. The addition of Y_2O_3 to the P/M alloy (which always contains a dispersion of Al_2O_3) did not significantly change this value. The similarities between Al_2O_3- and Y_2O_3-dispersed Fe-Al and c_{Al} values were observed from 600-1300°C.[20]

In attempting to explain the difference in c_{Al} between I/M and P/M version of Fe_3Al alloys, the respective starting grain sizes of these materials must be considered. For the I/M alloys, the average grain size is approximately 40 μm (or even larger) versus ~1 μm for the as-extruded P/M products. In addition, the oxide dispersions in the P/M alloys help to maintain the small grain size during elevated temperature exposures. Because of this, the finer alloy grain size of the P/M iron aluminides can promote more rapid transport of aluminum to the oxidizing surfaces and therefore lower the apparent c_{Al} as the time to the onset of nonprotective oxide formation (breakaway) is also dependent on (proportional to) the diffusion coefficient of aluminum in the alloy.[14,16,17]

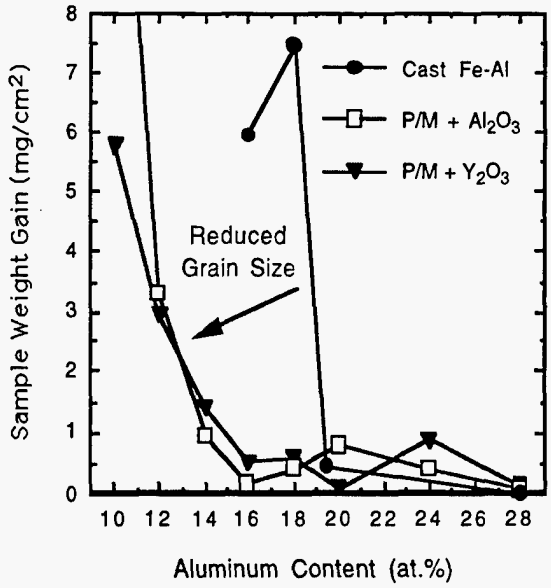

Fig. 6. Specimen weight change versus aluminum content after 100 h in air at 900°C for P/M and I/M Fe-Al alloys.

OXIDATION-SULFIDATION OF ODS Fe_3Al ALLOYS

Iron aluminides produced by conventional I/M procedures, have been shown to have excellent sulfidation resistance in H_2S-containing environments.[2,19,21,22] Therefore, it has been of continuing interest to learn whether ODS iron aluminides show similar corrosion behavior. Preliminary data, obtained by exposing as-extruded P/M FAS and FAS-Y_2O_3 to 5.4% H_2S-79.4% H_2-1.6% H_2O-13.6% Ar (by volume) showed that the oxidation/sulfidation rates of these iron aluminides were similar to that of many I/M Fe_3Al alloys.[9] Specifically, the isothermal weight gains of these P/M FAS alloys were somewhat greater than I/M FAS, but less than a Fe_3Al-5% Cr alloy produced by I/M processing. Subsequently, alloys of FAS-Y_2O_3 were produced from commercially-prepared powders.[4] These products were designated PMWY to distinguish them from the earlier ODS FAS-Y_2O_3 alloys; their detailed compositions and metallurgical characteristics are described elsewhere.[4] Specimen coupons were cut from recrystallized PMWY1 and PMWY2 (see ref. 4) and exposed to the same aggressive oxidizing/sulfidizing (H_2S-H_2-H_2O-Ar) environment at 800°C under both isothermal and thermal cycling conditions. The oxygen partial pressure, as determined by a solid-state oxygen cell, was 10^{-22} atm, and the sulfur pressure was calculated to be 10^{-6} atm. The isothermal results are shown in Fig. 7, which compares the thermogravimetric results for the PMWY alloys with similarly produced data for I/M Fe_3Al alloys with 2 and 5% Cr and the previous as-

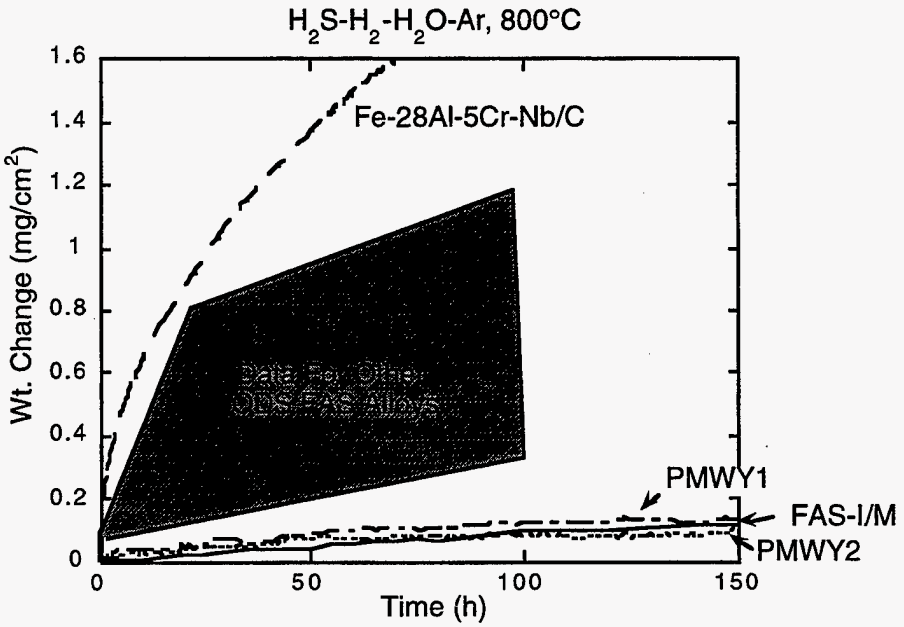

Fig. 7. Weight change versus time for specimens isothermally exposed to H_2S-H_2-H_2O-Ar at 800°C. The PMWY alloys are FAS-Y_2O_3 produced from commercially prepared powders and were exposed in the as-recrystallized condition. The specimen designated FAS-I/M was produced by ingot metallurgy processing and represents the benchmark behavior in this environment. The Fe_3Al - 5% Cr alloy was also produced by ingot metallurgy and contains 1% Nb and 0.2% C. The shaded area represents the range of data reported previously (see ref. 9) for as-extruded FAS and FAS-Y_2O_3 prepared from laboratory-produced powder mixtures.

extruded P/M FAS and FAS-Y_2O_3.[9] Note that the gravimetric curves for the PMWY alloys essentially mimic that for the benchmark I/M FAS composition. These weight gains are extremely low given the aggressiveness of the H_2S-H_2-H_2O-Ar gas. Indeed, under similar conditions, weight gains for Fe-20% Cr-10% Al alloys (such as APM) and stainless steels would be 1-3 orders of magnitude higher.[21,22] Furthermore, sulfidation resistance was maintained after a few thermal cycles; there was essentially no change in the rate of weight gain when a thermogravimetric experiment was periodically interrupted by cooling to room temperature and reheating to the exposure temperature.

The more rapid initial weight gains of the P/M FAS and FAS-Y_2O_3 specimens relative to those of the PMWY-1 and PMWY-2 may be related to grain size. It was previously hypothesized that the former alloys showed greater weight gains than the I/M FAS because their fine grain size allowed a more rapid diffusion of chromium to the reaction front and resulted in higher initial weight gains due to formation of chromium sulfides.[9] This argument may also explain the lower weight gains of the PMWY alloys shown in Fig. 7; the average grain size of

the PMWY coupons was significantly larger than that of the as-extruded P/M FAS and FAS-Y_2O_3 specimens due to the recrystallization heat treatment.[4]

OXIDATION-SULFIDATION OF IRON-ALUMINIDE WELD OVERLAYS AT 800°C

This section contains corrosion data on weld deposits produced by gas metal arc (GMA) welding. Results for coatings produced by the gas tungsten arc (GTA) process as well as initial data for GMA overlays have been reported previously.[7,9] The development efforts associated with the GTA and GMA processes used to produce the weld overlays are described elsewhere.[5,6]

Weld overlays were deposited on Fe-2.25 Cr-1 Mo (wt%) steel substrates by GMA. As in previous oxidation-sulfidation studies,[7,9] coupons were prepared by cutting rectangular specimens from the overlay pad and then grinding away all the substrate material so that only weld metal (approximately 1-2 mm thick) remained. In this way, only the corrosion behavior of the weld deposit, rather than the coating/substrate system, is evaluated.[7,9] Oxidation-sulfidation behavior was characterized by use of a continuous-recording microbalance to measure the weight of these specimens during exposure at 800°C to the H_2S-H_2-H_2O-Ar mixed gas already described above.

The use of welding to produce iron-aluminide coatings results in a loss of selected elements by vaporization and significant mixing of the filler metal and substrate alloys (dilution) during deposition.[5,6] Because there is essentially no aluminum in the Fe-Cr substrates, the concentration of this element in the overlay will be significantly less than that of the weld rod/wire used to produce it. The extent of this dilution in aluminum depends on vaporization losses during welding and the relative amount of substrate material melted and thus is affected by parameters such as current, voltage, polarity, travel speed, etc. When dilution is controlled such that the aluminum content of the weld deposit exceeds about 20%, good oxidation-sulfidation results.[7,9] Recent results for a GMA weld overlay with 21% Al and 1% Cr (denoted, for the purposes of this paper, as S2) consistently showed gravimetric behavior equivalent to the baseline FAS composition, which serves as the benchmark by which all other alloys are judged with respect to this mixed gas environment[21] (see Fig. 8). As shown in Fig. 9, S2 specimens showed better oxidation-sulfidation resistance than a previously examined GMA weld overlay[9] with the same Al level, but a significantly higher Cr concentration (because it was produced with a different weld wire). The deleterious effect of chromium on corrosion resistance in this environment is well documented,[2,21,22] and can explain the differences between the present and prior GMA results. Interestingly, as also shown in Fig. 9, the GMA S2 weld overlay had

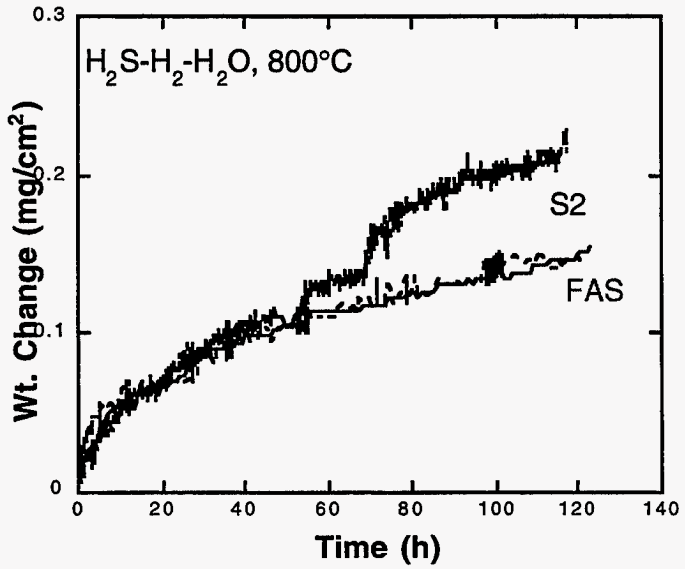

Fig. 8. Weight change versus time for I/M FAS and two specimens from a GMA weld overlay with a composition of Fe - 21% Al - 1% Cr (S2). Differences in behavior are negligible on this scale.

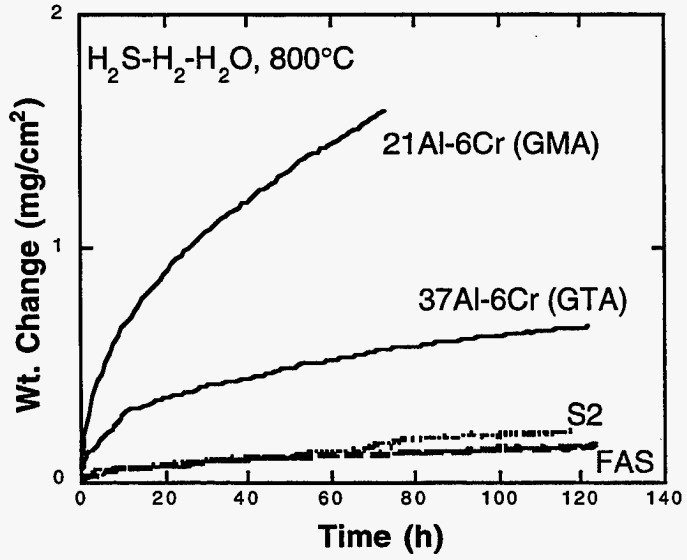

Fig. 9. Weight change versus time for I/M FAS and specimens from GMA and GTA weld overlays with compositions as shown. The curves designated S2 are the same as shown in Fig. 8 and are for a GMA weld overlay with a composition of Fe - 21% Al - 1% Cr. The FAS (I/M) curve is also the same as shown in Fig. 8.

better oxidation-sulfidation resistance than a GTA one with 31% Al. As discussed previously,[9] the GMA process, which involves a substantially higher energy input into the weld, may promote more complete mixing of the deposit and therefore result in more reproducible and better corrosion resistance in this environment than those overlays produced by GTA.

The present results indicate that, in combination with a low chromium concentration, the aluminum level of the S2 weld overlay appears to be sufficient to show excellent corrosion resistance in an aggressive oxidizing/sulfidizing environment under isothermal conditions. However, aluminum concentrations of 20 - 21% are marginal with respect to maintaining low corrosion rates over extended periods of time, particularly if thermal cycling exacerbates the aluminum depletion process.[9] Weldability problems notwithstanding,[5,6] higher aluminum concentrations in the overlays would delay any onset of accelerated reaction caused by depletion of this element and improve the corrosion behavior of iron-aluminide coatings containing substrate elements, such as chromium and nickel, that are deleterious to sulfidation resistance (compare the 21Al-6Cr and 37Al-6Cr gravimetric curves in Fig. 9).[21,22]

SUMMARY AND CONCLUSIONS

The long-term oxidation performance of ingot- and powder-processed Fe-28 at.% Al-(2-5)% Cr alloys with minor oxygen-active additions was characterized for exposures in air at 1000-1300°C. The oxidation-sulfidation behaviors of oxide-dispersion-strengthened Fe_3Al alloys and iron-aluminide weld overlays were also investigated.

Additions of Zr or yttria substantially improved the adhesion of alumina scales grown on iron aluminides. At lower temperatures, the ingot-processed alloys performed similarly to ODS Fe_3Al alloys and other alumina-formers. However, at 1200 and 1300°C, the oxidation resistance of the ingot-processed Fe_3Al was degraded due to deformation of the substrate and some localized reaction product growth. Other oxidation experiments showed that the addition of an oxide dispersion to iron aluminides reduced the critical aluminum concentration for protective alumina scale formation.

Alloys of Fe-28 at.% Al-2% Cr-Y_2O_3 were produced from commercially-prepared powders and exposed to an highly aggressive oxidizing/sulfidizing (H_2S-H_2-H_2O-Ar) environment at 800°C under isothermal and thermal cycling conditions. The results from these experiments showed that these alloys had excellent oxidation/sulfidation resistance that was comparable to that of the ingot-processed version of the base alloy.

Iron-aluminide coatings were prepared by a gas metal arc weld-overlay technique. Specimens cut from the weld deposits were isothermally exposed to the H_2S-H_2-H_2O-Ar environment at 800°C. Excellent corrosion resistance was observed for a weld overlay with 21% Al and 1% Cr, but higher aluminum concentrations will be necessary to assure long-term performance in this environment, particularly under thermal cycling conditions.

ACKNOWLEDGMENTS

The authors thank M. Howell for experimental support and J. R. DiStefano, G. M. Goodwin, and M. P. Brady for their reviews of the manuscript. This research was sponsored by the Fossil Energy Advanced Research and Technology Development (AR&TD) Materials Program, U S. Department of Energy, under contract DE-AC05-96OR22464 with Lockheed Martin Energy Research Corporation. B. A. Pint is supported by the U. S. Department of Energy Distinguished Postdoctoral Research Program administered by the Oak Ridge Institute for Science and Education.

REFERENCES

1. C. G. McKamey, J. H. DeVan, P. F. Tortorelli, and V. K. Sikka, "A Review of Recent Developments on Fe_3Al-Based Alloys," *J. Mater. Res.* 6 (1991) 1779-1805.

2. P. F. Tortorelli and J. H. DeVan, "Compositional Influences on the High-Temperature Corrosion Resistance of Iron Aluminides," pp. 257-70 in Processing, Properties, and Applications of Iron Aluminides, J. H. Schneibel and M. A. Crimp (eds.), The Minerals, Metals, and Materials Society, Warrendale, PA, 1994.

3. I. G. Wright, B. A. Pint, E. K. Ohriner, and P. F. Tortorelli, "ODS Iron Aluminides," pp. 359-71 in *Proc. Tenth Annual Conf. Fossil Energy Materials*, N. C. Cole and R. R. Judkins (comp.), U. S. Department of Energy, August 1996.

4. I. G. Wright, B. A. Pint, P. F. Tortorelli, and C. G. McKamey, "Development of ODS Fe_3Al Alloys," these proceedings.

5. G. M. Goodwin, P. J. Maziasz, C. G. McKamey, J. H. DeVan, and V. K. Sikka, "Weldability of Iron Aluminides," pp. 205-10 in *Proc. Eighth Annual Conf. Fossil Energy Materials*, N. C. Cole and R. R. Judkins (comp.), CONF-9405143, U. S. Department of Energy, August 1994.

6. G. M. Goodwin, "Weld Overlay Cladding with Iron Aluminides," pp. 381-92 in *Proc. Tenth Annual Conf. Fossil Energy Materials*, N. C. Cole and R. R. Judkins (comp.), U. S. Department of Energy, August 1996.

7. P. F. Tortorelli, J. H. DeVan, G. M. Goodwin, and M. Howell, "High-Temperature Corrosion Resistance of Weld Overlay Coatings of Iron Aluminide," pp. 203-12 in Elevated Temperature Coatings: Science and Technology I, N. B. Dahotre, J. M. Hampikian, and J. J. Stiglich (eds.), The Minerals, Metals, and Materials Society, Warrendale, PA, 1995.

8. K. Natesan and R. N. Johnson, "Corrosion Performance of Fe-Cr-Al and Fe Aluminide Alloys in Complex Gas Environments," pp. 591-99 in Heat-Resistant Materials II, K. Natesan, P. Ganesan, and G. Lai (eds.), ASM International, August 1995.

9. P. F. Tortorelli, B. A. Pint, and I. G. Wright, "High-Temperature Corrosion Behavior of Coatings and ODS Alloys Based on Fe_3Al," pp. 393-403 in *Proc. Tenth Annual Conf. Fossil Energy Materials*, N. C. Cole and R. R. Judkins (comp.), U. S. Department of Energy, August 1996

10. B. A. Pint, K. B. Alexander, and P. F. Tortorelli, "The Effect of Various Oxide Dispersions on the Oxidation Resistance of Fe_3Al," pp. 1315-20 in High-Temperature Ordered Intermetallic Alloys VI, J. A. Horton, I. Baker, S. Hanada, R. D. Noebe, and D. S. Schwartz (eds.), The Materials Research Society, Pittsburgh, PA, 1995.

11. B. A. Pint, A. J. Garratt-Reed, and L. W. Hobbs, "The Reactive Element Effect in Commercial ODS FeCrAl Alloys ," *Mater. High Temp.* 13 (1995) 3-16.

12. B. A. Pint, "Study of the Reactive Element Effect in ODS Iron-Base Alumina-Formers," submitted for publication in *Mater. Sci. Forum,* 1996.

13. B. A. Pint, "Experimental Observations in Support of the Dynamic Segregation Theory to Explain the Reactive Element Effect," *Oxid. Met.* 45 (1996) 1-37.

14. P. Kofstad, High Temperature Oxidation, 1988.

15. J. H. DeVan, P. F. Tortorelli, and M. J. Bennett, "Environmental Effects on Iron Aluminides," pp. 309 - 20 in *Proc. Eighth Annual Conf. Fossil Energy Materials*, N. C. Cole and R. R. Judkins (comp.), CONF-9405143, U. S. Department of Energy, August 1994.

16. W. J. Quaddakers and M. J. Bennett, "Oxidation Induced Lifetime Limits of Thin Walled Iron Based Alumina Forming Oxide Dispersion Strengthened Alloy Components," *Mater. Sci. Technol.*, 10 (1994) 126-31.

17. M. J. Bennett, J. H. DeVan, and P. F. Tortorelli, "The Oxidation Behavior of Iron Aluminides in Air at 1300°C," accepted for publication in *Proc. Third Int'l. Conf. on Microscopy of Oxidation*, S. B. Newcomb and J. A. Little (eds.), The Institute of Materials, London, September 1996.

18. B. A. Pint, P. F. Tortorelli, and I. G. Wright, "The Oxidation Behavior of ODS Iron Aluminides," *Werkst. Korros.* 47 (1996) 663-74.

19. J. H. DeVan and P. F. Tortorelli, "Oxidation-Sulfidation Behavior of Iron Alloys Containing 16 to 40 Atomic Percent Aluminum," *Corros. Sci.* 35 (1993) 1065-71.

20. B. A. Pint and J. Leibowitz, Oak Ridge National Laboratory, unpublished results, 1996.

21. J. H. DeVan, "Oxidation Behavior of Fe_3Al and Derivative Alloys," pp. 107-115 in Oxidation of High-Temperature Intermetallics, T. Grobstein and J. Doychak (eds.), The Minerals, Metals, and Materials Society, 1989.

22. J. H. DeVan and P. F. Tortorelli, "Oxidation/Sulfidation of Iron-Aluminum Alloys," *Mater. at High Temp.* 11 (1993) 30-35.

THE MICROSTRUCTURE AND MECHANICAL RELIABILITY OF ALUMINA SCALES AND COATINGS

K. B. Alexander, K. Prüßner, and P. F. Tortorelli

INTRODUCTION

In many high-temperature fossil energy systems, corrosion and deleterious reactions with gases and condensable products in the operating environment often compromise materials performance. The presence of a stable surface oxide (either as thermally-grown scale or deposited coating) can effectively protect the materials from these reactions if the oxides are slow-growing, dense and adherent to the substrate. However, the various factors which control the scale/coating integrity and adherence are not fully understood. Of fundamental interest is the microstructure and microchemistry of the metal/oxide interface as well as the oxide/oxide grain boundaries in the scale itself. Segregation of sulfur to the scale/metal interface was found to be detrimental for the oxidation performance, however the presence of reactive elements (RE) such as Y or Zr in the alloy can mitigate the effects of sulfur and thus improve the scale adherence.[1-5] Reactive elements segregate to the oxide/metal interface and scale grain boundaries and modify the growth mechanisms and the microstructure.[6,7]

The Oak Ridge National Laboratory (ORNL) research described in this paper is being conducted in collaboration with work sponsored by the Department of Energy's Office of Fossil Energy at Argonne National Laboratory (ANL) and Lawrence Berkeley National Laboratory (LBNL) as well as in concert with on-going interactions that are part of the Office of Basic Energy Sciences' Center of Excellence for the Synthesis and Processing of Advanced Materials. The Center of Excellence on Mechanically Reliable Surface Oxides and Coatings includes participants from ORNL, ANL, LBNL, Idaho National Engineering Laboratory (INEL) and Lawrence Livermore National Laboratory (LLNL).

This report will discuss work on the oxidation of iron aluminides, with and without alumina coatings, as well as recent work on the oxidation and segregation behavior of NiCrAl-based alloys. Iron-aluminides (Fe_3Al-type) are known to have good oxidation resistance, if the protective alumina scale can be maintained. It has been shown that small amounts of zirconium significantly reduce the oxidation rate and improve scale adherence. Zirconium-containing alloys form unconvoluted, uniform oxide scales with no evidence of spallation during thermal cycling, whereas a significant amount of spallation is observed after thermal cycling of a Zr-free alloy.[8,9]

The influence of an applied coating on the oxidation behavior of the alloy should allow the operative transport mechanisms during oxidation to be better examined. The deposition of a plasma-synthesized alumina coating prior to oxidation promoted the growth of metastable aluminas and thus increased the oxidation rate.[10] Both coated and uncoated specimens have needle-like surface morphologies.[10]

Unlike iron-aluminides, NiCrAl-based alloys form complex oxide scales with mixed oxides formed in the initial oxidation stages and an alumina layer underneath.[12,13] NiCrAl-based alloys of different compositions, involving a commercial superalloy as well as two model alloys were part of the study. Such alloys allow extension of the present work on alumina scales and coatings to a class of compositions that are of direct relevance to advanced turbine systems.

DISCUSSION OF CURRENT ACTIVITIES

The alloys used for the iron aluminide studies were FAL (Fe-28 at. % Al-5 at. % Cr-0.1 at. % Zr + 0.05 at. B) and FA186 (Fe-28 at. % Al-5 at. % Cr), prepared by arc melting and casting. The sulfur content was about 40 ppm. These alloys were rolled to a final thickness of between 0.8 and 1.3 mm and rectangular specimens (typically 12 x 10 mm) were prepared from these sheets for oxidation and crystallization studies.

Oxidation experiments of coated or uncoated iron-aluminides were performed under isothermal and cyclic conditions for 96 h at 1000°C in static air. Gravimetric data were recorded during the cyclic oxidation by exposing coupons in individual pre-annealed alumina crucibles to a series of 24-h exposures. Heat treatments of deposited alumina coatings were performed for 0.5 and 2 h in He at 1000°C.

Alumina coatings on iron aluminides were deposited using a magnetically-filtered cathodic-arc plasma-synthesis process.[13] During the deposition process, the substrate was pulse-biased to a high ion energy (2 kV) in the initial phase of the deposition process to provide atomic mixing of the substrate and film at the interface. A substantially lower energy (0.2 kV) was used to deposit the remaining thickness of the coating.

Three NiCrAl-based alloys of different composition (commercial superalloy René N5, NCASY and NCA3Y - Table 1), which form complex oxide scales, were examined after isothermal oxidation in air at 1200°C for 100 h.

Table 1: Composition of NiCrAl-alloys (at %; except S in ppm)

at %	Ni	Cr	Al	Fe	Ta	Hf	W	Re	Si	Co	Mo	Y	Zr	S*	C
N5	64.9	7.8	13.9	0.1	2.1	0.05	1.6	1.0	0.15	7.3	0.9	0.003	0.003	4	0.25
NCASY	80.1	7.2	12.5	0.01					0.14			0.012		18	0.05
NCA3Y	71.2	9.9	18.8	0.01					0.02			0.041		16	0.04

* sulfur contents in ppm

For all experiments, scanning electron microscopy (SEM) was performed on oxidized or heat treated coupons as well as on polished cross-sections through the scale and/or coatings. Field emission gun transmission electron microscopy/scanning transmission electron microscopy (FEG-TEM/STEM) of cross-sectional and plan-view specimens were used for the microstructural characterization of the scales. Energy dispersive x-ray spectroscopy (EDS) with high spatial resolution (1-2 nm probe) was used for the studies of interfacial segregation.

I. Oxidation Studies on Iron-Aluminides

1. Microstructure of Plasma-Deposited Alumina Coatings, As-Deposited

Plasma-deposited alumina coatings which were subsequently used for oxidation and segregation studies of iron-aluminides were amorphous in the as-deposited state (as determined by x-ray diffraction). Auger Electron Spectroscopy (AES) and Rutherford Backscattering (RBS) analyses showed that the films are slightly cation-deficient Al_2O_3.[14] Cross-sectional TEM showed that most coatings had two distinctly different layers: an inner layer which exhibits contrast features perpendicular to the interface and an outer layer, which is featureless (Fig. 1).

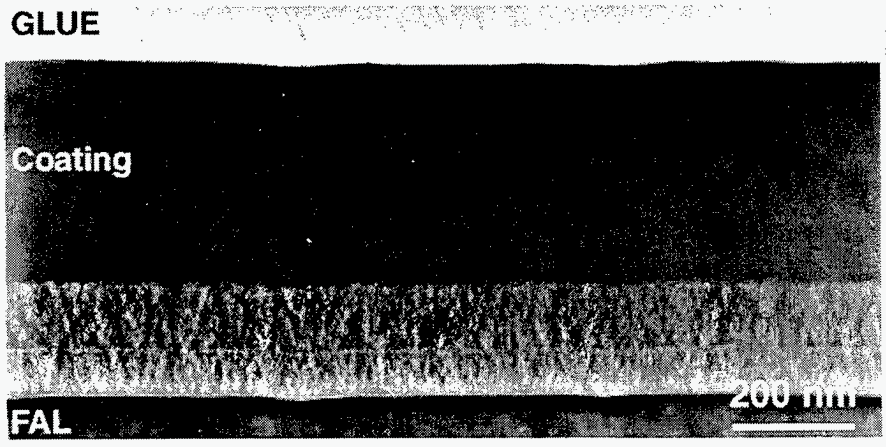

Fig. 1 TEM image of the structure of an as-deposited alumina coating (~ 0.7 μm thick).

The featureless portion was found by selected area diffraction (SAD) to be fully amorphous, whereas some fine-grained γ-Al_2O_3 was found in the inner part of the scale. The difference between the two regions was assumed to correlate with the change in pulse-biasing of the substrate from 2 kV to 0.2 kV during deposition. However, not all the coatings had these two layers. Further investigation of deposition parameter/structure correlations are underway.

2. Microstructural Development and Segregation During Heat Treatment of Alumina Coatings

Previous experiments concerning the segregation of sulfur to the scale/metal interface have only addressed segregation to interfaces between thermally-grown α-Al_2O_3 and an alloy.[3,4,15,16] Since α-Al_2O_3 grows by inward diffusion, the interface is not static but moving into the metal during oxidation. Therefore diffusion of sulfur to the interface and migration of the interface in the opposite direction are counter-processes. In this study, alumina coatings (0.2 and 0.8 μm thick), plasma-deposited on FA 186, were used to study the segregation of sulfur to a static scale/alloy interface (in the absence of thermal oxidation) and thereby isolate the effect.[16] As-deposited alumina coatings were heat treated in a He-atmosphere at 1000°C (for 0.5 or 2 h) in order to crystallize the initially amorphous coating, while preventing the growth of a thermal oxide scale (if thermal oxidation occurs, oxide needles can clearly be seen on the coating surface by SEM, and this was not observed).

SEM imaging revealed that although the scale/gas interface remained smooth during crystallization, the scale/metal interface showed imprints of distinct oxide grains with associated cracks and cavities as shown in Fig. 2a. The 0.8 μm coating developed a network of cracks and spalled in several areas. The 0.2 μm coating didn't develop these large through-coating cracks. It can be concluded that for the 0.8 μm coating the critical scale thickness for accomodation of thermal and growth/transformation stresses was exceeded.

TEM investigations showed that the heat treatment resulted in the transformation of the coating to metastable alumina (γ-Al_2O_3 and θ-Al_2O_3) and eventually to the nucleation of α-Al_2O_3 at the scale/metal interface (Fig. 3). During the transformation to the metastable aluminas, both interfaces remained fairly flat. The formation of α-Al_2O_3 on the other hand, resulted in roughening of the scale/metal interface. The grains visible as imprints in the top-down SEM images (Fig. 2) could be correlated to faceted grains of α-Al_2O_3 which grew into the alloy. Cavities were formed next to the α-Al_2O_3. Therefore considerable material transport seems to be associated with the phase transformation to α-Al_2O_3 although no thermal oxide growth occurs.

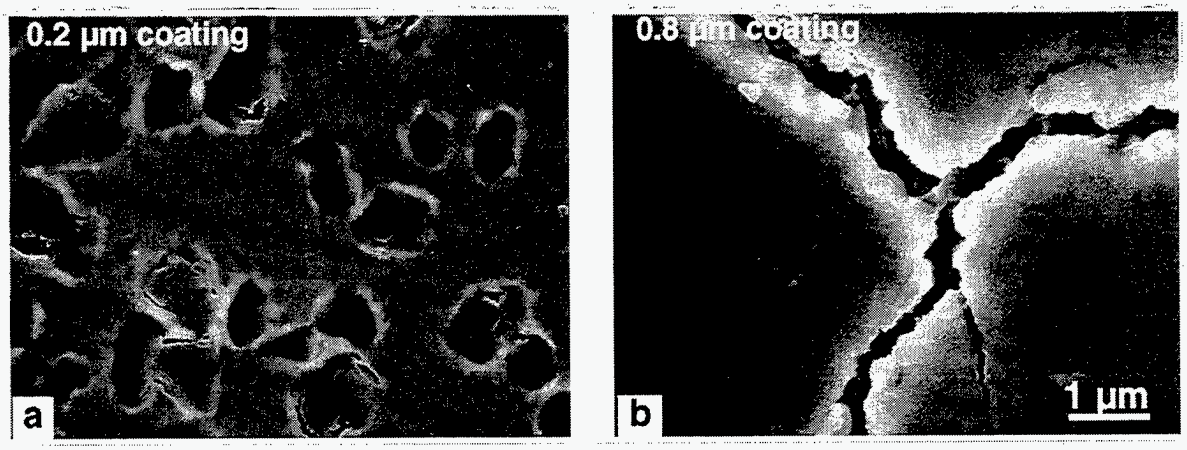

Fig. 2. SEM plan-views of the heat-treated coatings after 2 h in He at 1000°C. (a) 0.2 µm coating, (b) 0.8 µm coating.

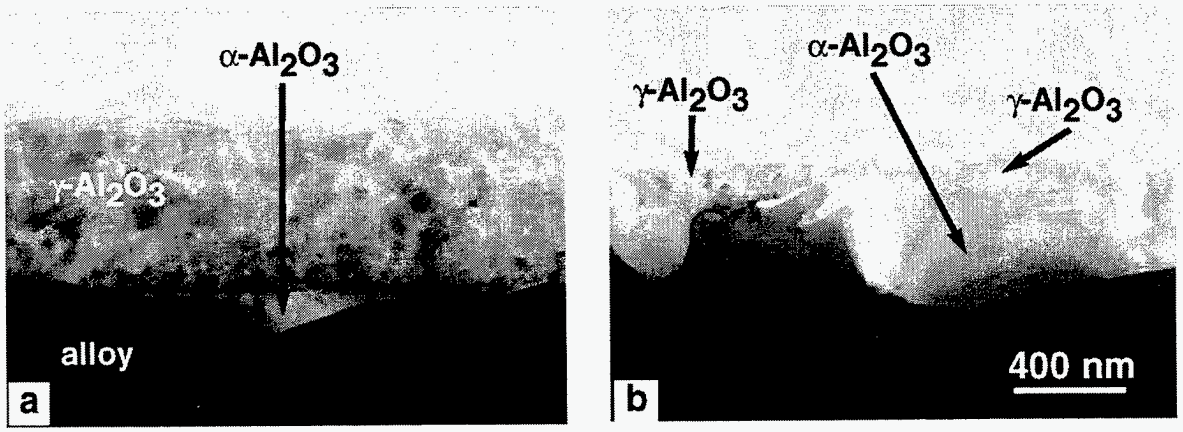

Fig. 3. TEM cross-section through heat-treated 0.2 µm thick coating after 2 h in He at 1000°C.

Studies with Auger electron spectroscopy (AES) on interfaces that were freshly exposed by an in-situ scratch-technique, showed that sulfur segregated to the scale/metal interface during the heat treatment.[16] The sulfur coverage of the interface increased with increasing annealing time and varied in different regions of the specimen. In order to study the correlation between different interface structures and the sulfur level at the interface, high spatial resolution EDS of TEM cross sections was used. Segregation of sulfur was found at α-Al_2O_3/alloy interfaces as well as at γ-Al_2O_3/alloy interfaces (Fig. 4). No interfacial voids were observed in these areas. Quantification of these data is complicated by the fine-scaled roughness of the γ-Al_2O_3/alloy interface (in contrast to the facetted α-Al_2O_3/alloy interface) which made edge-on orientation of

the interface impossible. Further analysis is underway to determine if the interfacial sulfur coverage is different for the two microstructures.

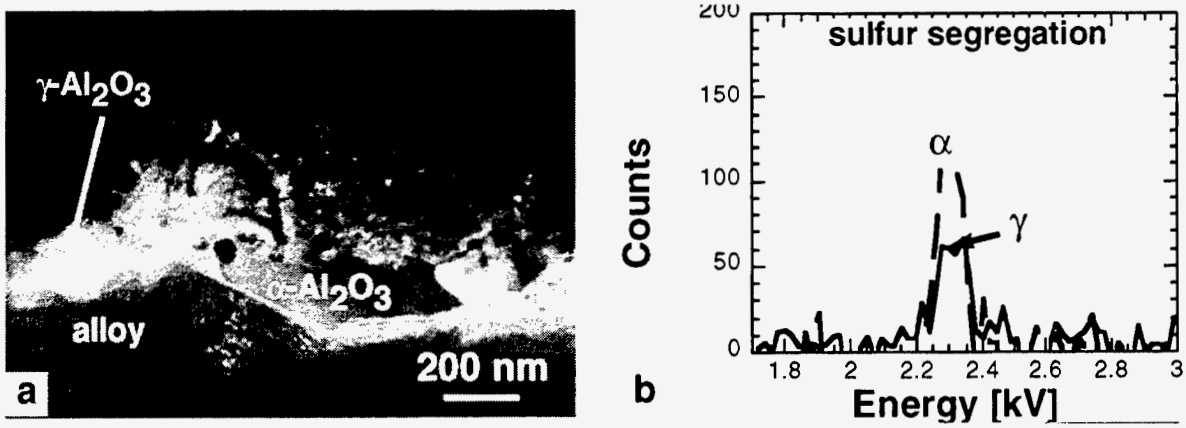

Fig. 4 a) STEM annular darkfield image of γ/alloy and α/alloy interface, b) EDS spectra showing segregation of sulfur at the γ/alloy and the α/alloy interface.

3. Influence of Alumina Coatings on Thermal Oxide Growth on Iron-Aluminides

To study the effect of an alumina coating applied prior to oxidation on the oxidation performance of iron-aluminides, FAL was coated on one side with a 0.1 μm alumina coating and oxidized in air at 1000°C for 96 h. On both sides, the coated and the uncoated one, oxide scales with a needle-like surface structure were formed (Fig. 5). Both oxide scales were well adherent. The recorded weight gain demonstrated that the coating enhanced the oxidation process. The oxide scale on the coated side was 1.5-2 μm thick, whereas on the uncoated side it was 0.8-1 μm (Fig. 6).

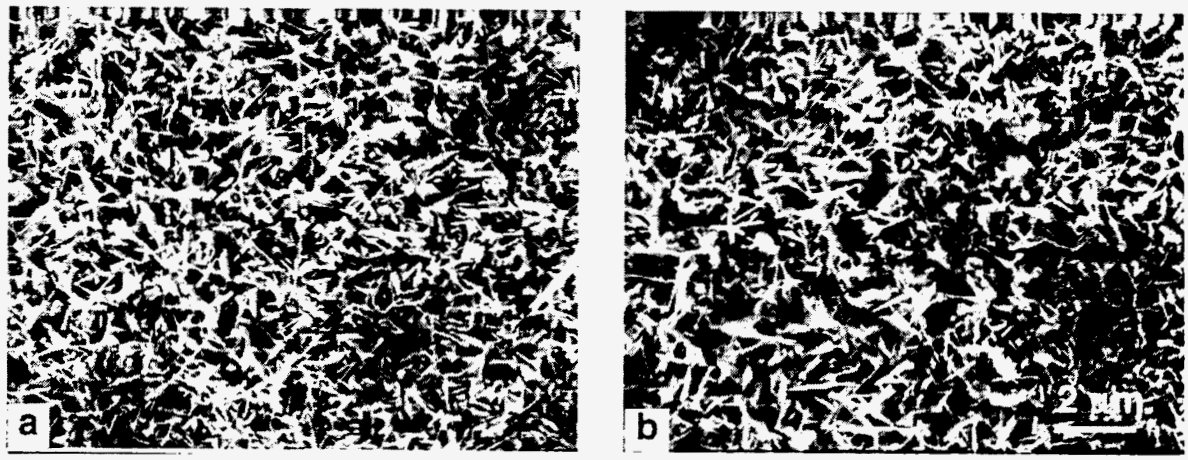

Fig. 5. SEM plan view of oxidized surfaces, a) FAL uncoated, b) FAL with 0.1 μm alumina coating.

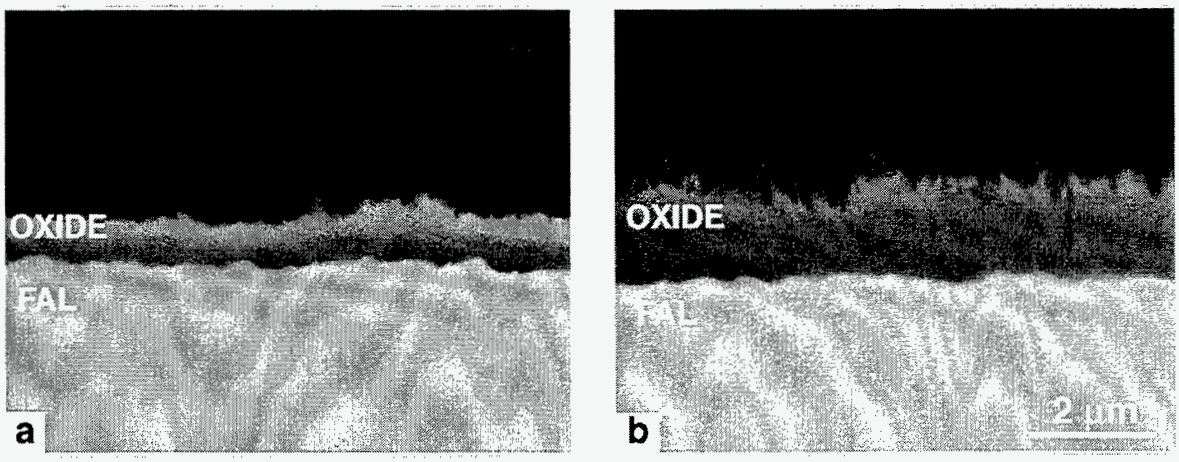

Fig. 6. SEM of polished cross section, a) FAL uncoated, b) FAL with 0.1 μm alumina coating.

On the coated side, the original location of the coating can be discerned in the TEM cross-section shown in Fig. 7. The grain size in the area of the original coating is typically 100-150 nm. The grains were identified as nearly dense, equiaxed α-Al_2O_3. The thermally-grown oxide on top of the coating was also α-Al_2O_3 however, it had a much coarser grain structure. Selected-area diffraction showed all portions of the oxide scale, even the oxide needles at the scale/gas interface were α-Al_2O_3, consistent with the pseudomorphic transformation of transient oxides to α-Al_2O_3.

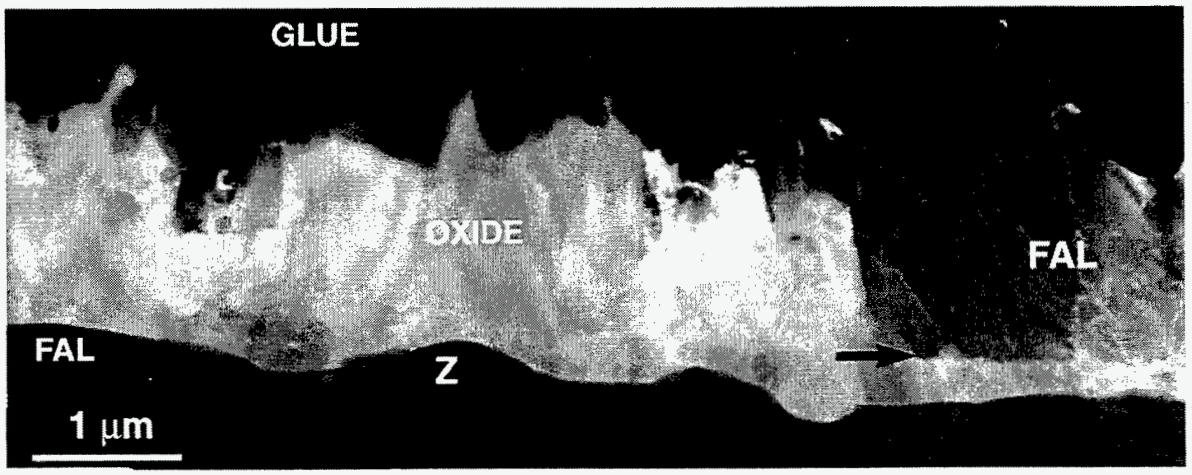

Fig. 7 STEM annular dark-field of coated-and-oxidized FAL. The location of the original coating is indicated by the arrow.

The identification of the original coating location in the bottom portion of the scale after oxidation implies that most of the scale growth on coated FAL occurred by transport of aluminum through the coating. Although the scale/metal interface on the coated FALwas intact, it roughened during oxidation. This indicates that some transformation of α-Al_2O_3 at the metal/coating interface occurred (similar to that described in the previous section). On the coated surface, Zr-rich metallic particles (typical size: 0.5-1 μm) were found at the scale/metal interface (marked "Z" in Fig. 7). The particles at the scale/metal interface were, compared to the FAL alloy, rich in Zr but contained less Fe and Cr and no oxygen. These particles were not observed at the scale/metal interface in the absence of the alumina coating. The fact that the Zr was not oxidized is consistent with the lack of inward diffusion of oxygen. It is proposed that the amorphous coating promotes the nucleation and growth of metastable alumina phases, resulting in slighly enhanced outwardly-growing oxidation and thicker scales. During the early stages of oxidation, the amorphous coating is therefore ineffective as a protective layer.

Fig. 8. Annular dark-field STEM image of cross-section through scale showing ZrO_2 particles within the scale.

Elemental analysis by EDS showed that zirconium segregated to oxide grain boundaries, both in the initial alumina coating and in the thermally-grown oxide. Segregation of zirconium at the scale/metal interface was also found, both in the coated and uncoated FAL. Auger analysis on metal/oxide interfaces exposed by scratching off the oxide in vacuo revealed the absence of sulfur at the metal/oxide interface.[14] In the portion of the scale above where the amorphous coating was originally located, ZrO_2 particles were found at grain boundaries as well as at the interface between the former coating and the thermally-grown oxide (Fig. 8). The formation of ZrO_2 particles in

the lower part of the oxide scale on coated-and-oxidized FAL must result from diffusion of zirconium into the coating and subsequent oxidation and/or formation of ZrO_2 during the growth of new oxide.

II. Oxidation Studies on NiCrAl-Alloys

Plan-view images of the three alloys after oxidation are shown in Fig. 9. Figure 10 shows the corresponding cross sections (polished or fractured). The oxide scale on René N5 (~5 μm) consists of columnar α-Al_2O_3 at the bottom (~4 μm) and a mixed layer of spinel (Ni, Co, Ta)(Al, $Cr)_2O_4$ and α-Al_2O_3 (~1 μm) at the top. The mixed oxide layer contains numerous precipitates of Ta,Y,Cr(Hf,Re)-oxides. These are concentrated at the interface between the columnar alumina and the mixed layer. This mixed layer of the scale is prone to spallation.

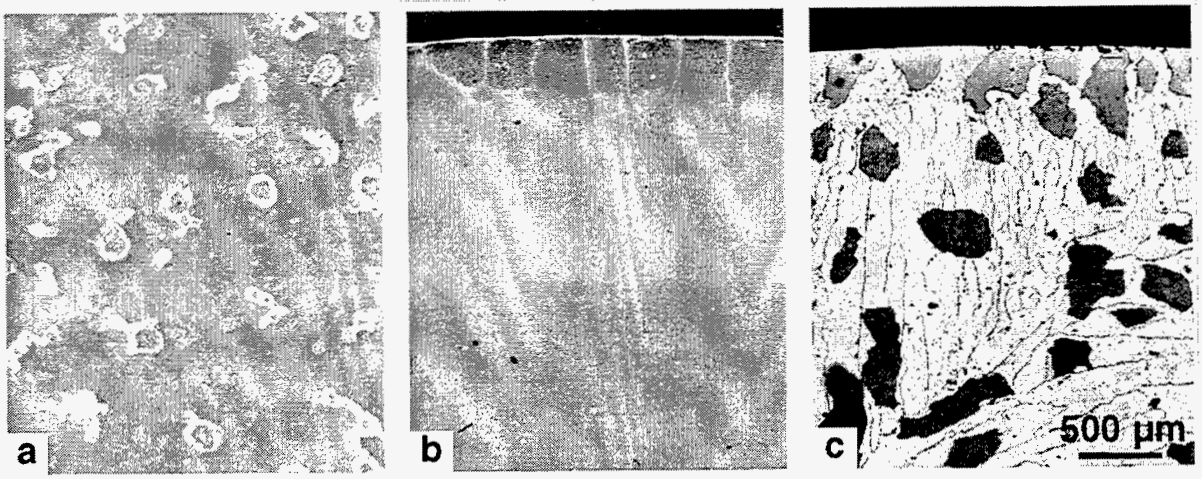

Fig. 9. SEM plan view images of a) René N5, b) NCASY and c) NCA3Y.

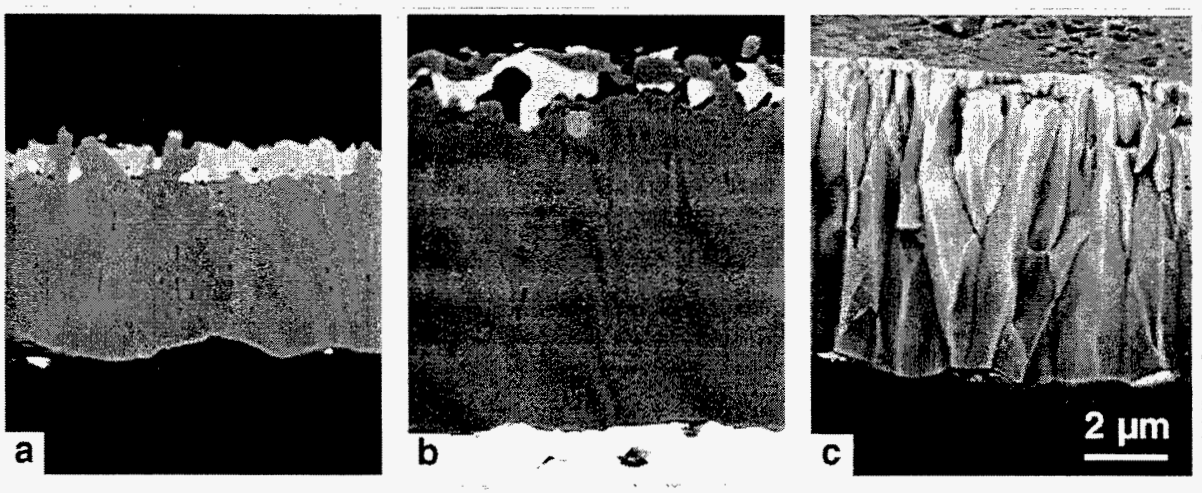

Fig. 10. SEM images of cross-sections of a) René N5, b) NCASY and c) NCA3Y.

Similar oxide particles can also be found on the scale surface. Spallation of the complete scale exposing the bare alloy occurs only around particles in the alloy, which consist of Ta,Y,Cr(Hf,Re)-oxide in the center, surrounded by spinel (Ni, Co, Ta) $(Al, Cr)_2O_4$ and α-Al_2O_3. Segregation of Ta and Y at oxide grain boundaries, both in the alumina and in the spinel, was found. Some oxide grain boundaries also exhibited segregation of Hf and Re.

On NCASY, the scale (~9 μm) consists mainly of columnar Cr-doped α-Al_2O_3. The grain structure of the scale resembles that found on many reactive-element-doped alumina formers (e.g. - Refs. 6, 7, 18) and indicates alumina growth primarily by inward oxygen diffusion.[17] A thin, porous mixed layer of equiaxed spinel ($NiAl_2O_4$) and α-Al_2O_3, as well as some NiO formed on top of the alumina. Over time, NiO transforms to $NiAl_2O_4$ and $NiAl_2O_4$ and eventually to α-Al_2O_3; both transformations are pseudomorphic. Spallation of the scale occurred only in a few areas associated with the formation of Y_2O_3, $Y_3Al_5O_{12}$ (garnet) and α-Al_2O_3 at Y-rich alloy grain boundaries. Yttrium-rich oxide particles can be found on the scale surface. Yttrium was also found to be segregated at oxide grain boundaries and at the scale/metal interface.

The NCA3Y alloy forms an oxide scale (~8 μm) that consists mainly of columnar Cr-doped α-Al_2O_3. Y-rich oxide particles can be found on the scale surface. The higher level of Y in this alloy results in the formation of Y-rich precipitates at all alloy grain boundaries. Preferential internal oxidation ultimately leads to the formation of Y_2O_3, $Y_3Al_5O_{12}$ (garnet) and α-Al_2O_3 at these grain boundaries. Due to the volume change associated with the formation of these phases, almost complete spallation of the oxide scale is initiated at these sites.

SUMMARY

Alumina scales on iron-aluminides (Fe_3Al-based) and NiCrAl-based alloys were characterized in order to develop the knowledge to control the oxidation performance of alloys by controlling the microstructure and microchemistry of their scales. Plasma-deposited amorphous alumina coatings on iron-aluminides were used to study phase transformations, transport processes in the scales and sulfur segregation to the scale/metal interface. It was found, that during heat treatment in the absence of oxidation, amorphous coatings first transform to γ-Al_2O_3 and eventually α-Al_2O_3 nucleates at the scale/metal interface. Sulfur from the Zr-free alloy segregates to the scale/metal interface during heat treatment. Thermally-grown scales on Zr-doped iron-aluminides were compared to those formed after oxidation of a specimen with an alumina coating. Microstructural and gravimetric results showed that the primarily amorphous alumina coating promoted the nucleation and growth of metastable alumina phases, which

resulted in more rapid oxidation. The thermally-grown oxide was found on top of the coating. The NiCrAl-based alloys formed columnar alumina scales underneath a layer of mixed oxides. Segregation of alloying elements like Y, Hf and Ta was found at both oxide grain boundaries and scale/metal interfaces. The results from both alloy systems are consistent with previous results on primary alumina-formers. Reactive elements present in the alloy diffuse into the oxide scale and segregate to grain boundaries where they change the diffusion processes resulting in a columnar grain structure of the alumina scale.

ACKNOWLEDGMENT

The authors thank M. Howell for experimental support, B.A. Pint and I.G. Wright for technical discussions and E. A. Kenik for review of the manuscript. This research was sponsored by the Fossil Energy Advanced Research and Technology Development (AR&TD) Materials Program and the Division of Materials Science, U S. Department of Energy, DE-AC05-96OR22464 with Lockheed Martin Energy Research Corp. Research was performed in part with the SHaRE User Facilities at ORNL.

REFERENCES

1. J.G. Smeggil, A.W. Funkenbusch, N.S. Bornstein, Met. Trans. 17A (1986) 923.
2. E. Schumann, J.C. Yang, M.J. Graham and M. Rühle, Oxid. Met. 46 (1996) 37.
3. E. Schumann, Scripta Mater. 34 (1996) 1365.
4. C. Mennicke, E. Schumann, C. Ulrich and M. Rühle, Mat. Sci. Forum (1996) in press.
5. G.H. Meier, F.S. Pettit and J.L. Smialek, Mat. Corr. 46 (1995) 232.
6. B.A. Pint, Oxid. Met. 45 (1996) 1.
7. B.A. Pint and K.B. Alexander, pp. 97-108 in Fundamental Aspects of High Temperature Corrosion, D. A. Shores, R. A. Rapp, and P. Y. Hou (eds.), Proc. Vol. 96-26, The Electrochemical Society, Pennington, New Jersey, 1997.
8. P.F. Tortorelli and K.B. Alexander, pp. 247-56 in *Proc. Ninth Annual Conf. Fossil Energy Materials*, N.C. Cole and R.R. Judkins (comp.), CONF-9505204, U. S. Department of Energy, August 1995.
9. P.F. Tortorelli and J.H. DeVan, pp. 257-70 in Processing, Properties, and Applications of Iron Aluminides, J.H. Schneibel and M.A. Crimp (eds.), The Minerals, Metals, and Materials Society, Warrendale, PA, 1994.
10. K.B. Alexander, K. Prüßner, P.Y. Hou and P.F. Tortorelli, 3rd Int. Conf. Microscopy of Oxidation, The Institute of Metals, London(1996) in press.
11. C.S. Giggins and F.S. Pettit, J. Electrochem. Soc. 118 (1971) 1782.
12. A. Kumar, M. Nasrallah and D.L. Douglass, Oxid. met. 8 (1974) 227.
13. I.G. Brown and Z. Wang, Proc. Ninth Annual Conf. Fossil Energy Materials, U.S. Department of Energy (1995) 239.
14. P.Y. Hou, Z. Wang, K. Prüßner, K.B. Alexander and I.G. Brown, 3rd Int. Conf. Microscopy of Oxidation, Cambridge (1996) in press.
15. P. Fox, D.G. Lees and G.W. Lorimer, Oxid. Met. 36 (1991) 491.
16. K. Prüßner, E. Schumann and M. Rühle, pp. 344-56 in Fundamental Aspects of High Temperature Corrosion, D. A. Shores, R. A. Rapp, and P. Y. Hou (eds.), Proc. Vol. 96-26, The Electrochemical Society, Pennington, New Jersey, 1997.
17. B. A. Pint, pp. 74-85 in Fundamental Aspects of High Temperature Corrosion, D. A. Shores, R. A. Rapp, and P. Y. Hou (eds.), Proc. Vol. 96-26, The Electrochemical Society, Pennington, New Jersey, 1997

ODS IRON ALUMINIDES

I. G. Wright, B. A. Pint, P. F. Tortorelli, and C. G. McKamey

INTRODUCTION

Interest in increasing the efficiency of coal-fired power plants has led to the examination of alternatives to the steam boiler-Rankine cycle systems, for which increases in efficiency have been limited by the slow progress in improving the ability to handle steam at temperatures much in excess of 565°C (1050°F). Indirect-firing of gas turbines in open or closed cycles is one approach to linking the higher efficiencies possible via the Brayton cycle with coal as the fuel. Current programs involving indirectly-fired gas turbine cycles are aimed at high cycle efficiencies, of the order of 47 percent based on the higher heating value (HHV) of the fuel, and involve open cycle systems in which air is heated to 760°C (1400°F) in a metallic heat exchanger, and then to 982°C (1800°F) in a natural gas-fired ceramic heat exchanger [1-3]. A variant of this approach is to pyrolyze part of the coal to produce the fuel gas used to fire the final heat exchanger or turbine; the air entering the turbine is then heated to 1288°C (2350°F).

Successful implementation of indirectly-fired cycle technologies will require the development of a durable coal-fired heat exchanger capable of heating the working fluid to very high temperatures, in addition to adapting a gas turbine for this particular duty. The ferritic ODS alloys based on Fe-Cr-Al have the potential for application at higher temperatures than the modified conventionally-strengthened alloys in which the strengthening mechanisms degrade as the precipitated phases become less stable with increasing temperature. Oxide dispersion-strengthened alloys can provide creep strength up to approximately 90 percent of the alloy melting temperature (which is ≈1480°C for FeCrAls). A heat exchanger of harp design, made from 4 m long, 2.5 cm diam. ODS-FeCrAl tubes, was recently shown to be capable of heating air to 1100°C in a closed-cycle demonstration plant [4]. Compared to ODS-FeCrAl alloys, ODS-Fe_3Al has potential advantages of lower cost, lower density, and superior oxidation and sulfidation resistance, provided that similar gains in creep strength can be realized through the ODS process.

DISCUSSION OF CURRENT ACTIVITIES

Alloy Preparation

Yttria-containing Fe_3Al alloy powder was prepared by the PM-ODS Werkstoffe division of Metallwerk Plansee (PM), using high-energy ball milling, from prealloyed Fe_3Al powder made by argon-atomization by Homogeneous Metals (HM). The chemical analysis of the starting powder is shown in Table 1; it was spherical in shape, and had a mean particle size of 75 μm (range 30 to 200 μm). The milling parameters used by PM were based on those used in the commercial production of its PM2000 alloy (Y_2O_3-dispersion-strengthened FeCrAl). The main difference was that three different milling environments (cover gas plus process control agents [PCAs]) were employed (Routes A, B, and C, in Table 1). After milling, the powder particle size ranged up to 480 μm for powder from Route C, whereas the use of PCAs resulted in smaller powder particle sizes with, for instance, the powder from Route A having a maximum particle size of 200 μm.

The bulk chemical analyses of the milled powders, shown in Table 1, indicate that the powder processed by Route C had picked up a significantly lower level of oxygen than had the other two powders. In contrast, the Route A powder exhibited significantly higher levels of nitrogen, carbon, and hydrogen than the other powders. The pickup of nitrogen, hydrogen and carbon

Table 1. Chemical Analyses of Fe_3Al Powders (wt %)

Element	As-Received		Route A	Route B	Route C
	HM	PM			
Fe	Bal.	79.6			
Al	16.3	18.20 (Bal.)			
Cr	2.4	2.18			
Zr	20 ppm	26 ppm			
O (total)	60 ppm	110 ppm	1,800 ppm	1,900 ppm	1,400 ppm
O (from Y_2O_3)			1,025 ppm	1,053 ppm	1,080 ppm
O bal.			775 ppm	847 ppm	320 ppm
O pickup			*665 ppm*	*737 ppm*	*210 ppm*
N	18 ppm	7 ppm	1,264 ppm	145 ppm	88 ppm
N pickup			*1257 ppm*	*138 ppm*	*81 ppm*
H		16 ppm	115 ppm	40 ppm	29 ppm
C		24 ppm	667 ppm	360 ppm	303 ppm
C pickup			*643 ppm*	*336 ppm*	*279 ppm*
O/Al			*0.010*	*0.010*	*0.008*
Fe/Al			*4.37*	*4.37*	*4.37*
C/Fe			*0.009*	*0.0005*	*0.0004*
C/Al			*0.004*	*0.002*	*0.002*
C/O			*0.37*	*0.19*	*0.22*

was similar for the powders from Routes B and C, with the Route C powder showing slightly lower levels.

Auger analysis of the surfaces of the as-milled powders indicated that the main difference was the carbon content. As shown in Table 2, the C/Fe, C/Al, and C/O ratios were greatest for powder milled by Route B. Comparison with the bulk analyses in Table 1 suggests that the powder particle surfaces were enriched in aluminum oxide and carbon. The presence of the surface oxide was expected; the surface carbon enrichment is presumed to result largely from interaction of the powder particles with the ball surfaces during milling.

Samples of each powder were canned in mild steel, hot degassed, and consolidated into bar by extrusion (9:1 ratio) at 1050°C following preheating for 45 min. The flow stresses measured during extrusion ranged from 810 to 850 Pa. After extrusion, all the samples exhibited a sub-micron size grain structure. The microhardness values (HV10) for these structures were 486, 413, and 399 kg/mm^2, for powder A, B, and C, respectively. The chemical compositions of the

Table 2. Auger Analyses of As-Milled Powders

Sample	Auger Analysis (%)				Relative Counts				
	C	O	Fe	Al	O/Al	Fe/Al	C/Fe	C/Al	C/O
A1	7.8	35.7	31.47	25.03	7.13	1.58	0.23	0.36	0.05
A2	9.11	36.11	31.17	23.61	7.65	1.66	0.27	0.44	0.06
B1	19.2	29.64	30.3	20.87	7.10	1.83	0.58	1.05	0.15
B2	21.2	31.49	28.19	19.1	8.25	1.86	0.68	1.27	0.15
C1	14.5	32.99	29.04	23.49	7.02	1.55	0.45	0.70	0.10
C2	12.4	31.73	29.86	26.04	6.09	1.44	0.38	0.54	0.09

consolidated alloys are shown in Table 3. Compared to the composition of the starting powder, some loss of aluminum is evident, with the greatest loss observed for Powder A (PMWY-1) which also showed the largest pickup of oxygen. The oxygen levels in PMWY-2 and -3 remained essentially the same as in the as-milled powders, but PMWY-2 showed an increase in nitrogen content after consolidation of the order of 900 wppm. The carbon levels of all three alloys were essentially unchanged after consolidation.

Recrystallization

The initial attempt to recrystallize the consolidated alloys used the same conditions as for PM2000, which involved annealing at 1380°C for 1 hr. Two of the alloys, PMWY-1 and 2,

exhibited a very large, elongated grain structure, whereas alloy PMWY-3 showed no signs of recrystallization. The recrystallized alloys also exhibited a significant amount of porosity which appeared to be associated with the recrystallization anneal, since the as-extruded alloys were pore-free, as was alloy PMWY-3 after the anneal.

Porosity similar to that observed in the alloys PMWY-1 and -2 has been observed in other ODS alloys [5-7]. The extent and size of the pores apparently depends not only on powder processing parameters, but also varies among alloys processed by the same route [8]. The source of the porosity has been attributed to gas bubbles resulting from argon adsorbed on the original powder particles, but pores were still found when hydrogen was used as the cover gas during the milling step [5]. One model discounts the effects of gas from dissolved or bonded oxygen and carbon or

Table 3. Chemical Compositions of Extruded Alloys (wt %)

Element	PMWY-1 (Powder A)	PMWY-2 (Powder B)	PMWY-3 (Powder C)
Fe	81.68	81.45	81.54
Al	14.67	15.36	15.43
Cr	2.61	2.33	2.33
Y	0.38	0.39	0.40
Zr	<100 ppm	<100 ppm	<100 ppm
O (total)	3,232 ppm	2,073 ppm	1,452 ppm
O (Y_2O_3)	1,025 ppm	1,053 ppm	1,080 ppm
O bal.	2,207 ppm	1,020 ppm	372 ppm
Overall O pickup	*2,097 ppm*	*910 ppm*	*262 ppm*
N	968 ppm	1,024 ppm	44 ppm
C	600 ppm	400 ppm	300 ppm
B	<3 ppm	<3 ppm	<3 ppm
Cu	0.01	0.01	0.01
Mn	0.04	0.03	0.02
Ni	0.05	0.03	0.03
P	0.008	0.008	0.008
Si	0.04	0.03	0.04
Ti	0.01	<0.01	<0.01
Y	0.38	0.39	0.40
(Y_2O_3	0.48	0.50	0.51)
S	22 ppm	20 ppm	16 ppm

nitrogen, and suggests a more likely cause is void condensation from stress-induced vacancy migration, with oxide shell growth around the pore walls by reduction of entrapped water vapor by the oxygen-active elements in the alloy [6]. Another model suggests that the voids result from plastic deformation by hydrogen liberated by the reduction of adsorbed water vapor (or hydroxides) on the original powder particle surfaces [7]. The source of the adsorbed gas is the

original gas atomization process and/or the milling process; the relative importance of these sources is unclear.

Based on reported observations that such porosity in ODS alloys is usually absent or is smaller at lower temperatures [7], samples of the alloys were annealed at various combinations of temperature and time to observe the recrystallization behavior and tendency to develop porosity. As mentioned above, Alloy PMWY-3 did not recrystallize under any of treatments used (up to 1hr at 1380°C). Alloy PMWY-2 did not recrystallize below 1200°C, and Alloy PMWY-1 did not recrystallize below 1300°C; the fine-grained microstructure of Alloy PMWY-1after annealing at 1300°C for 2 hr. is shown in Fig. 1. The microstructures of Alloy PMWY-2 after annealing for

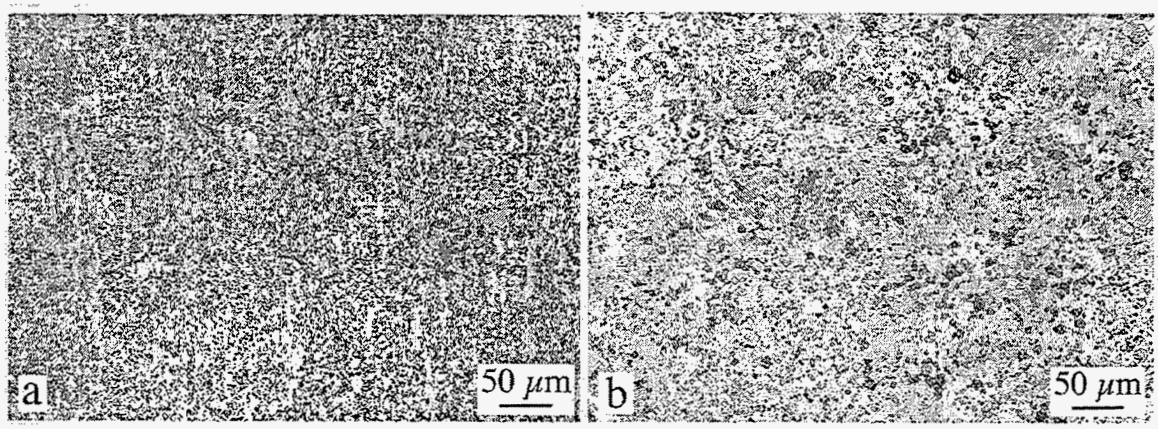

Fig. 1. Cross sections of Alloy PMWY-1 showing essentially no recrystallization after annealing for 2 hr at 1300°C: (a) longitudinal section, (b) transverse section.

2hr at 1200, 1250, and 1300°C are illustrated in Figs. 2-4 and show that, while recrystallization is essentially complete after 2hr at 1200, 1250, and 1300°C are illustrated in Figs. 2-4 and show that, while recrystallization is essentially complete after 2 hr at 1200°C, small areas of what appeared to be unrecrystallized grains persisted, even at 1300°C. These areas appeared as elongated dark-colored streaks in longitudinal cross sections (Fig. 2a), and as dark patches in transverse sections (Fig. 2b). With increasing temperature, the number and size of these areas tended to decrease, although one or two patches were still visible in typical transverse sections after 2 hr at 1300°C (Fig. 4b). Also evident in Figs. 2-4, especially in transveres sections, is the porosity that developed upon annealing, and which increased with increasing time and temperature.

The hardness of the alloys decreased on the order of 75-100 kg/mm^2 following the recrystallization anneal, and progressively decreased with increasing annealing temperature and time.

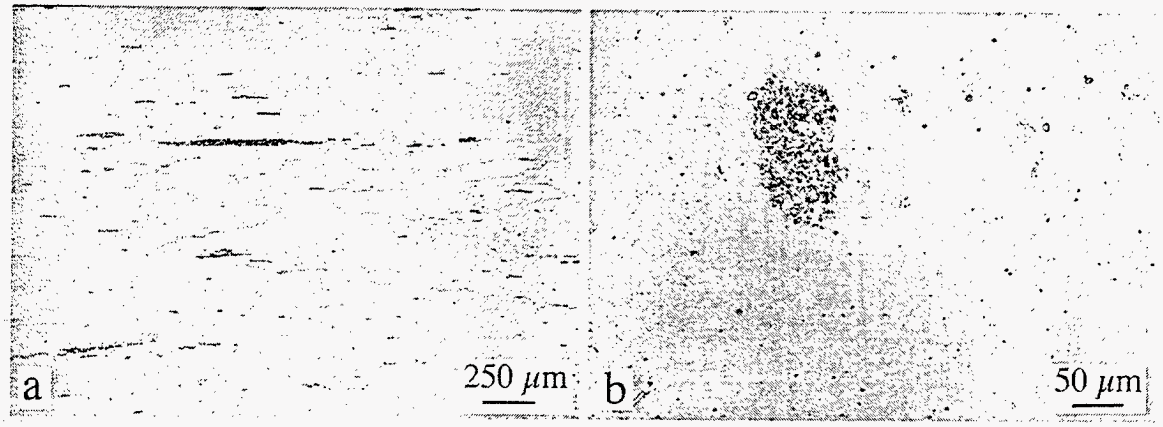

Fig. 2. Cross sections of Alloy PMWY-2 after annealing for 2 hr at 1200°C: (a) longitudinal, (b) transverse.

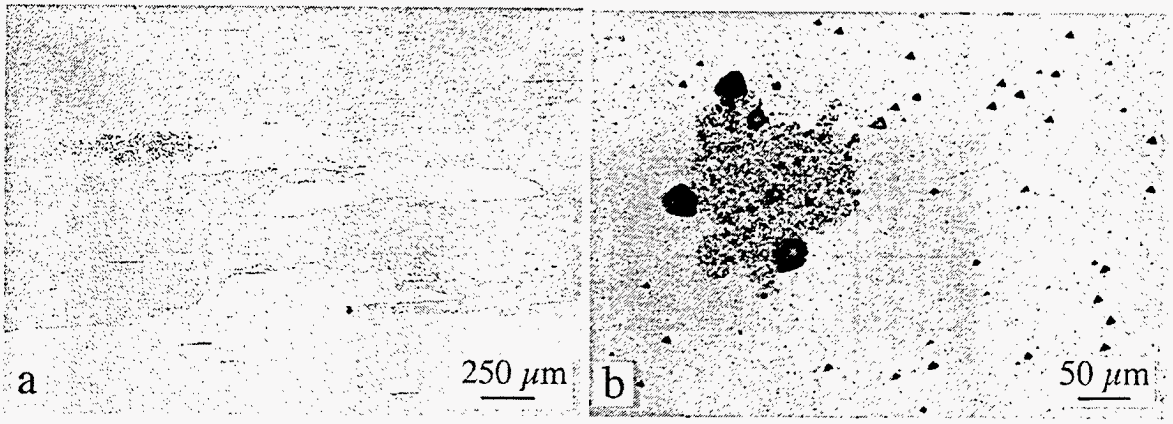

Fig. 3. Cross sections of Alloy PMWY-2 after annealing for 2 hr at 1250°C: (a) longitudinal, (b) transverse.

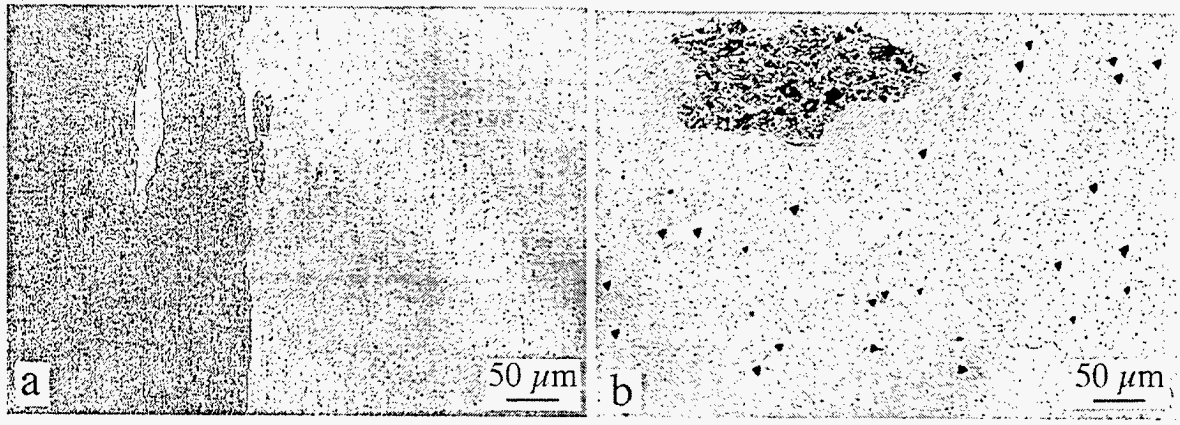

Fig. 4. Cross sections of Alloy PMWY-2 after annealing for 2 hr at 1300°C: (a) longitudinal, (b) transverse.

Creep Tests

Round creep-rupture specimens with a gage diameter of approximately 3 mm and a gage length of 17.8 mm were machined from bars of alloy PMWY-2 that had been recrystallized at 1300°C. Two initial creep rupture tests were performed in air. The first test, at 980°C and 48 MPa, failed in 68.4 hr with a final elongation of 1.7% and a minimum creep rate of 0.01%/hr. The next test at 1075°C at the same stress resulted in a creep-life of 8.3 hr, with a final elongation of 3.1% and a minimum creep rate of 0.04%/hr. The curves of life-versus-elongation are shown in Fig. 5. Both specimens exhibited low minimum creep rates when compared to precipitation-strengthened Fe_3Al-based alloys [9], at a higher temperature than possible with these alloys. The results of these two tests are compared with binary Fe_3Al, the precipitation-strengthened Fe_3Al-based FA-180 alloy, and two stainless steels in Fig. 6.

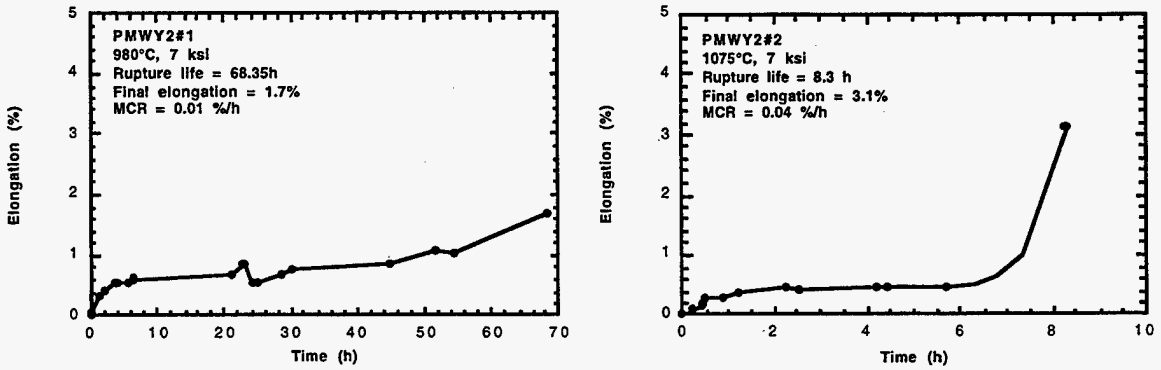

Fig. 5. Creep-rupture curves for PMWY-2 alloy tested at a stress of 48 MPa at (a) 980°C and (b) 1075°C in air.

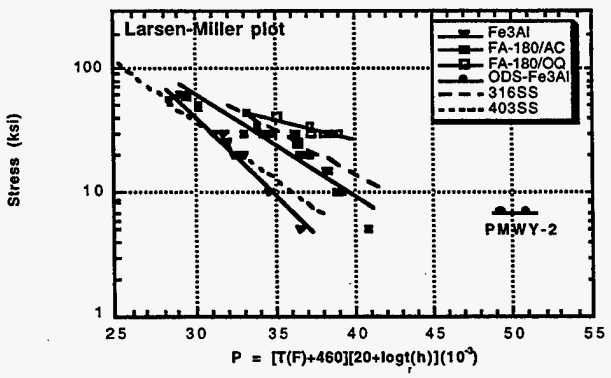

Fig. 6. Larson-Miller plot to compare creep performance of PMWY-2 with Fe_3Al, alloy FA-180 and two stainless steels.

Examination of the specimens after testing indicated that the mode of failure was not uniform, as illustrated in the scanning electron microscopy (SEM) secondary electron images in Fig. 7. Figure 8a shows that over half of the fracture surface of the 1075°C specimen exhibited had a brittle, transgranular appearance with dimples and pores characteristic of microvoid coalescence. There were also long stringer-like features which appeared more ductile and possibly contained particles (Fig. 8b). High magnification examination of the area of brittle fracture showed the presence of oxide (assumed to be the Y_2O_3 dispersion) and small pores (visible as black dots in Fig. 8c). However, there was no obvious origin of the crack in the area of either specimen that

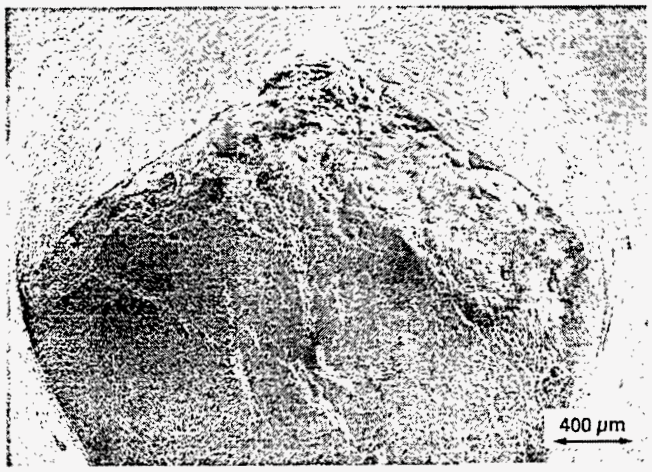

Fig. 7. SEM image of fracture face of specimen tested at 1075°C showing the non-uniform nature of the creep rupture.

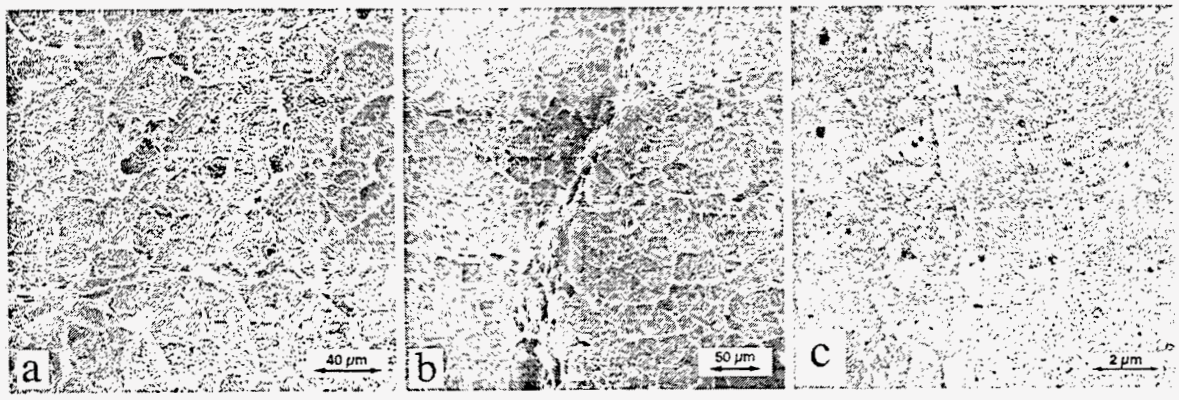

Fig. 8. SEM images showing typical features of the more brittle regions of the creep rupture surfaces of PMWY-2: (a) microvoids in specimen tested at 980°C, (b) stringer in specimen tested at 980°C, (c) cavities, oxide particles, and needle-like phase in specimen tested at 1075°C.

had experienced brittle fracture. Further creep testing was suspended until the cause of the brittle failure was found.

Figure 9 is an optical micrograph showing the creep rupture in the short-transverse direction parallel to the extrusion direction from the specimen tested at 1075°C. Approximately half of the specimen cross section that fractured transgranularly in a brittle manner apparently corresponded to one of the two grains that constituted the cross section of the gauge length (Fig. 9a), The roughly one-third of the specimen that had begun to neck down corresponded to the other main grain in the essentially bi-crystal specimen, and contained a large number of creep cavities and evidence of cavity growth and coalescence near the fracture (Fig. 9b). A light etch of the specimen indicated the possible existence of several elongated grains of up to 200 μm in width in the part of the specimen that had necked and elongated (Fig. 9b). Whereas the cross section of the gage length away from the fracture contained basically two visible grains running the length of the specimen, near the center of the section was a stringer about 3 mm long consisting of what appeared to be finer, unrecrystallizedgrains and inclusions; this region did not appear to play any part in the specimen

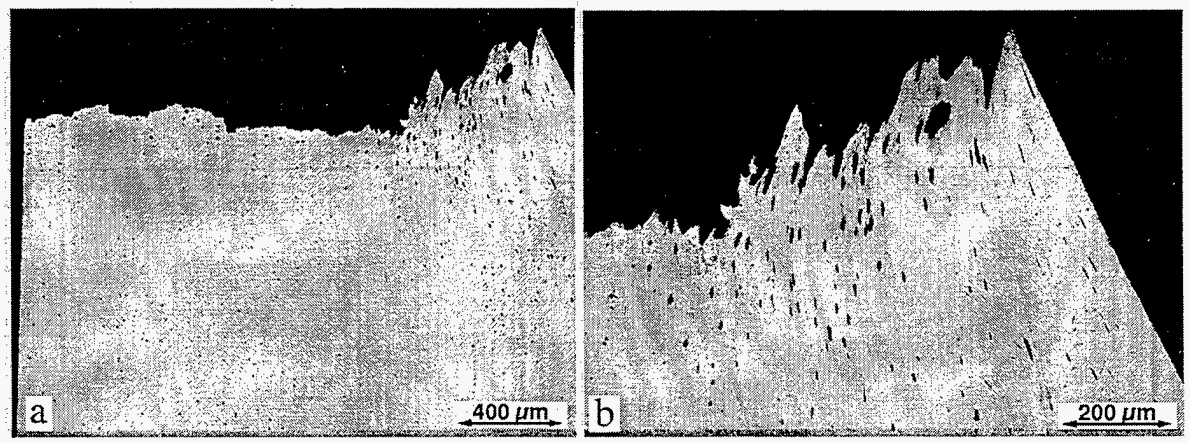

Fig. 9a. Cross section of fracture face of specimen tested at 1075°C, showing: (a) complete fracture section, and (b) enlarged view of necked region.

failure. Also visible in the necked area of the specimens were enlarged voids (or creep cavities) which had been distorted by the necking, and a phase with a needle-like morphology characteristic of a carbide phase such as Fe_3AlC [10] visible in Fig. 8c.

Reexamination of specimens used in the 1300°C recrystallization experiments indicated areas in one specimen of alloy PMWY-2 which exhibited internal cracks, as shown in Figs 10a and b. The appearance of these cracks suggested a crystallographic preference, and that they probably occurred after the annealing treatment. No such cracks were observed in any of the specimens annealed at temperatures from 1150°C to 1250°C, or at 1380°C. This examination is continuing.

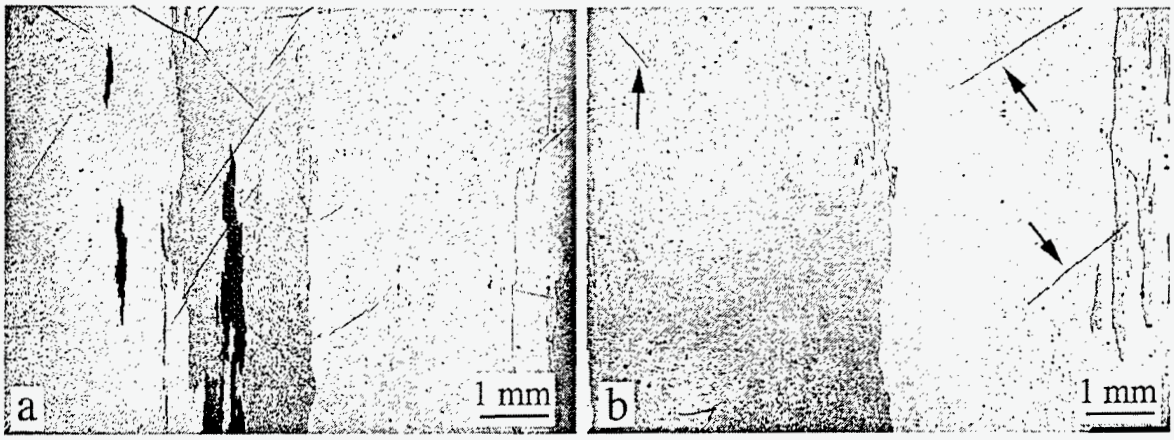

Fig. 10. Cracking in Alloy PMWY-2 annealed at 1300°C for (a) 1hr and (b) 2 hr.

Oxidation Lifetime Tests

Data for use in estimating the high-temperature oxidation lifetimes of a recrystallized alloy (PMWY-2) and non-recrystallized alloy (PMWY-3) were generated by means of thermal cycling tests using specimens exposed in individual, lidded alumina crucibles in air in a muffle furnace. The exposure temperature was 1100°C, and each thermal cycle lasted for 100 hr. The specimen weight changes in this test are compared in Fig. 11a with data for an earlier version of this alloy

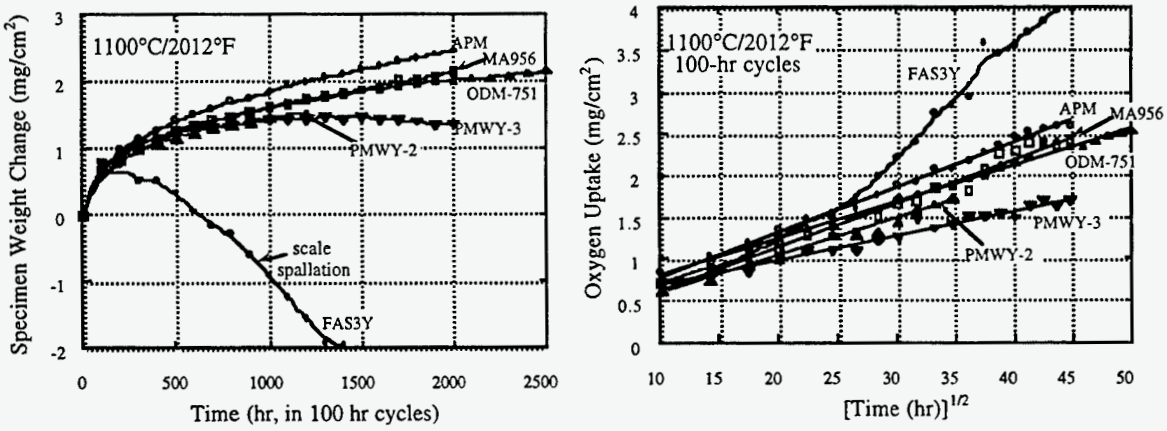

Fig. 11. Oxidation kinetics at 1100°C: (a) specimen weight gain plots, (b) parabolic oxidation plots

(FAS3Y) made at ORNL [11], and for three commercial ODS FeCrAl alloys (Kanthal APM, MA956, ODM-751). The most obvious result is the large reduction in scale spallation for the PMWY alloys compared to FAS3Y, although there still appears to be a tendency to some spallation at times longer than 1,200 hr. The reasons for this improvement are not immediately

clear; the PMWY specimens will be examined when the exposures are completed. Despite the tendency to some scale spallation, the overall weight change due to oxygen uptake (aluminum consumption), shown in Fig. 11a, was very similar for the PMWY alloys and the ODS-FeCrAl alloys. The fact that the kinetics for each PMWY alloy corresponded to a single parabolic rate suggested that any scale spallation that occurred did not affect the rate-controlling scale layer, at least within the sensitivity of the test method.

These new kinetic data were used to calculate the expected oxidation-limited lifetime of a 2.5 mm thick tube wall (following a procedure described previously [11]), with the result shown in Fig. 12. Whereas the scale spallation behavior of the FAS3Y alloy resulted in an oxidation lifetime at 1100°C equivalent to the commercial ODS-FeCrAl alloys despite its larger reservoir of aluminum (15.8 vs 4.5 to 5.5 weight percent), the reduced level of scale spallation from the PMWY alloys allowed the benefit of the larger aluminum reservoir to be realized. The projected oxidation-limited lifetime at 1100°C for the PMWY alloys ranges up to 63 x 10^6 hr, compared to 92,300 to 2.4 x 10^6 hr for the commercial ODS-FeCrAl alloys.

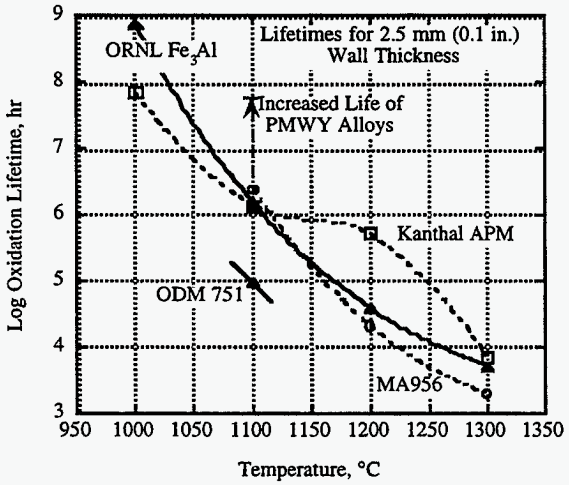

Fig. 12. Estimated oxidation-limited lifetimes for ODS alloys (2.5 mm wall thickness), with data for new ODS-Fe_3Al alloys indicated at 1100°C

SUMMARY AND CONCLUSIONS

The large, high aspect ratio grain structure desired in ODS alloys for good high-temperature creep strength has been achieved in yttria-strengthened Fe_3Al, with specimens exhibiting grains several centimeters long. The annealing treatment used to recrystallize the alloys also resulted in the formation of porosity in the alloy, which must be minimized in order to maximize the mechanical performance of the alloy. Initial creep tests at relatively high temperatures indicated good promise, but premature failure of the first specimens by a partially brittle mode prevented realization of the full potential of the grain structure. The cause of the brittle behavior is the subject of investigation, and was not obviously linked to pre-existing defects. The oxidation-limited lifetime at 1100°C in air for the alloys derived from commercially-processed alloy powder was significantly longer than for similar ORNL-processed alloys, due to a reduced tendency to scale spallation. The oxidation data for the ODS-Fe_3Al also suggest a longer life at 1100°C than competing commercial ODS-FeCrAl alloys.

REFERENCES

1. J. M. Klara,"HIPPS: beyond state-of-the-art, Part I," *Power Engineering*, 12, 37-39 (1993).

2. J. M. Klara, "HIPPS can compete with conventional PC systems: Part II," *Power Engineering*, 13, 20-23 (1994).

3. F. L. Robson, J. Ruby, and D. J. Seery, "Repowering with High-Performance Power Plant Systems (HIPPS)," Proc. Pittsburgh Coal Conf. (Sep. 1996), pp. 162-167.

4. Q. J. Mabbutt, The British Gas Closed Cycle Demonstrator-Final Year Report, British Gas Report (1995).

5. W. Lengauer, P. Ettmayer, D. Sporer, and G. Korbe, "Pore Formation in P/M Ferritic ODS Superalloys During High-Temperature Heat Treatment I. Considerations and Experimental Starting Points," Powder Metallurgy Intl., 22 (2), 19-22 (1990).

6. D. Sporer, W. Lengauer, P. Ettmayer, and G. Korbe, "Pore Formation in P/M Ferritic ODS Superalloys During High-Temperature Heat Treatment II. Thermodynamic Considerations and Conclusions," Powder Metallurgy Intl., 23 (3), 162-165 (1991).

7. B. Heine, R. Kirchheim, U. Stolz, and H. Fischmeister, "Studies on Pores Caused by Annealing ODS-Iron-Base Superalloys," Powder Metallurgy Intl., 24 (3), 158-163 (1992).

8. Q. J. Mabbutt, British Gas plc., private communication with I. G. Wright, 1996.

9. C. G. McKamey and P. J. Maziasz, "Effect of Heat Treatment Temperature on Creep-Rupture Properties of Fe_3Al-Based Alloys," Processing, Properties, and Applications of Iron Aluminides, Eds. J. H. Schneibel and M. A. Crimp, TMS, Warrendale, PA (1994), pp. 147-158.

10. M. Palm, and G. Indin, "Experimental Determination of Phase Equilibria in the Fe-Al-C System," Intermetallics, 3, 443-454 (1995).

11. I. G. Wright, B. A. Pint, E. K. Ohriner, and P. F. Tortorelli, "ODS Iron Aluminides," Proc. Tenth Ann. Conf. on Fossil Energy Materials, ORNL Report No. ORNL/FMP-96/1, CONF-9605167 (1996), pp. 359-371.(1996), pp. 359-371.

IRON-ALUMINIDE FILTERS FOR IGCCS AND PFBCS

P. F. Tortorelli, R. R. Judkins, I. G. Wright, and E. Lara-Curzio

INTRODUCTION

Hot-gas filtration is a key technological aspect of advanced coal-based power plants based on the Integrated Gasification Combined Cycle (IGCC) and pressurized fluidized bed combustors (PFBC). The use of filters to remove particles from hot gases produced by coal gasification or combustion is vital to achieving the economic and efficiency goals of these systems as they protect the gas turbine and other downstream components from degradation by erosion and erosion/corrosion. Consequently, reliability and durability of the hot-gas filtering devices is of special importance.

Materials used in hot-gas filters are required to withstand prolonged exposure to potentially corrosive, high-temperature gaseous environments as well as to condensable vapors and solid species, some of which may have the potential for localized interaction with the filter material after extended times. The gas streams may be oxidizing (PFBCs) or reducing, in which the sulfur species are largely in the form of H_2S (in the case of the product gas from IGCC processes or from carbonizers). Degradation of metallic filter elements has been observed as an environmental effect under oxidation, sulfidation, and/or carburization conditions and acts as a driving force for the development of ceramic hot-gas filters, particularly for the higher temperatures associated with advanced gasification and combustion designs. However, iron aluminides can also be considered for such applications because of their good to exceptional high-temperature corrosion resistance in a variety of sulfur-bearing environments relevant to coal-derived energy production systems.[1-11] In most cases, the results from these laboratory studies have been directly compared to austenitic stainless steels (particularly type 310). With respect to such alloys, iron aluminides with greater than about 20 at.% Al show exceptional corrosion resistance in coal-gasification environments (high p_{S_2}, low p_{O_2}), and sulfur present as H_2S).[1,4-6,8] While the relative differences in corrosion resistance between these iron aluminides and stainless steels are not as pronounced as in the gasification environment, Fe_3Al and its alloy modifications also show better corrosion behavior under many coal-combustion-gas conditions (high p_{O_2}, low p_{S_2}, and sulfur as SO_2)[2,4,5,8] and in the presence of $CaSO_4$ and circulating-PFBC-type ash deposits[4] up to at least 900°C. Therefore, because of their good to exceptional high-temperature corrosion resistance in such environments, Fe_3Al-based alloys may offer distinct temperature and reliability advantages as materials of construction for hot-gas filters used in advanced coal plants. The potential of using iron aluminides in this way is being

examined through studies in which Fe_3Al-based filter materials are exposed under environmental conditions appropriate to IGCCs and PFBCs.

DISCUSSION OF CURRENT ACTIVITIES

This work is structured to examine the corrosion behavior and associated environmental effects on properties relevant to the use of iron-aluminide hot-gas filters for advanced IGCC and PFBC systems. It consists of laboratory exposure and metallurgical and mechanical evaluation of dense and porous iron aluminides in mixed gases, both with and without the presence of ash and a collaborative effort with Pall Corporation, Cortland, New York, in the areas of alloy specification, thermochemical calculations, and specialized corrosion analyses. The work complements previous or ongoing research and development associated with the corrosion of iron aluminides in oxidizing/sulfidizing environments related to coal-based energy production (see, for example, refs. 6-9, 11, 12). It takes advantage of experience in iron-aluminide alloy development, materials processing, and corrosion testing in appropriate fossil environments at Oak Ridge National Laboratory and involves the expertise of Pall Corporation in producing porous iron aluminides and evaluation of filter performance.

Laboratory/Test Bed Evaluations

Dense and porous forms of iron aluminides are exposed in controlled laboratory environments containing either H_2S-H_2-H_2O or SO_2 and in test beds used to simulate subsystems of advanced coal plants. To date, the laboratory part of the project has focused on selected exposures of dense iron aluminides and development of a capability to conduct post-exposure evaluation of the strength of rings cut from as-fabricated or exposed cylinders. Ultimately, comparison of results for dense and porous materials will allow evaluation of any effects on corrosion behavior associated with differences in processing and the determination of whether previously generated data for cast and powder-processed iron aluminides can be used to guide material selection for the present hot-gas filter applications. Recently, selected Fe_3Al alloys were exposed to an air-1% SO_2 environment at 650, 750, and 900°C. It was expected from previous work in high-temperature air and SO_2-containing environments[2,6-8] that these alloys should show good resistance under these conditions, but a few additional exposures were deemed necessary to serve as a baseline for subsequent evaluation of porous iron aluminides and for strength determination of rings exposed to the same environment. (Some assessment of

the reaction kinetics of porous Fe_3Al in the mixed gas gasification-type environment has been done previously.[13])

It is important to evaluate the basic reaction product growth rate of potential filter media. Hot-gas filter applications place a fairly strict limit on the thickness of scale that can form on a material of construction before functional performance is adversely affected. This is of particular concern for the higher temperature operation of second-generation PFBCs. Dense specimens of FAS (Fe-28Al-2Cr, at.%) or FAL (Fe-28% Al-5% Cr-0.1% Zr-0.05% B) were exposed to a simulated combustion gas (air - 1% SO_2) at 650, 750, 900, or 950°C in a microbalance. As illustrated by the data shown in Fig. 1, dense iron aluminides displayed fairly low rates of reaction in this environment. These initial experiments confirmed the expected good resistance of these alloys to a gas containing SO_2; only thin products, with correspondingly small weight gains, were observed after these exposures. The Fe_3Al alloy with 2% Cr appeared to have slightly better resistance than the one with 5% Cr. The reaction rates of FAS and FAL in IGCC and PFBC-type environments at several temperatures so as to establish the ability to predict scale thickness at extended exposure times. In addition to the laboratory exposures, some Fe_3Al alloys have been supplied for exposure in the Transport Reactor Development Unit at the Energy and Environmental Research Center at the University of North Dakota to evaluate corrosion of iron aluminides under more prototypic filter conditions. Specimens from a previous exposure await metallographic analysis, while a second set should have recently completed a 200-h run under conditions similar to those relevant to the Wilsonville filter test facility or the Pinon Pine gasifier (air-blown gas composition, 550°C).

In addition to traditional corrosion characterization (gravimetric and microstructural analyses), the effects of these exposures on basic mechanical properties are being determined. In service, filters will be typically subjected to constant internal/external pressure, combined with periodic pulsing for cleaning purposes. Therefore, the mechanical performance of filters will be determined by the ability of the cylindrical component to withstand pressure (hoop strength) or, equivalently, by the tensile strength of the material. Consequently, appropriate methods to mechanically test tubular specimens of control and exposed alloys are being assessed so as to better characterize high-temperature environmental effects in terms of applicability to hot-gas filter components.

Several test techniques have been developed and used to evaluate the mechanical properties of cylindrical components and short sections of such. These test techniques include the internal pressurization of tubes[14] and the tensile and compressive loading of O- and C-rings. To determine the ability of cylindrical components to withstand pressure, internal pressurization techniques are preferred over the tensile or compressive evaluation of C- or O-

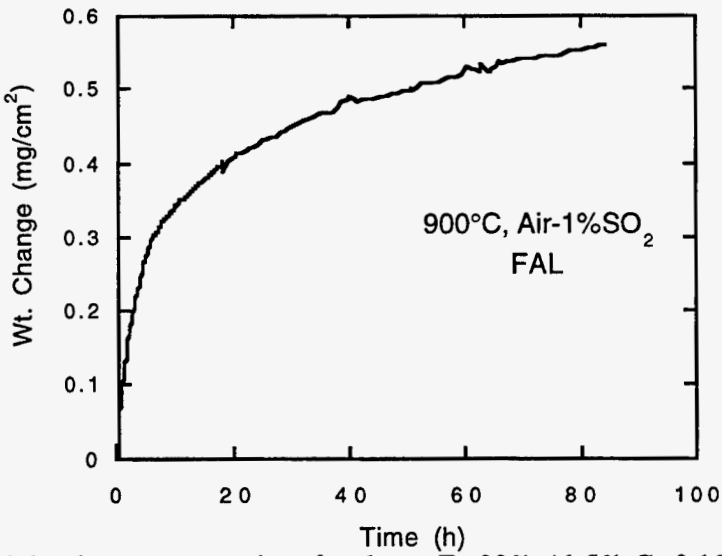

Fig. 1. Weight change versus time for dense Fe-28% Al-5% Cr-0.1% Zr-0.05% B (FAL) exposed to air-1% SO_2 at 900°C.

rings because the latter do not produce uniform loading conditions. Furthermore, by subjecting a larger volume of the specimen to the peak stress, internal pressurization techniques make a more efficient use of the material.

For the internal pressurization of cylindrical components, different media have been used to transfer the pressure to the walls of the specimen. These include gases, rubber bladders and inserts, and even molten glass for tests at high temperatures.[15] The axial compression of rubber inserts to induce a uniform pressure in cylindrical components has been successfully used for tests at ambient temperatures, and offers cost and safety advantages over the use of gases. However, this test technique is obviously limited to low temperatures. The use of gases and molten glass to conduct internal pressurization tests at elevated temperatures pose technical difficulties due to the potential reaction between the glass and the specimen and to assuring leak-free operation. Consequently, an alternative approach is being developed to measure the mechanical properties of sections of cylindrical filters at room and elevated temperatures. This technique consists in the internal pressurization of the cylindrical specimen using a mechanical wedge mechanism. A schematic of the test piece used in such an approach is shown in Fig. 2. A prototype has been fabricated and will be used for initial testing at room and elevated temperatures. The application of this experimental technique for the determination of the hoop strength of O-rings will be complemented by numerical analysis to account for frictional dissipation associated with the sliding of the wedges and by calibration tests using standard elastic materials instrumented for strain measurements.

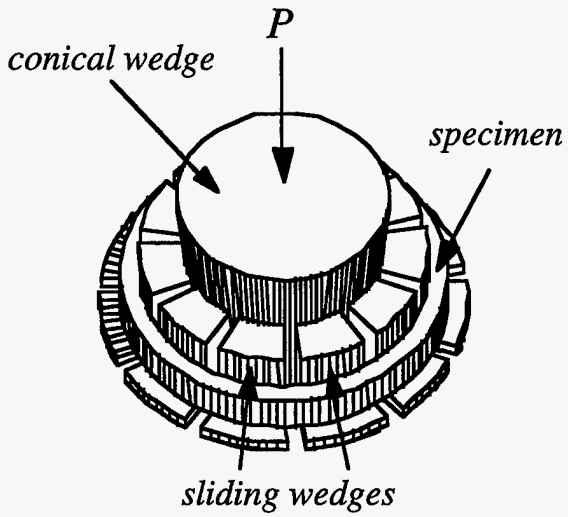

Fig. 2. Schematic of test piece utilizing a mechanical wedge mechanism for the internal pressurization of O-ring filter elements..

Evaluation of Pall Filter Materials

This part of the project is designed to directly support Pall Corporation's development of iron-aluminide hot-gas filters for high-temperature fossil energy systems and, in so doing, to relate the results for the laboratory/test evaluation task and collateral iron-aluminide work to that production effort. It includes analyses of porous media exposed by Pall at its test facility or elsewhere, thermochemical calculations to evaluate the most appropriate test environments for filter evaluation, and various interactions related to technical knowledge gained from ORNL's extensive research and technology efforts with iron aluminides and related materials and Pall's manufacturing and systems expertise related to filters.

To date, only a few porous media specimens have been received from Pall for analysis. These included iron-aluminides Hastelloy X, and type 310 stainless steel filter materials (in the form of partial O-rings). Several pieces (while parts of larger specimens) had been exposed at the Dakota Gas facility and subsequently evaluated at Pall, while control (unexposed) specimens were also provided. Parts of each were cut, mounted, and polished for metallographic examination. Comparison of the control and exposed specimens revealed little, if any, evidence of significant corrosion of any of the materials.

Thermochemical equilibria issues associated with corrosion in gases containing N_2, O_2, H_2O, CO, CO_2, and CH_4 typical of gasifiers have been addressed with respect to typical or targeted exposure conditions for testing of iron-aluminide filter elements. Results of thermochemical calculations and prior experience with iron aluminides were used to prepare

input on test conditions and alloy selection for the prototypic filter tests conducted by Pall Corporation. One aspect of this work involved thermochemical calculations (based on SOLGASMIX[16]) of the equilibrium gas compositions of representative air- and oxygen-blown synthesis gases at both actual gasifier pressures and that of the filter tests (1 atm). The results were used to determine the most appropriate 1-atm environment by adjusting the specification of the composition of the gas mixture for the laboratory exposures at Pall so as to obtain the closest possible agreement between the sulfur and oxygen partial pressures of the operating gasifiers and those used in the filter element test facility.[17]

ACKNOWLEDGMENTS

The authors thank M. Howell for experimental support. This research was sponsored by the U S. Department of Energy, Office of Fossil Energy, through the Advanced Research and Technology Development (AR&TD) Materials Program and the Federal Energy Technology Center (Morgantown) under contract DE-AC05-96OR22464 with Lockheed Martin Energy Research Corporation.

REFERENCES

1. J. H. DeVan, pp. 107-115 in *Oxidation of High-Temperature Intermetallics*, T. Grobstein and J. Doychak (eds.), TMS, 1989.

2. W. H. Lee and R. Y. Lin, "Molten Salt-Induced Hot Corrosion of Iron Aluminides," pp. 475-86 in *Proc. Fourth Annual Conf. Fossil Energy Materials*, R. R. Judkins and D. N. Braski (comp.), ORNL/FMP-90/1, U. S. Department of Energy, August 1990.

3. S. Van Wheele and J. L. Blough, Foster Wheeler Development Corporation report, ORNL/Sub/89-SA187/02, August 1991.

4. K. Natesan, "Corrosion Resistance of Iron Aluminides," pp. 271-82 in *Proc. Sixth Annual Conf. Fossil Energy Materials*, N. C. Cole and R. R. Judkins (comp.), U. S. Department of Energy, July 1992.

5. K. Natesan, "Corrosion Performance of Materials in Coal-Combustion Environments," pp. 353-62 in *Proc. Seventh Annual Conf. Fossil Energy Materials*, N. C. Cole and R. R. Judkins (comp.), U. S. Department of Energy, July 1993.

6. J. H. DeVan and P. F. Tortorelli, "Oxidation/Sulfidation of Iron-Aluminum Alloys," *Mater. at High Temp.* 11 (1993) 30-35.

7. K. Natesan and W. D. Cho, "High Temperature Corrosion of Iron Aluminides," pp. 227-37 in *Proc. Eighth Annual Conf. Fossil Energy Materials*, N. C. Cole and R. R. Judkins (comp.), CONF-9405143, U. S. Department of Energy, August 1994.

8. K. Natesan and R. N. Johnson, "Corrosion Performance of Fe-Cr-Al and Fe Aluminide alloys in Complex Gas Environments," pp. 591-99 in Heat-Resistant Materials II, K. Natesan, P. Ganesan, and G. Lai (eds.), ASM International, August 1995.

9. P. F. Tortorelli et al., "High-Temperature Corrosion Behavior of Iron-Aluminide Alloys and Coatings," pp. 289 - 300 in *Proc. Ninth Annual Conf. Fossil Energy Materials*, N. C. Cole and R. R. Judkins (comp.), U. S. Department of Energy, August 1995.

10. S. R. J. Saunders et al., "Behaviour of Fecralloy and Iron-Aluminide Alloys in Coal Gasification Atmospheres Containing HCl," accepted for publication in *Mater. Sci. Forum,* 1996.

11. J. L. Blough and G. J. Stanko, "Fireside Corrosion Testing of Candidate Superheater Tube Alloys, Coatings, and Claddings - Phase II," to be published in *Proc. Tenth Annual Conf. Fossil Energy Materials*, N. C. Cole and R. R. Judkins (comp.), U. S. Department of Energy, 1996.

12. P. F. Tortorelli, B. A. Pint, and I. G. Wright, "High-Temperature Corrosion Behavior of Coatings and ODS Alloys Based on Fe_3Al," pp. 393-403 in *Proc. Tenth Annual Conf. Fossil Energy Materials*, N. C. Cole and R. R. Judkins (comp.), U. S. Department of Energy, August 1996.

13. J. H. DeVan, Oak Ridge National Laboratory, unpublished results, 1992, 1993.

14. D. L. Shelleman, O. M. Jadaan, J. C. Conway, and J. J. Mecholsky, "Prediction of Strength of Ceramic Tubular Components: Part II -Experimental Verification," J. Testing and Evaluation 19 (1991) 192-200.

15. L. Chuck and G. A. Graves, "Hoop Tensile Strength and Fracture Behavior of Continuous Fiber Ceramic Composite Tubes from Ambient to Elevated Temperatures" *Proc. Symposium on Thermal and Mechanical Test Methods and Behavior of Ceramic Composites,* Cocoa Beach Florida, 1996.

16. T. M. Besmann, "SOLGASMIX-PV, A Computer Program to Calculate Equilibrium relationship in Complex Chemical Systems," ORNL/TM-5775, Oak Ridge National Laboratory, April 1977.

17. J. L. Hurley and M. R. June, "Advanced Hot Gas Filter Development Topical Report, May 1995 - December 1996", Pall Corporation, to be published.

MO-SI ALLOY DEVELOPMENT

J. H. Schneibel, C. T. Liu, L. Heatherly, J. L. Wright, and C. A. Carmichael

INTRODUCTION

The objective of this task is to develop new-generation corrosion-resistant Mo-Si alloys for use as hot components in advanced fossil energy combustion and conversion systems. The successful development of Mo-Si alloys is expected to improve the thermal efficiency and performance of fossil energy conversion systems through an increased operating temperature, and to increase the service life of hot components exposed to corrosive environments at temperatures as high as 1600°C. While $MoSi_2$ is highly oxidation resistant at elevated temperatures, it is extremely brittle at ambient temperatures. Molybdenum compounds with lower Si contents, such as Mo_5Si_3, which are potentially less brittle, do however not have the required oxidation resistance. As will be seen, boron additions are the answer to this problem.

As early as 1957, Nowotny et al.[1] pointed out that boron-containing silicides possess high oxidation resistance due to the formation of borosilicate glasses. Based on Nowotny et al's work, boron-containing molybdenum silicides based on Mo_5Si_3 were recently developed at Ames Laboratory[2-4]. These silicides consist of approximately 50 vol.% Mo_5Si_3 (T1), 25 vol.% Mo_5SiB_2 (T2), and 25 vol.% of Mo_3Si. They provide an exciting alternative to $MoSi_2$ for several reasons. First, they possess an oxidation resistance comparable to that of $MoSi_2$. Second, these three-phase materials may possess a higher fracture resistance than other high-temperature materials such as $MoSi_2$. Third, their creep strength is superior to that of $MoSi_2$.

At present, the mechanical properties of the new Mo-Si-B alloys have not been fully explored. One reason for this is simply the unavailability of sufficiently large test pieces. Due to the high processing temperatures and the high reactivity of Si, processing of Mo-Si-B alloys is a challenging task. Significant developmental work is therefore needed to produce sound Mo-Si-B material with controlled microstructures, the size of which is at the same time sufficiently large (e.g., 50 mm) to characterize the mechanical properties. An interaction between processing, microstructural characterization, and mechanical property measurements is required in order to improve and optimize this new class of materials.

RESULTS AND DISCUSSION

Processing via powder metallurgy

The previous annual report for this program focused on powdermetallurgical (PM) processing. Some additional microstructural, mechanical property, and compositional work is reported here. Based on the composition Mo-10.5 Si-1.1 B (wt%), five PM alloys (see also Table I) were produced by hot-pressing. In several cases, carbon was added to reduce the oxygen content. For the same reason, additions of Zr were made. The difference between the two approaches is that Zr removes oxygen in the form of internal oxides, while carbon additions remove oxygen in the form of gaseous CO/CO_2. Zirconium additions resulted in internal cracking, due to the formation of ZrO_2 particles and the associated thermal expansion mismatch. The Zr-containing alloys were therefore not further investigated.

Figure 1 illustrates the microstructure of a polished and etched specimen of alloy MSB1, which contained 0.2 wt% C as deoxidizer. The scanning electron microscope (SEM) image in Fig. 1 shows no microcracks, although a more detailed examination of the specimen from which this micrograph was obtained, revealed occasional microcracks. Numerous pores are seen at the grain and interphase boundaries. Their quasi-equilibrium shape suggests that they may have been stabilized by trapped CO/CO_2. The T2 phase (Mo_5SiB_2) etches readily and is therefore easily recognized. The different phases were identified via energy dispersive spectroscopy (EDS) in the SEM. Since B was difficult to detect, identification was performed on the basis of the Si to Mo ratio. Occasionally Mo-rich particles were found. These are either elemental Mo or borides of Mo. The fact that the three-phase Mo_3Si-T1-T2 equilibrium expected from the nominal composition[1] has not been reached, is consistent with recent results by Perepezko et al.[5] These authors found that annealing of similar alloys for 150 h at 1600°C did not establish complete equilibrium. Since the hot-pressing in this work was carried out at 1600°C, it is not surprising that full equilibrium was not reached.

The oxygen contents of several PM as well as cast Mo-Si-B materials are summarized in Table I. Several points are worth noting. First, the alloy MSB1, which was fabricated from $MoSi_2$ powder and addition of elemental powders, has by far the highest oxygen content. Second, as the carbon content is increased from 0.6 wt% (MSB2) to 1.0 wt% (MSB5), the oxygen content tends to decrease. This indicates that the carbon was indeed effective in deoxidizing the alloys. Third, as expected, the cast materials (MSB418 and MSB424) have much lower oxygen contents than the PM materials.

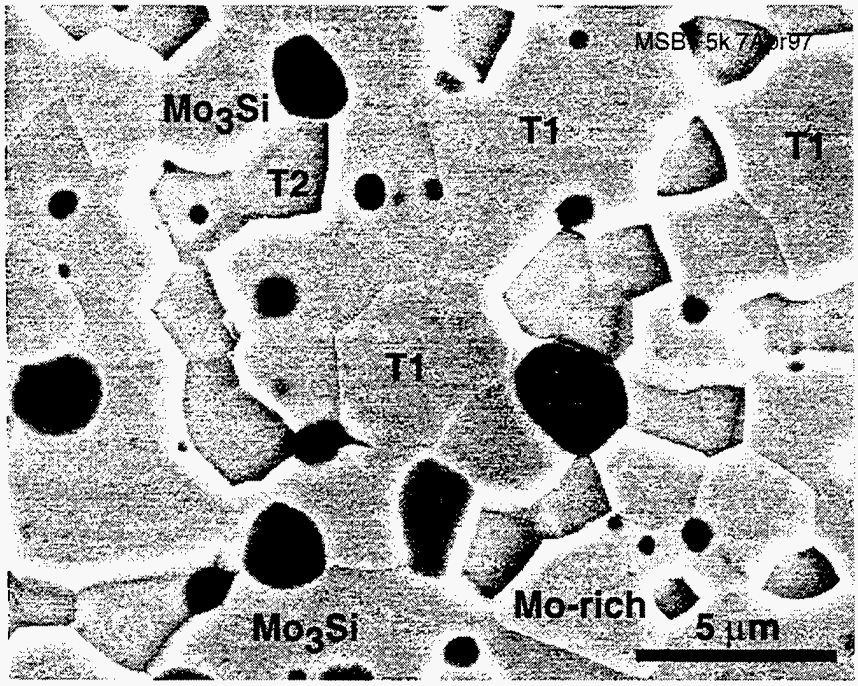

Fig. 1. SEM micrograph of alloy MSB1 (Mo-10.5 Si-1.1 B-0.2 C, wt%), after polishing and etching (Murakami's etch). The T2 phase is preferentially etched. In addition to Mo_3Si and Mo_5Si_3 (T2), a Mo-rich phase is found, which is either unreacted Mo or a boride of Mo.

Table I

Compositions and oxygen contents of Mo-Si-B alloys processed by powder metallurgy (PM) and hot pressing (HP) or by ingot metallurgy (IM). The oxygen contents are courtesy M. J. Kramer, Ames Laboratory, Ames, Iowa)

Sample ID	Processing	Composition, wt%	Oxygen, wppm
MSB1	PM/HP	Mo - 10.5 Si - 1.1 B - 0.2 C	7482
MSB2, analysis #1	PM/HP	Mo - 10.41 Si - 1.09 B - 0.60 C - 0.20 Zr	3195
MSB2, analysis #2	PM/HP	"	2275
MSB5	PM/HP	Mo - 10.4 Si - 1.1 B - 1.0 C	1938
MSB418 (center region)	IM	Mo - 10.5 Si - 1.1 B	486
MSB418 (near surface)	IM	"	222
MSB424	IM	"	217

Processing via ingot metallurgy

Alloys with the composition Mo-10.5 Si-1.1 B, wt%, were drop-cast into molds made from materials with different thermal conductivities in order to examine the effect of the cooling rate on the microstructures developing during solidification and cool-down. Casting into a 25 mm diam. Cu mold produced ingots which appeared to be uncracked as judged by visual examination of their outside. However, sectioning and polishing of these ingots always revealed macroscopic cracking. The microstructure of a cast and annealed specimen is shown in Fig. 2. Voids were not detected, but microcracks were occasionally observed.

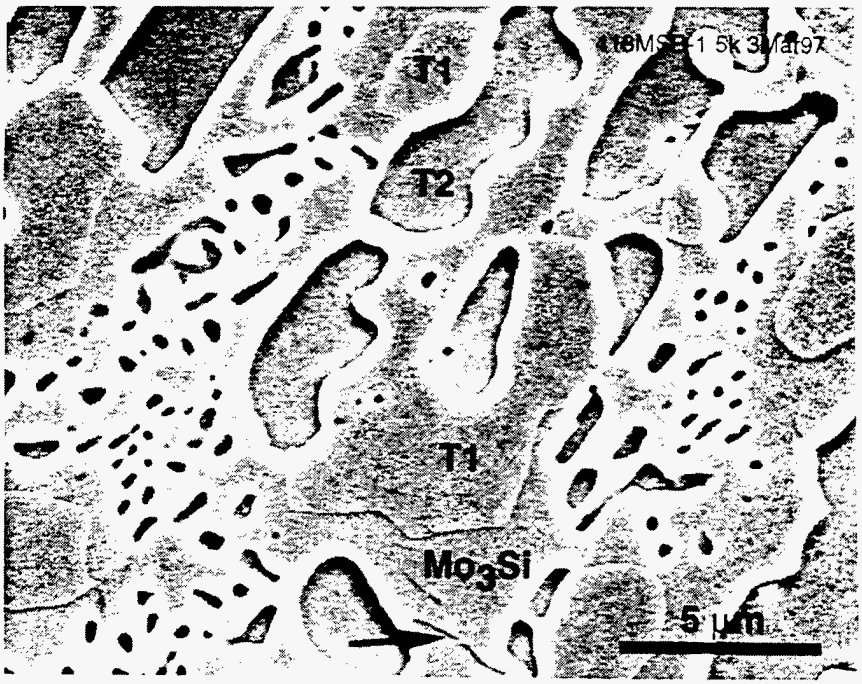

Fig. 2. SEM micrograph of polished and etched section of Mo-10.5 Si-1.1 B cast into a 25 mm diam. Cu mold and annealed for 24 h at 1400°C in vacuum (MSB418). The three phases expected according to the phase diagram[1] are all seen. The T2 phase is preferentially attacked by Murakami's etch. The absence of significant porosity is noted. A microcrack is indicated by an arrow.

Casting Mo - 10.5 Si - 1.1 B into a 25 mm diam. SiO_2 (sand) mold resulted in much lower cooling rates and eliminated macroscopic cracking. An approximately 1 mm thick reaction zone was observed on the outside of the ingot. A typical microstructure is

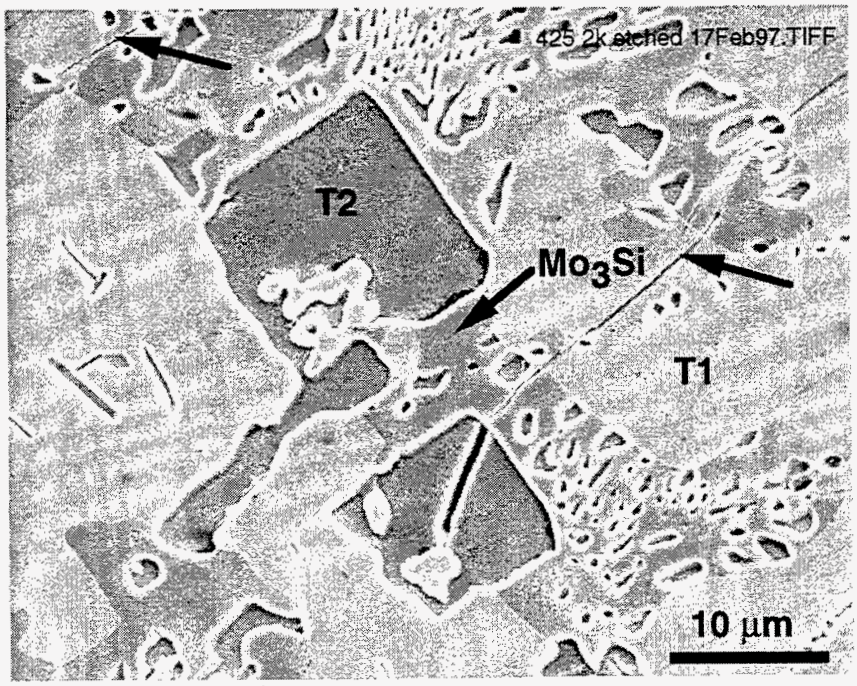

Fig. 3. SEM micrograph of polished and etched section of Mo-10.5 Si-1.1 B cast into a 25 mm diam. sand mold (MSB425). Several microcracks are indicated by arrows.

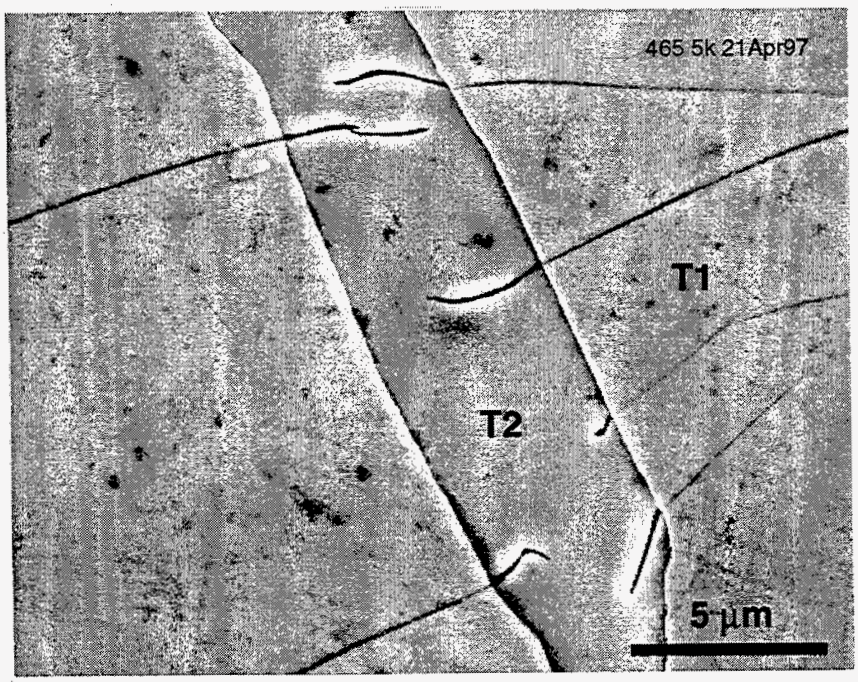

Fig. 4. SEM micrograph of polished and etched section of Mo-10.5 Si-1.1 B cast into a 25 mm diam. Al_2O_3/SiO_2 mold (MSB465).

illustrated in Fig. 3. As compared to Fig. 2, more microcracking is seen. Although a quantitative analysis has not been carried out, it appears that the lower cooling rate enhances microcracking. Since Mo_5Si_3 exhibits anisotropic thermal expansion, slower cooling and the associated larger grain/phase sizes are likely to enhance microcracking.

Casting Mo - 10.5 Si - 1.1 B into a 25 mm diam. porous Al_2O_3/SiO_2 mold resulted in the slowest cooling rate. Solidification occurred so slowly, that the melt reacted extensively with the mold. After cool-down, the casting had a diameter of approximately 50 mm, instead of the initial mold diameter of 25 mm. No macrocracks were observed. As verified by qualitative EDS analysis, this alloy picked up significant amounts of oxygen. Figure 4 illustrates the microcracks found in this material. Interestingly, the microcracks stop often in the T2 phase. Again, the presence of numerous microcracks demonstrates that slow cooling rates, while alleviating macrocracking, enhance microcracking.

Isothermal forging

An attempt was made to isothermally forge a cylindrical section of an alloy cast into a sand mold (MSB425). This experiment was carried out in a hot-pressing unit. An initial pressure of 35 MPa was applied. Consistent with the excellent high temperature strength of these materials no deformation occurred at temperatures up to 1800°C. At 1850°C, the specimen deformed by approximately 50% in 15 minutes . The external appearance of the deformed specimen suggested that the material was partially liquid during deformation. Microstructural analysis showed that some voids and cracks had formed during the processing. Since the material was partially liquid, this is not surprising.

Extrusion

A casting with the composition Mo - 10.5 Si - 1.1 B (MSB418) was encapsulated in an evacuated Mo can and extruded at 1800°C. The extrusion exhibited severe cracking and porosity and only small pieces were available for metallographic examination. Figure 5 shows an SEM of the extruded materials. According to EDS analysis, the microstructure consists of particles of Mo_3Si in a multiphase matrix. X-ray analysis will be needed to substantiate this surprising result. The multiphase matrix found between the Mo_3Si particles is depicted in Fig. 6. Due to the small scale, a reliable EDS analysis was not possible. However, it appears that the multiphase regions consist of the T2 phase, Mo_3Si, and either Mo or Mo boride. Encouragingly, the extrusion resulted locally in a very fine structure.

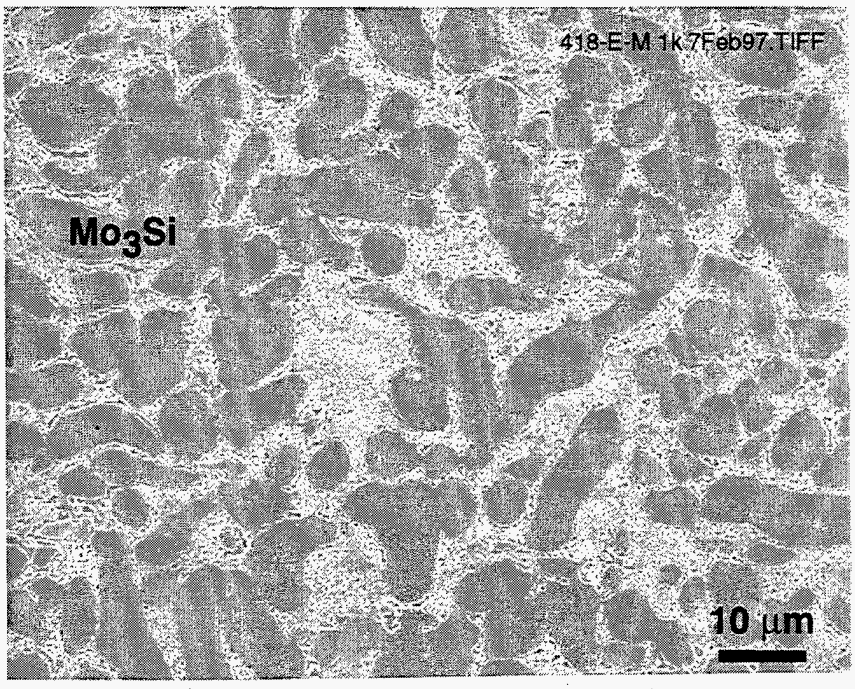

Fig. 5. SEM micrograph of a polished/etched section of extruded Mo-Si-B (MSB418-E).

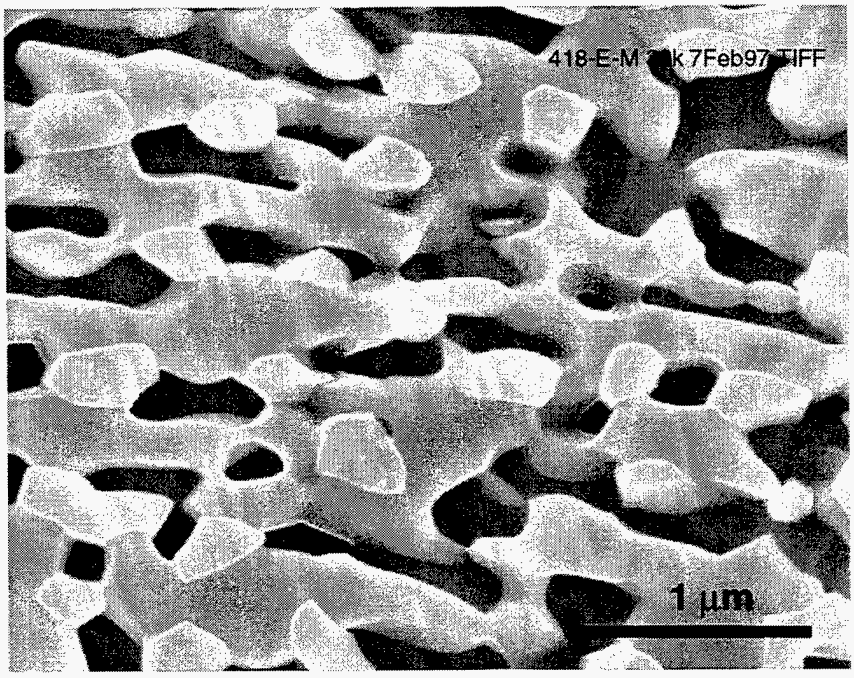

Fig. 6. High magnification SEM micrograph of matrix region of polished and etched section of extruded Mo-Si-B (MSB418-E).

Mechanical properties

In a previous report, the room temperature tensile strength of the PM alloy MSB1 was determined to be 186 MPa. Since the silicides investigated in this work are flaw-sensitive, it was decided to carry out a larger number of flexure tests in order to obtain statistical information. The results are represented in the Weibull plot in Fig. 7 and indicate, that flexure strengths of up to 300 MPa may be obtained. Since this particular material contained porosity (see Fig. 1) as well as substantial concentrations of oxygen (Table I), significantly better properties are expected for optimized processing.

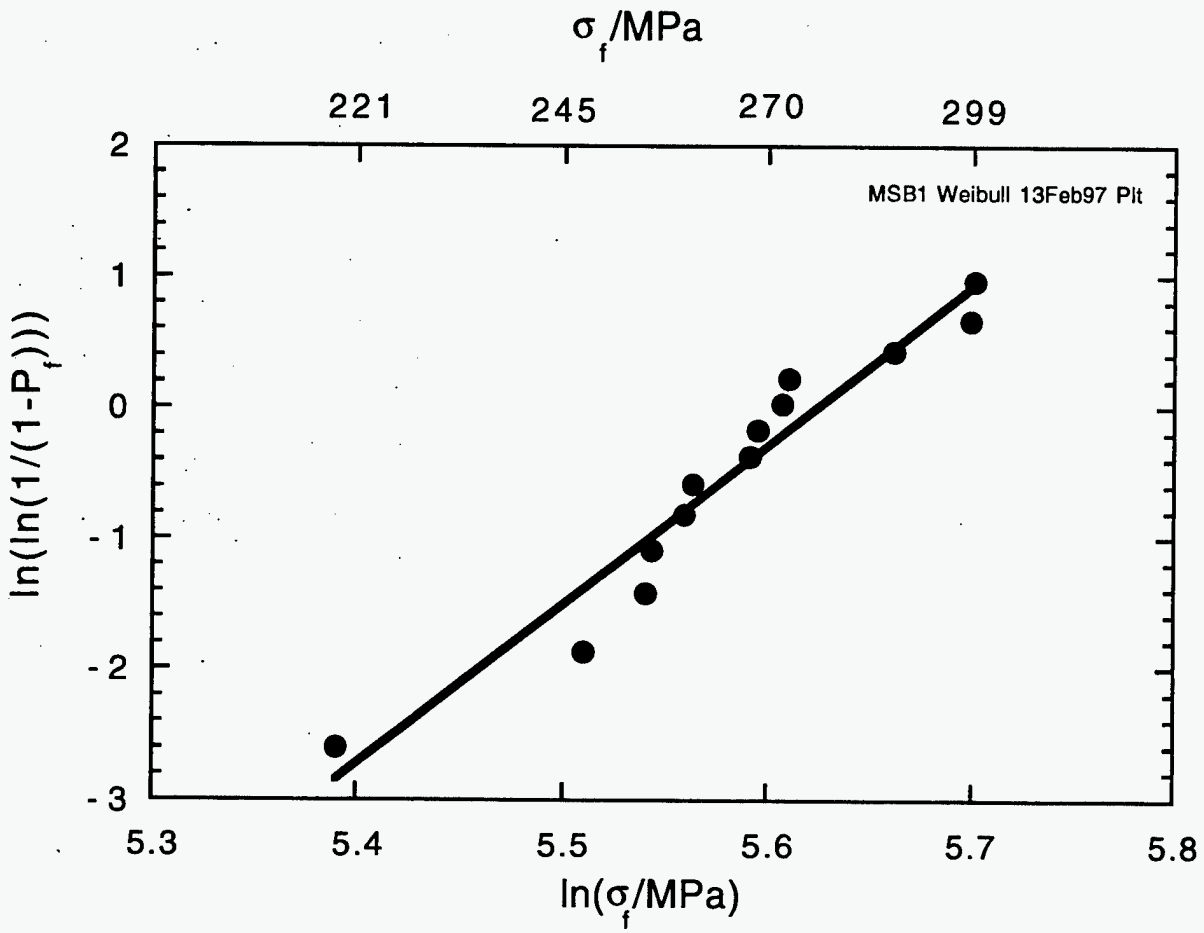

Fig. 7. Weibull Plot of the 3-point flexure strength of MBS1 (Mo - 10.5 Si - 1.1 B - 0.2 C, wt%). P_f is the fracture probability, and σ_f the maximum outer fiber stress.

Whereas the PM processed silicides contain no or few microcracks, the cast silicides do. The cast materials are therefore expected to have lower room temperature strengths than the powdermetallurgical ones. Table II shows this to be the case. Consistent with the observation of microcracks, isothermal forging at 1850°C did not improve the room temperature strength. At elevated temperatures, the microcracks may not be as detrimental to the strength than at room temperature. This could be caused by crack healing, crack blunting, as well as borosilicate glass formation at crack tips. Consistent with this, the 1200°C flexure strengths determined in air are much higher than those at room temperature, as demonstrated by the data in Table II. This result points out the continuing importance of optimizing the processing of these materials in order to achieve satisfactory mechanical properties. In the case of the IM materials, secondary processing is definitely required in order to minimize the size and number density of microcracks. Efforts are underway to improve the secondary processing.

Table II

Three-point flexure strengths of ingot metallurgy Mo-10.5 Si-1.1 B (wt%)

Specimen Number	Specimen Condition	Test Temperature, ℃	Fracture Strength, MPa
MSB425-1	as-cast	20	119
MSB425-2	as-cast	20	105
MSB425-3	as-cast	20	114
MSB425-H-1	isothermal forging at 1850°C	20	95
MSB425-H-2	isothermal forging at 1850°C	20	110
MSB425-4	as-cast	1200	221
MSB425-5	as-cast	1200	283

SUMMARY AND CONCLUSIONS

Molybdenum-silicon-boron intermetallics with the composition Mo-10.5 Si-1.1 B (wt%) have been fabricated by several processing techniques. Powder processing resulted in macrocrack-free material containing no or few microcracks. PM materials exhibited reasonably high room temperature strengths. However, they contained quasi-equilibrium

pores, and large concentrations of oxygen. Ingot metallurgy (IM) materials showed much lower oxygen concentrations. Depending on the cooling rate during solidification, they developed either primarily macrocracks or primarily microcracks. Due to the microcracks, the room temperature flexure strengths were low. However, the flexure strengths at 1200°C were up to 3 times higher than those at room temperature. This is attributed to crack healing. The IM materials require secondary processing to develop their full potential. Preliminary examinations of the secondary processing behavior include isothermal forging and hot extrusion, and further work is in progress to improve the secondary processing.

REFERENCES

(1) H. Nowotny, E. Kimakopoulou, and H. Kudielka, "Untersuchungen in den Dreistoffsystemen: Molybdän-Silizium-Bor, Wolfram-Silizium-Bor und in dem System: VSi_2-$TaSi_2$," Mh. Chem. 88 (1957) 180

(2) A. J. Thom, M. K. Meyer, Y. Kim, and M. Akinc, "Evaluation of $A_5Si_3Z_x$ Intermetallics for Use as High Temperature Structural Materials," in "Processing and Fabrication of Advanced Materials III, V. A. Ravi et al., eds., TMS, 1994, p. 413.

(3) M. K. Meyer, M. J. Kramer, and M. Akinca [sic], "Compressive Creep Behavior of Mo_5Si_3 with the Addition of Boron," Intermetallics 4 (1996) 273.

(4) M. Meyer, M. Kramer, and M. Akinc, "Boron-Doped Molybdenum Silicides," Adv. Mater. 8 (1996) 85.

(5) J. H. Perepezko, C. A. Nuñes, S.-H. Yi, and D. J. Thoma, "Phase Stability in Processing of High Temperature Intermetallic Alloys," in press, MRS Symposium Proceedings Vol. 460, C. C. Koch et al., eds.

MATERIALS SUPPORT FOR HITAF

K. Breder, R. J. Parten, and H. T. Lin

INTRODUCTION

The purpose of this project is to compare structural ceramic materials proposed for use in the air heater of a coal fired high temperature advanced furnace (HITAF) for power generation. Two teams were funded by Pittsburgh Energy Technology Center (PETC) under the Combustion 2000, Phase 1, program to develop such a system. One team is led by the United Technologies Research Center, and the other team is led by Foster Wheeler Development Corporation. These two teams have now entered Phase 2 and 3 of the Combustion 2000. Phase 2 is engineering development and testing, consisting of subsystem and materials testing, and Phase 3 consists of the detailed design, construction, operation and evaluation of a prototype plant. Phase 1 of the work performed here consisted of evaluation of the mechanical properties of three structural ceramics at high temperatures in air and a preliminary evaluation of mechanical properties of these structural ceramics after exposure to coal ash. This work is completed and the results will serve as baseline data for further work.[1] In Phase 2 of the present work an initial screening of candidate structural ceramics with respect to their creep properties in air at selected temperatures will be performed, and temperatures above which creep may become a design problem will be identified. Tubes and tube sections of the candidate ceramics will then be exposed to a combination of mechanical loads, coal ash exposure and high temperature; and corrosion behavior, mechanisms, and post exposure mechanical properties will be evaluated.

DISCUSSION OF CURRENT ACTIVITIES

Experimental Procedure

Tube specimens for the coal ash exposure test are: NT230 Si-SiC (Saint-Gobain/Norton), SiC_p/Al_2O_3 (Dupont Lanxide Composites Inc.), Sintered α-SiC (Carborundum Co.), and Sintered β-SiC (Coors Ceramics Co.). Previously, flexural creep experiments for the Si-SiC and the SiC_p/Al_2O_3 were reported. In this reporting period tensile creep testing of the SiC_p/Al_2O_3 has been performed. A block of material was obtained from Dupont Lanxide Composites Inc. and machined into tensile specimens that were subsequently loaded via a pin in hole arrangement. Before testing the specimens were surface treated by Dupont Lanxide Composites Inc. in the same manner as the test tubes. A few long time tensile tests at 1260°C have been completed and further testing is ongoing.

The slags for these experiments were gathered from the taps of three cyclone-fired utility boilers. Two types of Illinois #6 bituminous coals have been used; one from coal burned at the Central Illinois Public Service Coffeen Plant (Labeled Coffeen) produced from a low sulfur producing mine. The low sulfur (in the form of low FeS_2 content) leads to high viscosity of the slag, so therefore 1.5% limestone was added at the power plant to reduce the viscosity. The second Illinois #6 was from the Illinois Power Company Baldwin Plant (Labeled Baldwin) and was a mixture of Illinois #6 and Illinois #5, resulting in a typical slag with less Ca and more Fe than the batch from the Coffeen plant. The third slag was collected from the Northern States Power Riverside Plant and was a sub-bituminous coal slag from a Powder River Basin coal produced from the Rochelle mine in Wyoming (labeled Rochelle). This slag was the least viscous and most basic of the three slags. The slags were analyzed at the University of North Dakota Energy and Environmental Research Center (UNDEERC) and was split from the main barrel according to ASTM D 2013 "Standard Method of Preparing Coal Samples for Analysis." The chemical compositions of the three coal ashes are given in Table 1.[2]

Table 1. Chemical composition of the coal ashes.

Oxide, wt%	Baldwin	Coffeen	Rochelle
SiO_2	53.4	52.5	47.0
Al_2O_3	18.6	16.3	18.6
Fe_2O_3	17.6	13.5	5.3
TiO_2	0.7	0.7	1.4
P_2O_5	0.0	0.2	0.6
CaO	7.1	13.1	19.7
MgO	0.9	1.2	5.7
Na_2O	0.0	0.8	0.9
K_2O	1.7	1.6	0.4
SO_3	0.0	0.1	0.4
Basic Oxides/ Acidic Oxides	0.38	0.43	0.48

The test temperatures were 1090°C to produce a condition of sintered slag, 1260°C for a viscous molten slag, and 1430°C for a runny molten slag. The viscosities of the coal slags are compared in Fig. 1.

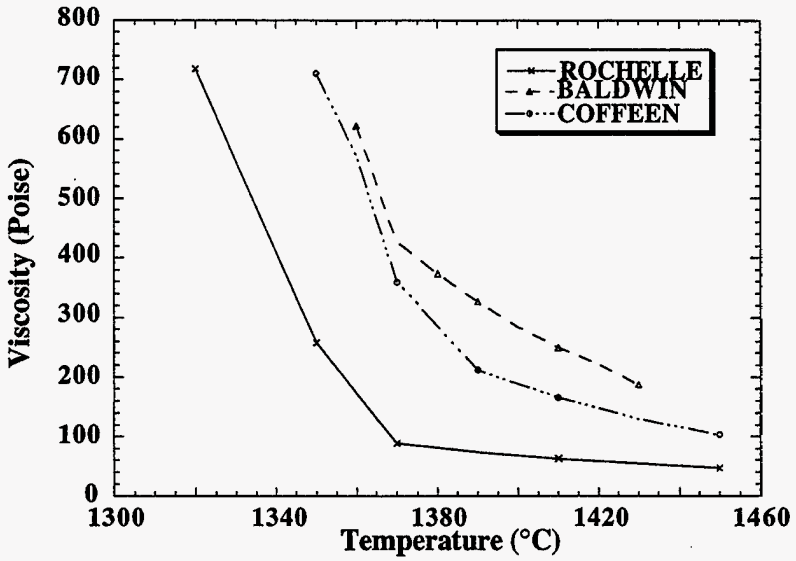

Fig 1. Viscosities of the coal slags.

Tube-sections 150 mm long were placed in a box furnace, an initial layer of coal slag was added and the furnace was brought up to temperature in 2 h. In order to replenish the coal slag 75 ml was added to each tube length every 48 h through the top of the furnace. Total exposure time was 500 h after which the furnace slowly was cooled to room temperature. After inspection each tube was cut into 14 C-ring specimens for strength testing. The C-rings were placed in a mechanical test system containing a box furnace, heated back up to the exposure temperature and loaded in compression to failure at a fast loading rate. The strength was evaluated using the appropriate formula for C-rings in compression.[3] Nine tubes were cut into C-rings and tested in the as-received condition in order to provide base-line strength data for each material at each test temperature. The strength data were analyzed using Weibull statistics, [4,5] and fractography was performed.

Occasionally the C-rings failed outside the maximum stress region, either due to localized thinning or pitting from the corrosive attack. The formula for calculating the stresses can be modified using a finite element analysis (FEA), and by performing such an analysis the regions for which corrections need to be performed has been evaluated. This work is in progress and some of the strengths reported below will be adjusted slightly. This will however, not change the major trends of the strength results.

The interfaces between the specimen surfaces and the coal slag were examined in an analytical microprobe using x-ray analysis and backscattered imaging. Identification of corrosion products and crystalline as well as amorphous glassy phases was performed in order to compare the corrosion reactions for the different combinations.

All 36 exposure conditions (3 coal slags at 3 temperatures for all four materials) have been completed and the strength testing of the resulting 14 specimens for each condition is complete. Analysis of the strength and of the corrosion mechanisms have been completed for one material and is ongoing for the remaining materials.

Results and Discussion

Figure 2 shows the total creep strain measured for two specimens of SiC_p/Al_2O_3 at 1260°C at two different stresses. As can be seen, a total creep strain of close to 0.1 % was accumulated over more than 3500 h. This is quite a bit more strain than traditional monolithic ceramics can accomodate at similar temperatures, and it is assumed that this is due to the presence of the aluminium alloy. As additional experiments finish, a comparison of the creep rates measured in flexure will be performed, and an assessment of the combined creep behavior of the ceramic will be made.

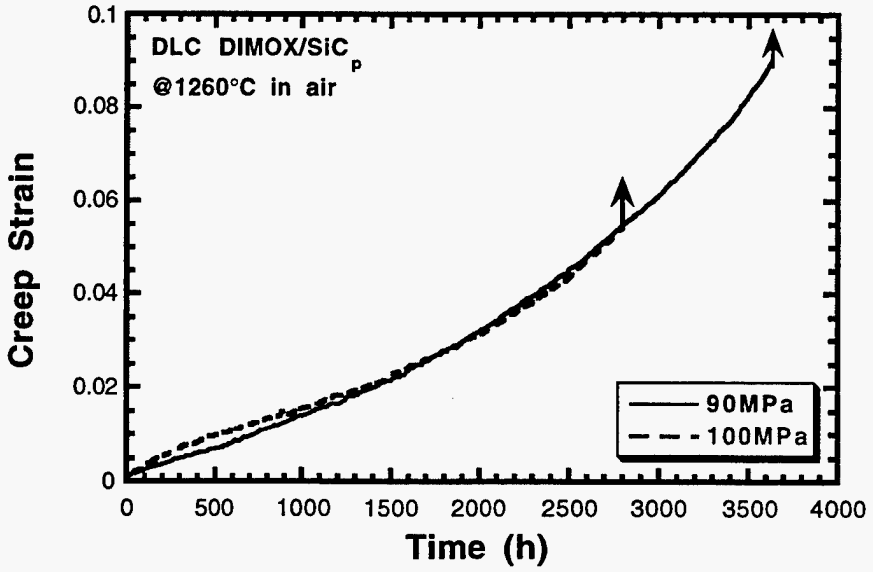

Fig. 2. Total tensile creep strain measured at 1260°C for SiC_p/Al_2O_3.

Table 2 is a summary of the average strength values obtained for the C-rings for each material. As described above, some of the specimens failed outside the maximum stress area, and these strengths will be adjusted somewhat, however, the work performed to date with the FEA indicates that these adjustments will be minor. The strengths measured after exposure was compared to the as-received strength and is given as a relative retained strength value. The relative retained strengths as a function of exposure temperature and coal slag type for each tested material are shown in Figs. 3 to 6.

Table 2. Strength of C-rings after exposure to coal slag.

MATERIAL & SPEC. #	*AVERAGE STRENGTH*	*TEMP.*	*SLAG*	*AS-RECEIVED STRENGTH*	*RELATIVE RETAINED STRENGTH*
NT230					
NT9A	274	1090	BALDWIN	204	1.34
NT3B	270	1090	COFFEEN		1.32
NT5A	195	1090	ROCHELLE		0.95
NT7A	126	1260	BALDWIN	262	0.48
NT4A	131	1260	COFFEEN		0.50
NT2A	37	1260	ROCHELLE		0.14
NT1A	cracked	1430	BALDWIN	61	
NT6A	22	1430	COFFEEN		0.37
NT3A	50	1430	ROCHELLE		0.83
LANXIDE					
LX2A	159	1090	BALDWIN	131	1.21
LX5B	155	1090	COFFEEN		1.18
LX4A	133	1090	ROCHELLE		1.02
LX5A	154	1260	BALDWIN	137	1.12
LX1A	75	1260	COFFEEN		0.55
LX3A	76	1260	ROCHELLE		0.55
LX2B	83	1430	BALDWIN	143	0.58
LX3B	81	1430	COFFEEN		0.57
LX4B	121	1430	ROCHELLE		0.85
HEXOLOY					
HX5A	267	1090	BALDWIN	230	1.16
HX1B	247	1090	COFFEEN		1.07
HX2B	252	1090	ROCHELLE		1.10
HX3A	334	1260	BALDWIN	225	1.48
HX4B	262	1260	COFFEEN		1.16
HX5B	100	1260	ROCHELLE		0.44
HX4A	171	1430	BALDWIN	244	0.70
HX2A	365	1430	COFFEEN		1.50
HX3B	142	1430	ROCHELLE		0.58
COORS					
CR12	328	1090	BALDWIN	320	1.03
CR3A	272	1090	COFFEEN		0.85
CR11	305	1090	ROCHELLE		0.95
CR10	292	1260	BALDWIN	313	0.93
CR2	289	1260	COFFEEN		0.92
CR9	123	1260	ROCHELLE		0.39
CR6	148	1430	BALDWIN	326	0.45
CR1	249	1430	COFFEEN		0.76
CR4	131	1430	ROCHELLE		0.40

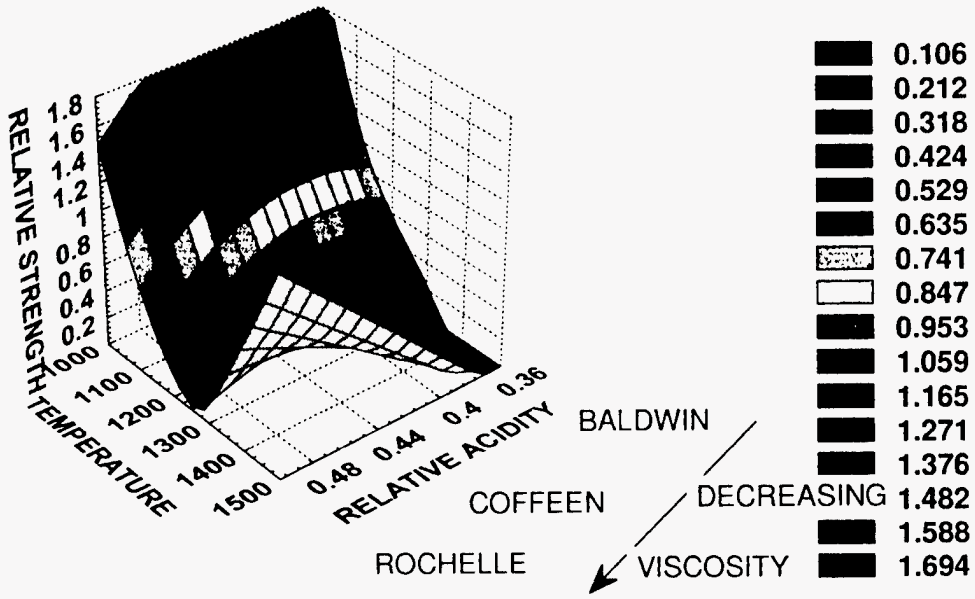

Fig. 3. Relative retained strength for the Si-SiC specimens after exposure for 500 h.

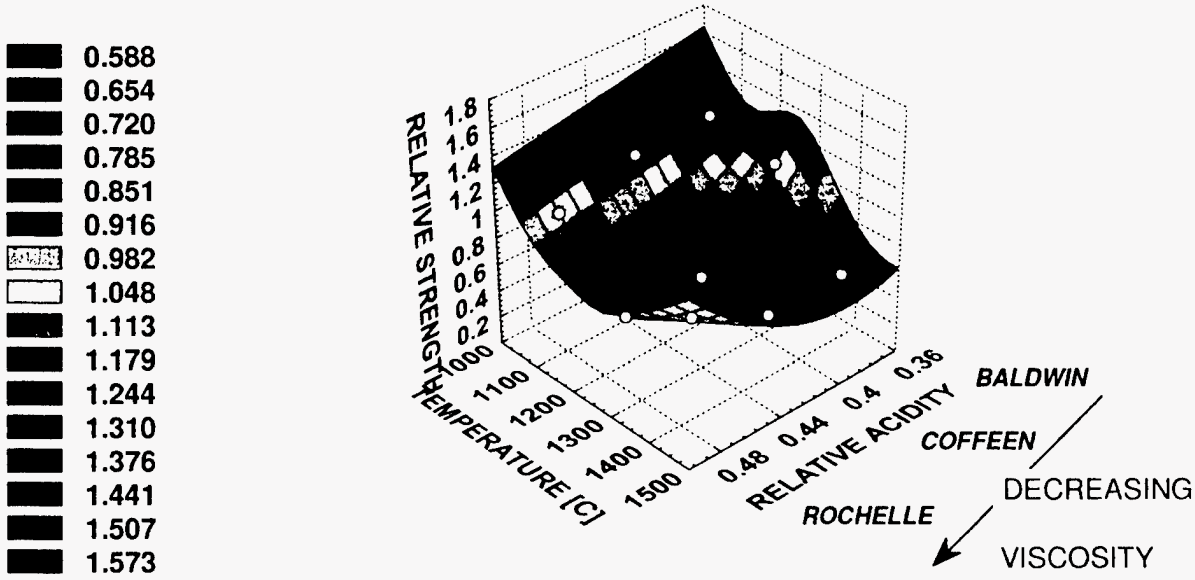

Fig. 4. Relative retained strength for the SiC_p/Al_2O_3 specimens after exposure for 500 h.

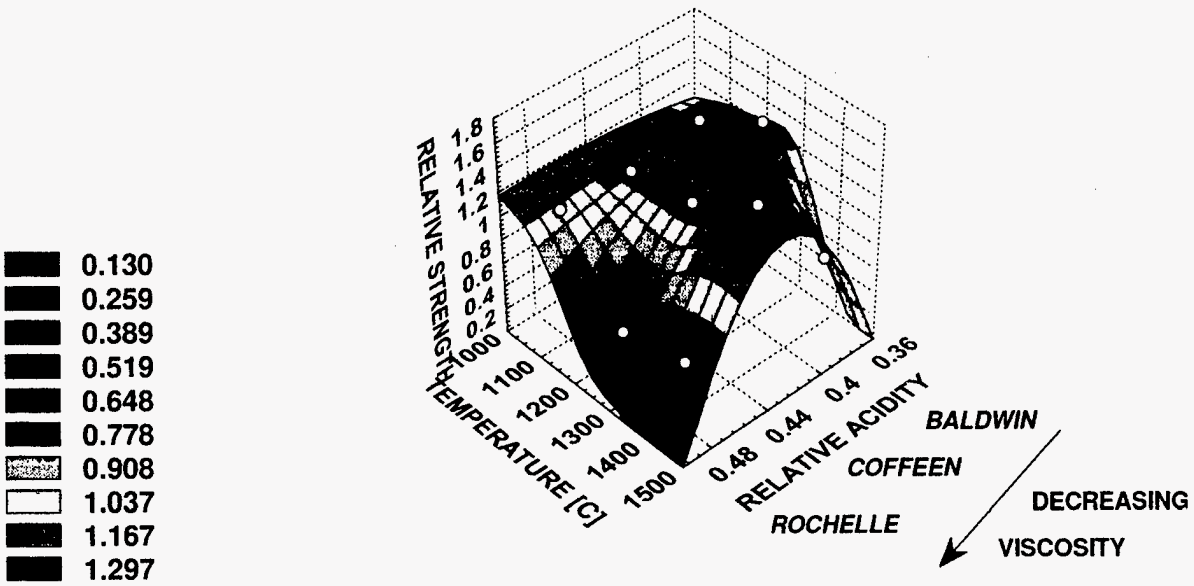

Fig. 5. Relative retained strength for the sintered α-Si specimens after exposure for 500 h.

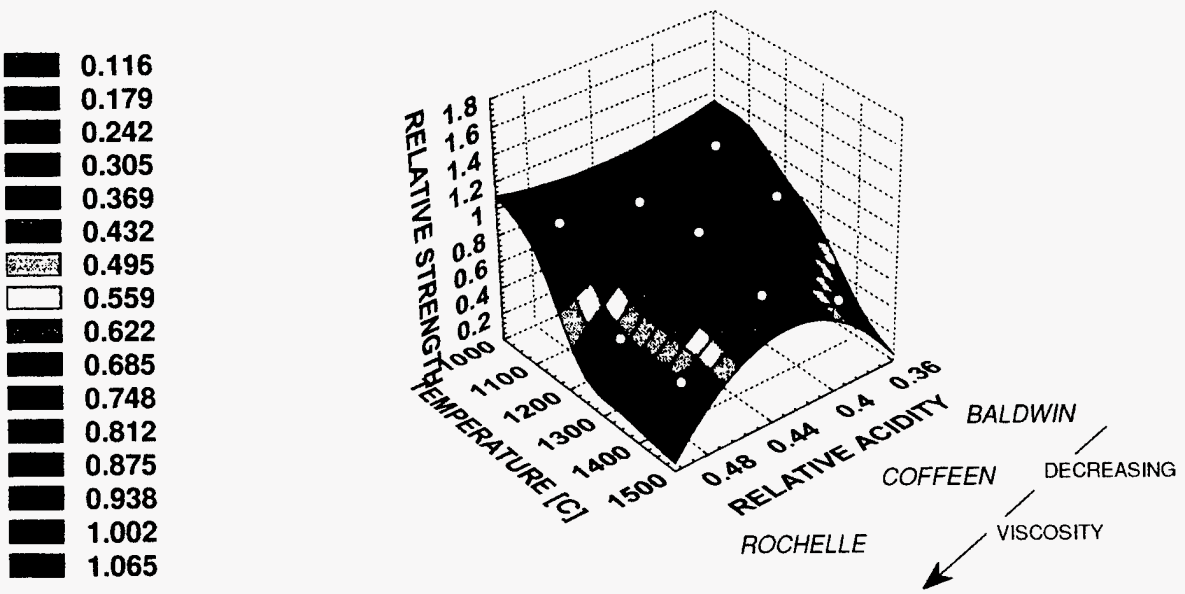

Fig. 6. Relative retained strength for the sintered β-Si specimens after exposure for 500 h.

The results for the Si-SiC in Fig. 3. clearly show that the material retained its strength after the exposure at 1090°C only. At this temperature there did not seem to be a significant difference between the slags, none were melted at that temperature and the slag was just lightly sintered together and to the tube specimens, and visual inspection showed that the tubes were intact after exposure. However, after exposure at 1260°C severe loss of strength was observed. The specimens exposed to Baldwin and Rochelle lost 50% of their strength, and the specimen exposed to Rochelle lost 85% of its strength. The visual inspection of the tubes after exposure showed that the slag had melted and fused onto the tubes and attacked the surface. Severe strength degradation was observed after exposure at 1430°C, in fact the tube exposed to the Baldwin slag contained cracks after cool-down, and fell apart during specimen cutting and no strength results were obtained for this condition.

Figure 4 shows the relative retained strength for the SiC_p/Al_2O_3 composite as a function of temperature and slag type. As can be seen the strength remained relatively unchanged after the exposure at 1090°C. After exposure at 1260°C the specimens exposed to Coffeen and Rochelle slags lost 45% of their strength while the Baldwin exposed specimens remained unchanged. At 1430°C a 45% loss of strength was observed for the specimens exposed to Baldwin and Coffeen slags, while the Rochelle exposed specimens only lost 15%.

Figure 5 shows the relative retained strength for sintered α-SiC as a function of temperature and slag type. This figure is significantly different from the two previous ones as there is now a region of fully retained strength for all temperatures. The specimens exposed to Coffeen slag retained the strength and in some cases experienced an increase in strength. The reasons for this will be discussed below. Severe loss of strength (about 50 and 30%, respectively) was seen for specimens exposed to Rochelle slag at 1260 and 1430°C

Figure 6 shows the relative retained strength for the sintered β-SiC as a function of temperature and slag type. The first important thing to note is the similarity between Figs. 5 and 6. The reason for this is likely the fact that these two materials are very similar in chemical composition and microstructure, and it was seen as an indication of the good reproducibility of the test method that these results were similar. Both materials withstood the 1090°C exposure and at 1260°C only exposure to the Rochelle slag caused severe strength loss. At 1430°C loss of strength occurred for all specimens, however, the exposure to Coffeen seemed less severe as indicated for the α-SiC specimens.

Complete Weibull analysis will be performed for all the strength data and full fractography will be performed. Further, in order to determine the corrosion mechanisms microprobe analyses will be performed for the different material/slag exposure combinations. Presently the analysis of the sintered α-SiC is complete, and the behavior of this will be discussed in further detail below.

Result summary for sintered α–SiC

The strengths were measured at an average of 14 specimens per condition. Each C–ring was inspected after the test in order to determine the fracture location and fracture origin. If the fracture location was off the maximum tensile region and in the cases with localized thinning the strengths were corrected appropriately with the aid of a finite element analysis. The complete Weibull graphs for the specimens are given in Figs. 7-9 for the three test temperatures respectively.

The first important observation was that the Weibull moduli were quite low with the as-received moduli being about 5 at all temperatures. The as-received strengths were determined from only 9 specimens and that results in a fairly low confidence in these m–values. The second observation was that the Weibull moduli remained rather unchanged throughout the experiments, with the exception of Rochelle exposed specimens which literally fell apart due to cracking after exposure at 1260 and 1430°C.

The fractography of the as-received specimens showed that the specimens generally failed from pores at or near to the surface, independent of test temperature. The results at 1090°C showed no significant change in strength as a result of the exposures. The fractography showed that the failures were from pores at and near the surface just as in the as-received case, consistent with the unchanged Weibull moduli.

The strength testing after exposure at 1260°C showed a much more differentiated picture. The strength of the Baldwin exposed specimens showed a significant increase in strength as compared to the as-received strength at 1260°C.

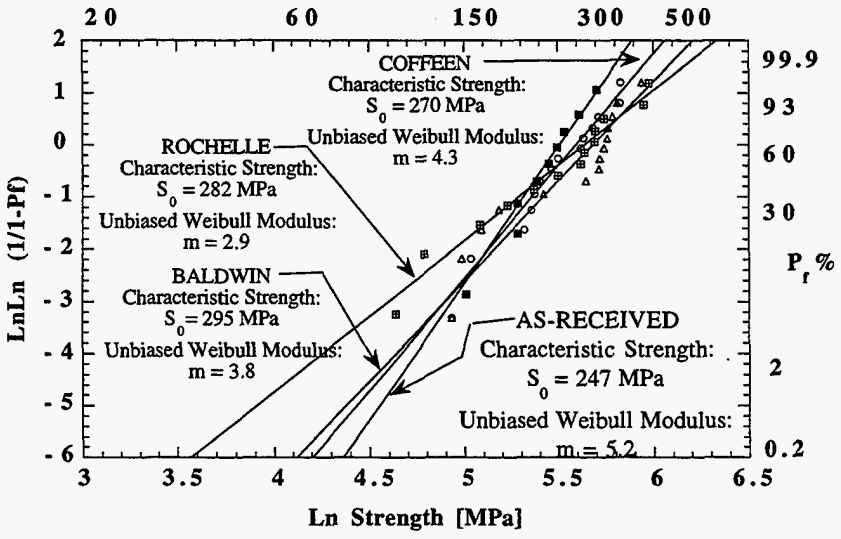

Fig. 7. Weibull analysis of C-rings exposed and tested at 1090°C.

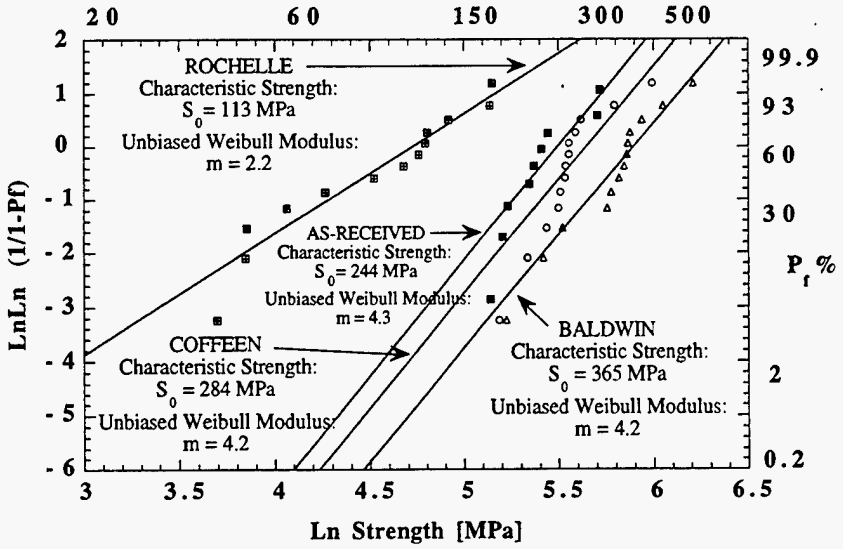

Fig. 8. Weibull analysis of C-rings exposed and tested at 1260°C.

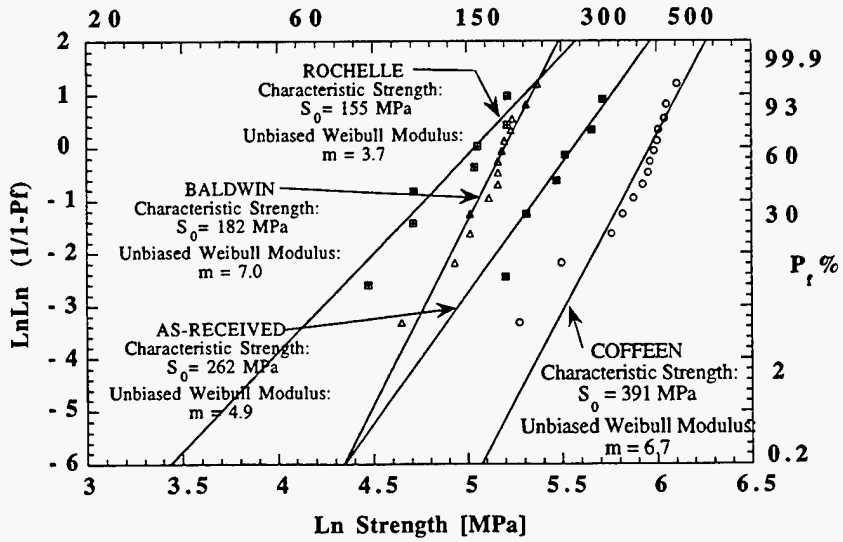

Fig. 9. Weibull analysis of C-rings exposed and tested at 1430°C.

The strength for the Coffeen exposed specimens remained unchanged while the Rochelle exposed specimens showed a significantly decreased strength. The fractography demonstrated that the Baldwin exposed specimens generally failed from surface connected pores as before, but in this case the pores were blunted by the viscous, glassy slag, see Fig 10. Based on this observation it could be expected that the Rochelle slag effectively would blunt pores, but in this case localized corrosive attack had occurred under the glassy

slag, and these corrosion pits in combination with cracks acted as fracture initiation points, see Fig. 11.

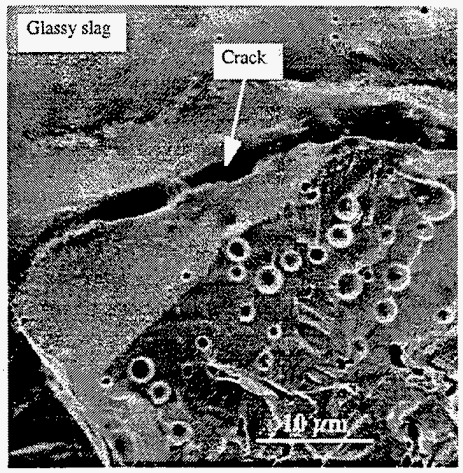

Fig. 10. Fracture origin in specimen exposed to Baldwin slag at 1260°C.

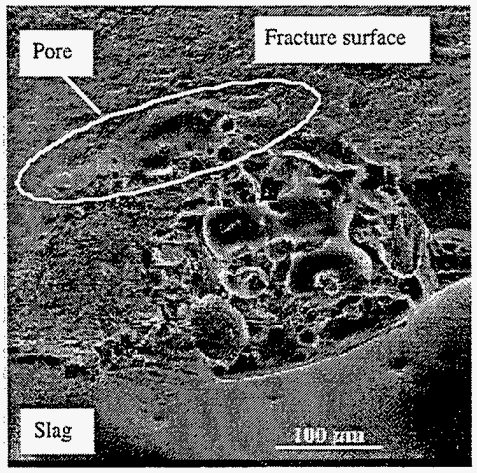

Fig 11. Fracture origin in a specimen exposed to Rochelle slag at 1260°C.

At 1430°C the Baldwin and Rochelle exposed specimens experienced a significant loss of strength, while the Coffeen exposed specimens increased somewhat in strength. The fractography showed that the weakened specimens generally failed from areas with corrosive attack. Especially in the case of the Rochelle exposed specimens a deep penetration and uniform thinning were observed, see Figs. 12 and 13. For the specimens exposed to Coffeen slag the fractography confirmed that the fracture origins were pores blunted by glassy slag.

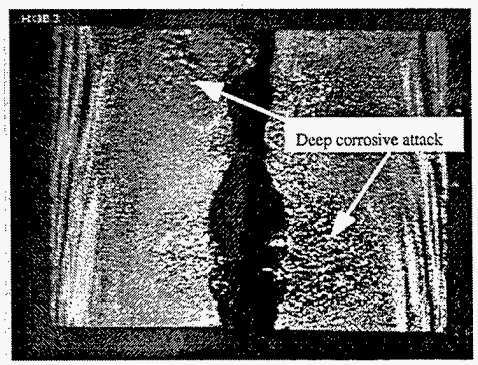

Fig 12. Fracture surfaces of a Rochelle exposed specimen at 1430°C showing material loss from the surface.

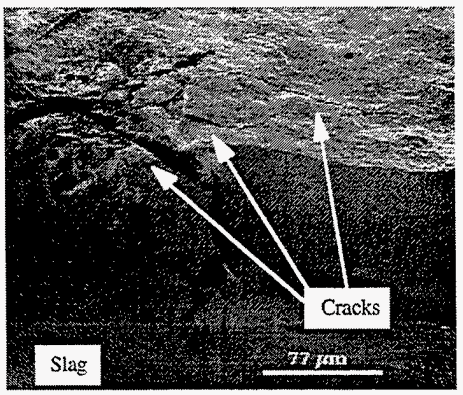

Fig. 13. Fracture origins in Rochelle exposed specimen at 1430°C were typically cracks at corrosion pits.

From the above discussion it is obvious that the degree of corrosive attack with subsequent loss of strength is a combination of coal slag chemical composition and viscosity. In order to investigate this further several specimens were studied using the microprobe. First it is important to emphasize that there were large local variations in the chemical composition as observed by the microprobe. This likely stemmed from the fact that there were large local variations in the composition of the coal slags, and that the coal slags were not sieved or treated in any way before the test. However, several general observations can be made to explain the differences in strength behavior.

As expected, there was little reaction at 1090°C. There was some coal slag stuck onto the surface of the specimens, and for the Baldwin and Coffeen exposed specimens some areas with 2-3 mm crystalline silica was observed. The Rochelle exposed specimens had a 60 mm thick glassy layer on the surface, but no general corrosive attack was observed.

At 1260°C the specimens exposed to Baldwin and Coffeen exhibited a relatively uniform glassy slag layer on top of a very thin (≈ 2 mm) layer of silica crystals, see Fig. 14. It is likely that the crystals protected the original surface from active corrosive attack. The Rochelle exposed specimens had experienced active corrosion at 1260°C, evidenced by the very uneven interface between the slag and the base material, see Fig. 15. The microprobe analysis showed segregation of iron to the interface resulting in formation of iron silicides consuming silicon from the substrate resulting in formation of corrosion pits.

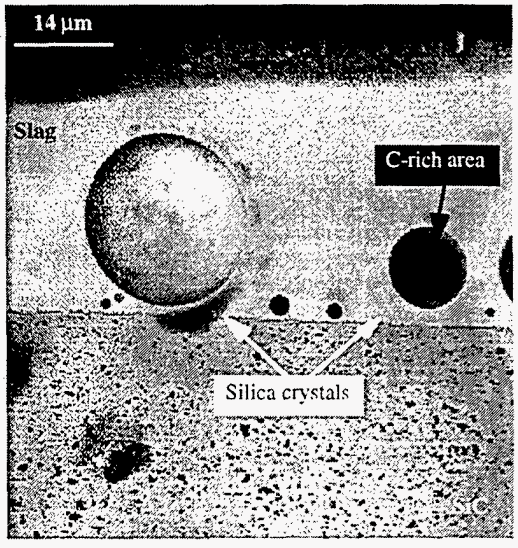

Fig. 14. Backscattered image of the slag/SiC interface for a specimen exposed to Baldwin slag at 1260°C.

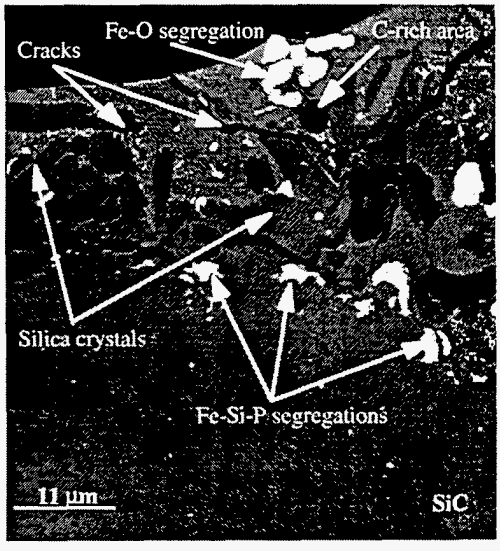

Fig. 15. Backscattered image of the slag/SiC interface for a specimen exposed to Rochelle slag at 1260°C.

A microprobe analysis of Rochelle exposed specimens at 1430°C was not performed. However, the significant loss of strength and cracking of specimens during exposure indicated that the process described above had progressed further.

The microprobe analysis of the specimens exposed to Baldwin (with strength loss) and Coffeen (with no strength loss) at 1430°C helped clarify the picture. The Baldwin exposed specimens had a glassy layer on top of a layer of silica crystals, but a segregation of Fe with subsequent formation of iron silicides had produced sizable corrosion pits, see Fig. 16. For the Coffeen exposed specimens the layer of silica crystals had protected the base material and no corrosion pits were observed.

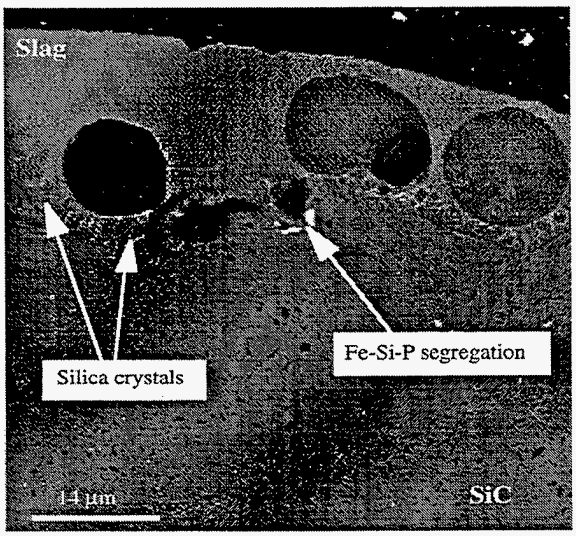

Fig. 16. Backscattered image of the slag/SiC interface for a specimen exposed to Baldwin slag at 1430°C.

SUMMARY

The static exposure tests have been proven to be useful in identifying areas, i.e., coal slag chemical composition and temperature combinations for which the tube specimens lost strength due to corrosive attack. The corrosion mechanisms have been thoroughly studied for one of the materials so far, and it is clear that the strength was degraded due to the formation of strength limiting pits of ironsilicides. There was further evidence that the viscosity of the coal slag played an important role in easing or limiting the transport of certain species to the specimen surface. The general trend was clear however, each of the materials survived well at all conditions at the lower temperature, and subsequently all the materials experienced loss of strength for a combination of increasing temperature and decreasing viscosity of the slag. A detailed microprobe analysis for the remaining three ceramic materials will provide more detailing of this picture.

ACKNOWLEDGEMENTS

Research Sponsored by the U.S. Department of Energy, Office of Fossil Energy, Pittsburgh Energy Technology Center, Advanced Combustion Technology Program, DOE/FE AA 20 10 00 0, under contract DE-AC05-96OR22464 with Lockheed Martin Energy Research Corp.

REFERENCES

1. K. Breder and V. J. Tennery, "Materials Support for HITAF, Final report for Phase 1," TM 12815, Oak Ridge National Laboratory, August 1994.

2. J. P. Hurley, "Support Services for Ceramic Fiber-Ceramic Matrix Composites" ORNL/Sub/94-SS112/01, Oak Ridge National Laboratory, Oak Ridge, TN 1995.

3. M. K. Ferber, J. Ogle, V. J. Tennery, and T. Henson, "Characterization of Corrosion Mechanisms Occurring in a Sintered SiC Exposed to Basic Coal Slags," *J. Am Ceram. Soc.* **68** [4] 191 (1985).

4. W. Weibull, "A Statistical Theory for the Strength of Materials, "Ingeniörsvetenskapsakademien, Handligar, No. 151 (1939).

5. S. Duffy and E. Baker, Manual for Spread Sheet Macro for Estimation of Weibull Parameters Based on the Maximum Likelihood Method, Civil Eng. Dep., Cleveland State University, Cleveland Ohio, 1995.

ENVIRONMENTAL ANALYSIS SUPPORT

R. L. Miller

Activities in environmental analysis support included assistance to the Federal Energy Technology Center (FETC) at Morgantown and Pittsburgh in reviewing and preparing documents required by the National Environmental Policy Act (NEPA) for projects selected for the Clean Coal Technology (CCT) Program and the Combustion 2000 Program. An important activity was the preparation for Morgantown of an Environmental Assessment (EA) for the proposed atmospheric circulating fluidized bed (CFB) technology to be demonstrated in Seward, Pennsylvania. Another important activity was the initiation for Pittsburgh of an Environmental Impact Statement (EIS) for a new coal-fired Low Emission Boiler System (LEBS) for electric power generation at the proof-of-concept scale.

ENVIRONMENTAL SUPPORT TO THE CLEAN COAL TECHNOLOGY PROGRAM

R. L. Miller

Work during this period focused on the preparation – for DOE's Federal Energy Technology Center (FETC) at Morgantown – of an Environmental Assessment (EA) to evaluate the potential environmental impacts associated with constructing and demonstrating an atmospheric circulating fluidized bed (CFB) combustor in Seward, Pennsylvania. The technology would be demonstrated at the Pennsylvania Electric Company's (Penelec's) Seward Station, and the costs would be shared by DOE and Penelec under the first round of the Clean Coal Technology (CCT) Program.

The CFB combustor would replace Seward Station's existing coal-fired boilers to produce steam that would be used to generate electricity. The CFB boiler allows combustion of low-quality coal that contains high volumes of moisture and/or ash. Limestone within the bed captures sulfur dioxide (SO_2) in the combustion chamber, eliminating the need for expensive scrubbers. Atmospheric CFB technology operates at lower temperatures than conventional boilers, thus reducing the thermal production of oxides of nitrogen (NO_x).

The proposed project would demonstrate atmospheric CFB technology on a scale which is large enough to evaluate environmental, economic, and technical performance data necessary for commercialization of the technology. Although there are many small, mostly industrial atmospheric CFB combustors in the United States, utility-scale CFB boilers of 200 megawatts (MW) and greater are not yet accepted as commercial technology in the utility market. The largest atmospheric CFB combustor currently operating in the United States is 150 MW, while the conventional pulverized-coal boilers used by electric utilities are predominantly 250-400 MW units. The proposed 232-MW (gross) Seward project would bridge the gap between the scale of proven CFB technology and the size of most conventional facilities. While the risk associated with advancing the technology to a scale of 200 MW or more is too high for the private sector to assume in the absence of strong economic incentives or legal requirements, the risk can be reduced by demonstrating the technology as part of the cost-shared CCT Program. Subsequently, the private sector would have the data upon which to make an informed decision as to the commercial readiness of the technology.

Seward Station is located in Indiana County, Pennsylvania, about 12 miles northwest of Johnstown and 45 miles east of Pittsburgh. Construction of Seward Station began in 1919 and operations commenced with three coal-fired boilers in 1921. Through the years, the facility has continuously been upgraded and remodeled with new units coming on line and older equipment being retired. Currently, two boilers with identical capacities which were installed in 1949 serve a 66-MW (gross) steam turbine, and another boiler which was installed in 1957 powers a 147-MW (gross) steam turbine, yielding a station total of 213 MW.

The existing Seward Station consumes a total of about 470,000 tons of bituminous Pennsylvania coal per year to generate electricity. Annual air emissions at Seward Station include about 15,600 tons of SO_2, 3500 tons of NO_x, 350 tons of particulate matter, 120 tons of carbon monoxide (CO), 36 tons of volatile organic compounds (VOCs), and 1,400,000 tons of carbon dioxide (CO_2). About 150,000 gallons per minute of water from the Conemaugh River are pumped once through the condenser tubes to cool the steam from the turbines and then the heated water is returned to the river.

Potential resource areas of concern associated with the project included atmospheric resources, surface water resources, ecological resources, waste management, and traffic. In particular, the potential effect of the heated discharge of once-through cooling water from the turbine condensers on aquatic life in the Conemaugh River was evaluated. The remaining topics were analyzed to a lesser extent, commensurate with the potential for impacts on those resource areas.

Also during this period, work began – for DOE's Federal Energy Technology Center (FETC) at Pittsburgh – on an Environmental Impact Statement (EIS) to evaluate the potential environmental impacts associated with constructing and demonstrating a new coal-fired Low Emission Boiler System (LEBS) for electric power generation at the proof-of-concept scale. The EIS will support a DOE decision on providing funding to design, construct, and demonstrate one or more of three promising LEBS technologies. As part of the Combustion 2000 Program, the LEBS Program is intended to provide the U.S. power industry with a reliable, economic, highly efficient, and environmentally preferred alternative to current coal utilization technologies. DOE's role is to accelerate the development and deployment of technologies that meet LEBS objectives, ensure a better product through competition and involvement of the power industry, and share the cost of

development. The cost-shared contribution by DOE for proof-of-concept demonstration would help reduce the risk by the participating teams in developing LEBS technology to the level of maturity needed for commercial decisions.

DOE initially awarded three LEBS contracts in 1992. DB Riley, ABB-Combustion Engineering, and Babcock & Wilcox are the prime contractors for the three participating teams. The LEBS contracts include four work phases that are planned for completion by the year 2000. Phase I work, which consisted of preliminary engineering designs for a conceptual LEBS power plant, was completed in 1994. In Phase II, research and development and subsystem tests were performed at scales ranging from 3 to 10 MW to verify concept performance. In Phase III, conceptual design was performed to confirm the engineering feasibility of integrating subsystem test results into a proof-of-concept facility in the 10 to 75 MW size range. In Phase IV, which is the subject of the EIS, DOE would provide up to 50% of the funds required for constructing and demonstrating one or more of the proposed technologies as a coal-fired power plant at a scale of 10-75 MW, which is considered to be an appropriate size for verifying the technologies' technical performance and economic viability. Among the three teams, DOE does not have a preferred technology at this stage in the LEBS program.

If the DB Riley technology is selected for Phase IV, DOE would provide funding for a new 70-MW coal-fired power plant adjoining Turris Coal Company's existing Elkhart Mine in Elkhart, Illinois. The technology would use a slagging combustor with air staging and coal reburning to reduce NO_x emissions; a fly ash reinjection system; a copper oxide regenerable desulfurization system with NO_x removal capability; advanced low temperature heat recovery; and a baghouse for particulate removal.

If the ABB-Combustion Engineering technology is selected, DOE would provide funding for repowering the existing 35-MW Unit 1 at Richmond Power & Light Company's Whitewater Valley Station in Richmond, Indiana. Repowering refers to replacing Unit 1's coal pulverizers, boiler, steam turbine, and electrical generator with the ABB-Combustion Engineering technology, which would boost Unit 1's electrical generation capacity to approximately 50 MW. The technology would use advanced firing with staged combustion for in-furnace NO_x reduction;

advanced dry lime scrubbing for SO_2 removal; an ammonia/water mixture rather than water only as the working fluid for heat recovery; and a baghouse for particulate removal.

If the Babcock & Wilcox technology is selected, DOE would provide funding for demonstrating the technology at Babcock & Wilcox's existing 10-MW-equivalent Clean Environment Development Facility in Alliance, Ohio. For this technology, all major equipment necessary for the demonstration is already installed within the Clean Environment Development Facility (electricity would not actually be generated), and testing has already been performed on the subsystems; therefore, only minor modifications would be required for Phase IV. The technology would use an advanced boiler design with staged combustion; low-NO_x burners; limestone injection with dry scrubbing for SO_2 removal; and an electrostatic precipitator and baghouse for particulate removal.

The following issues associated with construction and demonstration of LEBS technology at the proof-of-concept scale have been identified as requiring detailed analysis and assessment in the EIS:

(1) potential air, surface water, and noise impacts produced during facility modification or construction;
(2) potential air, surface water, and noise impacts produced during facility operation;
(3) potential transportation impacts produced during facility modification, construction, and operation;
(4) pollution prevention and waste management practices, including potential solid waste impacts, during facility modification, construction, and operation;
(5) potential socioeconomic and environmental justice impacts to the surrounding communities as a result of implementing the proposed projects;
(6) potential cumulative or long-term impacts from the proposed projects and other past, present, or reasonably foreseeable future actions;
(7) potential irreversible and irretrievable commitment of resources;
(8) compliance with all applicable Federal, state, and local statutes and regulations; and
(9) safety and health of workers and the public during construction and operation of the proposed projects.

Issues of lesser importance will be discussed in lesser detail, as appropriate to clarify and distinguish impacts among alternatives. Of the issues listed above, the most detailed analyses in the EIS will focus on the level of impacts expected to air quality.

BIOPROCESSING RESEARCH

E. N. Kaufman

This section describes research and development activities performed for the Fossil Energy Bioprocessing Research Program. This program includes fundamental research for coal applications that investigates advanced reactor design for conversion of coal and coal liquids, the use of enzymes in pure organic media, and development of biological processes for the conversion of coal residuum. In addition, the program includes studies on advanced bioreactor systems for the treatment of flue gases and the conversion of synthesis gas to liquid fuels, removal of heteroatoms from heavy oils, renewable hydrogen production, and remediation of oil containing soils. The program also includes natural gas and oil technology partnership support and studies on crude oil composition and oil recovery.

FUNDAMENTAL BIOPROCESSING RESEARCH FOR COAL APPLICATIONS

E.N. Kaufman

INTRODUCTION

The purpose of this program is to gain a fundamental understanding and sound scientific technical basis for evaluating the potential roles of innovative bioprocessing concepts for the utilization and conversion of coal. The aim is to explore the numerous ways in which advanced biological processes and techniques can open new opportunities for coal utilization or can replace more conventional techniques by use of milder conditions with less energy consumption or loss.

There are several roles where biotechnology is likely to be important in coal utilization and conversion. These include potential bioprocessing systems such as: conversion of coal synthesis gas to liquid fuels and chemicals, biocatalytic beneficiation of coal-derived liquids for the removal of heteroatoms or heavy metals, biocatalytic upgrading of coal-derived liquids and conversion to useful chemical feedstocks, biocatalytic removal of SO_X and NO_X from coal combustion off-gas, environmental control technology for the removal or destruction of hazardous materials in process effluents and/or solid residues, and the removal and utilization of CO_2 from combustion off-gas. Effective bioprocesses for such applications will require detailed knowledge of the biological process mechanisms and advanced bioreactor technology that can be optimized for high productivity, as well as supporting upstream and downstream processes that will allow an effective integrated bioprocess.

DISCUSSION OF CURRENT ACTIVITIES

The efforts in FY 1996-7 have been directed toward 3 primary areas of research: (1) advanced bioprocessing concepts for the **Bioconversion of Coal Synthesis Gas**; (2) use and enhancement of **Biological Catalysts in Organic Media**; and (3) **Electrochemical Regeneration of Reduced Cofactors**.

Bioconversion of Coal Synthesis Gas

In order to be economically feasible, all of the potential applications of biotechnology to coal processing will require efficient and inexpensive bioreactors and contactors. The aim of this task is to develop advanced bioreactor concepts that are compatible with continuous operation and maximum throughput. In previous years we have developed a fluidized bed reactor for solid coal conversion and an electro-spray reactor for the

efficient mixing of aqueous and organic phases that may be utilized for the biological processing of coal liquid. We are currently developing reactor systems for the biological utilization and conversion of coal synthesis gas to liquid fuels and chemicals. Coal synthesis gas represents a plentiful, generic feedstock for the production of numerous chemicals including ethanol, acetic acid, methanol, methane and hydrogen. Biological processes are capable of these conversions at more mild operating conditions, and with greater product specificity than thermochemical systems.

Coal synthesis gas contains a variety of sulfur species that may be corrosive to equipment and may foul conventional catalysts. Through a contract with ARCTECH Inc., Chantilly, VA, we have investigated the biological mineralization of sulfur bearing compounds in synthesis gas. We have also investigated the possible toxicity of other syn-gas components to the biocatalyst used in this process. Mineralization of hydrogen sulfide was not found to be affected by the presence of carbon monoxide, ammonia, or cyanide (when CN was presented as a ferric salt). While the biocatalyst was initially sensitive to cyanide when presented as a potassium salt, the culture was able to be adapted to this salt at concentrations as high as 100 ppm. Mineralization of H_2S to S occurred at rates between 2,000 and 3,000 ppm/hr*L.

Through collaborative work with Bioengineering Resources Inc., Fayetteville, AR, we are demonstrating the biological conversion of coal synthesis gas to ethanol (see also section 4.2). This year, BRI has adapted their proprietary bacteria from synthesis gas originating from a carbon black manufacturer to a syn-gas mixture more representative of coal gasifiers. They have studied coal gasifier selection, and have achieved ethanol concentrations as high as 30 g/L with gas residence times in their reactors of minutes.

Besides the conversion of synthesis gas directly into fuels and chemicals, it may be utilized biologically as a carbon and energy source for other biological reactions. For instance, bacteria catalyzing the desulfurization of flue gases may use the CO and H_2 as sources of reductant in the conversion of SO_x to H_2S which may further be processed to elemental sulfur. This year we have demonstrated syn-gas utilization in the desulfurization of both SOx, and in the conversion of flue gas desulfurization waste gypsum. One disadvantage of synthesis gas is that it is only sparingly soluble in the aqueous environments in which most biological reactions take place. To facilitate the transport of syn-gas into bioreactors, we have designed and operated a micro-bubble generator in which surfactant stabilized foams of syn-gas 50 μm in bubble diameter may be fed into a reactor. This 50 μm emulsion is much smaller than the bubbles formed by conventional sparging, and their small size further increases their residence time within the reactor. A schematic of the microbubble generator and bioreactor as well as a graph showing SO_x conversion in a microbubble fed reactor are shown in Figures 1 & 2.

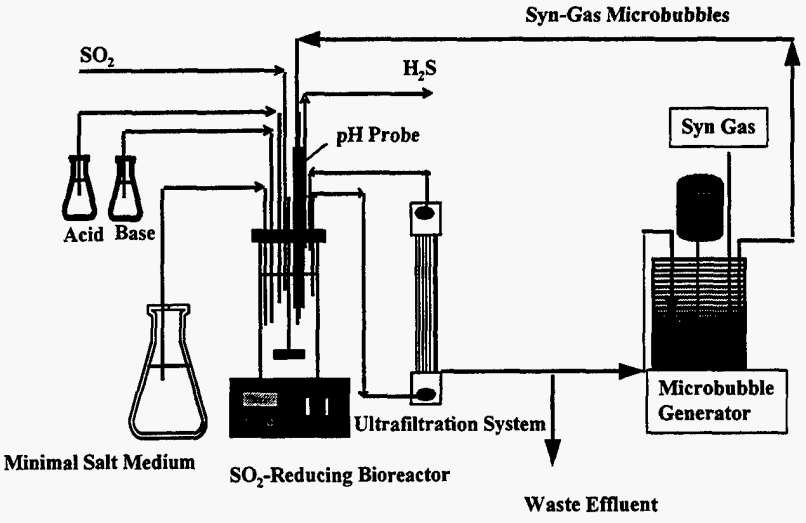

Figure 1: Schematic of microbubble generator and bioreactor for SOx conversion using coal synthesis gas as a carbon and energy source.

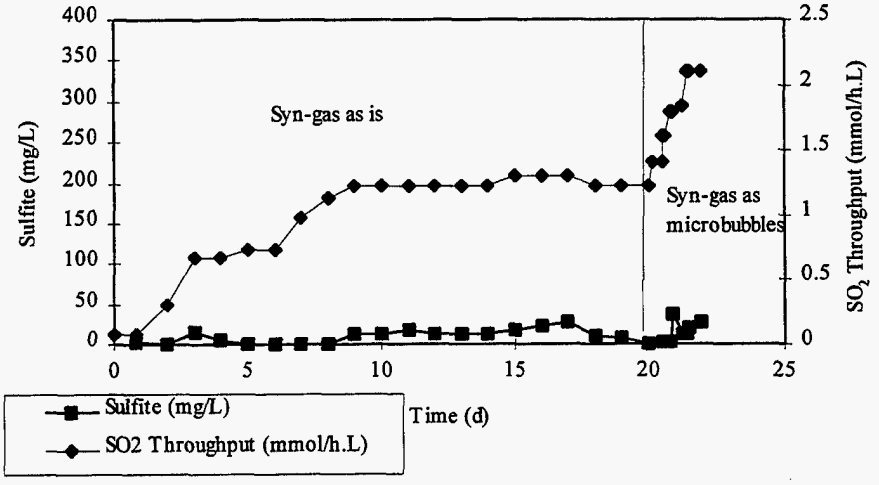

Figure 2: Biodesulfurization of SOx using coal synthesis gas as a carbon and energy source. The rate of desulfurization has been markedly increased by the introduction of synthesis gas as microbubbles rather than conventional gas sparging.

Biological Catalysts in Organic Media

There are several potential coal bioprocessing concepts that could use an organic solvent or produce liquid organic products, for example, the bioconversion of coal to liquids in an organic solvent or the bioprocessing of coal-derived liquids. For such a process, the biocatalyst (microorganism or enzyme) must be compatible with the organic medium. Naturally occurring enzymes may be modified by covalently attaching hydrophobic

groups that render the enzyme soluble and active in organic solvents and have the potential to greatly expand applications of enzymatic catalysis. The reduction of elemental sulfur to hydrogen sulfide by a hydrogenase isolated from *Pyrococcus furiosus* has been investigated as a model system for organic biocatalysis. While the native hydrogenase catalyzed the reduction of sulfur to H_2S in aqueous solution, no activity was observed when the aqueous solvent was replaced with anhydrous toluene. Hydrogenase modified with PEG *p*-nitrophenyl carbonate demonstrated its native biocatalytic ability in toluene when the reducing dye benzyl viologen was also present. Sulfide production in toluene was tenfold higher than that produced in an aqueous system with equal enzyme activity demonstrating the advantages of organic biocatalysis. Applications of bioprocessing in nonaqueous media are expected to provide significant advances in the areas of fossil fuels, renewable feedstocks, organic synthesis, and environmental control technology.

This year, in collaboration with the University of Georgia, we have investigated the fundamental mechanisms of enzyme modification using PEG *p*-nitrophenyl carbonate. SDS-page analysis of heat treated modified hydrogenase has revealed that the PEG is covalently attached to the protein. Gel filtration has shown that the modified enzyme exists as aggregates. We have further demonstrated that the modified enzyme exhibits a broader temperature range of activities and is also more active than the native enzyme at the reduction of electron mediating dyes. Ferredoxin is a low molecular weight analog of hydrogenase and has been utilized to better ascertain mechanisms of enzyme modification. We have achieved solubilities of 7 mg/L in toluene and have demonstrated that the active site of ferredoxin is not altered by enzyme modification.

Electrochemical Regeneration of Reduced Cofactors

The presence of reduced cofactors such as NADPH or NADH or their surrogates in the form of reduced electron carrying dyes such as benzyl viologen or neutral red are required for many enzymatically catalyzed reactions. Examples include the production of ethanol from synthesis gas, desulfurization of oil and coal, as well as the production of hydrogen from sugars. The availability of these reduced cofactors has been demonstrated to dictate product ratios and alter nutrient utilization in a number of fermentation reactions. In our current research, we have begun to examine whether reduced cofactors and electron carriers may be supplied electrochemically in order to increase the rates, product spectrum, and economics of enzymatically catalyzed reactions. In our work on organic biocatalysis, we recently used hydrogenase to reduce a synthetic dye in order to effect the reduction of sulfur to hydrogen sulfide. This year, we have demonstrated that the dye may be directly reduced electrochemically to effect this same reaction, thus eliminating the need for an enzyme. We are currently investigating if electrochemistry may alter

substrate utilization in the desulfurization of SOx, and will investigate alteration of acetate / ethanol ratios in the conversion of synthesis gas to liquid fuels.

ACKNOWLEDGMENTS

This work was supported by the Advanced Research and Technology Development Program of the Office of Fossil Energy, U.S. Department of Energy under contract DE-AC05-96OR22464 with Lockheed Martin Energy Research Corp.

REFERENCES

E.N. Kaufman and B.E. Dale, "Emerging Topics in Industrial Biotechnology." 1997, *Applied Biochemistry and Biotechnology*. (in press).

E.N. Kaufman, M. H. Little, and P.T. Selvaraj, "A Biological Process for the Reclamation of FGD Gypsum Using Mixed Sulfate-Reducing Bacteria with Inexpensive Carbon Sources." 1997, *Applied Biochemistry and Biotechnology*. (in press).

E.N. Kaufman, M. H. Little, and P.T. Selvaraj, "Recycling of FGD Gypsum to Calcium Carbonate and Elemental Sulfur Using Mixed Sulfate Reducing Bacteria with Sewage Digest as a Carbon Source." 1996, *Journal of Chemical Technology and Biotechnology*. **66**: 365-374.

P.T. Selvaraj, M.H. Little, and E.N. Kaufman, "Biodesulfurization of flue gases and other sulfite/sulfate waste streams using immobilized mixed sulfate reducing bacteria." 1997, *Biotechnology Progress*. (submitted for publication).

P.T. Selvaraj, M.D. Bredwell, M.H. Little, and E.N. Kaufman, "Biodesulfurization of flue gases using synthesis gas delivered as microbubbles." 1997, *American Chemical Society*. (in press).

P.T. Selvaraj, M.H. Little, and E.N. Kaufman, "Analysis of immobilized cell bioreactors for desulfurization of flue gases and sulfite/sulfate laden waste water." 1997, *Bioremediation*. (in press).

P.T. Selvaraj, G. B. Meyer, and E.N. Kaufman, "Microbial reduction of sulfur dioxide in immobilized, mixed cultures of sulfate reducing bacteria with sewage digest as carbon and energy source." 1996, *Applied Biochemistry and Biotechnology*. **57/58**: 993-1002.

Tsouris, C., V. M. Shah, M. A. Spurrier, and M. K. Lee, "Experiments on Electrostatic Dispersion of Aqueous Droplets into an Organic Stream," *Chem. Eng. Commun.* (1997). in press.

Tsouris, C., H. M. Lizama, M. A. Spurrier, T. L. Takeuchi, and T. C. Scott, "Hydrodynamics of Bioreactors Systems for Liquid-Liquid Contacting," *Appl. Biochem. And Biotech.* (1996) **57**: 581-592.

C.A. Woodward and E.N. Kaufman, "Enzymatic Catalysis in Organic Solvents: Polyethylene Glycol Modified Hydrogenase Retains Sulfhydrogenase Activity in Toluene." 1996, *Biotechnology and Bioengineering*. **52**: 423-428.

ADVANCED BIOREACTOR SYSTEMS FOR GASEOUS SUBSTRATES: CONVERSION OF SYNTHESIS GAS TO LIQUID FUELS AND REMOVAL OF SO_X AND NO_X FROM COAL COMBUSTION GASES

P. T. Selvaraj & E. N. Kaufman

INTRODUCTION

The objective of this task is to study of bioreactor concepts for the efficient conversion of coal synthesis gas to liquid fuels and the utilization of coal synthesis gas as a carbon and energy source for bioconversion processes of interest to the coal industry. With large reserves of coal in the United States, coal synthesis gas production will emerge as an important technology in the future. Synthesis gas, primarily a mixture of carbon monoxide (CO), hydrogen (H_2) and carbon dioxide (CO_2) represents an easily obtainable, generic feedstock for the production of fuels and chemicals. Synthesis gas may be obtained directly as a waste gas from many manufacturing processes, or it may be obtained through gasification of any carbonaceous material such as agricultural, municipal, and paper wastes, coal natural gas, or direct utilization of produced biomass. Conventional processes such as catalytic processes may be used to convert synthesis gas into a variety of fuels and chemicals such methane, methanol, acetic acid etc. Biological processes have been found a potentially viable processes and promised to be less costly in producing fuels. In addition, the synthesis gas may also be used as a carbon and energy source for other bioprocessing applications.

We previously demonstrated a biological process of desulfurizing flue gas utilizing mixed sulfate reducing bacteria (SRB) culture with sewage digest as a carbon source and energy source. A columnar reactor with mixed SRB cultures immobilized in BIO-SEP polymeric porous beads with sewage digest as carbon and energy source exhibited conversion rate of 16.5 mmol sulfite/h•L (32 kg/d•m^3) with 100% conversion to H_2S. Though municipal sewage digest is a readily available low-cost carbon source, the real cost of the medium depends on the location of the sewage and power plant and the transportation to bring the sewage back and forth from the sewage plant. Therefore the research has been focused on using synthesis gas as an alternative low-cost feedstock for SRB as they desulfurize flue gases, recycle flue gas desulfurization waste gypsum, and treat acid mine drainage waste waters. Synthesis gas are only sparingly soluble in the aqueous environments encountered in conventional bioreactor systems. Advanced bioreactor concepts are needed to increase synthesis gas mass transport and utilization.

A gas mixture containing 36% H_2, 47% CO, 10% CO_2, 5% CH_4 and balance N_2 as a model coal synthesis gas was utilized in these studies. This composition is typical of an oxygen blown, coal fed gasifier. Initially, with development of mixed SRB culture using

the syn-gas as sole carbon and energy source, a stirred tank and trickle bed reactors were operated with syn-gas fed as gaseous feed. The mass transfer characteristics were determined under these conditions. Following this, the syn-gas has been fed as microbubbles to enhance the mass transport properties.

In synthesis gas conversion to liquid fuel, *Clostridium lungdhalli* have been shown to convert syn-gas to ethanol. With biocatalyst development, a CSTR and trickle bed reactors have been operated with syn-gas feed stock. Reactor conditions such as pH, temperature, and agitation rate are being monitored to obtain maximum ethanol production. Microbubble syn-gas feed and solvent systems will be investigated to improve syn-gas mass transport and utilization.

Syn-Gas Utilization by Mixed Sulfate Reducing Bacteria

Utilization of syn-gas by mixed SRB culture developed from municipal sewage was investigated in a serum bottle containing minimal salt medium and SO_2 as terminal electron acceptor. The head space of the bottle was then filled with synthesis gas mixture containing 36% H_2, 47% CO, 10% CO_2, 5% CH_4, and balance N_2. The bottle was inoculated with mixed SRB culture and incubated at 30°C with shaking at 200 rpm. The syn gas utilization is shown in Fig. 1. Initially, a decrease in CO concentration was observed with no change in H_2 concentration. However, hydrogen sulfide was detected during this time in the head space of the serum bottle. This indicates that the CO was utilized by certain type of bacteria and produced H_2 as shown in the equation below.

$$CO + H_2O \rightarrow H_2 + CO_2$$

With limited SO_2 reduction due to a possible CO inhibition at higher concentration, as seen in the Fig. 1, hydrogen concentration declined only after the CO concentration was less than about 5% in the mixture. This suggests that the mixed culture developed from sewage solids would be able to use CO as sole carbon and energy source and produce H_2. Kinetically, the CO utilization was much faster than hydrogen utilization by SRB cultures.

Figure 1. Syn-Gas Utilization by Mixed SRB

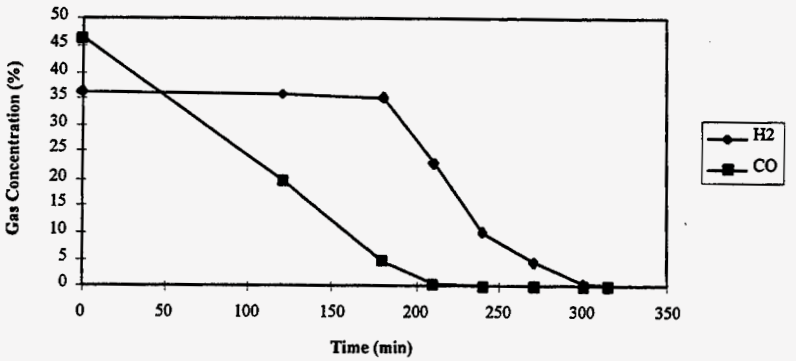

Following the development of culture in serum bottle, a 2-L chemostat was operated with mixed SRB culture and SO_2 gas as terminal electron acceptor. Initially, the reactor was fed with syn gas, minimal salt medium and SO_2 gas mixture containing 1% or 5% SO_2, 5% CO_2, and balance nitrogen. The effluent reactor medium was recirculated through a hollow fiber membrane to recycle the biomass into the reactor to achieve higher biocatalyst concentration in the reactor. At these conditions, the maximum productivity of the reactor was 1.2 mmol SO2/h•L with 100% conversion SO_2 into H_2S.

In an effort to develop a bioreactor for the above process with better mass transfer for syn gas, a trickle bed reactor has been operated with BIO-SEP beads as carrier medium for biocatalyst. Initially, as shown in Fig. 2, the SO_2 feed rate was at 2.7 mmol/h•L. The SO_2 feed rate was then increased incrementally with no sulfite detected in the effluent. Presently, the reactor has been operated at 9.5 mmol SO_2/h•L with 98% conversion.

Figure 2. Trickle Bed Reactor with BIO-SEP Beads
Syn-gas as Feedstock

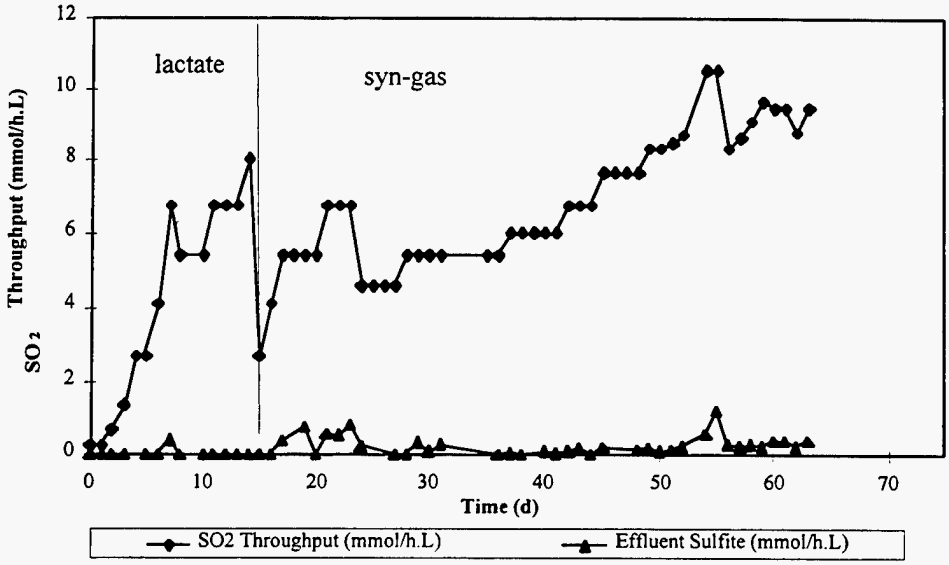

In an effort to improve the mass transfer properties of syn-gas, the CSTR reactor was then fed with syn-gas microbubbles as follows.

Microbubbles are small, surfactant coated bubbles of gas that are generated by creating a gas-liquid interface in a high-shear zone. The bubbles are between 50 μm and 100 μm in diameter and the surfactant coating helps to prevent coalescence by electrostatic repulsion from the diffuse electric double layer around the bubble. In our work, the microbubble dispersions were generated using a spinning disk apparatus. This microbubble generator (MBG) uses a high speed motor that spins a 4 cm disk as speeds above 4000 RPM. The bubble size measurements were performed using laser diffraction technique.

Initially, a 2 L chemostat was operated with mixed SRB culture with syn-gas fed as gaseous feed. The pH, temperature, and agitation rate were 6.8, 30°C, and 300 rpm, respectively. The reactor effluent was recirculated through a hollow fiber membrane to recycle the cells back into the reactor. At these conditions, the maximum productivity of the reactor was 1.2 mmol SO_2/h•L with 100% conversion of SO_2 into H_2S. At this time, the syn-gas feed was fed as microbubbles into the reactor. With syn-gas fed as microbubbles, the reactor was able to convert more SO_2 into H_2S reaching maximum productivity of 2.1 mmol SO_2/h•L in 33 h (Fig. 3). The biomass concentration in the reactor prior to the microbubble operation was 5 g/L. The increase of productivity from 1.2 to 2.1 mmol/h•L within 33 h at the same biomass concentration of 5 g/L indicated that the mass transport was a limiting parameter in the above process.

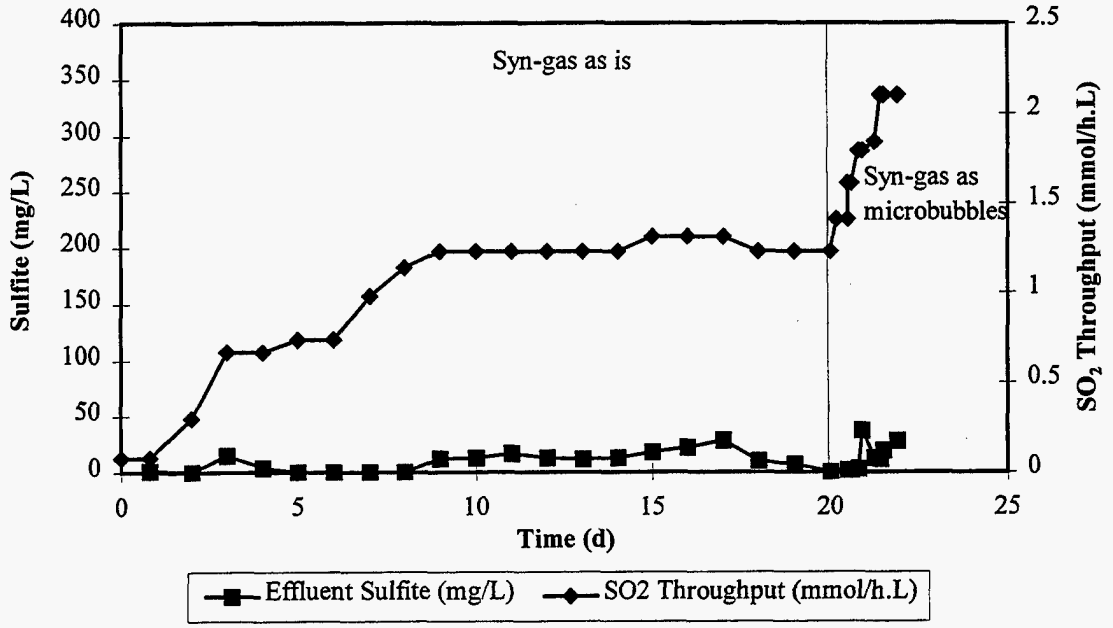

Figure 3. Sulfite conversion in a CSTR with syn-gas as feedstock. With syn-gas fed as microbubbles, the reactor productivity was increased from 1.2 to 2.1 mmol/h.L in 33 h.

Mass Transfer Properties in SO_2-reducing Bioreactors

The mass transfer property of syn-gas was studied in three different reactor systems: serum bottle, CSTR and trickle bed. In serum bottle experiments, the syn-gas (specifically H_2 and CO) utilization was determined using different biocatalyst concentrations to confirm that the rate of depletion of syn-gas was not due to the biocatalyst concentration. In a mass transport limits system, the rate of depletion will not depend on biocatalyst concentration. In CSTR, the mass transport property of syn-gas was determined by varying the flow rate of syn-gas. The mass transfer coefficients were 30.6 h^{-1} for CO and 74.64 h^{-1} for H_2 at agitation rate of 300 rpm. With similar experiments in trickle bed reactor, the mass transfer coefficients of syn-gas were 26.0 h^{-1} for CO and 20.2 h^{-1} for H_2.

Syn-Gas Conversion to Ethanol

The microorganism *Clostridium lungdhalii* was obtained from American Type Culture Collection (ATCC). The cells were revived in phosphate buffered basal (PBB) medium containing fructose under anaerobic conditions. Following this, the cells were

adopted to syn-gas by transferring to a another serum bottle containing non-fructose PBB medium with syn-gas as carbon and energy source in the headspace. The syn-gas utilization and ethanol production were observed indicating the conversion of syn-gas into ethanol. The culture were routinely transferred into new PBB medium with syn-gas as carbon and energy source and used as stock culture.

The working culture of *Clostridium lungdahlii* was prepared in 1 L chemostat by inoculating 5 mL of stock culture in 1 L PBB medium with yeast extract. The chemostat was maintained at temperature 37°C, pH 6.0 and agitation rate 200 rpm. The syn-gas was fed to the reactor at a rate of 10 mL/min. In the batch mode, ethanol production was as high as 2.0 g/L in 30 d, The reactor is presently operated in a continuous mode with cell recycle through ultra filtration system.

In trickle bed reactor operation, the liquid medium (PBB) and syn-gas is fed co-currently from top of the column containing the *Clostridium* cells immobilized in polymeric BIO-SEP porous beads. Subsequently, the reactor will be switched over to continuous mode with continuous feed of medium and syn-gas. The residence time of liquid medium and syn-gas will be varied to obtain maximum reactor productivity.

ACKNOWLEDGMENTS

This work was supported by the Advanced Research and Technology Development Program of the Office of Fossil Energy, U.S. Department of Energy under contract DE-AC05-96OR22464 with Lockheed Martin Energy Research Corp. Material contribution and analytical assistance from the DuPont Chemical Company and the Conoco Company, respectively, are greatly appreciated.

REFERENCES

P. T. Selvaraj, M. H. Little, & E. N. Kaufman, "Analysis of Immobilized Cell Bioreactors for Desulfurization of Flue Gases and Sulfite/Sulfate-Laden Wastewater" submitted for publication in the B*ioremediation*

P. T. Selvaraj, M. H. Little, & E. N. Kaufman, "Biodesulfurization of Flue Gases and other Sulfate/Sulfite Waste Streams using Immobilized Mixed Sulfate Reducing Bacteria" submitted for *Biotechnology Progress*.

REMOVAL OF HETEROATOMS AND METALS FROM HEAVY OILS BY BIOCONVERSION PROCESSES

E. N. Kaufman & A. P. Borole

INTRODUCTION

Biological removal of organic sulfur from crude oil offers an attractive alternative to conventional thermochemical treatment due to the mild operating conditions afforded by the biocatalyst. In order for biodesulfurization to realize commercial success, reactors must be designed which allow for sufficient liquid / liquid and gas / liquid mass transfer while simultaneously reducing operating costs. To this end, we have investigated the use of electro-spray reactors (Figure 1.) for the desulfurization of the model compound dibenzothiophene (DBT) as well as actual crude oil. The electro-spray reactor (ESR) creates an emulsion of aqueous biocatalyst (5 - 20 μm diameter droplets) in the organic phase by concentrating forces at the liquid /liquid interface rather than imparting energy to the bulk solution as is done in impeller mixed reactors. Experiments are being conducted in the ESR to determine the rates of DBT oxidation and are being compared to results obtained in a batch stirred reactor (BSR).

This program is a cooperative research and development program with the following companies: Baker Performance Chemicals (BPC), Chevron, Energy BioSystems, Exxon and Texaco. Energy BioSystems has been providing the biocatalyst for the experiments. Texaco is providing analytical support and Chevron is conducting economic analysis of the desulfurization process. BPC has addressed some of the safety issues in the experimental system. Unocal was also one of the CRADA members until February 97, when they teminated their participation due to lack of internal support for the project.

DISCUSSION OF CURRENT ACTIVITIES

Biodesulfurization experiments were conducted in the ESR and BSR to evaluate oxygen mass transfer limitations, effect of nutrients supply on biocatalyst activity and effect of biocatalyst density on rate of DBT oxidation. It was found that oxygen transport was not a limiting parameter in either the ESR or the BSR. Supplementing additional nutrients to the biocatalyst IGT-S8 had minimal effect on the 2-HBP production rate. The half-life of the biocatalyst was on the order of 10-24 hours. In order to explore the advantages of the high surface area achievable in the ESR, the biocatalyst density was increased over a 30-fold range to make the process mass transfer limited with respect to DBT. Oxygen mass transfer was not a limiting factor even at such high catalyst densities. Contrary to our expectations, comparison of the ESR with the BSR

showed equal activities in both reactors. Our experiments showed that the biocatalyst would have to be 10-20 times more active to be able to demonstrate the benefits of the ESR. Aditionally, the biocatalyst was found to be extracted into the organic phase, which may be a major factor why ESR did not show improved performance over BSR.

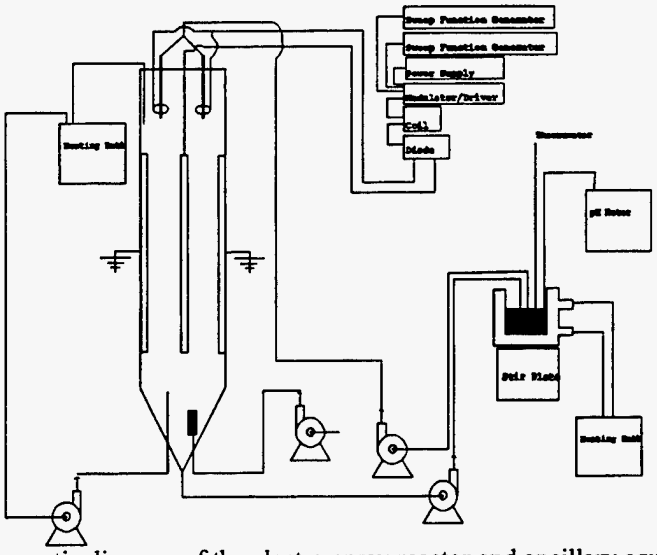

Figure 1. Schematic diagram of the electro-spray reactor and ancillary equipment.

Experiments were conducted with Van Texas and Sand Flat crude oil in the BSR. Analysis of the samples by Unocal has shown decreases of up to 60-90% in unsubstituted, C1, and C2 substituted DBTs in Sand Flat oil after 48 hours of treatment and decreases of > 90% for unsubstituted, C1, and C2 substituted DBTs in Van Texas oil.

Further experiments will be conducted using mineral oil as an organic phase to better simulate crude oil in the desulfurization experiments. Exxon has developed a biocatalyst by introducing a dszC gene (responsible for the biochemical pathway of conversion of DBT to DBT sulfone) into an E. Coli organism. Exxon will be bringing the biocatalyst to ORNL to test it in the ESR. Energy BioSystems has also promised to provide ORNL with a biocatalyst having higher activity than IGT-S8. ORNL and Energy BioSystems are in the process of making secrecy agreements to make this feasible. We are also planning to conduct some experiments with crude oils having higher API gravity (~16-17), which will be obtained from the oil companies.

ACKNOWLEDGMENTS

This work was supported by the Office of Oil & Gas Processing, U.S. Department of Energy under contract DE-AC05-96OR22464 with Lockheed Martin Energy Research Corp.

REFERENCES

E.N. Kaufman, J.B. Harkins, M. Rodriguez, S.E. Murphy, P.T. Selvaraj and C. Tsouris, "Development of an Electro-Spray Bioreactor for Crude Oil Processing." 1997, *Fuel Processing Technology*. in press.

H.M. Lizama and E.N. Kaufman, "Biotreatment of H_2S in the Petroleum Industry," in D.S. Holmes and R.W. Smith (eds.), *Minerals Bioprocessing II*, The Minerals, Metals and Materials Society, Warrendale, PA, 1995, 241-253.

Tsouris, C., H. M. Lizama, M. A. Spurrier, T. L. Takeuchi, and T. C. Scott, "Hydrodynamics of Bioreactors Systems for Liquid-Liquid Contacting," *Appl. Biochem. And Biotech.* (1996) vol. 57, 581-592.

Tsouris, C., V. M. Shah, M. A. Spurrier, and M. K. Lee, "Experiments on Electrostatic Dispersion of Aqueous Droplets into an Organic Stream," *Chem. Eng. Commun.* (1997). in press.

H.M. Lizama, L.A. Wilkins, and T.C. Scott, "Dibenzothiophene Sulfur Can Serve as the Sole Electron Acceptor During Growth by Sulfate-Reducing Bacteria," (1995) *Biotechnology Letters,* **17**: 113-116

RENEWABLE HYDROGEN PRODUCTION FOR FOSSIL FUEL PROCESSING

James Weifu Lee and Elias Greenbaum

INTRODUCTION

Present energy systems are heavily dependent on fossil fuels. The processing of fuels, however, is heavily dependent on the use of molecular hydrogen as a chemical feedstock, the source of which is itself a fossil fuel, usually natural gas. It is the objective of this research program to produce renewable hydrogen via photosynthetic water splitting. In principle, hydrogen production by biophotolysis of water can be an ideal solar energy conversion system for sustainable development of human activities in harmony with the global environment. In photosynthetic hydrogen production research, there are currently three main efforts: (1) direct photoevolution of hydrogen and oxygen by photosynthetic water splitting using the ferredoxin/hydrogenase pathway, (2) dark hydrogen production by fermentation of organic reserves such as starch that are generated by photosynthesis during the light period, and (3) Two-stage hydrogen production in a combined fermentative and light-driven algae/bacteria system. In this chapter, the advantages and challenges of these approaches for hydrogen production are discussed in relation to a new opportunity brought by our recent discovery of a new photosynthetic water-splitting reaction [*Nature*, **373**, 438-441 (1995); *Science*, **273**, 364-367 (1996)], which, theoretically, has twice the energy efficiency of conventional water splitting via the two-light-reaction Z-scheme of photosynthesis.

Hydrogen is a versatile, clean, and environmentally acceptable energy carrier. It can be produced by photolysis of water, an inexpensive and inexhaustible raw material. Photolysis can be performed using either inorganic systems such as semiconductors or living organisms such as cyanobacteria or green microalgae. It is now clear that green algae are probably better for H_2 production than cyanobacteria, since the latter use the more energy-intensive enzyme, adenosine triphosphate (ATP)–requiring nitrogenase, for production of H_2. Based on a recent feasibility analysis (*1*), H_2 production by green algae can be more cost-effective than semiconductor photovoltaic electronics. The discussion in this article is focused on H_2 production by photosynthetic water splitting.

FUNDAMENTALS OF PHOTOSYNTHESIS AND H_2 PRODUCTION

Photosynthesis is the fundamental biological process that converts the electromagnetic energy of sunlight into stored chemical energy that supports essentially all life on Earth. In green algae as in higher plants, photosynthesis occurs in a specialized organelle, the chloroplast. Light energy captured by the photosynthetic reaction centers is stored predominately by reduction of CO_2, using water as the source of electrons. As illustrated in Figure 1, the key components of the photosynthetic apparatus involved in light absorption and energy conversion are embedded in thylakoid membranes inside the chloroplast. They are two chlorophyll (chl)–protein complexes, Photosystem I (PSI) with a reaction center, P700, and Photosystem II (PSII) with another distinct reaction center, P680. According to the current and prevailing concept of oxygenic photosynthesis, the Z-scheme, first proposed by Hill and Bendall (*2*) and now described in many textbooks (*3–7*), PSII can split water and reduce the plastoquinone (PQ) pool, the cytochrome (Cyt) b/f complex, and plastocyanin (PC), while PSI can reduce ferredoxin (Fd)/nicotinamide adenine dinucleotide phosphate ($NADP^+$) and oxidize PC, the Cyt b/f complex, and the PQ pool. As a result, the electrons derived from water splitting are transferred to Fd/$NADP^+$, which provides the reducing power for reduction of CO_2 to carbohydrate in the stromal region of the chloroplast by a series of enzymatic reactions collectively called the Calvin cycle. Electron transport in the membrane is coupled with proton transport from the stroma into the lumen, generating a proton gradient across the thylakoid membrane. The proton gradient drives phosphorylation through the coupling factor CF_o-CF_1 to make essential ATP for the reduction of CO_2. This is the common description of oxygenic photosynthesis.

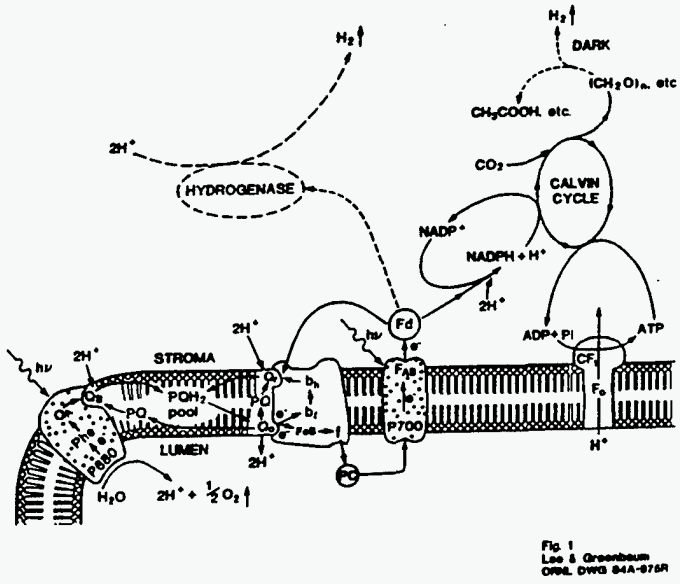

Fig. 1. Conventional photosynthetic pathway based on the Z-scheme.

In many green algae, such as *Chlamydomonas*, there is a hydrogenase that can be induced under anaerobic conditions (*8*, *9*). The hydrogenase can catalyze the reduction of protons to produce H_2 using electrons from the reduced Fd as shown in Figure 1. Since protons are also produced by water splitting at PSII, the net result of this Fd/hydrogenase pathway is simultaneous photoevolution of H_2 and O_2, using water as the substrate and light energy as the driving force.

Under anaerobic conditions and darkness, H_2 may be produced by fermentative metabolic degradation of organic reserves such as starch (Fig. 1). This fermentative metabolic process has been well studied (*10*, *11*). Since the substrate of the fermentative pathway is generated photosynthetically by reduction of CO_2, the net result of the sequential process, photosynthesis and fermentation, is still splitting water to H_2 and O_2, with CO_2 as an intermediate.

HYDROGEN PRODUCTION BY DIRECT PHOTOSYNTHETIC WATER SPLITTING

The discovery of photosynthetic H_2 production is based on the classic work of Gaffron and Rubin in 1942 (*12*). However, only since 1973, at the time of the energy crisis, has photosynthetic H_2 production been investigated as a potential source of energy (*13–41*). Sustained photoevolution of H_2 and O_2 by microalgae was first demonstrated by Greenbaum in 1980 (*15*). Under anaerobic conditions, sustained photoevolution of H_2 and O_2 in microalgae can be readily demonstrated using a reactor-flow-detection system (Fig. 2). Figure 3 presents a typical measurement of H_2 and O_2 production in *Chlamydomonas* in a helium atmosphere using the reactor-flow-detection system. The data clearly demonstrate that photoevolution of H_2 and O_2 can occur stably with a stoichiometric ratio of H_2 to O_2 of nearly 2:1 as expected for water splitting. Photoevolution of H_2 and O_2 can be sustained for weeks.

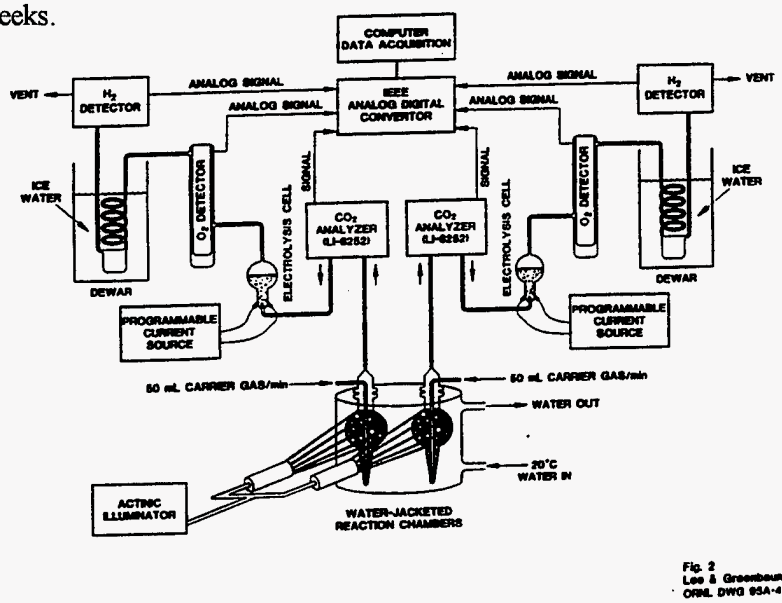

Fig. 2. Schematic illustration of a dual-reactor-flow system for simultaneous detection of H_2, O_2, and CO_2. The dual-reactor system permits two independent experiments to be performed simultaneously.

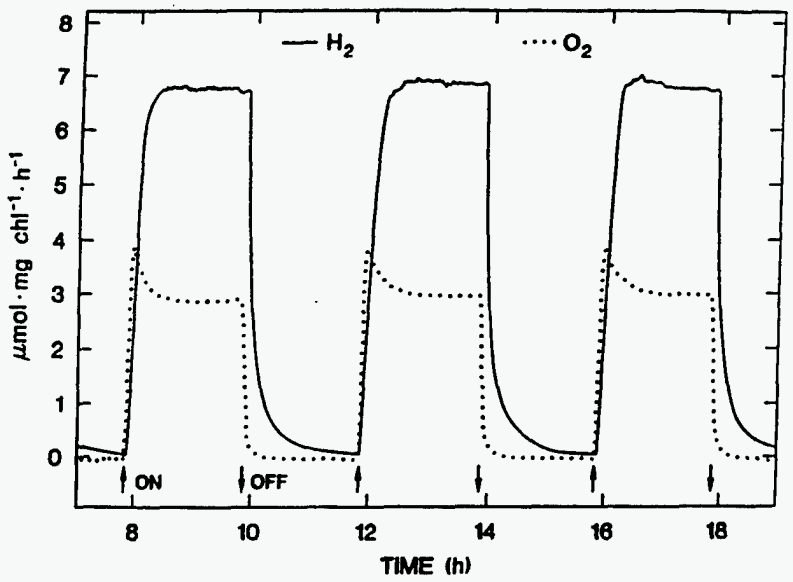

Fig. 3. Sustained photoassimilation of H_2 and O_2 in *Chlamydomonas* 137c under anaerobic conditions and in the absence of CO_2. (Reproduced with permission from Ref. *35*, Copyright 1996 Macmillian Magazines Limited.)

The advantage of the simultaneous H_2 and O_2 photoevolution is that it can potentially have a high energy conversion efficiency since electrons energized by the light reactions are used directly in the reduction of protons to produce H_2 by the Fd/hydrogenase pathway (Fig. 1). However, H_2 production by this mechanism requires gas product separation since both H_2 and O_2 are produced simultaneously in the same volume. Furthermore, until an O_2-insensitive hydrogenase is developed (*42*, *43*), the O_2 concentration in the algal suspension has to be kept low to maintain H_2 production since the hydrogenase is sensitive to O_2. Therefore, an efficient and inexpensive technique to separate and remove gas products is needed.

Another important aspect is that the photoevolution of H_2 and O_2 in microalgae is often saturated at a relatively low actinic intensity. This is probably due to three factors: (1) accumulation of a back-proton gradient because of the limited permeability of the thylakoid membrane to protons and the loss of ATP utilization due to the inactivation of the Calvin cycle, (2) partial inactivation of PSII activity owing to loss of CO_2 binding at a regulatory site on the PSII reaction center in the absence of CO_2, and (3) the normal nonlinear response of the light saturation curve of photosynthesis. Therefore, the potential still exists to improve the efficiency of photosynthetic H_2 production. Further research is needed to eliminate these limiting factors. The first limitation may be solved on a short-term basis by using an appropriate proton uncoupler that dissipates the proton gradient across the thylakoid membrane (*44*), whereas the second could be overcome by eliminating the requirement of CO_2 binding through molecular engineering. The third limitation can, in principle, be overcome by reducing the antenna size of the photosynthetic reaction centers.

To avoid gas product separation and to increase efficiency, we have previously proposed a PSI and PSII reactor system that can potentially produce H_2 and O_2 in two separate compartments (*32*). This reactor system is based on the structure and function of isolated PSI and PSII reaction centers and on the catalytic activity of metallic platinum and osmium for H_2 production (*45–49*). As illustrated in Figure 4, O_2 and protons are produced by water splitting by an array of PSII reaction centers in the PSII compartment. The electrons acquired from water splitting are wired to the reducing side of a PSI array where the electrons are energized again by PSI photochemistry. The PSI-energized electrons are then used to evolve H_2 by platinum- (or osmium-) catalyzed reduction of protons that come from the PSII compartment through a proton-conducting channel. As described previously, this system should be able to operate continuously since the number of protons and electrons generated can be balanced with the number consumed. We believe this is an important direction for future research. In this laboratory, research progress has been made in this direction (*50–52*). Recently, we have constructed a two-dimensional spatial array of PSI reaction centers on a gold surface at nanometer scale by a platinization anchoring technique (*52*).

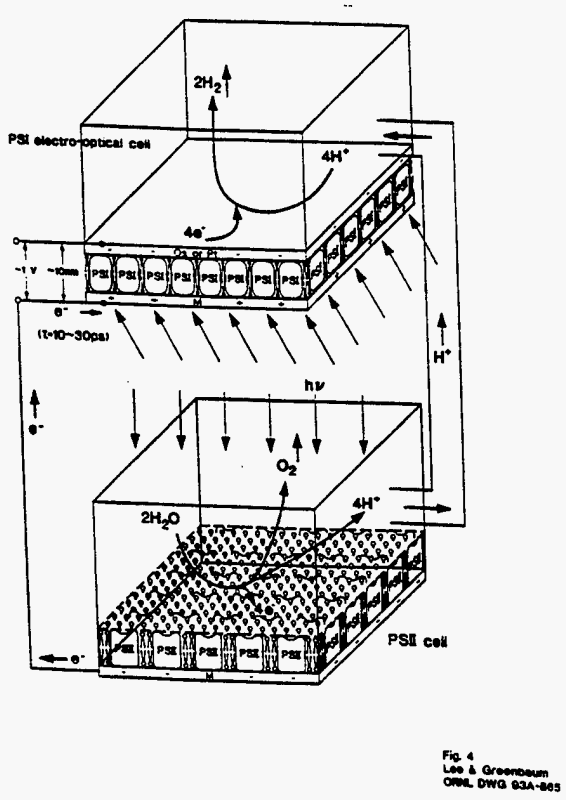

Fig. 4. A photosynthetic reactor system made of PSI and PSII electrooptical cells for production of H_2 and O_2 in separate compartments. (Reproduced with permission from Ref. *32*, Copyright 1996 Human Press, Inc.)

HYDROGEN PRODUCTION BY DARK FERMENTATION OF PHOTOSYNTHETIC PRODUCT

An advantageous feature of fermentative H_2 production is its temporal separation from photosynthesis (Fig. 1). That is, O_2 evolution and CO_2 photoassimilation by photosynthesis occur during the day, whereas fermentative H_2 production by degradation of photosynthetic product (starch) can occur during the night. By taking advantage of this temporal separation between O_2 evolution (day) and H_2 production (night), one can potentially develop an algal H_2 production technology that avoids the problem of gas product separation. This approach is a major project by scientists in Japan (*22*, *29*, *33*, *34*), and important progress has been made. Miura et al. (*34*) have demonstrated algal fermentative H_2 production that is temporally separated from photosynthesis (CO_2 fixation and O_2 evolution), using a combination of green algae and photosynthetic bacteria comprising over 100 L of green algae.

The challenge, as always, in this fermentative H_2 production approach is the efficiency. Figure 5 presents a typical measurement of photosynthesis and fermentative H_2 production in wild-type *Chlamydomonas* in a helium atmosphere in the presence of CO_2 under cycles of 12 h of moderate actinic illumination (PAR, 200 $\mu E \cdot m^{-2} \cdot s^{-1}$) and 12 h of darkness, using the flow-detection system (Fig. 2). From the data, it can be clearly seen that the rate of fermentative H_2 production is very slow—less that 5% of the rate of oxygen evolution during the day. Therefore, enhancing the rate of dark fermentative H_2 production is the key challenge.

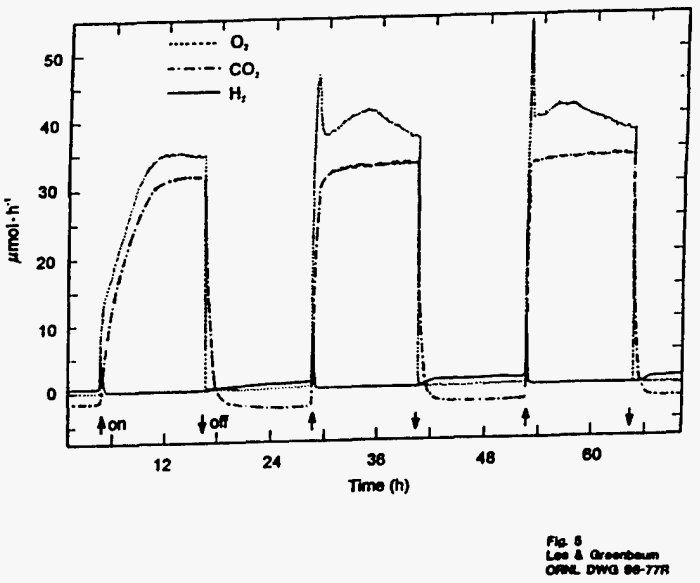

Fig. 5. Photoassimilation of CO_2 and evolution of H_2 and O_2 by *Chlamydomonas* 137c in the presence of 700 ppm CO_2 in helium.

NEW OPPORTUNITIES BROUGHT BY A RECENT DISCOVERY

In this laboratory, our current research has focused on improving the energy efficiency of photosynthetic hydrogen production. Using mutants of *Chlamydomonas* that lack PSI but contain PSII, we have demonstrated a new type of photosynthesis: that is, photoevolution of O_2 and H_2 and photoassimilation of CO_2 by PSII light reaction alone (*35*, *36*). This work builds on the original demonstration by Biochenko et al. (*53*) of hydrogen and oxygen transients in PSI-deficient mutants of *Chlamydomonas*. Based on studies of the electron transport pathway (Lee and Greenbaum, 1996, unpublished), the newly discovered water-splitting reaction for H_2 and O_2 production (reaction 1) or for CO_2 fixation and O_2 evolution (reaction 2) may require only half the number of photons of conventional Z-scheme photosynthetic reactions 3 and 4.

Newly Discovered PSII Photosynthesis:

$$H_2O + 2\,h\nu \longrightarrow H_2 + 1/2\,O_2 \qquad \Delta G^\circ = -115 \text{ kJ/mol} \qquad (1)$$
Energy efficiency = 67.4% (λ = 680 nm)

$$CO_2 + H_2O + 4\,h\nu \longrightarrow 1/6(C_6H_{12}O_6) + O_2 \qquad \Delta G^\circ = -224 \text{ kJ/mol} \qquad (2)$$
Energy efficiency = 68.2% (λ = 680 nm)

Conventional Z-scheme Photosynthesis:

$$H_2O + 4\,h\nu \longrightarrow H_2 + 1/2\,O_2 \qquad \Delta G^\circ = -446 \text{ kJ/mol} \qquad (3)$$
Energy efficiency = 33.7% (λ = 680 nm)

$$CO_2 + H_2O + 8\,h\nu \longrightarrow 1/6(C_6H_{12}O_6) + O_2 \qquad \Delta G^\circ = -927 \text{ kJ/mol} \qquad (4)$$
Energy efficiency = 34.1% (λ = 680 nm)

Both reactions 1 and 2 have a significantly large negative value of ΔG°. They should be able to occur spontaneously. Therefore, although the discovery is surprising and novel, it still obeys the laws of thermodynamics. Since reactions 1 and 2 require half the number of photons of reactions 3 and 4, the discovery can potentially lead to H_2 production and/or CO_2 fixation technology with twice the energy conversion efficiency of conventional Z-scheme photosynthesis.

The demonstration of photosynthesis by a single light reaction proved that a single light reaction can span the potential difference between water oxidation and proton reduction for sustained evolution of H_2 and O_2, which was previously thought to be difficult to achieve (*54*). Therefore, we can now propose a new reactor system containing biometallocatalysts that requires only a single type of photochemical reaction center (Fig. 6) but is able to perform the same function as the reactor system

in Fig. 3. As illustrated in Figure 6, when water is split to O_2 and protons by PSII, electrons from the reducing side of PSII should, neglecting resistive loss, be able to reduce protons on a platinum catalyst surface to evolve H_2 in a separate compartment without PSI.

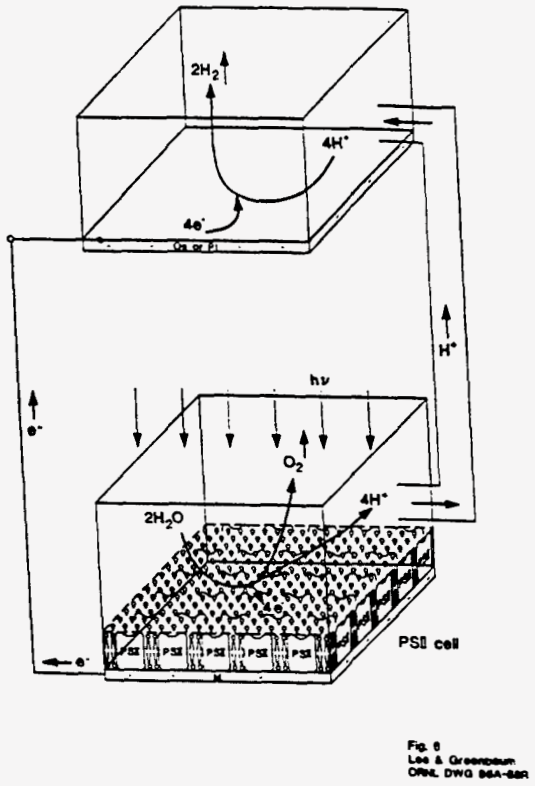

Fig. 6. A proposed biometallocatalytic reactor system for production of H_2 and O_2 in separate compartments by a single light reaction (PSII).

At low light intensity and under ideal laboratory conditions, the maximum sunlight to H_2 energy conversion efficiency for Z-scheme photosynthesis has been measured to be about 10% (*55*). From a practical point of view, application of PSII photosynthesis can potentially double the sunlight conversion efficiency from 10 to 20% (*35*). This potentially higher efficiency can put photosynthetic H_2 production in a much more competitive position vis-à-vis other solar technologies. Moreover, since PSII photosynthesis can also photoassimilate CO_2, it should also be able to improve the energy efficiency of photosynthesis (CO_2 fixation) in general. Therefore, the discovery also provides a new opportunity to improve energy efficiency for production of H_2 by the photosynthesis/fermentation combined system of Miura et al. (*34*).

REFERENCES

1. Benemann, J. R., *Xth Proc. World Hydrogen Energy Conf.*, pp. 931–40, 1995.

2. Hill, R. and Bendall, F., *Nature* **186**, 136–137, 1960.

3. Stryer, L., *Biochemistry*, 4th ed.; W. H. Freeman and Company: New York, NY, pp. 617–618, 658–664, 676–677, 1995.

4. Salisbury, F. B. and Ross, C. W., *Plant Physiology*, 3rd ed.; Wadsworth Publishing Company: Belmont, CA, pp. 191–194, 1985.

5. Goodwin, T. W. and Mercer, E. I., *Introduction to Plant Biochemistry*, 2nd ed.; Pergamon Press: Oxford, UK, pp. 117–124, 1986.

6. Alberts et al., *Molecular Biology of the Cell*; Garland Publishing, Inc.: New York, NY, pp. 517–519, 1983.

7. Darnell, J., Lodish, H., and Baltimore, D., *Molecular Cell Biology*; Scientific American Books, Inc.: New York, NY, pp. 901–903, 1986.

8. Roessler, P.G. and Lien, S., *Plant Physiol.* **76**, 1086–1089, 1984.

9. Boichenko, V. A. and Hoffmann, P., Photosynthetica **30**, 527–552, 1994.

10. Gfeller, R. P.and Gibbs, M., *Plant Physiol.* **75**, 212–218, 1984.

11. Chen, C., Ph.D. Dissertation, Brandeis University, Waltham, MA, pp. 99–109, 1992.

12. Gaffron, H. and Rubin, J., J. Gen. Physiol. **26**, 219–240, 1942.

13. Greenbaum, E., *Science* **196**, 879–878, 1977.

14. Bishop, N. I., Frick, M., and Jones, L. W., In *Biological Solar Energy Conversion*; Mitsui, A., Miyachi, S., and San, P. A., and Tamura, S., Eds.; Academic Press: New York, NY, pp. 2–22, 1977.

15. Greenbaum, E., *Biotechol. Bioeng. Symp.* **10**, 1–13, 1980.

16. Bamberger, E. S., King, D., Erbes, D., and Gibbs, M. *Plant Physiol.* **69**, 1268–1273, 1982.

17. Greenbaum, E. and Ramus, J., *J. Phycol.* **19**, 53–57, 1983.

18. Greenbaum, E., Guillard, R. R. L., and Sunda, W. G., *Photochem. Photobiol.* **37(6)**, 649–655, 1983.

19. Hoopen, H. T., Snellink, L. J., Gemert, J. V, Fuchs, A., and Roels, J. A., *Prog. Ind. Microbiol.* **20**, 191–196, 1984.

20. Greenbaum, E., *Photobiochem. Photobiophys.* **8**, 323–332, 1984.

21. Aparicio, P. J., Azuara, M. P., Ballesteros, A., and Fernadez, V. M., *Plant Physiol.*, **78**, 803–806, 1985.

22. Miura, Y., Ohta, S., Mano, M., and Miyamoto, K., *Agric. Biol. Chem.* **50(11)**, 2837–2844, 1986.

23. Mahro, B. and Grimme, L. H., *Arch. Microbiol.* **144**, 25–28, 1986.

24. Greenbaum, E., In Algae And Human Affairs, Lembi, C. A., and Waaland, R. J., Eds.; Cambridge University Press: Cambridge, MA, pp. 283–304, 1988.

25. Graves, D. A., Reeves, M. E., and Greenbaum, E., *Plant Physiol.* **87**, 603–608, 1988.

26. Graves, D. A., Tevault, C. V., and Greenbaum E., *Photobiochem. Photobiophys.* **50**, 571–576, 1989.

27. Greenbaum, E., *Adv. Hydrogen Technol.* **2**, 743–754, 1990.

28. Graves, D. A., Spradlin, G. M., and Greenbaum, E., *Photobiochem. Photobiophys.* **52**, 585–590, 1990.

29. Miura, Y., Saitoh, C., and Matsuoka, K., *Biosci. Biotech. Biochem.* **56**, 751–754, 1992.

30. Cinco, R. M., MacInnis, J. M., and Greenbaum, E., *Photosyn. Res.* **38**, 27–33, 1993.

31. Lee, J. W., Blankinship, S. L., and Greenbaum, E., *Appl. Biochem. Biotechnol.* **51/52**, 379–385, 1995.

32. Lee, J. W. and Greenbaum, E., *Appl. Biochem. Biotechnol.* **51/52**, 295–305, 1995.

33. Miura, Y., *Process Biochem.* **30**, 1–7, 1995.

34. Miura, Y. et al., *Energy Convers. Mgmt.* **36**, 903–906, 1995.

35. Greenbaum, E., Lee, J. W., Tevault, C. V., Blankinship, S. L., and Mets, L. J., *Nature* **376**, 438–441, 1995.

36. Lee, J. W., Tevault, C. V., Owens, T. G., and Greenbaum, E., *Science* **273**, 364–367, 1996.

37. Lien, S. and San, P. A., "An Inquiry into Biophotolysis of Water to Produce Hydrogen," NSF RANN Grant GI 40253, Indiana University, Boomington, IN.

38. Weaver, P. F., Lien, S., and Seibert, M., *Sol. Energy* **24**, 3–45, 1980.

39. Rao, K. K. et al., *J. Photochem. Photobiol. B: Biol.* **5**, 379–389, 1990.

40. Hall, D. O. and Rao, K. K., *Chimicaoggi* , 41–47, 1989.

41. Hall, D. O., Rao, K. K., and Park, I. H., *Proc. 8th Intl. Conf. Photochem. Convers. Storage Sol. Energy*, Palermo, Italy, 1990.

42. McBride, A. C., Lien, S., Togasaki, R. K., and San, P. A., In *Biological Solar Energy Conversion*, Mitsui, A., Miyachi, S., San, P. A., and Tamura, S., Eds.; Academic Press: New York, NY, 1977.

43. Ghirardi, M. L., Togasaki, R. K., and Seibert, M., *Appl. Biochem. Biotechnol.*, in press, 1996.

44. Nicholls, D. G. and Ferguson, S. J., *Bioenergetics*, 2nd ed.; Academic Press Inc.: San Diego, CA, pp. 31–33, 1992.

45. Greenbaum, E., *Science* **230**, 1373–1375, 1985.

46. Greenbaum, E., *J. Phys. Chem.* **92**, 4571–4574, 1988.

47. Greenbaum, E., *J. Phys. Chem.* **94**, 6151–6153, 1990.

48. Greenbaum, E., *J. Phys. Chem.* **96**, 514–516, 1992.

49. Lee, J. W., Tevault, C. V., Blankinship, S. L., Collins, R. T., and Greenbaum, E., *Energy Fuels* , **8(3)**, 770–773, 1994.

50. Lee, J. W., Lee, I., Laible, P. D., Owens, T. G., and Greenbaum, E., *Biophys. J.* **69**, 1–8, 1995.

51. Lee, I., Lee, J. W., Warmack, R. J., Allison, D. P., and Greenbaum, E., *Proc. Natl. Acad. Sci. USA* **92**, 1965–1969, 1995.

52. Lee, J. W., Lee, I., and Greenbaum, E., *Biosensors Bioelectronics* **11**, 375–387, 1996.

53. Biochenko, V. A., Allakhverdiev, S. I., Ladygin, V. G., and Klimov, V. V., *Dokl Akad Nauk SSSR* **290**, 995–998, 1986.

54. Bolton, J. R., *Science* **202**, 705–711, 1978.

55. Greenbaum, E., *Biophys. J.* **54**, 365–368, 1988.

BIOLOGICAL QUALITY OF SOILS CONTAINING HYDROCARBONS AND EFFICACY OF ECOLOGICAL RISK REDUCTION BY BIOREMEDIATION ALTERNATIVES

A. J. Stewart, B. E. Sample, G. E. Napolitano, G. W. Suter, II, L. F. Wicker, J. E. Richmond, K. T. Klasson, and V. R. Parker

INTRODUCTION

This project provides data and technical guidance to Petroleum Environmental Research Forum (PERF), a consortium of petroleum-producing companies, about environmentally acceptable endpoints in relation to ecological risk of petroleum hydrocarbon residuals in soils. Our project focuses on the relationship between 'chemically available' and 'biologically available' measurements of petroleum hydrocarbon compounds in soils, from a risk-based perspective. Clean-up standards for soils contaminated with petroleum hydrocarbons compounds typically are based either on concentrations of total petroleum hydrocarbons (TPH), or on concentrations of particular chemicals of concern (e.g., benzene, benzo[a]pyrene, etc.), as measured in solvent extracts of soil samples. However, various studies indicate that chemicals present in TPH may be able to permeate into soil particles. If this occurs, the particle-embedded hydrocarbons may be extractable by use of organic compounds, and yet be unavailable biologically. This condition clearly would reduce risk to biological receptors, which should be taken into consideration in (1) setting risk-based clean-up standards, and (2) developing and verifying efficacy of bioremediation clean-up techniques. These ideas serve as the focus for our studies.

DISCUSSION OF CURRENT ACTIVITIES

Efforts in FY 1996 included work on four tasks: (1) development of an ecological risk-assessment framework that could be used to guide cost-effective clean-up strategies for TPH-contaminated soils; (2) biological characterization of various TPH-contaminated soils, based on toxicity to earthworms in standardized tests; (3) development of chemical analysis methods for rapid and quantitative assessment of TPH constituents in soils; and (4) a "white paper" review of the effectiveness of bioremediation techniques for meeting clean-up objectives at petroleum-contaminated sites. Progress in these four areas is summarized below.

Development of ecological risk assessment framework

A document titled "A Framework for Assessing Ecological Risks of Petroleum-Derived Materials in Soil" was prepared and distributed for internal and external review before being published and distributed as an ORNL publication in May, 1997[1]. Arrangements are now being made to "ground truth" ideas outlined in the ecological risk assessment framework document by conducting simple biological surveys at petroleum-contaminated sites. The site surveys will involve close collaboration with site representatives at petroleum producing and refining facilities, and are expected to occur during late spring and early summer, 1997.

Testing of TPH-contaminated soils for toxicity to earthworms

Ten soil samples contaminated with TPH compounds and nine non-contaminated reference soils were shipped to ORNL and tested for acute and chronic toxicity to the earthworm, *Eisenia foetida*. The data from these tests were analyzed and submitted formally to members of the PERF's Environmentally Acceptable Endpoints Work Group in December, 1996. Endpoints for the 21-day tests included earthworm survival, growth and reproduction; the test method followed procedures outlined in an earlier publication[2], and was applied to mixtures of contaminated soil and that soil's non-contaminated reference, to obtain dose-response information.

Only four of the ten petroleum-contaminated soil samples showed evidence for toxicity. Earthworms lost weight in higher concentrations of these four soils, but gained weight in lower concentrations of the soils. The concentration of solvent-extractable organics associated with zero earthworm growth, in the four soils that had good dose-response relationships for earthworm growth, ranged from about 180 mg/kg to 5,600 mg/kg. Several of the soils that contained moderately high concentrations of petroleum hydrocarbon compounds did not adversely affect the survival, growth, or reproduction of *Eisenia*. Conversely, some of the soils that contained lower concentrations of petroleum hydrocarbons inhibited earthworm growth or reproduction. The reasons for these differences could include (1) the presence or absence of co-contaminants; (2) bioavailability differences due to contaminant binding; (3) soil-to-soil differences in the concentrations of specific petroleum hydrocarbon chemicals; and/or (4) intrinsic differences among soils unrelated to contaminants (e.g., the relative proportions of sand and clay, the concentrations of organic matter,

etc.). One significant finding from studies in this task was that one cannot reliably estimate "risk to *Eisenia*" by measurements of TPH concentration alone.

Several other experiments were conducted to identify non-contaminant factors that might account for soil-to-soil differences in earthworm growth and reproduction. These experiments showed that age of the food (fermented alfalfa) and the amount of food added to the test chamber influenced earthworm growth and reproduction. The interaction term between soil type and food level was also highly significant. In some soils, 1 g of food (fermented alfalfa) per 150 g of soil containing a pair of earthworms is not sufficient to saturate either growth or reproduction. We also found that the test method's recommended hydration step (pre-test hydration is used to saturate the worms and allow them to purge their gut contents) was suspect. Growth of the worms is estimated by change in weight over the 21-day test, and error in initial wet-weight values of the worms due to differences in initial hydration can approach 17%. From the results of these experiments, we recommend three changes in the published method: (1) reducing pre-test earthworm hydration duration from 24 h to 8 h; (2) increasing the amount of food added per replicate, from 1 g to 5 g; and (3) reducing the fermenting time for alfalfa added as food, from two weeks to one week. The results of these experiments are now summarized in a manuscript that will be submitted to *Environmental Toxicology and Chemistry*.

Chemical analysis methods for assessment of TPH constituents in soils

The PERF soils that were tested for toxicity to earthworms were also analyzed for four classes of TPH constituents -- saturated hydrocarbons, aromatic hydrocarbons, and resins and asphaltenes -- by use of an Iatroscan lipid analyzer, after we had developed a satisfactory protocol for soil-extraction and chromatographic separation. Through experiments, we found that the following methods yielded excellent separation of the four TPH classes: (1) overnight extraction of soil with 1:1 (v:v) methanol and chloroform; (2) spotting 1 to 2 μL of soil extract on a silica-coated quartz Chromarods (III); (3) conducting three successive chromatographic developments, using solvent systems of increasing polarity (hexane, toluene, and dichloromethane:methanol). After separation as described above, the hydrocarbon constituents were quantified by flame ionization detection, at a rate of up to 10 samples per hour. A report outlining the method, and summarizing results obtained by applying the method to the PERF soils, was prepared and submitted to PERF

Environmentally Acceptable Endpoints Work Group members in June, 1996. Several other experiments and validation tests were completed later that summer to verify the procedure. We then prepared a draft manuscript outlining the method. This manuscript is in internal review, and will be submitted to *Environmental Toxicology and Chemistry.*

Effectiveness of bioremediation alternatives for TPH in soils

Work on this task area, previously delayed for funding reasons, began in autumn, 1996. An extensive literature search has been conducted to identify cases where bioremediation alternatives have been used, or are being used, to meet environmental clean-up objectives at sites contaminated with petroleum hydrocarbons. For more than 100 such cases, we have now identified key information, including a principal technical contact; facts about the site (e.g., location, type of contaminant, extent of contamination, etc.); the type of bioremediation method(s) used; regulatory driver and clean-up objectives, etc. Presently, starting with cases listed as "complete" based on the search above, the principal technical contacts for the cases are being contacted, by telephone, for additional information. A 20-point questionnaire has been developed to help standardize the information obtained by this means: it includes detailed questions relating to "lessons learned", the types of data collected to support risk-based clean-up objectives, procedures for monitoring the effectiveness of the bioremediation method, etc. Personnel in the Environmental Protection Agency actively involved with bioremediation projects be contacted to help decide how the information we collect could be most effectively compiled to maximize its value to those interested in bioremediation of petroleum compounds, from regulatory and user perspectives.

Miscellaneous progress

Co-ordination and effective communication of research findings among PERF participants is an important aspect of this project's success due to the project's fundamentally collaborative nature. In this reporting period, the following trips were made to foster this condition:

Drs. A. J. Stewart and G. E. Napolitano met with PERF participants at DuPont facilities in Delaware on July 9, 1996. Data from recently completed PERF soil biological and chemical characterization activities were presented by the two ORNL representatives.

Dr. B. E. Sample attended a PERF Task Work Group Leaders Meeting in Chicago, hosed by the Gas Research Institute, on July 16, 1996. At this meeting, Dr. Sample outlined weight-of-evidence approaches, based on biological survey data, that could be used to support ecological risk assessments of petroleum-contaminated sites.

A. J. Stewart and G. E. Napolitano attended the annual meetings of the Society for Environmental Toxicology and Chemistry, in November 17-22, 1996, in Washington, D.C; there, they presented posters summarizing data from the PERF soil toxicity tests and Iatroscan hydrocarbon-class analyses.

A. J. Stewart attended the PERF Annual Meeting on March 25, and the PERF/American Petroleum Institute (API) Workshop on Particulates on March 26, 1997; these meetings were hosted by ORNL, in Oak Ridge, Tennessee. During the PERF/API workshop, A. Stewart presented a talk titled "Particles, Toxic Contaminants, and a Biodetector for Particulates in Freshwater Studies".

A. J. Stewart attended a PERF (Environmentally Acceptable Endpoints for Contaminated Soils Task 4/Task 5 Work Group) meeting in Houston, Texas, hosted by Shell Development (Westhollow Technology Center), during April 2-3, 1997. Project updates were provided by a number of speakers. Fruitful discussion also identified several areas for future research projects relevant to PERF needs.

REFERENCES

(1) Suter, G. W., II., "A Framework for Assessing Ecological Risks of Petroleum-Derived Materials in Soils", ORNL/TM-13408, Oak Ridge National Laboratory, Oak Ridge, TN, 1997.

(2) M. H. Gibbs, L. F. Wicker and A. J. Stewart, "A method for assessing sublethal effects of contaminants in soils to the earthworm, *Eisenia foetida*," *Environ. Tox. Chem.*, **15**,360-368 (March, 1996).

NATURAL GAS AND OIL TECHNOLOGY PARTNERSHIP SUPPORT

T. W. Schmidt

INTRODUCTION

The Natural Gas and Oil Technology Partnership expedites development and transfer of advanced technologies through technical interactions and collaborations between the national laboratories and the petroleum industry - majors, independents, service companies, and universities.

The Partnership combines the expertise, equipment, facilities, and technologies of the Department of Energy's national laboratories with those of the U.S. petroleum industry. The laboratories utilize unique capabilities developed through energy and defense R&D including electronics, instrumentation, materials, computer hardware and software, engineering, systems analysis, physics, and expert systems. Industry contributes specialized knowledge and resources and prioritizes Partnership activities.

The areas of technology are:

Diagnostics and Imaging Technology addresses cutting-edge geophysical methods for improved reservoir characterization with a focus on improved borehole hardware and computational efforts for seismic processing and other exploration issues. The Partnership catalyzed formation of a 25-company collaboration which has become the industry focal point for this technology.

Oil and Gas Recovery Technology addresses a broad range of technologies aimed at improving production from existing fields and with specific emphasis on assisting independent producers. The industry interface is an Industry Review Panel consisting of more than 20 individuals representing independents, majors, and the service companies.

Drilling, Completion, and Stimulation Technology aims at better access to the reservoir through improved drilling and completion technologies. Currently, the laboratories participate in several joint industry projects fostered by two industry organizations: the Drilling Engineering Association (DEA) and the Completion engineering Association (CEA).

Environmental Technology addresses new technologies that are needed to produce more oil and gas from mature domestic sources while safeguarding the environment. Key issues to be addressed include: 1. Produced Water, 2. Stationary Source Emissions, 3. Risk Assessment, 4. Tank Bottoms and Sludge, 5. NORM, 6. Soil Remediation, 7. Vapor Recovery, 8. Offshore Structure D&D, and 9. Drilling Wastes.

Process and Refining Technology is an area under review by the Partnership as a logical extension of its existing activities.

DISCUSSION OF CURRENT ACTIVITIES

During 1997, T. W. Schmidt participated in the development of the recommendations for funding of the Partnership Programs on behalf of Oak Ridge National Laboratory. In addition T. W. Schmidt developed a collaborative project with the Idaho National Energy and Engineering Laboratory (INEEL) for funding of an Oil and Gas Recovery Technology Program. ORNL also was successful in obtaining funding in Diagnostic and Imaging Technology for a seismic interpretation project as well as a DeepLook project on reservoir imaging. Other activities include program planning with the Partnership, selection of a Partnership Steering Committee, hosting the 1997 Spring Meeting of the Petroleum Environmental Research Forum (PERF), and project monitoring.

CRUDE OIL COMPOSITION AND OIL RECOVERY

C. P. Thomas, M. R. Ally and N. R. Morrow

INTRODUCTION

Waterflooding is by far the most widely applied method for improved oil recovery and accounts for more than one-half of U.S. domestic oil production; similar proportions hold world wide. Waterflooding is still not well understood and estimation of oil recovery by waterflooding and accurate determination of waterflooding reserves remain serious problems.

The injected brine in a waterflood is obtained from the most convenient source and is usually of different composition than the connate water. Treatment of injected water and modification of its composition are dominated by considerations related to avoiding formation damage, principally fines migration and clay swelling, and mitigation of souring and corrosion. It has generally been believed that composition of the injected brine is immaterial to the efficiency of oil displacement. However, a growing body of laboratory data shows that the brine composition can have a highly significant effect on crude oil/brine/rock (COBR) interactions as evidenced by oil recovery by waterflooding and spontaneous imbibition.[1,2,3] For example, Fig. 1 shows that a change in brine composition can result in waterflood recovery differences of 16% of original oil in place (OOIP); Fig. 2 shows that diluting synthetic reservoir brine results in a systematic increase in oil recovery by up to about 50% OOIP. Although results are strongly dependent on crude oil composition, this trend has been observed for three distinctly different types of crude oil (an asphaltic crude oil, a highly waxy crude, and a crude with extremely low asphaltene content). Changes in oil recovery with cation valency and radius of hydration have also been observed. Crude oil properties (particularly the solvency of high molecular weight polar components) and modest increases in temperature have also been shown to have a major effect on COBR interactions and oil recovery. All of the observed phenomena appear to be dominated by the effect of COBR interactions on wettability. Selection, or adjustment, of injection brine composition in a way that alters wettability to advantage is a novel method of increasing oil recovery at low cost.

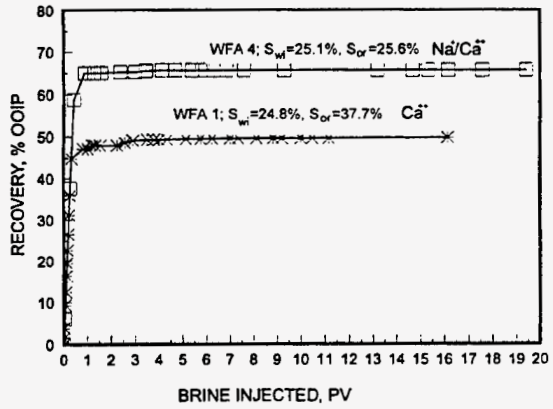

Fig. 1. Effect of brine composition on oil recovery.

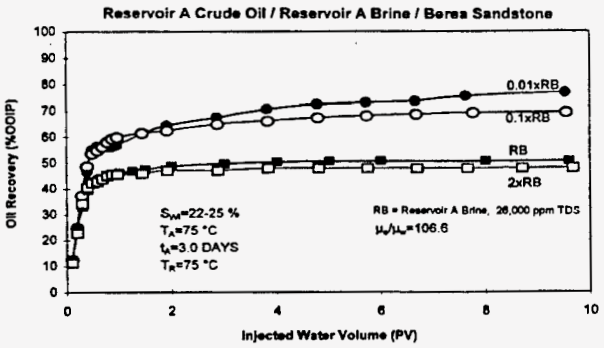

Fig. 2. Effect of brine dilution on oil recovery at reservoir temperature.

The objective of this project is to obtain a more complete understanding of the effects of brine composition, temperature, and crude oil properties on wettability and its effects on oil recovery. Results obtained to date for sandstone will be extended to other outcrop and reservoir cores of different mineralogy and pore structure (e.g., sandstones with varying clay content, and carbonates), and a broader range of crude oils. The final product will be a framework based on laboratory experiments and field evaluation, backed by theory, that can be used by operators (majors and independents) to improve waterflood oil recovery from specific reservoirs.

DISCUSSION OF CURRENT ACTIVITIES

The efforts in FY 1997 have focused n modeling pore structure and on stability and interfacial properties.

Wettability and pore structure are primary factors in determining the capillary behavior of porous media. A key characteristic of pore structure of real porous media is the angular corners of the pores. As a model of pore structure, angular tubes are much more realistic than the commonly used cylindrical tube model. However, their behavior is quite complicated because contact angle, corner angle, and the meniscus in the corners are all variables. The Mayer and Stowe-Princen (MS-P) theory of drainage, together with a detailed model of meniscus behavior in a corner during

imbibition, enables the relationships between capillary pressure and saturation to be investigated as a function of contact angle and pore geometry.

In this study,[4] a general relationship between contact angle, corner angle, liquid saturation, and the curvature of a meniscus in the corner of an *n*-sided tube is derived. For any corner angle, there is a critical contact angle at which the meniscus becomes flat and the capillary pressure falls to zero. Drainage of polygonal tubes (having cross-sections such as equilateral triangles and squares) is analyzed as a function of contact angle using the MS-P theory. For imbibition, there are two filling mechanisms: the tube can be filled by a meniscus advancing along the tube or it can be filled by expanding the menisci from the tube corners. For both mechanisms, the contact angle is treated as having either zero or finite contact angle hysteresis. Systematic changes in drainage and imbibition capillary pressure curves with contact angle are obtained. The results are qualitatively consistent with several features of the behavior of natural porous media, including the effect of wettability on the displacement efficiency of crude oil by water.

To investigate the use of a two parameter model for phase stability condition at liquid-liquid interfaces, the thermodynamic stability condition for the Brunauer-Emmett-Teller (BET) model was developed. The condition involves solution of two simultaneous quadratic equations to determine whether there are ranges of composition, site number (r) and the BET energy parameter (c), where c is a function of temperature and absorption energy, that predict instability of a single phase. A algorithm for the solution appears feasible.

REFERENCES

(1) X. Zhou, N. R. Morrow, and S. Ma, "Interrelationship of Wettability, Initial Water Saturation, Aging Time, and Oil Recovery by Spontaneous Imbibition and Waterflooding," SPE 35436, SPE/DOE Tenth Symposium on Improved Oil Recovery, Tulsa, OK, April 21-24,1996.

(2) J. S. Buckley, Y. Liu, X. Xie, and N. R. Morrow, "Asphaltenes and Crude Oil Wetting--The Effect of Oil Composition," SPE 35366, SPE/DOE Tenth Symposium on Improved Oil Recovery, Tulsa, OK, April 21-24,1996.

(3) H. O. Yildiz and N. R. Morrow, "Effect of Brine Composition on Recovery of Moutray Crude Oil by Waterflooding," *JPSE,* (in press).

(4) S. Ma, G. Mason, and N. R. Morrow, "Effect of Contact Angle on Drainage and Imbibition in Regular Polygonal Tubes,"*Colloids and Surfaces A: Physicochem. Eng. Aspects* **117**, 273-291, (1996).

COAL COMBUSTION RESEARCH

C. S. Daw

This section describes research and development related to coal combustion. The key activity involves the application of chaos theory for the diagnosis and control of fossil energy processes. It is known that fossil energy combustion devices, such as fluidized beds and pulsed combustors, can exhibit characteristic features of deterministic chaos. The ability to measure and describe chaotic components will contribute to greatly improved methods for characterizing, modeling, designing, and controlling commercial fossil energy processes such as combustion, coal gasification, hot-gas cleanup, and oil retorting. The Fossil Energy Program is involved in the evaluation of chaotic components in data from fluidized beds and other coal combustion processes.

ANALYSIS OF FBC DETERMINISTIC CHAOS

C. S. Daw

DISCUSSION OF CURRENT ACTIVITIES

Background

It has recently been discovered that the performance of a number of fossil energy conversion devices such as fluidized beds, pulsed combustors, steady combustors, and internal combustion engines are affected by deterministic chaos. It is now recognized that understanding and controlling the chaotic elements of these devices can lead to significantly improved energy efficiency and reduced emissions. Application of these techniques to key fossil energy processes are expected to provide important competitive advantages for U.S. industry.

Status Summary

A low level of activity involving theoretical and experimental data analysis has continued through this reporting period. The experimental data involved have consisted of time series measurements from fluidized beds and a bubble column. Theoretical studies have focused primarily on conceptual evaluations of chaos control as it might be applied to pulsed combustion. No new Fossil Energy Program funds have been received in FY 97, and we anticipate that this activity will be closed out by the end of the current fiscal year.

Fluidized Beds and Bubbles

A paper on experimental observations of the dynamics of a single column of rising bubbles was published in a special issue of Chemical Engineering Journal [1]. A key result described in this paper was that even though the overall dynamics are spatio-temporal, localized observations can be characterized in terms of low-dimensional chaos.

Investigations of passive acoustic signals from fluidized beds have shown that it is possible to develop very effective diagnostics using such signals. Two conference presentations were made [2,3] and a journal paper is being submitted [4]. Acoustic signals appear capable of providing much of the same information as pressure signals with a completely non-intrusive sensor.

Pulsed Combustion

A collaboration to study control of chaos in pulsed combustion has been started with researchers from the Naval Surface Warfare Center. To begin, we have focused on investigating extending the practical lean operating limit by means of feedback perturbations to the fuel and/or air inlet flows. Results of a theoretical investigation using a previously developed dynamic model have been submitted for publication [5].

REFERENCES

1. K. Nguyen, C. S. Daw, P. Chakka, M. Cheng, D. D. Bruns, C. E. A. Finney, and M. B. Kennel, "Spatio-temporal dynamics in a train of rising bubbles" Chemical Engineering Journal, Dec. 1996, Vol. 64, No. 1, pp 191-197.

2. J. S. Halow, C. S. Daw, and C. E. A. Finney, "Interpretation of Acoustic Signals from Fluidized Beds," Poster presentation, 5th World Congress of Chemical Engineering, San Diego, July, 1996.

3. C. E. A. Finney, M. B. Kennel, C. S. Daw, and J. S. Halow, "Nonlinear Time-Series Diagnostics of Fluidization Quality," Oral presentation, AIChE 1996 Annual Meeting, Chicago, November 14, 1996.

4. C. E. A. Finney, C. S. Daw, and J. S. Halow, "Measuring Slugging Bed Dynamics with Acoustic Sensors," Submitted to KONA: Powder and Particle, No. 15.

5. V. In, M. L. Spano, J. D. Neff, W. L. Ditto, C. S. Daw, K. D. Edwards, K. Nguyen, "Maintenence of Chaos in a Computational Model of a Thermal Pulse Combustor," submitted to CHAOS.

FOSSIL FUELS SUPPLIES MODELING AND RESEARCH

P. N. Leiby

The Strategic Petroleum Reserve (SPR) is a government-owned stockpile of crude oil intended to serve as a buffer against possible oil market disruptions. The overall purpose of this project is to develop and apply improved models and tools for SPR management. Current project efforts emphasize developing new modeling tools to explicitly and flexibly portray oil market uncertainty and SPR planning risk. Another task in this program area is the development of advanced computational tools for three-dimensional seismic analysis.

STRATEGIC PETROLEUM RESERVE PLANNING AND MODELING

P. N. Leiby

INTRODUCTION

The Strategic Petroleum Reserve (SPR) is a government-owned stockpile of crude oil intended to serve as a buffer against possible oil market disruptions. The overall purpose of this project is to develop and apply improved models and tools for SPR management. Current project efforts emphasize developing new modeling tools to explicitly and flexibly portray oil market uncertainty and SPR planning risk.

DISCUSSION OF CURRENT ACTIVITIES

Oak Ridge National Laboratory (ORNL) conducts model development and planning analyses for Strategic Petroleum Reserve (SPR) drawdown, distribution and other management activities, in support of the Office of Management Operations, Petroleum Reserves. The roles and objectives are:

1. to utilize, maintain, modify, and report on SPR analysis models;
2. to support development of SPR oil valuation and bid analysis tools;
3. to evaluate potential applications of DIS-Risk model approach to related energy policy issues;
4. to study role and value of risk information in SPR planning;
5. to evaluate SPR planning alternatives and roles of SPR; and
6. to provide analytical support for the SPR office.

Activities This Year

- Finished updating the DIS-Risk model to use the latest DOE oil market assumptions, consistent with recent AEO/IEO. This is part of the normal model

maintenance tasks required. NEMS modules were used to produce the needed reference data. The model was tested with the aforementioned changes.

- Provided a brief discussion of the benefits of the Strategic petroleum Reserve, based on numerical estimates from the DIS-Risk model. "Benefits of the U.S. Strategic Petroleum Reserve Program," Paul N. Leiby, February 15, 1996.

- Modifed the DIS-Risk Model, and tested it. Documentation of these changes and the results were provided in the draft report "Updates to DIS-Risk Model: Model Changes and Results Documentation," Draft, February 29, 1996, Paul N. Leiby and David C. Bowman.

- Delivered the report: "Updates to DIS-Risk Model: Model Changes and Results Documentation," Revised Draft, October 10, 1996, Paul N. Leiby and David C. Bowman.

- Participated in Energy Modeling Forum workshop on Energy Security, (November 12-13, 1996, (Washington D.C.) which explored the prospects for oil market disruptions. This EMF workshop will generate a new "influence diagram" approach to estimating likelihood of oil market supply disruptions, with input from industry, government, and academia. The resulting disruption probability curves may be used as another possible alternative set of inputs to SPR size and draw-rate planning analysis.

- Collaborated with DOE and ICF Inc. on SPR Model Review for Drawdown Rate Analysis.

ORNL also provided general analytical support to the SPR Office, including:

- Reviewing DOE analyses of SPR leasing approaches. ORNL produced two memoranda offering ideas on this topic: "Ideas Regarding the Leasing of Storage Capacity and the Economics of Negotiation," letter to W. Chilman from Paul Leiby, October 24, 1995; and "Ideas Foreign Storage of Strategic Oil Reserves in U.S. SPR Facilities," Donald Jones and Paul Leiby, January 1996.

ADVANCED COMPUTATIONAL TOOLS FOR 3-D SEISMIC ANALYSIS

J. Barhen C. Glover D. Reister V. Protopopescu

INTRODUCTION

The development of 3-D structural and stratigraphical models of hydrocarbon reservoirs is crucial for the future ability of the exploration industry to economically discover and produce oil and gas. It requires extensive use of 3-D seismic data. The corresponding computational tasks are extremely expensive and new ideas and methods are necessary to render them timely, efficient, and cost-effective. An important step for the advancement of the state of the art in 3-D seismic technology has been the collaborative 3-D Seismic Modeling Project undertaken by the United States' Society of Exploration Geophysicists (SEG), the European Association of Exploration Geophysicists (EAEG), and US Department of Energy (DOE) under GONII. This international collaboration has designed realistic subsurface models for two challenging and relevant exploration plays: a sub-salt reservoir and an overthrust structure. Two extensive 3-D seismic surveys have been carried out over these geological models, using thousands of supercomputer CPU hours and generating terabytes of data.

The present effort is conducted as part of the ACTI Program. Topics under investigation at CESAR/ORNL include time-parallel algorithms for solving the acoustic wave equation, global optimization methods for addressing the residual statics grand challenge, neural networks for seismic parameter estimation, and holographic visualization of seismic data.

Specific Project Objectives

The primary goal of CESAR is to spearhead computational innovations that would enable a revolutionary advance in 3-D seismic analysis. Our efforts under current limited funding focus on two tasks:

Global Optimization - A major degradation of seismic signals usually arises from near-surface geologic irregularities. The most important consequence of such irregularities is a distorted image of the subsurface structure, due to misalignment of signals caused by unpredictable delays in recorded travel times of seismic waves in the neighborhood of every source and receiver. The occurrence of severe residual statics (timing adjustments that can not be directly derived from topographic and well measurements), and the significant noise contamination render the automatic identification of large static shifts extraordinarily difficult.. This problem has usually been formulated in terms of Global Optimization, and, to date, Monte Carlo techniques (e.g., simulated annealing, genetic

algorithms) have provided the primary tools for seeking a potential solution. Such an approach is extremely expensive, and a major need exists for a break through paradigm which would enable the accurate and efficient solution of large scale problems. The ***objective of this task*** is to investigate the applicability of the TRUST methodology (developed at CESAR) to residual statics problems, to enhance the algorithms, and to carry out demonstrations using the SEG/EAEG dataset.

Neural Networks - The long-term objective of this effort is to demonstrate the viability of Artificial Neural Network (ANN) algorithms in estimating oil field reservoir parameters from remotely sensed seismic data. To accomplish this, one must first develop techniques to obtain an unbiased accuracy measure from a finite sample set. This measure should allow for meaningful comparisons not only between different ANN methods and architectures, but also with more conventional data processing schemes. The ***specific objectives of this task*** are then to (1) demonstrate the use of the k-fold cross validation technique to obtain confidence bounds on an ANN's accuracy statistic from a finite sample set; (2) demonstrate that the classification accuracy of an ANN can be dramatically improved by transforming data into an appropriately defined feature space; and (3) develop faster learning algorithms.

Benefits to DOE Mission

Since 1974, a core mission for DOE has been to reduce dependence on imported oil. In the "1995 National Assessment of United States Oil and Gas Resources" (USGS Circular 1118) by the U.S. Geological Survey, the total remaining oil in the onshore areas and State waters of the U.S. were estimated at 112.6 BB (Billion Barrels). Of this total, 20 BB are proved reserves, 60 BB are reserve growth in known fields, and 30 BB are undiscovered conventional resources.

The key to oil discovery is to use scientific techniques to find oil structures without having to drill expensive exploratory oil wells. The primary scientific techniques used to find oil structures is 3-D seismic analysis. The goal of this project is to develop advanced computational tools that reduce the cost and increase the precision of 3-D seismic analysis. Thus, it is directly focused on the DOE mission to reduce oil imports. It will also significantly contribute to the strategic plan issued by the Secretary of Energy (see, e.g., "Fueling a Competitive Economy", April 1994) in the area of Science and Technology.

This project also supports ORNL core competencies. In particular, our effort corresponds to the programmatic goal of developing and deploying "numerical algorithms for solving large-scale scientific and engineering problems" (see, e.g., ORNL R&D Strategic Plan, page 37), and contributes to the building of a world-class program in computational sciences.

Relation to Other DOE-funded Projects

The overall CESAR effort is undertaken as part of a set of collaborative tasks between three national laboratories (LANL, LLNL and ORNL), six universities (Caltech, Stanford, Colorado School of Mines, Houston, Rice, and Southern Alabama), and industry. SEG acts as the coordinator of the industry efforts and fourteen U.S. companies are participating. The global objective is to develop computational tools for 3-D seismic analysis, and test the products using the SEG/EAEG datasets. Topics being pursued at Los Alamos and Livermore include elastic modeling of the 3-D structures for comparison with the acoustic results, physical model development, imaging the SEG/EAEG dataset using approximate methods, evaluation of new cost-effective 3-D prestack imaging methods, and seismic imaging and inversion via multilevel distributed parallel processing. Individual tasks are linked in that they all make use of the SEG/EAEG datasets and have as their common goal the testing of new methods for evaluating the subsurface structures for oil and gas prospects.

SCIENTIFIC AND TECHNICAL ELEMENTS

In this section, we discuss the relation of our tasks to research being conducted by others in these fields. We highlight the importance of solving the problems being addressed, and comment on the significance of the underlying scientific and technical issues. A summary of the approach taken is presented, and a schedule of major activities is included. Each task is discussed separately.

Global Optimization for Residual Statics

In many geophysical experiments seismic energy is detected by receivers that are regularly spaced along a grid that covers the domain being explored. A source is positioned at some grid location to produce a shot. Time series data is collected from the detectors for each shot; then the source is moved to another grid node for the next shot.

A major degradation of seismic signals usually arises from near-surface geologic irregularities [1, 2, 3]. These include uneven soil densities, topography, and significant lateral variations in the velocity of seismic waves. The most important consequence of such irregularities is a distorted image of the subsurface structure, due to misalignment of signals caused by unpredictable delays in recorded travel times of seismic waves in a vertical neighborhood of every source and receiver. To improve the quality of the seismic analysis, timing adjustments (i.e., "statics corrections") must be performed. One typically distinguishes between "*field statics*", which correspond to corrections that can be derived directly from topographic and well measurements, and "*residual statics*", which incorporate adjustments that must be inferred statistically from the seismic data. The common occurrence of severe residual statics (where the dominant period of the recorded data is significantly exceeded), and the excessive

noise contamination render the automatic identification of large static shifts extraordinarily difficult. However, calculation of residual statics corrections is one of the economically most important optimization problems in the oil and gas industry. The corrections must be applied to all data that is recorded on land, and to many data sets that are recorded underwater. Every major oil company and seismic consulting firm has a group of experts on this problem. This problem has generally been formulated in terms of global optimization, and, to date, Monte-Carlo techniques (e.g., simulated annealing, genetic algorithms) have provided the primary tools for seeking a potential solution [3, 4, 5]. Such an approach is extremely expensive, and a major need has existed for a breakthrough paradigm which would enable the accurate and efficient solution of large-scale problems.

The statics corrections are typically done in a surface consistent manner to seismic traces corrected for *normal moveout* [2]; consequently, the correction time shifts depend only on the shot and receiver positions, and not on the ray path from shot to receiver. Shot corrections $\mathbf{S}$ correspond to wave propagation times from the shot locations to a reference plane, while the receiver corrections $\mathbf{R}$ are propagation times from the reference plane to receiver locations. From an operational perspective, data D_{ft} are provided by trace ($t = 1, \ldots N_t$), and sorted to common midpoint offset coordinates (CMP*stacking*). For each trace, the data consist of the complex Fourier components ($f = 1, \ldots N_f$) of the collected time series. Each trace t corresponds to seismic energy travel from a source s_t to a receiver r_t via a midpoint k_t. Assuming the availability of N_k common midpoints, we seek statics corrections $\mathbf{S}$ and $\mathbf{R}$ that maximize the total power E in the stacked data:

$$E = \sum_k E_k = \sum_k \sum_f |\sum_t \exp[2\pi i f (S_{s_t} + R_{r_t})] D_{ft} \delta_{kk_t}|^2 \ . \tag{1}$$

The above expression highlights the multimodal nature of E which, even for relatively low dimensional $\mathbf{S}$ and $\mathbf{R}$, exhibits a very large number of local minima. This is illustrated in Figure 1.

We can combine $\mathbf{S}$ and $\mathbf{R}$ into a single statics corrections vector, $\mathbf{x}$. If N_s is the number of source positions and N_r is the number of receivers, $\mathbf{x}$ is an N-vector, where $N = N_s + N_r$. Each parameter x_j can influence many components of the total stack power. Hence, the conventional formulation of this problem is tightly coupled, resulting in a dramatic increase of complexity with problem size.

The *key idea* we propose to explore in FY'97 is the introduction of new variables that would enable the stack power to be decoupled into N_k components. The advantage of such an approach is that it replaces the solution of *one* large-scale, usually intractable problem, with the massively parallel solution of a large number of much smaller problems. Some difficulty is, however, added by this paradigm. It concerns the solution of the inverse mapping, needed to recover the optimal statics in the original coordinate system.

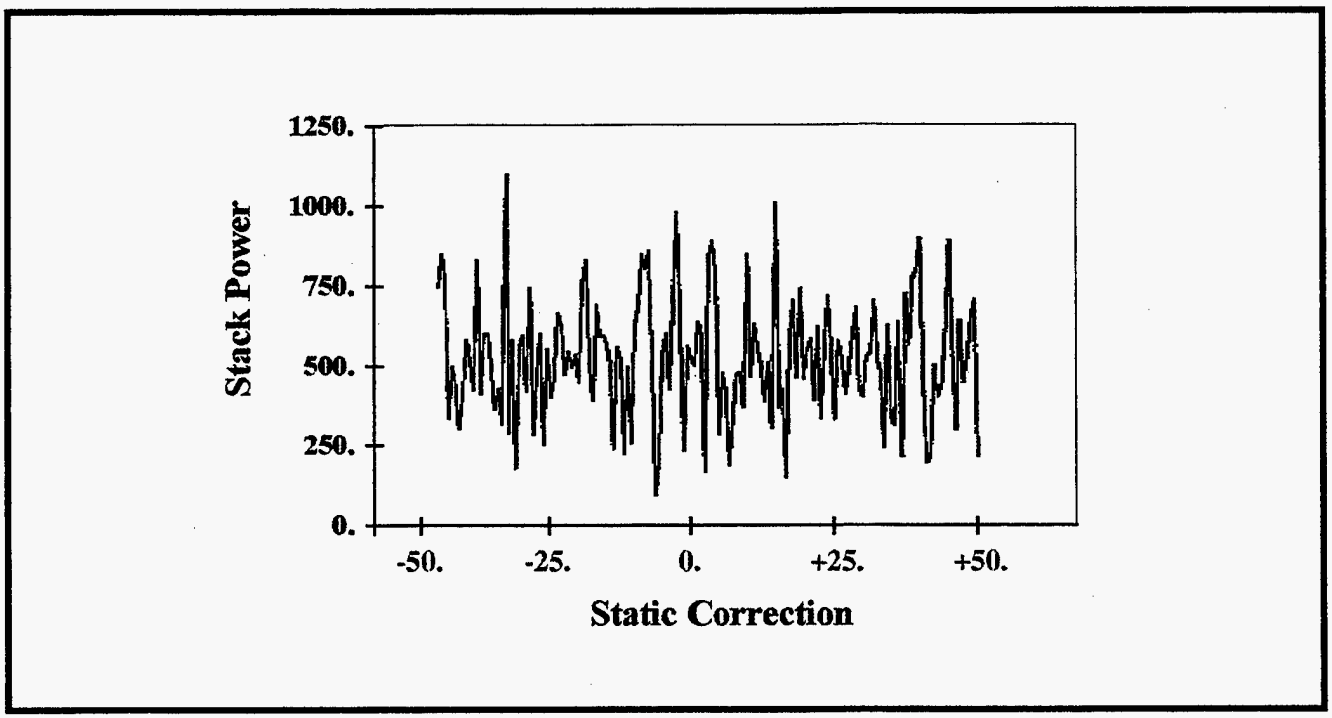

Figure 1. One-dimensional slice through a 154-dimensional objective function associated with a residual statics problem.

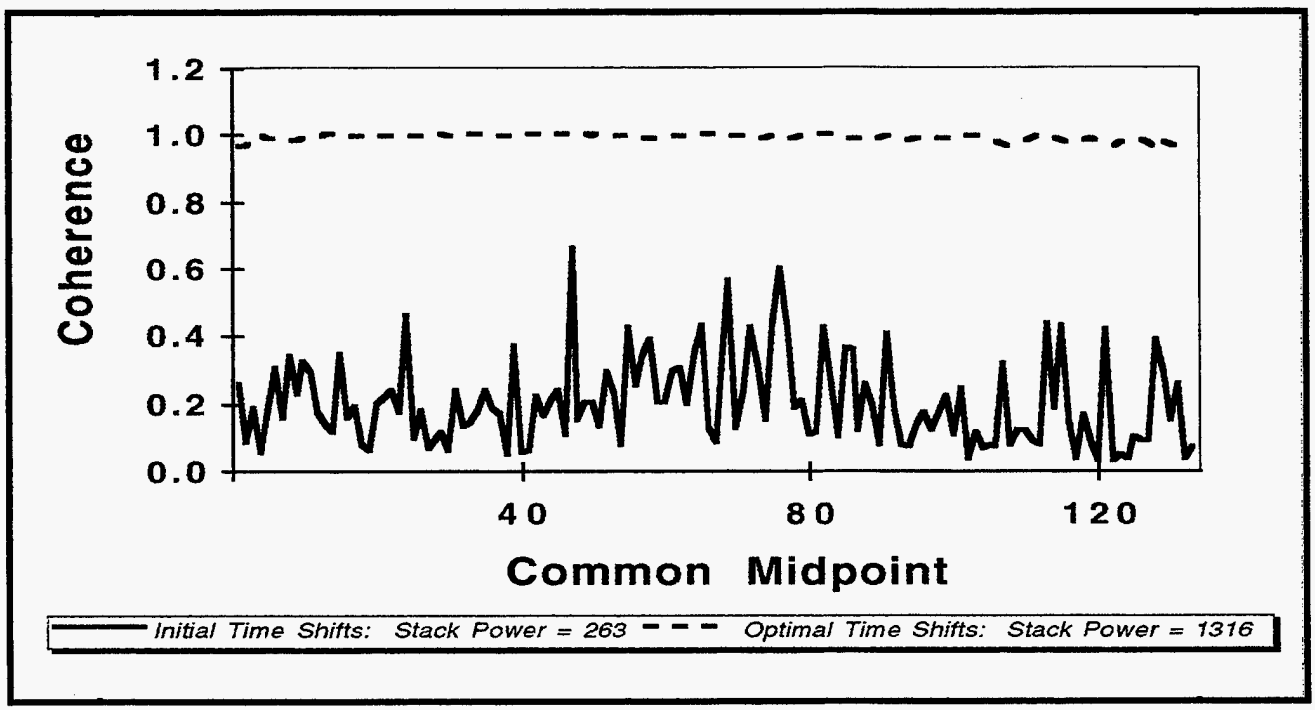

Figure 2. The coherence factors, i.e., the dimensionless ratios E_k / B_k, are plotted for each common gather using the initial and the optimal time shifts ("residual statics"). Ideally, at the global optimum, these ratios should be equal to one.

We will proceed as follows. Let $\mathbf{v} = \mathbf{Ax}$, where the matrix $\mathbf{A}$ specifies which sources and receivers are combined for each trace. From Eq (1), we observe that each k-contribution to E depends on a unique subset of $\mathbf{v}$, (i.e., ${}^k\mathbf{v}$, the subset of all traces with common CMP k). Since $\{{}^k\mathbf{v}\} \cap \{{}^{k'}\mathbf{v}\} = \emptyset$ for $k \neq k'$, the problem is fully decoupled. One must still determine the optimal parameter values, ${}^k\mathbf{v}_g$, that globally maximize the contribution of the k-th CMP gather to the total stack power. Notwithstanding the fact that $N_k \ll N$, this remains a formible obstacle for conventional optimization techniques. A specialized version of our novel global optimization methodology TRUST provides the opportunity for achieving a major breakthrough in this area.

TRUST_RS [6] solves the following optimization problem: given an objective function $f({}^k\mathbf{v})$, where ${}^k\mathbf{v}$ is an N_k dimensional vector that is constrained to lie in a domain $({}^kV)$, find the global minimum ${}^k\mathbf{v}_g$; that is, find a point ${}^k\mathbf{v}_g$ in ${}^kV$ such that $f({}^k\mathbf{v}_g) \leq f({}^k\mathbf{v})$ for all ${}^k\mathbf{v}$ in ${}^kV$. Since the goal in the residual statics problem is to maximize the total stack power (E), the objective function for TRUST_RS is: $f({}^k\mathbf{v}) = -E_k({}^k\mathbf{v})$. The TRUST_RS methodology combines the concepts of subenergy tunneling and non-Lipschitzian "terminal" repellers. The evolution of a deterministic nonlinear dynamical system incorporating these concepts provides the computational methanism for reaching the global minimum.

From an operational perspective, a series of cycles is executed. At the start of each cycle, TRUST_RS tunnels from a local minimum $({}^k\mathbf{v}^*)$, reached during the previous cycle, along a direction $\mathbf{p}$. The specific choice of $\mathbf{p}$ is discussed in [6]. For the first cycle, ${}^k\mathbf{v}^*$ is the initial point $({}^k\mathbf{v}^I)$. Define the function $h({}^k\mathbf{v})$ by: $h({}^k\mathbf{v}) = f({}^k\mathbf{v}) - f({}^k\mathbf{v}^*)$. Initially, ${}^k\mathbf{v} = {}^k\mathbf{v}^* + \delta\mathbf{p}$, and the algorithm tunnels in the $\mathbf{p}$ direction until either $h({}^k\mathbf{v})$ is negative or ${}^k\mathbf{v}$ escapes from ${}^kV$. If $h({}^k\mathbf{v})$ is negative, TRUST_RS finds the local minimum and the next cycle begins. When ${}^k\mathbf{v}$ escapes from ${}^kV$, the last found local minimum is the global minimum.

In a rigorous proof we have shown [7] that TRUST will always find the global minimum for the one-dimensional case (where ${}^k\mathbf{v}$ is a scalar). In the multi-dimensional case, only global descent has been proven to date. In practice, however, TRUST has been very successful in solving the standard SIAM benchmark problems.

To assess the potential performance of TRUST_RS, we considered a problem involving 77 shots and 77 receivers. A dataset consisting of 1462 synthetic seismic traces folded over 133 common midpoint gathers was obtained from CogniSeis Corporation [8]. It uses 49 Fourier components for data representation. Even though this set is somewhat smaller than typical collections obtained during seismic surveys by the oil industry, it is representative of the extreme complexity underlying residual statics problems. To derive a quantitative estimate of TRUST_RS's impact, let B_k refer to the upper bound of E_k in terms of $\mathbf{S}$ and $\mathbf{R}$. Using a polar coordinates representation for the trace data D_{ft}, i.e., writing $D_{ft} = \alpha_{ft} \exp(iw_{ft})$, we can prove that

$$B_k = \sum_f (\sum_t \alpha_{ft}\, \delta_{kk_t})^2 \ . \qquad (2)$$

The TRUST_RS results, illustrated in Figure 2, show the dramatic improvement in the coherence factor of each common gather. This factor is defined as the ratio $\kappa_k = E_k/B_k$, and characterizes the overall quality of the seismic image.

Major FY'97 Milestones: 1. apply TRUST_RS to large-scale seismic survey field data (6/97); **2.** submit technical article to *Geophysics* (8/97); **3.** submit second patent disclosure (9/97).

References

[1] Rothman, D., "Nonlinear Inversion, Statistical Mechanichs and Residual Statics Estimation", *Geophysics*, **50**(12), 2784-2796 (1985).

[2] Yilmaz, O., *Seismic Data Processing*, Society of Exploration Geophysicists, Tulsa, OK (1988).

[3] DuBose, J., "Practical Steps Toward Realizing the Potential of Monte Carlo Automatic Statics", *Geophysics*, **58**(3), 399-407 (1993).

[4] Scales, J. A., M. L. Smith and T. L. Fischer, "Global Optimization Methods for Multimodal Inverse Problems", *Jour. Comp. Phys.*, **103**, 258-268 (1992).

[5] Stoffa, P. L. and M. K. Sen, "Nonlinear Multiparameter Optimization Using Genetic Algorithms: Inversion of Plane Wave Seismograms", *Geophysics*, **56**,(11), 1794-1810 (1991).

[6] Barhen, J.,V. Protopopescu and D. Reister, "TRUST: An Algorithm for Global Optimization", to appear in *Science* (Early 1997)

[7] Barhen, J., and V. Protopopescu, "Generalized TRUST Algorithm for Global Optimization", in State of the Art in Global Optimization, C.A. Floudas and P.M. Pardalos eds., pp. 163-180, Kluwer Academic Press (1996).

[8] Dubose, J., personal communication (1996).

Neural Networks for Reservoir Parameter Estimation

The overall goal of our research is to demonstrate the effectiveness ANN computing techniques in providing an accurate estimation of petrophysical parameters that describe reservoir properties. The specific question we are attempting to address is whether ANNs can obtain accurate functional relationships between variations in subsurface rock properties (e.g., sand layer thickness, effective porosity, ratio of clay to sand, and saturation) and seismic response information (e.g., depth, s- and p-wave velocities, amplitude-versus-offset (AVO) slope and intercept).

The oil industry acquires and processes large volumes of seismic data. Various types of geoscience data (e.g., log, core, geochemical, gravity, magnetic, remote sensing)

are utilized in attempts to locate and characterize prospective oil and gas reservoirs. This data is extensively manipulated before it is analyzed and interpreted. Every data manipulation step is important and data processing can be time consuming and extraordinarily expensive. It is therefore imperative that the efficiency of data manipulation and data reduction be improved. It is expected that ANN technology can benefit the oil industry in two regards: (1) improved efficiency in data processing;and (2) more accurate characterization and prediction of reservoir properties obtained when training an ANN with measured or known data. In this task we focus on the latter aspect.

Historically, many "hydrocarbon indicators" have been proposed for qualitative prediction (for a detailed review, see [1]). In recent years, with the advent of modern computing, emphasis has shifted toward quantitative estimation. Some of the seminal contributions in that area are the seismic clustering analysis of Aminzadeh and Chatterjee [2] and the fuzzy pattern recognition method of McCormack [3]. Neural networks have also been considered [4,5], but the algorithms implemented in these studies did not take full advantage of the computational capabilities of the paradigm.

Approach. To test the effectiveness of ANNs in predicting different reservoir properties, we start with a suite of well logs from a known oil field. The first step is to generate blocked logs that have a limited number of layers with constant layer properties, for example using the method described in deFigueiredo [6]. Then we construct a suite of elastic models by perturbing the following reservoir properties in the depth interval of interest: water saturation, effective porosity, sand thickness, and sand/shale ratio. For everyone of these perturbations we generate a synthetic seismic shot gather. For every gather, we compute records of different seismic attributes within a time window. Our specific objectives and milestones for FY'97 are then as follows.

a. ***Develop accuracy measure***. We will seek and demonstrate (12/96) an unbiased first-order technique to validate a statistic p from a finite sample set (eg, K-fold cross validation).

b. ***Data dimensionality reduction.*** Much of the success with any regression or classification algorithm comes in the analysis and preparation of the input data. Traditionally, principal component analysis (PCA) has been used to determine whether variables are highly correlated and should be combined. It also indicates "insignificant variables". Here, however, these "insignificant variables" may represent the greatest separation between seismic classes of interest, whereas the "significant variables" may represent highly overlapping class distributions. Thus, we will seek a nonsingular transform that preserves class separation, while mapping the original input space into a lower dimensional space. We propose to construct it by simultaneusly diagonalizing the within (S_w) and between-class(S_b) covariance matrices associated with the seismic data (03/97).

c. ***Fast Learning algorithms.*** We will adapt fast neural learning algorithms we recently proposed (adjoint operators[7], alternating directions singular value decomposition) to the seismic estimation problem (09/97).

To obtain a preliminary assessment of the validity and benefits of our proposed approach, we have performed some computations using data provided by Unocal [8,9]. Figure 3 displays the mean accuracy and 95% confidence intervals for ANNs with one and two hidden layers and with a differing number of nodes in the hidden layers. Feature space transformation was *not* used, and all parameters in the Unocal dataset were included. The lower curve represents a single hidden layer. The upper curve represents an ANNs with 10 (5x5), 20 (15x5), 25(15x10), 30 (20x10), and 40 25x15) nodes in two hidden layers.

Figure_3

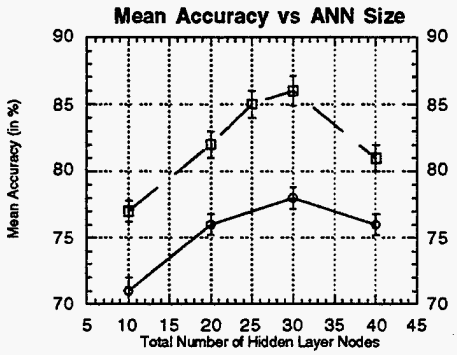

Figure_4

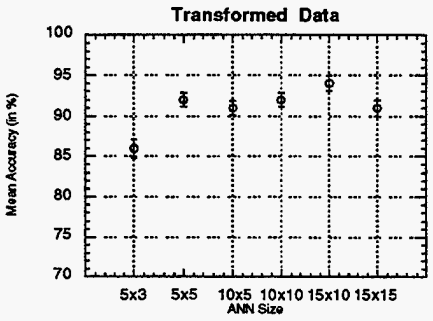

Figure 4 displays the mean accuracy and confidence intervals for an ANN with two hidden layers, where the *input data dimension was reduced using the generalized eigenspace transform.* These results seem to indicate that classification accuracy for estimating the sand thickness in an oil field reservoir is dramatically improved by our simultaneous eigendecomposition transform.. The new input space represents a feature space that maximizes linear separation between classes. Convergence time and accuracy are improved because the ANN must merely find nonlinear perturbations to the starting linear decision boundaries.

References

[1] Aminzadeh,F. and M.Simaan, *Expert Systems in Exploration*, SEG (1991).

[2] Aminzadeh, F. and Chatterjee, S. L., "Application of clustering in exploration seismology", *Geoexploration*, **23**, 147-159(1984).

[3] McCormack, M. D., "Neural computing in geophysics", *The Leading Edge of Exploration*, **10**(1), 11-15 (1990).

[4] Huang,H. and M.A.Williamson, "Geological Pattern Recognition and Modeling with a General Regression Neural Network", *Can.J.Expl.Geoph.*, **30**(1), 60-68 (1994).
[5] Vukelic, M. and E.Miranda, "Neural Networks in Petroleum Engineering", *Int.J.Neur.Sys.*,**7**(2), 187-194 (1996).
[6] deFigueiredo, R., F.Aminzadeh, and Maccato, A., "A Visualization Tool for Well Log Blocking", *Seismic Exploration*, **5**(1), 79-92 (1996).
[7] Barhen,J. and N.B.Toomarian, "Neural Network Training by Integration of an Adjoint System of Equations forward in time", *U.S. Patent pending* (NPO-18586-1-CU); ***see also:*** Toomarian, N.B. and J.Barhen, "Fast Temporal Neural Learning using Teacher Forcing", *U.S. Patent No. 5,428,710* (March 28,1995).
[8] Glover, C. et al. , "Neural Network Accuracy Measures and Data Transforms Applied to Seismic Parameter Estimation", *NEURAP'97* ,pp 161-168 Marseille, France (1997).
[9] Toomarian, N.B. et al., "Oil Reservoir Properties Estimation using Neural Networks", *NEURAP'97*, pp 133-136, Marseille, France (1997).

Project Output

There were two major technical accomplishments: the methodology development and demonstration of TRUST_RS, and the successful proof-of-concept application of neural networks to reservoir parameter estimation. These accomplishments are documented in one journal article (***Science***) and two refereed conference papers (NEURAP'97. There was also one patent disclosure (with an additional forthcoming):

- Reister,D. and J.Barhen, "Method for Calculating Residual Statics for Seismic Data" (July 24, 1996).

A nondisclosure agreement was signed with CogniSeis, which also expressed interest in licensing the TRUST_RS technology.

ADVANCED TURBINE SYSTEMS

MATERIALS/MANUFACTURING ELEMENT OF THE ADVANCED TURBINE SYSTEMS PROGRAM

M. A. Karnitz

INTRODUCTION

The DOE Offices of Fossil Energy and Energy Efficiency and Renewable Energy have initiated a program to develop advanced turbine systems for power generation. The objective of the Advanced Turbine Systems (ATS) Program is to develop ultra-high efficiency, environmentally superior, and cost competitive gas turbine systems for utility and industrial applications. One of the supporting elements of the ATS Program is the Materials/Manufacturing Technologies Task. The objective of this element is to address the critical materials and manufacturing issues for both industrial and utility gas turbines.

DISCUSSION OF CURRENT ACTIVITIES

No contribution was received for work performed during this reporting period.

INTERNAL DISTRIBUTION

1. M. R. Ally
2. J. Barhen
3. T. M. Besmann
4. R. A. Bradley
5. K. Breder
6. T. D. Burchell
7–10. P. T. Carlson (4)
11. D. F. Craig
12. C. S. Daw
13. G. M. Goodwin
14. E. Greenbaum
15–19. R. R. Judkins (5)
20. E. N. Kaufman
21. P. N. Leiby
22. C. T. Liu
23. C. G. McKamey
24. R. L. Miller
25. T. W. Schmidt
26. J. H. Schneibel
27. J. Sheffield
28. V. K. Sikka
29. A. J. Stewart
30. D. P. Stinton
31. R. W. Swindeman
32. P. F. Tortorelli
33. I. G. Wright
34. Central Research Library
35. Laboratory Records, ORNL-RC
36–37. Laboratory Records, OSTI (2)

EXTERNAL DISTRIBUTION

38. C. T. Alsup, U.S. Department of Energy, Federal Energy Technology Center, 3610 Collins Ferry Road, P.O. Box 880, Morgantown, WV 26507-0880
39. W. T. Bakker, Electric Power Research Institute, P.O. Box 10412, 3412 Hillview Avenue, Palo Alto, CA 94303
40. A. L. Baldwin, U.S. Department of Energy, Federal Energy Technology Center, 626 Cochrans Mill Road, P.O. Box 10940, Pittsburgh, PA 15236-0940
41. D. J. Beecy, U.S. Department of Energy, Fossil Energy Office of Advanced Research, FE-72, 19901 Germantown Road, Germantown, MD 20874-1290
42. R. G. Bidwell, Jr., U.S. Department of Energy, Office of Planning and Financial Management, Petroleum Reserves, FE-431, 3G-043/FORS, Washington, DC 20585
43. H. G. Borgstrom, U.S. Department of Energy, Office of Planning and Financial Management, Petroleum Reserves, FE-43, 3G-038/FORS, Washington, DC 20585
44. R. J. Braitsch, Department of Energy, FE-4, 4G-055/FORS, Washington, DC 20545
45. R. A. Carabetta, U.S. Department of Energy, Federal Energy Technology Center, 626 Cochrans Mill Road, P.O. Box 10940, Pittsburgh, PA 15236-0940
46. H. F. Chambers, U.S. Department of Energy, Federal Energy Technology Center, 626 Cochrans Mill Road, P.O. Box 10940, Pittsburgh, PA 15236-0940
47. A. B. Crawley, U.S. Department of Energy, National Petroleum Technology Office, P.O. Box 3628, Tulsa, OK 74101
48. R. A. Dennis, U.S. Department of Energy, Federal Energy Technology Center, 3610 Collins Ferry Road, P.O. Box 880, Morgantown, WV 26507-0880
49. Department of Energy, Deputy Assistant Manager for Energy, Research and Development, Oak Ridge Operations Office, P.O. Box 2008, Oak Ridge, TN 37831-6269
50. L. W. R. Dicks, Shell Development Company, P.O. Box 1380, Houston, TX, 77251-1380
51. H. Feibus, U.S. Department of Energy, FE-23, 19901 Germantown Road, Germantown, MD 20874-1290

52. S. G. Fishman , Office of Naval Research, Code 431, 800 N. Quincy Street, Arlington, VA 22217
53. R. D. Furiga, U.S. Department of Energy, FE-40, 3G-024/FORS, Washington, DC 20585
54. D. W. Geiling, U.S. Department of Energy, Federal Energy Technology Center, 3610 Collins Ferry Road, P.O. Box 880, Morgantown, WV 26507-0880
55. F. M. Glaser, U.S. Department of Energy, Office of Fossil Energy, FE-72, 19901 Germantown Road, Germantown, MD 20874-1290
56. P. M. Goldberg, U.S. Department of Energy, Federal Energy Technology Center, 626 Cochrans Mill Road, P.O. Box 10940, Pittsburgh, PA 15236-0940
57. L. E. Graham, U.S. Department of Energy, Federal Energy Technology Center, 3610 Collins Ferry Road, P.O. Box 880, Morgantown, WV 26507-0880
58. L. G. S. Gray, Alberta Research Council, Oil Sands Research Department, P.O. Box 8330, Postal Station F, Edmonton, Alberta, Canada T6H5X2
59. J. S. Halow, U.S. Department of Energy, Federal Energy Technology Center, 3610 Collins Ferry Road, P.O. Box 880, Morgantown, WV 26507-0880
60. S. Harding , Consolidation Coal Company, 4000 Brownsville Road, Library, PA 15129
61. A. M. Hartstein, U.S. Department of Energy, Office of Fossil Energy, FE-32, D-122/GTN, Washington, D.C. 20585
62. J. L. Hebb, U.S. Department of Energy, Federal Energy Technology Center, 626 Cochrans Mill Road, P.O. Box 10940, Pittsburgh, PA 15236-0940
63. N. T. Holcombe, U.S. Department of Energy, Federal Energy Technology Center, 3610 Collins Ferry Road, P.O. Box 880, Morgantown, WV 26507-0880
64. C. M. Huang, Tennessee Valley Authority, Energy Demonstration & Technology, MR 2N58A, Chattanooga, TN 37402-2801
65. W. J. Huber, U.S. Department of Energy, Federal Energy Technology Center, 3610 Collins Ferry Road, P.O. Box 880, Morgantown, WV 26507-0880
66. D. S. Jewett, U.S. Department of Energy, Office of Fossil Energy, FE-222, 713/ROSS, Washington, D.C. 20585
67. S. S. Kim, U.S. Department of Energy, Federal Energy Technology Center, 626 Cochrans Mill Road, P.O. Box 10940, Pittsburgh, PA 15236-0940
68. S. R. Lee, U.S. Department of Energy, Federal Energy Technology Center, 626 Cochrans Mill Road, P.O. Box 10940, Pittsburgh, PA 15236-0940
69. Lloyd Lorenzi, Jr., U.S. Department of Energy, Federal Energy Technology Center, 626 Cochrans Mill Road, P.O. Box 10940, Pittsburgh, PA 15236-0940
70. A. M. Manaker, Tennessee Valley Authority, 1101 Market Street, 3A Missionary Ridge, Chattanooga, TN 37402-2801
71. G. V. McGurl, U.S. Department of Energy, Federal Energy Technology Center, 626 Cochrans Mill Road, P.O. Box 10940, Pittsburgh, PA 15236-0940
72. T. J. McMahon, U.S. Department of Energy, Federal Energy Technology Center, 3610 Collins Ferry Road, P.O. Box 880, Morgantown, WV 26507-0880
73. H. S. Meyer, Gas Research Institute, 8600 West Bryn Mawr Avenue, Chicago, IL 60631
74. P. J. Musser, U.S. Department of Energy, Office of Fossil Energy, FE-232, C-129/GTN, Washington, D.C. 20585
75. H. M. Ness, U.S. Department of Energy, Federal Energy Technology Center, 3610 Collins Ferry Road, P.O. Box 880, Morgantown, WV 26507-0880
76. J. E. Notestein, U.S. Department of Energy, Federal Energy Technology Center, 3610 Collins Ferry Road, P.O. Box 880, Morgantown, WV 26507-0880
77. J. Oakey, British Coal Corporation, Coal Technology Development Division, Stoke Orchard, Cheltenham, Glocestershire, England GL52 4ZG

78. Aksel Olsen, Risoe National Laboratory, P.O. Box 49, DK-4000, Roskilde, Denmark
79. M. H. Rawlins, Department of Energy, Oak Ridge Operations, P.O. Box 2008, Building 4500N, MS 6269, Oak Ridge, TN 37831
80. S. E. Rogers, U.S. Department of Energy, Federal Energy Technology Center, 626 Cochrans Mill Road, P.O. Box 10940, Pittsburgh, PA 15236-0940
81. L. A. Ruth, U.S. Department of Energy, Federal Energy Technology Center, 626 Cochrans Mill Road, P.O. Box 10940, Pittsburgh, PA 15236-0940
82. T. A. Sarkus, U.S. Department of Energy, Federal Energy Technology Center, 626 Cochrans Mill Road, P.O. Box 10940, Pittsburgh, PA 15236-0940
83. C. E. Schmidt, U.S. Department of Energy, Federal Energy Technology Center, 626 Cochrans Mill Road, P.O. Box 10940, Pittsburgh, PA 15236-0940
84. D. K. Schmidt, U.S. Department of Energy, Federal Energy Technology Center, 3610 Collins Ferry Road, P.O. Box 880, Morgantown, WV 26507-0880
85. R. C. Searles, Mobil Research & Development Corporation, P.O. Box 1026, Princeton, NJ 08540
86. J. D. Shages, U.S. Department of Energy, Office of Planning and Financial, Management, Petroleum Reserves, FE-432, 3G-052/FORS, Washington, DC 20585
87. T. B. Simpson, U.S. Department of Energy, Office of Fossil Energy, FE-231, 3003/270, 19901 Germantown Road, Germantown, MD 20874-1290
88. Marvin I. Singer, Senior Advisor, Department of Energy, Advanced Research Policy and Planning Team, 4G-052/FORS, Washington, DC 20585
89. W. C. Smith, U.S. Department of Energy, Federal Energy Technology Center, 3610 Collins Ferry Road, P.O. Box 880, Morgantown, WV 26507-0880
90. J. Stringer, Electric Power Research Institute, P.O. Box 10412, 3412 Hillview, Avenue, Palo Alto, CA
91. T. M. Torkos, U.S. Department of Energy, Federal Energy Technology Center, 626 Cochrans Mill Road, P.O. Box 10940, Pittsburgh, PA 15236-0940
92. M. Van de Voorde, European Communities Joint Research Centre, Petten Establishment, P.O. Box 2, 1755 ZG Petten, The Netherlands
93. J. K. Wachter , U.S. Department of Energy, Federal Energy Technology Center, 3610 Collins Ferry Road, P.O. Box 880, Morgantown, WV 26507-0880
94. T. C. Wesson, U.S. Department of Energy, National Petroleum Technology Office, P.O. Box 3628, Tulsa, OK 74101
95. C. M. Zeh, U.S. Department of Energy, Federal Energy Technology Center, 3610 Collins Ferry Road, P.O. Box 880, Morgantown, WV 26507-0880

Report Number (14) ORNL--6924

Publ. Date (11) 199707

Sponsor Code (18) DOE/FE, XF

UC Category (19) UC-101, DOE/ER

DOE